MONITORING OF TREE SPECIES USING OBJECT BASED TIME SERIES ANALYSIS: -A CASE STUDY OF ACACIA XANTHOPHLOEA SPP IN LAKE NAKURU NATIONAL PARK, KENYA

ANNE ACHIENG OSIO
B.Sc. (TUK); M.Sc. (Egerton)
EEGX/06446P/2017

A Thesis Submitted in Partial Fulfilment of the Requirements for the Award of the Degree of Doctor of Philosophy in Geoinformatics
in
The School of Surveying and Spatial Sciences
of
The Technical University of Kenya

(August, 2023)

DECLARATION

This Thesis is my original work and has not been presented in any other Institution for a degree award or other qualification.

ANNE ACHIENG OSIO

REG. No EEGX/06446P/2017

Signature... ....Date......08/08/2023....................................

This Thesis has been submitted with our Approval as Supervisors

Signature........ ....Date..........07/08/2023...................

PROF. SEBASTIEN LEFEVRE

PROFESSOR IN COMPUTER SCIENCE

UNIVERSITY OF SOUTH BRITTANY, VANNES, FRANCE

Signature..... ....Date..........10/08/2023.................

DR. SAMSON AYUGI

SENIOR LECTURER IN GEOINFORMATION SCIENCE

THE TECHNICAL UNIVERSITY OF KENYA.

DEDICATION

This thesis is dedicated to my family, whose unwavering love and understanding have been my rock throughout this journey. Their constant support has been the driving force behind my success.

ACKNOWLEDGMENT

I would wish to thank the institutions and persons whose assistance and guidance were instrumental in the completion of this project. I want to express my thankfulness to God, without whom I could not have finished my course. My sincere gratitude to my supervisors, Dr. Samson Ayugi and Prof. Sebastien Lefèvre, for their advice throughout this study. The Kenya National Research Fund (K-NRF), the Kenya National Council for Science, Technology, and Innovation (NACOSTI), The University of South Brittany (UBS), The Hubert Curien Partnership (PHC), and Campus France were the organizations that provided funding for the collaboration between The Technical University and the University of South Brittany (UBS), France. Sincere thanks to Dr. Kirui and Dr. Simon Langat (NACOSTI), who in the initial stages made arrangements for my internship to attend Laboratory sessions in UBS, France. To Dr. Onsare, who took up the responsibility of grants management from NACOSTI thus ensuring smooth running of the project. To Kenya wildlife services (KWS) who gave us the chance to conduct Drone surveys in Lake Nakuru National Park. To The Technical University Vice-Chancellor Prof. Francis Aduol, who consistently provided me study leave whenever need arose.

To the French Embassy in Kenya who provided Return Air tickets and VISA at subsidized rates on the basis of my PHD internship in UBS. I would also like to register my gratitude to the OBELIX Research team at the UBS under the leadership of Prof. Sebastien Lefèvre for their support during my numerous visits in Vannes, France. I highly appreciate the free Laboratory space provided by UBS on the basis of their collaboration with TUK. The scientific support provided by members of the OBELIX team at the French Laboratory was so immense that at no time did I feel deprived of the much-required scientific support. The possibility of free access to data especially from the European Space Agency (ESA) and AIRBUS DS was made possible through the UBS laboratory space, hardware and software. Acquisition and analysis of Big Data from their satellite space was made possible during the numerous visits abroad. Many thanks to AIRBUS DS for the providing us with access to Pleiades-1A imageries through DUNAMIS (THEIA). My sincere gratitude to UBS for providing me with opportunity for collaborative paper writing and publishing in State-of-the-art Journals. In addition, I would like to thank Raccine-Divet, an intern at the University of South Brittany for having implemented the OBIA for time series code (OBIATS.py). To Christian Weise (Trimble, Germany) for constantly providing me with updated eCognition Developer License since the inception of my studies in year 2017. I am deeply indebted to everyone who took part in this journey, including my colleagues Mr. Fredrick Onyango and Mr. Peter Odwe from the School of Surveying and Spatial Sciences (TUK) who participated in carrying out Drone Surveys around Lake Nakuru National Park.

TABLE OF CONTENTS

LIST OF TABLES

LIST OF FIGURES

LIST OF ABBREVIATIONS AND ACRONYMS

AOI	Area of Interest
AP	Attribute Profiles
BOA	Bottom of The Atmosphere Reflectance
DL	Deep Learning
DN	Digital Number
EMS	Electro-Magnetic Spectrum
ESA	European Space Agency
ETM+	Enhanced Thematic Mapper plus
GEOBIA	Geographical Object Based Image Analysis
GIS	Geographical Information Systems
HH	Horizontal-Transmit, Horizontal-Receive
HV	Horizontal-Transmit, Vertical-Receive
ISODATA	Iterative Self Organizing Data Analysis Technique
K-NN	K-Nearest Neighbor
LAI	Leaf Area Index
LIDAR	Light Detection and Ranging
LULC	Land Use Land Cover
MMU	Minimum Mapping Unit
MODIS	Moderate Resolution Imaging Spectroradiometer
MSI	Multispectral Imager

NDBI	Normalized Difference Burnt Index
NDVI	Normalized Difference Vegetation Index
NDWI	Normalized Difference Water Index
NIR	Near Infra-Red
OBIA	Object Based Image Analysis
RADAR	Radio Detection and Ranging
RBF	Radial Basis Function
ROC	Receiver Operator Characteristics
SAR	Synthetic Aperture Radar
SMO	Sequential Minimal Optimization
SPOT	Satellite Pour l'Observation de la Terre
SWIR	Short Wave Infra-Red
TM	Thematic Mapper
TOA	Top of The Atmosphere Reflectance
TWDTW	Time Warping Dynamic Time Warping
UAV	Unmanned Aerial Vehicles
USGS	United States Geological Surveys
UTM	Universal Transverse Mercator
WEKA	Waikato Environment for Knowledge Analysis
WGS	World Geographic Surveys

DEFINITIONS OF TERMS USED

Remote Sensing (R.S) – Is the Art and Science of obtaining information about an object, area or phenomena through the analysis of data acquired that is not in contact with the device, area or phenomena under investigation.

Geographic Information Systems (G.I.S) – Is a conceptualized framework that provides the ability to capture, store and analyze spatial and geographic data for the sake of visualization on the final map.

Geographic Resource Analysis Support System (GRASS) – One stop shop that integrates Geographical Information Systems (G.I.S), image processing and analysis.

Orfeo Toolbox (OTB) – Is an open-source project for state-of-the-art remote sensing, developed by an open-source community that can process high resolution optical, multi-spectral and Radar imageries at terabyte scale.

TIMESAT– Is an open-source program that can handle long time-series, hence providing information on the shifts in the spatial distribution of vegetation and enabling exploration and extraction of seasonality parameters from a given series of data.

eCognition Developer – Is a commercial software used for automatic feature extraction by emulating the human cognitive powers to fuse geospatial data (pixels/points) not in isolation but in context through iterations hence recognizing groups of pixels and objects turning them into picture form.

Quantum-G.I.S (QGIS) – Is an open-source cross platform desktop Geographic Information System (G.I.S) application that supports viewing, editing and analysis of geospatial data.

SLIC-K Algorithm – A combination of the state-of-the-art SLIC superpixel segmentation and the K-means classification algorithms.

.

Sensor2Cor plugin – The plugin that consists of a processor that converts the Sentinel-2 Level-1C Top-of-The-Atmosphere (TOA) reflectance products to Sentinel-2 Level-2A which is the Bottom-of-The Atmosphere reflectance product (Gašparović & Jogun, 2018).

SNAP – Is an open-source-software developed by European Space Agency (ESA) for the purpose of analyzing products from the Sentinel Missions.

Phenology – Is the study of plant’s life cycle and how these will be affected by seasonal changes in the climatic and Environmental Aspect.

Physiological Parameters – are parameters that are used to measure the altered physiological response of living organisms caused by physical, chemical or biotic environmental factors that tend to shift the equilibrium away from its optimal Thermodynamic state (Füzy et al., 2019).

RADAR – Is a Method of finding the position and velocity of an object by bouncing a radio wave off it and analyzing the reflected wave. It's an acronym for Radar Detection and Ranging.

Difference Image is the image prepared by subtracting the digital values of pixels in one image from those in the second image to produce a third set of pixels. This third set is used to form the difference image.

.

ABSTRACT

The significance of wetlands as suppliers of ecosystem services to flora and wildlife in conservation zones is examined in this study. *Acacia xanthophloea* trees in Kenya's Lake Nakuru National Park are the subject of particular attention since they are in danger of going extinct as a result of repeated floods. This study attempts to detect and quantify the damage to the trees over time in order to comprehend the rate of their deterioration in order to address this issue. To identify and categorize Acacia xanthophloea trees in the Lake Nakuru riparian reserve, the study used an object-based image approach to determine the most efficient model for this task, a variety of spaceborne and aerial sensing technologies were used, including multi-temporal and multi-spatial. The overall goal of the study was to quantify Acacia xanthophloea and related plant species in terms of spectral, spatial, and contextual features in order to determine their degree of deterioration in both space and time. The study shows that the OBIA-Random Forest model and particular training techniques successfully and accurately identified Acacia xanthophloea trees. To identify riparian vegetation before and after floods, various algorithms were used, revealing changes in vegetation coverage brought on by flooding. The health and changes in vegetation degradation were monitored over time using NDVI (Normalized Difference Vegetation Index) maps. Classification of non-degraded forests, degraded forests, and submerged degraded forests was done using temporal profiles based on Landsat time series. The study also tested a variety of data processing methods, including the use of CNN frameworks on datasets based on UAVs and high-resolution Pleiades-1A images. The findings indicated alterations in Acacia xanthophloea coverage throughout various time periods and places, pointing to both gains and losses in tree populations. The importance of wetlands and Acacia xanthophloea trees in providing ecosystem services is highlighted by this study's findings. The study used a range of remote sensing tools and analysis techniques to identify, measure, and monitor the damage done to these trees over time. The results have consequences for conservation initiatives and offer guidance for managing and preserving biodiversity in ecosystems with similar wetlands. In order to stop the extinction of Acacia xanthophloea trees and improve general conservation practices, the technique chosen, incorporating the OBIA approach, provides a useful tool for swift response and management plans.

Keywords*: *OBIA, Acacia xanthophloea, Phenology, Machine Learning, Deep Learning, Landsat, ALOS PALSAR, Pleiades, Sentinel-1, Sentinel-2, Synthetic Aperture Radar, Unmanned Aerial Vehicles, Time series

CHAPTER ONE:

INTRODUCTION

1.1 BACKGROUND

Dynamic changes on East African wildlife ecosystem Landscapes are primarily attributed to anthropogenic changes in recent past. These factors are partly attributed by long-term climatic perturbations and landscape-scale changes (Githumbi et al., 2018). According to (Western et al., 2019) loss of biodiversity remain a major threat to the tourism sector in Kenya. Recent findings have pointed out factors that are impacting pressure on the East African ecological Landscape which includes human population explosion and it's developments (Payn et al., 2015) and the herbivore population as the major cause of pressure on water resources (Galvin et al., 2004).

These factors have led to wildlife landscape degradation (i.e. National Parks and reserves) (Gowreesunkar et al., 2022) and biodiversity loss (Western et al., 2019). To understand the effect of flooded wetlands on riparian vegetation degradation, it's important to use the existing Multi-date and Multi-Temporal Remote sensing imageries i.e. both Optical and Radar and techniques and Object Based Image Analysis (OBIA) in conjunction with Machine learning and Deep learning techniques to extract information on species degradation over time.

Lake Nakuru National Park is located 170-km northwest of Nairobi. It is situated in the east-west transportation corridor that runs the length of the nation, connecting the coast of Kenya with the area around Lake Victoria and the neighbouring country of Uganda (Odada et al., 2004). One of the highest lakes in the Rift Valley's central Kenya dome is Lake Nakuru (1759.0 meters above sea level). The hydrological equilibrium of the lake is impacted by it's high elevation. There are perennial springs along the eastern shoreline, including the Baharini Springs. Lake Nakuru's hydrology depends on catchment supplies from rivers, necessitating catchment integrity to maintain lake levels (Mbithi, 2016).

The lake is a hydrologically damaged environment due to its shallow depth, high evaporation rates, and seasonal rivers because it lacks the capacity to endure the hydrological impacts brought on by watershed processes (Western et al., 2019). The untreated sewage from Nakuru Town as well as four seasonal rivers Makalia, Nderit, Naishi, Njoro, and Larmudiac drain into Lake Nakuru (Alon et al., 2019). On the Lake’s riparian reserve lies Acacia xanthophloea tree strands providing a buffer around the lake and other open water bodies against siltation and pollutants. Acacia xanthophloea trees have existed around Lake Nakuru riparian over the years, providing ecosystem services to the lake by regulating siltation and trapping of pollutants.

In recent times, the lake has been swelling beyond it’s designated boundary (Caroline ngweno,2010) since the year 2010 (Onywere et al.,2013), hence causing massive degradation on the Acacia trees around the lake (See figure 1.1). The absence of Acacia xanthophloea has caused great harm to the zooplankton and phytoplankton that exists inside and on the periphery of the lake (Odada et al., 1981 ; Alon et al., 2019). Since the flamingos also depend on the phytoplankton for their survival, they ended up dying from the consumption of contaminated aquatic plants (Avni, 2020).

Recent studies have confirmed that most of the waterfowls were reported to have migrated to cleaner waters such as Lake Natron, located in the neighboring country, Tanzania (Thampy, 2023). The status of Lake Nakuru as ‘wetland of international importance’, calls for the wildlife managers, conservationists and policy makers to make wise use of wetlands and to implement policies engraved in the Ramser Convention of 1971 (Osio et al., 2022) of which Kenya is a signatory. This study aimed at assessing the rate of Acacia xanthophloea degradation around Lake Nakuru National Park using an Object based Image Analysis (OBIA) Approach, hence providing policy makers, conservationists, hydrologists and wildlife Managers with a decision making tool.

1.2 IMPORTANCE OF WETLANDS

Wetlands provide many advantages to the environment and humans such as Purification of water, flood risk regulation, buffering of shorelines, soil and water conservation, trapping of pollutants, as well as provision of aesthetic and recreational values among many (Merchant et al., 2019; Franklin & Ahmed, 2017; Ji et al., 2015).

Wetlands are also a great habitat for humans, flora and fauna including one-third of all endangered species (Merchant et al., 2019; Arthington et al., 2016). Due to their vital biological services, wetlands have been called the kidneys of nature (Sharma & Singh, 2021) and are important indicators of environmental health (Merchant et al., 2019). Other than the countless natural benefits of wetlands, the local economy is dependent on wetlands for fisheries and grazing (Kumsa et al., 2019).

Although wetlands provide numerous ecosystem services, previous studies have shown that wetlands have been replaced by agricultural and urban Land use (Ansari & Golabi, 2019; Ji et al., 2015). Recent studies have also pointed out climate change drivers as one of the factors affecting the integrity of wetlands (Boon et al., 2016; Huo et al., 2019; Ji et al., 2015). Furthermore, wetlands continue to be seriously affected by adverse land irrigation practices, extraction of ground water from nearby aquifers (Merchant et al., 2019).

1.3 ECONOMIC BENEFITS OF WETLANDS

The whole economic worth of a wetland's ecological functions, services, and resources may be accurately calculated. Consider the financial benefits of putting the area to another use. The advantages of temperate wetland ecosystems (Turner & Jones, 2013) have been evaluated in several economic studies, but not those of tropical wetlands, Kenya inclusive . Recent studies have pointed out the importance of tropical wetlands (whether inland or freshwater) in developing countries on economic development (Asgher et al., 2021).

Ecology typically distinguishes between an ecosystem's regulatory environmental functions (such as nutrients) it's structural elements (such as biomass, abiotic materials, species of flora and fauna) and its cycles, microclimatic functions and energy flows (Austin, 2014). Additionally, ecosystems as a whole frequently possess characteristics such as biological diversity and cultural originality/heritage) that encourages particular economic uses (Medici, 2021;Carrion Gordon, 2018).

The economic value provided by any ecosystem falls under three categories i.e. direct, indirect and non-direct. Direct benefits entails values obtained through the direct interaction between the wetland's resources and services (Souza et al., 2021). Indirect values entail the natural activities of a wetland that indirectly support and safeguard economic activity and property, sometimes known as regulatory "environmental" services (Goulder & Kennedy, 2011). Non-use values are values derived neither from Direct or non-direct use of ecosystem services and their interactions (Abbasov et al., 2022).

1.4 IMPORTANCE OF LAKE NAKURU WETLANDS

Lake Nakuru, is an important lake situated within Lake Nakuru National Park (LNNP), a conservation area managed by the Kenya Wildlife Services. The Lake was declared a Ramser site through the Ramser Convention of 1971 (Mbithi, 2016). Lake Nakuru catchment basin is a closed drainage system that covers an area of 1800 km^2 (Ng'weno et al., 2010a). LNNP has a solar powered and insulated fence which forms a buffer zone between human activities and the lake. Areas of human settlement with lower biodiversity values lie between these two zones but are nonetheless dependent, either directly or indirectly, on the biological services offered by the high biodiversity zones.

The ecological stability of the forests and the National Park, on the other hand, is impacted both directly and indirectly by the places where people live (Alon et al., 2019). There are eleven major ecological habitats in LNNP ranging from the lake and the mud flats and salt marshes surrounding it to mosaics of open and wooded grassland, dense forest, bush and cliff habitat. The park has a very high concentration of wildlife consisting of 70 mammal species, 400 bird species and over 200 plant species.

Lake Nakuru, which forms the centrepiece of this showcase of wildlife is internationally renowned for the large concentrations of lesser flamingos (Thampy, 2023). Lake Nakuru National Park receives about 200,000 visits per year include both local and foreign tourists, bringing in over US$ 4.5 million in gate collections alone (Odada et al., 2004). It is the first Ramser site in Kenya, the first bird sanctuary in Africa, and a UNESCO World Heritage Site (Alon et al., 2019).

1.5 FACTORS AFFECTING LAKE NAKURU WETLANDS

As a Ramser site (No. 476), which is a "Wetland of International Importance, particularly as a Waterfowl Habitat, Ramser Convention," LNNP was given this designation in 1990 (Chrisphine et al., 2016). LNNP has evolved into an island of nature encircled by a sea of people. Neighbouring LNNP is Nakuru Township, an industrial, commercial and service centre for the surrounding agricultural hinterland (Alon et al., 2019). Nakuru County had a population of roughly 1.6 million as per the 2009 National Population and Housing Census. According to the National population and housing Census 2019 (Kithiia et al., 2020) the County had 2.1 million people, consisting of 1,084,835 females and 1,077,272 males. The same population statistics revealed that Nakuru County had 616,046 Households with an average house hold size of 3.5. This insularization's prospective implications are particularly worrisome. Nakuru residents consume a lot of resources and generates a lot of waste, like most cities do.

A total of 9,000 m^3 of sewage is produced daily and processed in two treatment plants before being released into the lake, despite the fact that only 19% of the town is sewered. Inadequate resources limit the ability to handle solid waste, which caused a dispersed build-up of garbage in the environment. Early in the 1970s, the township of Nakuru was made available for industrialization, but little consideration was given to how industry might have affected the ecology of the land environment or the lake, and no deliberate effort was made to exclude certain industries that might pose significant environmental issues.

At the onset of industrialization, a fungicide (copper oxychloride) factory was built in the town and ran for a full year before its environmental effects and potential to contaminate the Lake were realized. As a result, the factory was relocated to another region of the country at a significant cost to the government. After the factory relocation, Black Rhino *Dinecous bicopris* sanctuary was established in LNNP which boosted tourism and revenue generation for the conservation of the lake. Heavy metal enrichment and pesticide residues were discovered in recent analyses of river water and lake bottom sediments. Farmers were still using banned or restricted organo-chlorine pesticides like DDT, endosulfan, Aldrin, and dieldrin, according to an assessment of pesticide use in the catchment basin (Avni, 2020).

All of the pesticide and heavy metal residues found in the Lake are known to be poisonous to fish and birds. *Arthrospira fusiformis*, which serves as the foundation of the food chain in the Lake, is likewise known to grow more slowly when copper is present. The degree of heavy metal and pesticide enrichment of the Lake's bottom sediment had drastically increased in contrast to the examinations conducted there in 1975 (Eliud, 2013), especially in respect to copper, cadmium, mercury, and organochlorine pesticides.

Cumulatively the factors that had a negative effect on the Lake Nakuru ecosystem are as follows: Important signs that the lake Nakuru ecosystem is stressed, dates back to 1990 when there were widespread fish fatalities, followed by flamingo deaths in 1993 (Omara et al., 2023), and lake drying in 1994 as a result of a cascading series of terrible negative effects on the watershed that led to the lake’s environmental degradation (Brönmark & Hansson, 2002).

The Lake's *Arthrospira fusiformis* population had not been seen there very often or for very long since 1995. Between 1992 and 2002, flamingo occupancy of the Lake showed a similar trend of diminishing numbers (Brönmark & Hansson, 2002). The unwanted blue-green algae species *Microcystis sp*. and *Anabaena sp*. had mainly replaced *Arthrospira fusiformis* in the lake's algal makeup (Tan et al., 2022). Both of these species were capable of producing strong hepatic and neurotoxins that are toxic to birds and fish, and both are known to thrive in nutrient-rich streams with high organic content.

1.6 EFFECT OF FLOODING ON LAKE NAKURU VEGETATION

Despite the already fragile ecosystem caused by pollution and other factors, LNNP still suffers from stress due to the floods that took center stage since the year 2010. According to studies by Chrisphine et al., 2016, the lake has swollen beyond the designated boundary, with 60% of the Parks infrastructure submerged in the swollen waters. Vegetation species that once existed on the lake's riparian reserve were partly or completely immersed in the swollen waters (Osio et al., 2022). Acacia xanthophloea tree species being the most important tree (Mutangah, 1994) in LNNP are being destroyed by the persistent floods. This has remained a cause for concern amongst ecologists, hydrologists, conservationists and wildlife managers. Figure 1.1 shows the effect of floods on Acacia xanthophloea around Lake Nakuru riparian reserve. Studies have also confirmed that the Olive Baboon (*Papio anubis*) Rothschild giraffe (*Giraffa camelopardalis rothschildi*) and the black rhinoceroses (*Diceros bicornis*) depend on Acacia xanthophloea tree species as their fodder (Pellew, 1983; Okello, 2007).

Figure 1.1: Left: Is the aerial view of Lake Nakuru riparian Right: Close range photography showing the effect of floods on vegetation and Park infrastructure. **Source:** Photo by Author, August, 2014.

Studies in East African National Parks have indicated that Acacia woodland disturbance have been attributed by several factors such as climate and fire (Anderson et al., 2008) herbivore population fluctuation (Kiffner et al., 2017) and human disturbance (White et al., 2019). The tree pattern has been observed as even-sized strands in various studies (MacGregor, 2000;Dharani et al., 2006). Density of Acacia woodlands may also change as they mature and these conclusions were drawn from studies carried out in Serengeti, in relations to the effect of several factors on Acacia woodland degradation (Kiffner et al., 2017; MacGregor, 2000; Pellew, 1983). The Serengeti National Park is anticipated to eventually lose over 70% of its species, and Nairobi National Park is predicted to eventually lose over 80% of its species due to a similar situation (Evans et al., 1979). According to Huqa, 2015, Elephants in the Amboseli might have destroyed the Acacia trees and this was pointed out as one of the cause of woodland disappearance. However, studies carried out by (Hake, 2022 ; Moss et al., 2011) reiterated this finding indicating that long term climatic change could have been the possible cause of the disappearing woodland species. They provided evidence indicating that increased soil salinity associated with periods of high rainfall and rising ground water table in a closed drainage basin could have been the main cause of stress that killed the trees. However, studies by Avni, (2020) attributed loss of Acacia xanthophloea to increase in agricultural and industrial activities in Nakuru and it's environs.

The author (Avni, 2020) confirmed that Acacia xanthophloea woodlands were under threat due to domestic and industrial wastes which consist of heavy metals and pesticides from agricultural establishments. Mutangah, 1994 confirmed that Acacia xanthophloea species was the most important of all woodland species in Lake Nakuru National park. Since the year 1997 Mau forest catchment has suffered massive degradation due to the various change in Land Use from forest to agriculture and settlement, hence causing reduction in the discharge rates in most of the rivers in the catchment. The effect of Land use change had great impact on the Lake Nakuru Park ecosystem (Chrisphine et al., 2016). Mangi et al. (2022) carried out studies on Lake Nakuru and confirmed that the lake has been flooding it's riparian reserve since 2010.

Similar research carried out by Osio et al.(2022) confirmed that the Lake had flooded it's bank hence affecting the health of the riparian vegetation, with the Acacia xanthophloea spp along the North western part of the Lake being severely damaged. Acacia woodlands occur in different parts of Lake Nakuru Riparian reserve are associated with high water table (Mutangah, 1994). These changes in the woodland structure, composition and species regeneration have disturbed both ecologists, Land and Park managers hence calling for more sustainable approach in Monitoring the disturbance on the yellow barked Acacia tree within closed National park ecosystem.

CHAPTER TWO:

LITERATURE REVIEW

2.1 INTRODUCTION TO THE LITERATURE REVIEW

In this section the author gives a review of similar works that have been done in relation to the main objective and specific objectives of the study. Various variables are captured in the review including the authors, date of publication, concepts, key arguments, items used (software and materials), the methods used (supervised, unsupervised, Pixel Based (PB), Object Based Image Analysis (OBIA) knowledge based and Object Detection using deep learning etc., key findings, and the inherent gaps. The problems/solution approach will be used in organizing the review.

2.2 IMPACT OF OBIA ON FOREST MAPPING

The performance of Object Based Image Analysis (OBIA) has been tested on various studies including Guan et al., 2013 who used machine learning techniques and recent advancements in OBIA to automate feature selection in a classification process, hence lessening the need for manual interpretation of images. Strasser & Lang (2015), also presented a semi-automated object based image analysis (OBIA) approach for the mapping of riparian forests by utilizing habitat class modeling based on the European Habitats Directive (HabDir) Annex 1 and the European Nature Information System (EUNIS) habitat classifications. Other studies by Aziz et al.(2015) evaluated the use of Landsat imagery archives for ecological change. The authors utilized cloud-free subset satellite photos which were collected in May 1988, February 1995, December 1999, March 2001, December 2009, and November 2013. While the accuracy of the Pixel-Based (PB) method was noted to be unstable due to mixed pixels, the area-based accuracy assessment method achieved a steady classification performance, hence depicting a strong link between accuracy and training set size (Ma et al., 2017). In order to maximize their use for object-based agriculture pattern recognition tasks, the goal of (Ma et al., 2017) was to assess the impact of the advanced feature selection techniques used by well-known supervised classifiers i.e. Support Vector Machines (SVM) and Random Forest (RF) for the example of object-based (OBIA) mapping of an agricultural area using Unmanned Aerial Vehicle (UAV) imagery. Moskal et al., 2011 assessed LULC Mapping in Seattle USA using publicly available aerial photography and a true color multi-spectral Landsat Imagery. Their study compared results based on OBIA LULC and Pixel-Based (PB) classification. OBIA driven mapping was found to be more superior than Pixel-Based (PB) approach, although spectral aspect of the imageries added more value to their results than the hyper spatial (Very high Spatial) aspect.

Kavzoglu, (2017) proposed an experimental research study on the application of object-based image analysis (OBIA) and random forest (RF) ensemble learning for classifying different types of land use and land cover on Quickbird-2 images. The author created a novel technique that combines object-based post-classification refinement (OBPR) and CNNs for LULC mapping using Sentinel optical and SAR data in order to produce object-based thematic maps (Liu et al., 2019). However, the notion of LCZ may have proven useful to explore land use dependent thermal patterns in Global South cities, which is the key research subject investigated, with the increased and reasonable availability of (very) high-resolution images (Simanjuntak et al., 2019). In order to increase the thematic accuracy of land cover mapping based on satellite images, Gudmann et al., 2020 also analyzed the impact of landscape metrics that have not yet been employed in image categorization. Predicted data were compared with manually digitized lupine coverage maps, and the classification model was used to construct maps of lupine distribution in test locations (Wijesingha et al., 2020). Further studies by Moskal et al. (2011) evaluated the capability of OBIA on their forest study. The author engaged Second Order texture (SOT) to classify a hyperspatial imagery to fine detail levels of tree crowns, shadows and understory, with the aim of detecting tree density and its variability between pre and post fire burn incidents. Hierarchical classification at level 1 achieved an OA of 78.8% while Level 2 and 3 stood at 89.1% respectively. Their results suggested that hyperspatial (high-spatial) imageries can be applied to post-fire density and regeneration mapping.

2.2.1 OBIA Versus Pixel-Based approach in Remote Sensing

Previous studies have used single-date optical and SAR based imageries to classify urban vegetation using Pixel-Based (PB) approach (Mubea & Menz, 2012) and realized that fusion of multi-date images from both sensors improved their classification results. However, recent studies by Mahdianpari et al. (2020) used the multi-year and multi-summer satellite imageries to create the first Newfoundland Vegetation Inventory Map. The authors embraced the use of Sentinel-1 (SAR) and Sentinel-2 (Optical-based) fusion techniques, comparing OBIA's performance against PB on the classified imageries. Their results depicted an improved performance of OA 88.4% and kappa (0.85) on a fused S1 and S2 multi-date stack imagery using OBIA approach, with the inclusion of SLIC algorithm segmentation technique into the workflow. Their study corroborates well with (Manaf et al., 2018) who compared the performance of OBIA's segmentation algorithms namely; Felzenswalb, Quickshift, and SLIC. Again SLIC segmentation together with 15 machine learning classifiers used to classify images of Langkawi Island, was faster than Felzenswalb and Quickshift by as much as 37 times and 500 times, respectively. In comparison to the other methods evaluated in their study, SLIC segmentation algorithm and an extra tree classifier were able to reach 100% overall accuracy in the object-based Image Analysis (OBIA) classification in three out of four situations.

Nieuwenhuis et al. (2022) analysed 230 drone orthophotos of Heron Reef in Australia and used the OBIA-Random Forest approach to differentiate between coral, sand, and rock/dead coral substrates. Overall accuracy was 86% for their study while living coral cover was mapped with 92% accuracy. When processing drone imagery for calibrating and validating satellite imagery, their approaches were helpful since they enabled quick processing of drone imagery of any environment. Similar studies by Dabiri & Lang (2018a), explored the use of hyperspectral images to characterize vegetation species along River Salzach riparian reserve in Austria . The authors used ESA-APEX hyperspectral bands to discriminate between several kinds of wetlands. According to their report, they were able to attain an overall accuracy (OA) of 63% for Optical-based sensed imageries, engaging Minimum Noise Fraction (MNF) and pixel-based (PB) approaches. An improvement on their accuracy by 22% was noted when OBIA-MNF approach was implemented, taking the lead in the classification performance than PB-MNF approach.

2.2.2 Traditional OBIA Versus Deep Learning Approach

Tan et al. (2019) presented an object-based method for automatic change identification in high-resolution (HR) remote sensing images utilizing multiple classifiers and multi-scale uncertainty analysis (OB-MMUA). In the Toroud-Chahshirin Magmatic Belt (TCMB), North of Iran, hydrothermal alteration zones connected to epithermal polymetallic vein-type mineralization were mapped using remote sensing data from the Advanced Spaceborne Thermal Emission and Reflection Radiometer~ASTER (Noori et al., 2019). How well can deep learning-based approaches for classifying land cover and detecting objects on high resolution remote sensing imagery perform? is a question investigated by Zhang et al. (2020). A thorough analysis of methods for item detection and land cover categorization using high resolution (HR) imagery was provided. Shi et al., 2020 goal was to suggest a fresh Artificial Intelligence (AI) technique for choosing object-based samples. The classification process was object-oriented, to categorize a huge feature space made up of a very high spatial resolution satellite picture (VHR) in particular using object-based image analysis approach (OBIA) as demonstrated by Rida et al., 2022. ATD-LinkNet's AT block was a replaceable module that Qi et al. (2020) proposed, employing multi-scale convolution and attention mechanisms as it's building blocks. Practically, a number of image processing procedures were used to edit the imageries. According to (He et al., 2020), multi-layer perceptron's (MLPs) can approximate or formulate these pixel-independent processes. Feizizadeh et al., 2021 integrated Fuzzy object-based image analysis (FOBIA) and Deep Learning (FOBIA-DL) approach for monitoring the land use/cover (LULC) and respective changes and compared it to three machine learning (ML) algorithms, namely the support vector machine (SVM), random forest (RF), and classification and regression tree (CART). Their study involved LULC impacts on drought by analysing Landsat satellite images from 1990 to 2020 for the Urmia Lake area in northern Iran. Their findings showed that the FOBIA-DL excelled more than the other techniques, closely followed by the SVM, with accuracies of 90.1% to 96.4% and a spatial certainty of 0.93 to 0.97. The authors indicated that the FSE-DST technique significantly increased the spatial accuracy of the object-based classification maps, while the integration of Fuzzy-OBIA and

DCNNs strengthened and improved the robustness of the OBIA's decision rules. The combination of object-based image analysis (OBIA) with Fuzzy and Deep Learning (DL) results were found to be more flexible and reliable than OBIA-DT model for image analysis and classification with OBIA already being regarded as a paradigm shift in GIScience. The authors pointed out that their methodological approach could be used to support lake restoration initiatives, drought mitigation, land use management and precision agricultural programs. Image analysis and remote sensing are effective techniques for process monitoring. Oddi et al., 2021 compared the effectiveness of human and semi-automatic classification approaches while statistically assessing the possibilities of using high-resolution UAV imagery to monitor the encroachment process during it's early growth. Other studies Zheng et al. (2022) compared the efficiency of Object Based Image Analysis (OBIA), Pixel Based (PB) and Deep Learning (DL) on coastal vegetation. DL technique achieved the most promising predictive results, hence reflecting the realistic distribution of the vegetation. Deep learning (DL) not only outperforms conventional methods in terms of accuracy, but also solves a number of problems that have been present in the past, according to the thorough review and meta-analysis (Neupane et al., 2021; Tan et al., 2019).

Table 2.1: Example of Radar Instruments and their characteristics

Sensor	Cosmo-Sky Med	SENTINEL-1(SAR)	ALMAZ-1	ALOS-PALSAR2	AIRSAR
Frequency band	X	C	S	L	P
Frequency (GHz)	7.5-12.0	3.75-7.5	2.0-3.75	1.0-2.0	0.25-5.0
Wavelength (Range)	2.5-4.0	4.0-4.80	8.0-15.0	15.0-30.0	60.0-120

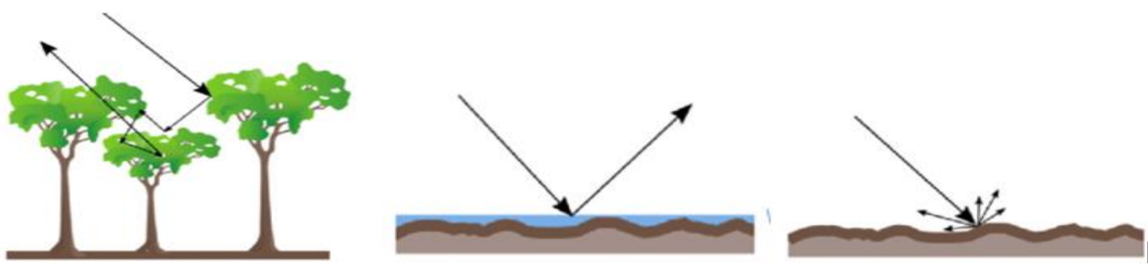

Figure 2.1: Illustration of different surface Reflectance. Left: Complex volume scattering on tree crowns (Gomes et al., 2018). Right: Specular reflectance on water; Diffuse reflectance on Land (Umar & Magawata, 2019)

2.2.3 OBIA Versus Pixel-wise Approach in Wetland Mapping

Muñoz et al. (2019) in their study provided a methodology used to automate salt marsh elevation adjustment in estuary systems in order to update emergent herbaceous wetlands (i.e., those defined in the 2016 National Land Cover Database (NLCD) to current circumstances. A thorough analysis of methods for item detection and land cover categorization using high resolution imagery was proposed. Landsat 8OLI image-based cover change mapping in a semi-arid environment was carried out by Moayedi et al. (2020). Chen & Tian, (2020) also examined how well Pixel-Based (PB) and object-based (OBIA) support vector machine algorithms perform when used with Gaofen-5 (GF-5) and co-polarized SAR data for tea plantation mapping in Wuyishan, China.

The authors compared the classification accuracies based on MMP as a feature vector against those without MMP as a feature vector using the Support Vector Machine (SVM) and Maximum Likelihood (ML) classification algorithms (Tsoeleng et al., 2020). The research sought to create a Landsat 8 data composition and classification process using Google Earth Engine (GEE) with the overall goal of creating a 2018–2020 Land Use/Land Cover (LULC) map of the Maiella National Park (central Italy), useful for a future long-term LULC change analysis. In this procedure, two pixel-based (PB) and two object-based (OB) approaches were compared in order to weigh the benefits of incorporating textural information in the PB strategy (Tassi et al., 2021). Other works by Schoening & Kasper, (2011) used a combination of Spot 5, aerial image and orthophotos to map wetlands in Galant County in rural Arkansas. Their study compared supervised PB against Unsupervised PB approaches and realized that Supervised approach performed better than Unsupervised approach by 2.5% on the multi-temporal and multi-spatial Images. Moreover, engaging OBIA into their multi-spatial imageries increased the classification accuracy by 15% better than supervised PB approach.

In the Momoge Ramser wetland site, two vegetated cover types (water and bare land) and four major plant communities (*Phragmites australis*, *Typha orientalis*, *Suaeda glauca*, and *Scirpus triqueter*) were identified and categorized (Du et al., 2021). Zhou et al. (2021) assessed the viability of acquired RGB images for the classification of wetland vegetation at the species level using data from the DJI Mavic Pro, with a focus on Honghu, which is designated as a wetland of international importance. It has become increasingly clear that the conventional pixel-based (PB) detection method is ineffective. In order to detect changes in forest cover using satellite photos with extremely high spatial resolution, a unique change detection method was thus proposed (Houphlet et al., 2023).

2.3 INTEGRATION OF OBIA INTO GISCIENCE & REMOTE SENSING

The complexity of wetland landscapes calls for the use of variant remote sensing satellite sensors for spectral difference detection existing between species, hence providing a basis for riparian reserve vegetation characterization. For example Ozesmi & Bauer, 2002, did a review of wetland studies engaging a range of satellite based sensors with Landsat MSS, Landsat TM, and SPOT being the major satellite systems that have been used to study wetlands. Other systems are NOAA AVHRR, IRS-1B LISS-II and radar systems, including JERS-1, ERS-1 and RADARSAT hence promoting visualization and classification using unsupervised Iso-Cluster algorithm and supervised Maximum Likelihood Classification Approach. The author emphasized that due to the spectral confusion between species on the landscape, there was need to include ancillary data such as soil data, elevation and topography. In most case studies, aerial photographs were used as reference data and concluded that application of different approaches including fuzzy classification, sub-pixel classification, spectral-mixture analysis may provide detailed analysis on wetlands. Further observation led them to recommend hybrid or rule-based approach for better results than more traditional methods. Moreover, they pointed out that radar and optical data could provide the most promising results for improvement of wetland classification.

The main purpose of Lee & Marsh, (1995) was to evaluate the agricultural information that could be derived from both high and low spatial resolution data in areas where there is very often limited ground information. Fourteen cover types were delineated from 1:15 000 air photos (enlarged to 1:5000 in an image processing system) using manual interpretation techniques, with 89% accuracy (Harvey & Hill, 2001). Data sources used included geo-referenced Landsat Thematic Mapper (TM) images, digital topographic map data, digital vegetation data, and colour infrared aerial photographs (Bronge & Näslund-Landenmark, 2002).

Huang & Zhang, (2007) investigated the population expansion pattern of an exotic species of *Spartina alterniflora* for a period of 7 years, after it had been newly introduced to the neonatal shoals of Jiuduansha (GPS), in the Yangtze Estuary, Shanghai. Owor et. al. (2007) studied wetland change detection and inundation north of lake George, Western Uganda using Landsat data. A similar remote sensing approach could be used for monitoring temporal and spatial aspects of other wetlands in the region. Remote sensing (RS) and geographical information system (GIS) as cost-effective techniques were used to develop a catchments-based approach for identifying critical sites of agricultural riparian buffer restoration (Gu & Liu, 2010).

Oliver et al., 2012 described a preliminary study of a small stand of mangrove and saltmarsh that involves measuring of elevation change and accretion, mapping of wetland communities, and modelling of their potential response to sea-level rise. Maleki et al. (2016) focused on habitat mapping as a tool for water birds conservation planning in an arid zone wetland: specifically, the case study of hamun wetland. Their approach could be practically applied in the management of water habitats in arid and semi-arid areas facing water limitations. Kaplan & Avdan, (2018) also investigated the ability of fusing two fine spatial resolution satellite data, Sentinel-2 and the

Synthetic Aperture Radar (SAR) Satellite, Sentinel-1, for mapping wetlands, realizing desirable results. The advantage of using SAR products lies in the possibility of capturing backscatter response (see Figure 2.2) for characterization of riparian vegetation (Deus, 2016).

In recent studies, Yan et al., 2020, also used Sentinel-1-time series data to assess the 60661 wetland samples that had previously been collected and in addition Normalized Difference Vegetation Index (NDVI) and Normalized Difference Water Index (NDWI) time series extracted from Landsat 8OLI to create a wetland sample classification with seasonal information. Wetland specialists analysed the samples in conjunction with high spatial-temporal resolution images, and the outcome demonstrates the sample set's high accuracy. Gašparović & Klobučar, (2021) concentrated on mapping floods using remote sensing and geospatial data. According to the research, improvements in remote sensing methods and a data-fusion strategy could enable enhanced wetland mapping accuracy while speeding up processing compared to conventional methods (MacFaden et al., 2021). Using the Normalized Difference Vegetation Index (NDVI), Nordin et al. (2022) tracked the mangrove forest changes in Pulau Kukup, Ramser Site Johor from 2013 to 2021. According to Al-Mulla et al. (2022), the systematic approach included examining changes in a variety of parameters before and after the cyclone, such as vegetation coverage, the detection of build-up damage in agricultural lands, a detailed study on coastline changes, and inundations in agricultural areas and urban communities.

Lang et al. (2019), examined the spatial prospects and GEOBIA accomplishments in the age of ‘Big earth’ observation data. The term "object-based image analysis" (OBIA) was tentatively coined in the field of Geographic Information Science (GIScience) in 2006. However, Blaschke, 2010 offered a method that incorporates object-based processing into the procedure for classifying images. The author examined how segmentation and object-based image analysis/classification techniques enhance current pixel-based image analysis/classification techniques. Recently, Convolutional neural networks (CNN) has been used to explore semantic segments before a conditional random field (CRF) model was used to represent the contextual information between semantic segments (Zhao et al., 2017). The results showed that the unsupervised method was more effective since it does not require reference segmentation objects, whereas the supervised method is more suited for use in heterogeneous land cover (Bai et al., 2019). Based on low-level and mid-level feature representation utilizing conventional machine learning methods, a thorough overview of historical trends was provided (Mahmood et al., 2022). Among other important works are Cui et al., (2003) and Li et al., (2010).

Kim & Song, (2023), built a modified Mask R-CNN approach that combines bottom-up and top-down procedures for water recognition using the excellent "self-learning ability" of deep learning. Yang et al., (2021) used a technique for determining how well a windbreak protects against the wind. Based on low-level and mid-level feature representation utilizing conventional machine learning methods, a thorough overview of historical trends has been provided (Mehmood et al., 2022). Confusion about geographical features was evident in sizable portions of the background data, which negatively impacts the effectiveness of detection. However, GIS users still require a way to use several data sets using conventional tools. Hajjaji et al., (2021) suggested a technique for integrating Apache Hadoop and its ecosystem with ArcMap. Among other important works is Airoldi et al., (2005). The YOLOX-SAR method is suggested by Guo et al., (2022) has been suggested as a solution to these issues. The R programming language has also been used to create an image analysis framework for Landsat-8 Operational Land Imager and Thermal Infrared Sensor (OLI/TIRS) scenes (Lemenkova & Debeir, 2022).

2.3.1 Integration of Textural variables into OBIA

Research on extraction of impervious surface has developed for decades, but it is still quite challenging to obtain impervious surface information with high accuracy, especially from multispectral remote sensing imageries (Feng & Fan, 2019). Ma et al., (2017) investigated the use of Morphological Attribute profiles (M-APs), establishing the relationship between APs and the characteristics of buildings/shadows in Very High Resolutions (VHR). The variables used included high local contrast, internal homogeneity, shape and size. However, Pham et al., (2018) inco-operated local feature based (LFAPs) which is beyond the standard APs so as to have a better characterization of each APs filtered pixel within its neighborhood. In order to test the effectiveness of LFAPs against the newly developed Local Feature Based Self Dual APs (LBSDAPs), the authors used high spatial and hyperspectral datasets and supervised classification approach, engaging SVM and Random Forest approach. Their findings suggested that additional variables on standard APs, could improve their performance considerably.

Tan et al., (2019) used an Object Based approach for automatic change detection using multiple classifiers and multi-scale uncertainty analysis (OB-MMUA) in high resolution (HR) remote sensing imageries The three-layer classification scheme was developed by Cai et al., (2019) for deriving detailed urban LULC information by integrating newly launched Chinese GF-1 (medium resolution) and GF-2 (very high resolution) satellite imagery and synthetically incorporating geometry, texture, and spectral information through multi-resolution image segmentation and object-based image classification (OBIA).

The Formulae for calculating the Second order (SOT) i.e. homogeneity of Grey Level Co-occurrence Matrix (GLCM) is as follows:

$(P(i, j) / (1 + |i - j|)) = \text{homogeneity}$

Where;

The normalized co-occurrence probability of the GLCM pixel pairings with intensity values i and j is represented by P (i, j).

The intensity values of the pixel pairings are i and j.

The absolute difference between i and j is represented as $|i - j|$.

The symbol in this formula denotes summation.

The co-occurrence matrix P (i, j) must be calculated by examining the presence of pixel pairings with particular intensity values in an image in order to determine the homogeneity of a GLCM. The matrix should then be normalized so that the total probability is equal to 1.

Figure 2.2 shows an illustration of Sentinel-1 (Ground range detected) image whose Polarimetric bands VV and VH were converted into texture bands with subsequent compositing.

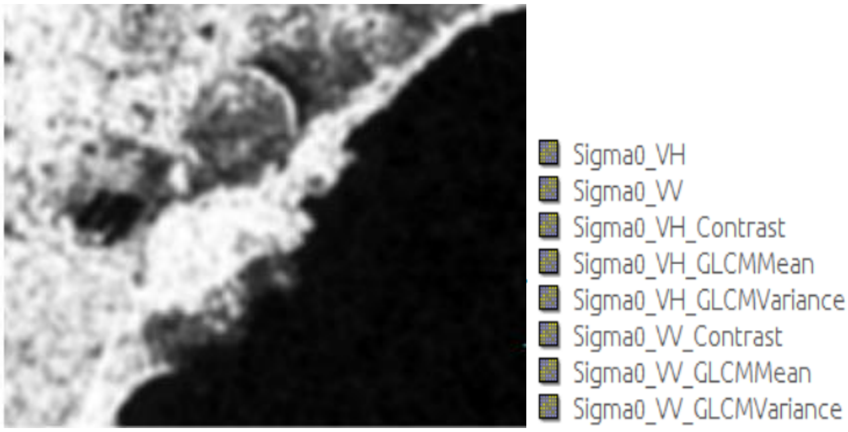

Figure 2.2: Illustration of different Grey Level Co-occurrence metrics used on Seninel-1 SAR-C VV and VH Polarimetric bands representing the North western part of Lake Nakuru riparian.(Mandal, et al., 2020)

Han et al., (2020) studied automatic shadow detection for multispectral satellite remote sensing images in invariant colour spaces. The proposed algorithm was verified with many images from WorldView-3 and WorldView-2 acquired at different times and sites. Chen et al., (2020) used a pixel-level remote sensing image fusion method which was based on combining the principal component analysis (PCA) and the curvelet transformation (CT) hence experiencing improved results. Rusmadi & Hasan, 2020 used a mixed methodological approach in their study, engaging a range of machine learning algorithms namely; Support Vector Machine (SVM), Random Forest (RF), K-Nearest Neighbour (K-NN), Decision Tree, and Bayes and OBIA to map coastal habitats from Sonar derived imageries.

The authors derived 8 textural layers from a mosaic of sonar-based imageries based on the GLCM Technique and P.C.A for dimensionality reduction within the dataset. Their results derived 4 classes namely coral, sand, silt and mud, with SVM having recorded the highest detection rate with an Overall Accuracy (OA) of 81.25%, followed by K-NN, Random Forest, Decision Tree

(DT) and Naïve Bayes (NB) (68.75%, 66.25%, 57.5% and 45% respectively) respectively. The authors concluded that the use of textural variables on sonar could improve the classification that enables visualization of the spatial distribution of aquatic vegetation in water, hence enabling future monitoring.

Focusing on the semi-arid savannah ecosystem in the central Kalahari. Mishra & Crews, (2014) examined the suitability of a hierarchical OBIA approach combined with insitu data and an ensemble classification technique for mapping vegetation morphology types at landscape scale. Liao et al., (2014) described the overall study on land water in the program of global land cover remote sensing mapping. The Earth Observation Hyperion hyperspectral sensor data has been evaluated for regolith and gossan mapping using the object oriented image classification technique Farooq & Govil, (2014). To minimize the spectral distortion Hnatushenko & Vasyliev, (2016) proposed a remote sensing image fusion method which combines the Independent Component Analysis (ICA) and optimization wavelet transforms Chen et al., (2020). Halabisky et al., (2018) provided a method to identify wetlands using a time series of Landsat imagery by building a Random Forest model using each image observation as an explanatory variable. Other influential works include (Jahjah & Ulivieri, 2010).

Further research on textural variables include Malik & Robertson, (2021) who proposed a simple yet effective texture –based CNN (Tex-CNN) via feature concatenation framework which resulted in capturing and learning texture descriptors. Zhou et al., (2021) evaluated the feasibility of RGB imagery obtained from DJI Mavic Pro for wetland vegetation classification at the species level, with a specific application to Honghu, which is listed as wetland of international importance. Blurring effects and resolution loss induced by de-speckling procedure can degrade the estimation accuracy of SAR features and therefore artifacts are introduced into data fusion. Zhao & Jiang, (2022) presented a method to solve this problem using SAR feature estimation , driven by both optical and dual polarimetric SAR imageries.

2.4 OBIA ON SPATIO-TEMPORAL CHANGE DETECTION

Luo & Mornya, 2019 in their study used a mixed method approach engaging OBIA and Machine learning on wide wetland areas in Hubei province China. The authors used Landsat and HJ-CCD satellite-based images and OBIA with binary Decision tree (DT) and Tasselled Cap Transformation (TCT) on field samples for monitoring of changes on wetlands. Their results depicted an overall increase in wetlands over Hubei Province by 171.03km^2 during 2000-2010 epoch. Increase on lakes and reservoirs stood at 40.21% (108.97km^2) and 59.17% (160.37km^2) respectively. The authors reported that increase at administrative level i.e. Shiyan prefecture (153.53km^2) and Fangxian County (317.33km^2) contributed majorly to the increase of wetlands in Hubei province. Luo & Mornya, (2019), drew their conclusion by pointing out that the overall increase of wetlands in the area was caused by the implementation of the ecological projects during the 2000-2010 epoch.

Baker et al., (2021) utilized an OBIA-DT approach to map urban forest tree canopies in Maple Grove Minnesota in the U.S.A. The authors engaged Lidar technology and variables such as spatial, spectral and textural to classify forest cover. Their results showed an increase of 1.26% in overall tree canopy cover over the period under review. Desirable results were also achieved on the 2008 image with an Overall Accuracy of 85.5% and 2017 which stood at 89.5% respectively.

Their study corroborates with Karlson et al., (2014) who used GEOBIA in combination with spectral and geometric information to delineate individual tree crown clusters on Worldview-2 realizing an overall accuracy of 85.4% . However, further experiments engaged by Baker et al., (2021.) beyond OBIA was the Gaussian Mixture Model (GMM) method. Results showed an improvement with an OA of 93.31% using DT and GMM approach.

Long et al., (2021) engaged Sentinel-2 optical based image and in addition the DEM data to map China's inland wetland which was experiencing biodiversity loss. The experiment was carried out in Google Earth Engine (GEE) interface based on the LandTrendr algorithm to analyse vegetation dynamics from 1999-2018 on Landsat normalization time series. Random Forest had superior (OA, 94.6%) detection rate than SVM. Overall change detection for all three categories namely 'vegetation gains', 'vegetation loss' and 'no changes' stood at 83.67%. The authors also noted that in the past 20 years, 2,604.43 and 5,458.84 Km^2 of the landmass had experienced vegetation loss and gain respectively. Increase in areas covered by Forest, reed and sedges in wetland were 1330.39, 86.42 and 136.97Km^2 respectively. Long et al., 2021 concluded that the overall condition of the wetland vegetation around Dongting lake was good due to the role played by their wetland ecological protection policy.

In another study Meng et al., (2022), used GEE platform to map planted forests in the arid region of North-western China by applying a time series stack of NDVI based on Landsat imageries. The overall experimental accuracy results achieved stood at an OA of 93.65% and a kappa value of 0.92. Both the UA and PA metrics of the planted and natural forest classes were detected at high rates (>90%), with the average area of the planted forest estimated to be 3608.72km^2 in 2020, hence recording an increase of 20.60%. The authors suggested that their method was suitable for the application of ecological engineering and ecosystem services and stability of planted forest.

Günen, (2022) used Sentinel-2MSI optical images to map wetlands in Turkey and validated using EuroSat dataset. The accuracy, recall, precision, specificity, F-score, and image quality assessment metrics of proposed deep learning-based 1D convolutional neural networks (CNN) and traditional machine learning techniques (i.e., support vector machine, linear discriminant analysis, K-nearest neighbourhood, canonical correlation forests, and AdaBoost.M1) were compared. Finally, pairwise comparison using McNemar's test based on chi-square was performed. With the exception of the support vector machine vs. linear discriminant analysis in Test area 1, there was a statistical difference between 1D CNN and machine learning methods. In terms of non-linear function approximation and the capacity to identify and articulate data features, CNN models beat machine learning techniques. The author reported that strongly connected and highly correlated discrete signals can be successfully segmented using 1D CNNs since they can process data in a very complex and distinctive feature space.

Other works include Alqurashi & Kumar, (2016), who used two sets of Landsat images from 1985 and 2014 to map and monitor the spatial distribution of the urban extent among five Saudi Arabian cities: Riyadh, Jeddah, Makkah, Al-Taif and Eastern Area. Immitzer et al., (2016) who presented the preliminary results of two classification exercises assessing the capabilities of pre-operational (August 2015) Sentinel-2 (S2) data for mapping crop types and tree species. Chettri et al., (2013) who described spatial and temporal land use cover change over the period of 34 years (1976-2010) in Koshi Tappu Wildlife reserve (KTWR), Nepal. Wetland research themes reviewed include wetland classification, habitat or biodiversity, biomass estimation , plant leaf chemistry, water quality, mangrove forest and sea level rise (Guo et al., 2017).

2.4.1 OBIA on Spectral Change Detection

The use of spectral indices in vegetation detection started with earlier studies by Tucker et al., (1979) who used spectrometer generated indices to measure the relationships between linear combinations of red and IR radiances , their ratios and square-roots, biomass, leaf water content and chlorophyll content to map grass canopies on seasonal data. Red-IR ratios were more significant than green-red combinations, according to regression research. The amount of photosynthetically active vegetation was discovered to have an effect on the IR/red ratio, the square root of the IR/red ratio, the vegetation index (IR-red difference divided by their total), and the converted vegetation index (the square root of the vegetation index + 0.5). These variables have been found to be significant in linear measurement of vegetation in relation to their degradation.

Over the years, there has been a culmination of IVs in wetland /vegetation detection measurements. A case in point is where McFeeters, (1996) developed the Normalized Difference Water Index (NDWI) to delineate open water features and enhance their presence in remotely sensed digital imagery. The index makes use of the near-infra-red radiation and visible green light to enhance the presence of soil and terrestrial vegetation and hence recommended for turbidity estimations using RS digital data. Later (Xu, 2006) developed Modified Normalized Water Index (MNDWI) based on Mcfeeters NDWI. The Modified version of NDWI had the capability of enhancing open water features while efficiently suppressing and removing built-up land noise and other noise brought about vegetation and soil. The index is significant especially over areas whose background is dominated by built-up land areas because of it's advantage in reducing and even removing built-up land noise over NDWI.

Wang et al., (2017) used multiple temporal HR imageries in their study in China. The authors' major goal was to increase the precision of change detection performed automatically from high-resolution multi-temporal datasets. Due to the evaluation of spatial displacement and spectral differences across multi-temporal images, their method efficiently lowered change detection errors. A total of four cross-fused images were created using multi-temporal images, and the fused images are then subjected to the iteratively re-weighted multivariate alteration detection (IR-MAD) approach, which measured the spectrum distortion of change information. In this experiment, multi-temporal IKONOS-2, WorldView-3, and GF-1 satellite pictures were used to extract the maps of land cover change. Their approach showed that the suggested strategy outperformed alternative unsupervised change detection techniques. Results on scenario 1 and 2, showed that the proposed technique had overall accuracies of 80.51% and 97.87%, respectively. Additionally, in comparison to the current change detection techniques, they reported that the method outperformed all the rest, since it separated the water from the vegetation.

Mukherjee & Pal, (2021) used the landscape specific approach and metrics to characterise river ganga in Diara region, India. The key variables included in their classification were spatial, hydrological and landscape ecology. Other methods include. Hydro-period analysis, water presence, threshold dependent NDWI-NDVI which were used to measure hydrological dynamics. In addition, a new technique i.e. Mean NDWI-NDWI Depth (MNND) was also introduced to enhance hydrological change detection on the wetlands. The outcome demonstrates how the Ganga River's behaviour had a significant impact on wetland dynamics and how highly unpredictable they were. Due to the 2010 floods, the wetland area had increased dramatically, rising to 12095.37 ha in 2011 from 6795.9ha in 1991 and a decrease to 5725.35ha. in 2019. The centroid of the wetland in 2019 was located 2.14 kilometres away from the centroid in 1991, where the River Ganga flows. Only 10% of the core wetlands remained because the majority of the wetlands had severely been fragmented into smaller sections.

Studies by Rokni et al., (2014) has shown that time series of Landsat satellite based sensors could be used to derive indexes including Normalized Difference Water Index (NDWI), Modified NDWI (MNDWI), Normalized Difference Moisture Index (NDMI), Water Ratio Index (WRI), Normalized Difference Vegetation Index (NDVI), and Automated Water Extraction Index (AWEI) for the extraction of surface water. Since NDWI was found to be superior than other indices, it was used to model the Spatio-temporal changes of the lake under study. Addition of Principal components (PCA) into the model was also proposed and implemented in their study. Their results indicated an intense decrease of Lake Umria during the 2003-2013 epoch. The authors reported that greatest effect was felt between 2010 and 2013, recording loss on the surface area by one-third. The results also illustrated the efficacy of the NDWI-PCs model on water surface change detection.

El-Burullus Lake is one of the four Egyptian Ramser sites that make up internationally significant wetlands due to its abundance in water bird species and great biodiversity. But during the past few decades, wetlands in El-Burullus Lake and the surrounding area have come under numerous challenges. It was for this reason that Eid et al., (2020) carried out a study covering 2 decades

(1990-2019) using Landsat Time series datasets. The authors engaged two IVs namely Normalized Difference Vegetation Index (NDVI) and Normalized Difference Water Index (NDWI) in order to assess the change in their area of study. Vegetation species had increased significantly over the period under review, while the water body had shrunk to reveal bare-soil. Results showed that ~53km^2 (7.0%) of water body and 8.7 km^2 (1.3%) of open soil were lost, while areas covered by vegetation ~29.9 km^2 (7.4%) respectively. In their conclusion, the authors pointed out several factors that might have negatively affected the wetland ecosystem namely; reclamation projects, fish farms, spreading of reed beds (mainly phragmites) which covered 20% of El-Bullurus lake, leading to the drying of the lakes. Finally, the authors suggested urgent intervention on the remaining wetland for sustainable development.

Chouari, (2021), in their quest to map Al-Asfar wetlands i.e. the largest wetlands located in the Arabian peninsula engaged the use of multi-date Landsat and Sentinel-2 optical datasets captured between 1990 and 2020 in their workflow. Normalized Difference Vegetation Index (NDVI) and Normalized Difference Water Index (NDWI) were used in the evaluating ecosystem change around the wetland. Their results showed significant increase (24.69%) over the surface of the water body in 3 decades, while the areas covered by vegetation was reported to have increased by ~17.2%. The authors pointed out the causes of change and pegged it on the discharge of Agricultural pesticides, semi-treated sewage water and the spread of the weeds i.e. *Phragmites australis* which has covered ~23.8% of the Al-Asfar wetland in 2020. Chouari, (2021) gave his suggestion that the remaining part of the unaffected wetlands in Saudi Arabia should be protected on the basis of sustainable development.

Studies carried out in Yala swamp, Kenya Wanjala et al., (2020) demonstrated how flood inundation had been influenced by the seasonality and the period of inundation, altering its inherent variability. In order to understand the patterns related to inundation, the authors included cellular automata and Markov chain analysis (CA–MCA) model to simulate the 2029 dry season inundation variation across Yala swamp. Datasets used in their study included the Tasselled Cap Wetness Index (TCWI), topographic and population distribution data. There was a strong negative correlation between the inundation patterns and the land use practices around the wetland, since a decrease ~35% was noted on the wetlands. Their model projected that an additional loss of ~12% is likely to occur by the year 2029. Wanjala et al., (2020) suggested that anthropogenic processes should be controlled, since they were the major cause of change on inundation processes in Yala swamp.

Other similar studies include Byun & Han, (2018) who applied Multi-variate Alteration Detection (MAD) hence enabling radiometric normalization of bi-temporal VHR imageries, with an aim of detecting flood induced changes. Panuju et al., (2020) who reviewed bi-temporal and multi-temporal 2-DimensionLand Surface Change Detection (CD) with a focus on multispectral imageries. The authors reported different approaches including; binary changes, direction or amount of changes, "from-to" information of changes, likelihood of changes, temporal pattern, and prediction of changes, as the most appropriate techniques used. For understanding the context of improvements, advantages, constraints, difficulties, and opportunities were recognized. Such findings are expected to give future development on multi-temporal and temporal CD approaches and techniques for understanding land cover dynamics.

2.5 OBIA TIME SERIES ON WETLAND MAPPING

Studies on OBIA time series aiming at vegetation health monitoring have taken central stage in recent times especially in the field of agriculture where plant phenology (growth) patterns are detected using NDVI time series. In most of the studies, remote sensing imageries such as the freely available coarse resolution and medium resolution imageries datasets such as MODIS Landsat TM, ETM+ and recently OLI (TIRS) have been used. Thresholding of remote sensing signals are carried out by smoothing the phenology metrics using available filters and fitting them onto a curve has proven to be effective as demonstrated in recent studies.

Scientists have developed free software such as TimeStats (Udelhoven, 2011), TiSeG (Colditz et al., 2008), HANTS Roerink et al., (2000) and TIMESAT Jönsson and Eklundh, (2004) can be used to collect time series on any vegetation health and phenology. Previous studies by Hird and McDermid, (2009) confirmed that models used in TIMESAT software are highly competitive and preserves signal integrity. The importance of engaging OBIA-Time series of satellite imageries in landscape characterization is based on previous studies. For example, Serra and Pons, (2008) engaged Landsat Imagery at 30-meter spatial resolution for crop type mapping in an agricultural landscape. Thirty-six Landsat time series stack collected between 2002 and 2005 were used for signature extraction and final classification on six Mediterranean crops. Previous studies by Simonneaux et al., (2008) also engaged Landsat times series collected on different dates to identify four main classes, namely bare soil, trees on bare soil, understory trees and annual vegetation.

Li et al., (2015) in their studies on OBIA-based times series mapping on cropland engaged a combination of 10 (ten) optimal features of MODIS-Landsat time series NDVI and TSI's in crop type detection and mapping in South-West Missouri in 2007. The authors engaged OBIA, Decision

Tree (DT) and feature selection strategy on their classification procedures realizing an overall classification (OA) of 90.78% and Kappa coefficient of 0.89. The authors noted that although a desirable OA was achieved (Foody, 2002), certain limitations were noted including the error propagation caused by implementing different segmentation scales on different geometric objects generated using OBIA metrics. Spectral NDVI's generated from class soybean and corn were similar hence causing confusion between classes. Future use of textural variables included in the processing chain could help in class separation. The authors also noted that uncertainties related to their classification include the presence of cloud residues on the imageries, lack of atmospheric correction on the pre-processing stage and problems related to geo-registration in the MODIS-Landsat time Series stack. The research proposed that feature selection, OBIA-metrics and Decision Tree (DT) approach can be applied on larger agricultural areas and cropland mapping.

Busetto et al., (2019), in their studies on Paddy rice mapping in India used a fused stack TSI of MODIS and Chinese based HJ-JA/B spectral bands and some NDVI temporal features collected from different vegetation phenological metrics.

The multi-spectral data from the HJ-JA/B, which provided the pattern variation of paddy rice, were the greatest contributors to the resultant classification with an Overall Accuracy of 84.4% and a kappa coefficient of 0.68, respectively, hence observation on crop growth. Their results also indicated that the use of temporal features improved the overall classification accuracy on single-date multi-spectral image from 65.62% to 84.37% hence an increase of 18.75% was achieved. OBIA paradigm on the image with temporal features led to a near perfect classification with the Decision Tree (D.T) classifier algorithm providing a better performance than the traditional C.4.5 classification algorithm. Busetto et al., (2019) noted that although data cleaning and pre-processing was done prior the implementation process, the difference in the spatial resolution of MODIS and HJ-CCD satellite imageries could have contributed to uncertainties in the classification in the data fusion stage. Moreso, some paddy rice fields were very small to be detected at 30m spatial resolution and mixed pixels still observed in the resultant classification.

Busetto et al., (2019) concluded that future works should investigate texture and geometric features as additional variables to the OBIA based paddy rice mapping approach to improve on class separation. The use of a more sophisticated machine learning (ML) algorithms like Random Forest (RF) and Neural Networks (NN) have been proposed in the future to enhance categorization. Table 2.2 depicts similar works done in literature with regards to wetland mapping across different parts of the world. The variant approaches used, knowledge gaps and future works are also captured.

Table 2.3: Summary of relevant literature on riparian vegetation mapping from the year 2010-2020.

Authors(s)	**Data used/Landscape type**	**Method/Approach** **Problem**	**Key results** **Research Gap**
(Dabiri & Lang, 2018)	ESA-APEX hyperspectral- imagery used in characterizing Riparian reserve in Salzburg, Germany (year,2018)	Models used were OBIA-MNF model and Pixel based-MNF approach. Under segmentation and over segmentation influenced the final detection rates. Due to the high number of channels used i.e. 288, the results were influenced by 'curse of dimensionality'.	OBIA + MNF, OA=85% (Kappa=0.805). Pixel based+MNF, OA=63% (Kappa=0.559) McNear's Test proved an existing significance between OBIA and Pixel based classification @ p-value>0. 0001.Future works to engage spatial variables i.e., area, length, width and direction criteria. In addition, morphological criteria such as shape and texture.
(Kaplan & Avdan, 2018c)	Landsat5TMand Landsat 7ETM+ to characterize Mau forest wetlands in Kenya (year,2016).	OBIA and MR segmentation with more weights given to VH, NIR, SWIR. Contextual variable (Rectangular-fit added @0.6 value). Bareland and the low vegetated wetlands. Moreso, High vegetated wetland areas mixed with agricultural fields.	OBIA based classifier yielded > 89% OA. (Kappa =0.88). Rectangular fit @0.6 value added value to the classification by adding two extra classes. Future works to engage multi-temporal fusion of Sentinel-1/ Sentinel-2 to map riparian vegetation and to compare pixel-based against Object-based classification.
(Flavio C. et al., 2019	ALOS/PALSAR2/L-band/HH+HV, VH+VV used in mapping the Brazilian Tropical savanna wetland and Dry sub forest (year,2018)	A total of 9 classes were produced using OBIA-Machine Learning approach. Significant difference using McNemar's Z-test at p-value greater than α=0.5 achieved amongst Naïve Bayes; Multilayer Perceptron (MLP), Support-Vector Machine(SVM), Random Forest (RF). Landscape complexity caused Confusion between classes and high number of instances caused substantial classification accuracy in WEKA.	RF, MLP and SVM-present most accurate performance. Naive Bayes, J48 and DT low performance. However, J48 discriminated urban from natural vegetation. OBIA- RF had the overall best performance with N-Tree=200 samples used for training. OA=73.2% (Kappa=0.66). Future works suggest evaluation of evaluation of multi-temporal SAR imageries and Polin-SAR technique in the Sentinel-1(C-band) could be tested separately OR in combination with ALOS/PALSAR2 data, testing unsupervised classification using $H\alpha$ attribute space to better understand the scattering processes.

(Tian et al., 2016)	Pleaides-1A andLandsat-8OLI bands to characterize China wetlands in Northern Xianchiang region near river Ertrix (Year,2016)	Fusion of Pleiades-1A and Landsat8OLI bands was embraced. Some spectral(NDVI), geometric (shape index), textural(GLCM) and machine learning algorithm used i.e. RF, ANN, PCA-1 and PCA-2 respectively. NDVI and GLCM reduced spectral similarity between classes. Pleiades and Landsat 8OLI used alone produced inferior classification results. SVM and ANN not suitable for water classification	Results obtained were OBIA-RF=98.7% (200trees), SVM=89.9%, ANN=90.2%. Overall classification using ground truth and RF=92.5% (10- 15% higher than SVM and ANN). Geometry (shape) aspect improved the boundary between water and farmlands. Future works suggest use of statistical analysis on the probability of the adjacent land cover classes as well as their spatial distribution patterns of various wetland land cover.
Boit,2016	Landsat5TMand Landsat 7ETM+ to characterize Mau Forest wetlands in Kenya (year,2016).	Supervised Maximum Likelihood classification, Pixel-based approach, Images and NDVI used. No Machine Learning algorithm used.	Overall Acc; 1989=76%, 2000=81%,2010=83%. Forest area reduced from 15% to 13% in 2010. Water bodies increase from 1.4% to 1.5% per year between 1989 and 2000. Water levels decreased by 1.3% by the year 2010.Future works to map the dynamism of water bodies(Lakes)especially within the Kenyan Rift valley.
(Weih & Riggan, 2010)	SPOT5,Aerial image and Digital orthophoto used in characterizing wetlands in Garland County within Arkansas Rural with pasture and hot- springs/Hot spring National Park.(2010)	Supervised and Unsupervised classification, OBIA, Pixel-based, Multi-spatial, Multi-temporal. A kappa analysis and pairwise Z-test significant at $\alpha = 0.05$. Adding multi-temporal/multi-spatial data didn't improve classification accuracy. Problem with the (Congalton & Green, 2019) approach since the image looked improved visually but not statistically.	OBIA with OA=82% (kappa 0.78). Supervised classification-pixel based OA=66.9% (kappa 0.61) and unsupervised classification pixel based, OA=64.4%(kappa=0.57).Multitemporal+multispatial+OBIA=OA,82%.Multi-spatial alone+OBIA=78.2%. OBIA not statistically significantly different from the non-OBIA classifications, but it was statistically different. Future use to engage OBIA-based spectral and contextual variables in order to improve the classification accuracy. instead of using (Congalton & Green, 2019) approach, the standard error approach to be used instead (Gao & Mas, 2008)

(T. Berhane et al., 2017)	Quick bird and Pan bands bands, plus other bands including VI's (NDVI) Ratio transformed bands(nir/red) Texture metrics (dissimilarity) Topography-metrics (aspect) Total number of bands used (37) used to characterize Lake Barkal drainage networks in Russia (year 2013).	Methods used include; ISOCLUSTER algorithm, Unsupervised pixel based (maximum Likelihood) and Supervised OBIA-based. Correlation analysis between the bands to determine the most suitable variables. All variables realize an average Pearson correlation coefficient at R=0.89.No significant difference achieved(Gao & Mas,2008).Increased segmentation scales reduced model performance. increase in features (22 variable), reduced classification accuracy.	OBIA-RF approach with 5 band combination and scale 5metres with a low Out of the Bag error (OOB) had the highest OA (90. 4%).Pixel based RF may be most suitable for wetland classification. The hybrid OBIA-RF approach can likely be applied in similar settings where spectral information has more influence than shape in wetland class distinction and should be further explored
(Heumann, 2011a)	Worldview2, Quick bird and their pan-bands including their spectral bands and their spectral bands and ratios(NIR/RED)(NIR/blue)(RE1/b lue)(Yellow edge/Blue), to characterize the mangrove forests in Galapagos Island National Park (year,2010)	OBIA-SVM, OBIA- Decision Tree models. OBIA-Worldview and OBIA+DT+SVM). Hybrid combination on Quick bird and Worldview2 using Jeffries Matutisa separability. Lack of clear boundary between mangrove species. Mixed pixels between mangrove species on the fringes of the ocean when they are sparse or degraded. GLCM texture variables did not improve the separability of fringe mangroves.	SVM based classifier using the non-linear RBF led to an OA of 94% with true mangroves being classified. Tree mangroves had a higher producers and user accuracies except for buttonwood and black mangrove which yielded lower accuracies. Future research to use hyper spectral images to enhance spectral and class separability between species. Lidar signals to enhance image segmentation based on canopy structure and spectral property.
(Mubea & Menz, 2012)	Landsat5TM,7ETM+Worldview2, ALOSPALSAR(HH+HV,VH+VV). Red,Green,Blue,NIR/SWIR and a DEM to map Nakuru urban Municipality in Kenya (Year,2010).	Support Vector Machine (SVM) and Maximum Likelihood classifiers used. Performance-evaluation using method by (Congalton & Green, 2019**).** Increasing the values of Radial Basis Function(RBF) in SVM reduced classification accuracy.	ALOS/PALSAR'S(HH+VV)+Land-Sat,realized OA(94.64%kappa=0.88).SVM(RBF=0.33)onAL OS/PALSAR-standalone (2010) yielded OA (84.1%;kappa=0.69);DownscaledLandsat7ETM+ (2010) from 30m to 12.5m did not increase classification accuracy. using SVM, the same applied to Landsat TM (1986) Upscaling WV2 from 0.5m to 28.5m yielded inferior results with OA (76.76%) using SVM classifier. 6 classes were generated lake Nakuru inclusive. In general, SVM

			proved to be superior than MLC. Combine WV2 with Landsat of the improve overall performance.
(Mason et al.,2012	TerraSAR-X/3m/X used to characterize, the urban(UK) flooding in Tewkensbery region (year 2007)	Methods used were Thresholding and OBIA segmentation Approach. The problems noted with thresholding include certain aspects i.e. vegetation masking some of flooded vegetation, Dry and smooth bare soil exhibiting backscatter similar to the water surfaces(Giustarani et al.2015) and Double bounce due to the emerging vegetation or buildings from-inundated areas(Hoang et al.2015)	Rural areas automatically map floods in close to real time. 89 percent of aerial photography-derived flooded regions have an accurate overall Accuracy. The same method can be applied to other flooded areas of similar landscapes.
Moskal et al., 2011a	Aerial-image (National Land- cover NAIP imagery (2009) depicting Reiner valley. Quick bird image (2007) 4bands, NIR (0.6m res) city of Seattle. Oblique photography (2009) of King County True color image were used to characterize wetlands in Reiner Valley (Seattle USA) Puget sound Region (West of Washington)/seaward park with tree cover.	OBIA based segmentation approach embraced. Textural, spatial and textural variables included. Tree, shrub, and grass distinguished using variables i.e. Greenness Index, brightness, and difference. GLCM length to width variables and proximity to objects of interest analysis. Problems encountered include ;difficulty in spectral separation, grass mixed with shrubs, Impervious surface mixed with grass or shrubs and building mixed with grass.	OBIA separated Built-up, Impervious and tree species with OA (71. 3%).Built-up (85.3%)and impervious (72.1%) classes had the highest Producer's accuracy. OBIA on Naip imagery produced an OA (72.1%) and an OA (83.3%) on Quick bird image. Among all the case study the Tree class had the highest user's (80.8%) and Producer's accuracy (89. 4%).The image with the highest-spectral characteristic-achieved the highest accuracy while the image with the highest spatial characteristics had the lowest OA results. Future research to add LIDAR data into their classification.
Adromachi et al.,2017	Sentinel-1(SLC)-2016), Sentinel-2MSI(Jan and August,2016.STRM C/X-band Radar(2005) used to characterize wetlands in the Northern Greece's National Park of Koronia and Velva (NPKV) features a semi-urban setting.	Predictor variables included Texture (GLCM, PCA), MNF, Slope Aspect and Elevation(STRM). Resampling of all datasets to 10m Res. (Bilinear convolution). Problems encountered include; distinguish inland vegetation from aquatic plants was difficult. Difficult to	OBIA on S2 revealed an OA (90.8%) while OBIA on Multispectral S1 and S2 an OA (93.9%) hence an increase of 3%. Adding PCA and Knowledge base on S1and S2 Multi-temporal combination increased the OA by 1%. Combining S1-S2 MT data was able to separate wetlands from non-wetland areas. Adding NDVI, NDWI, PCA, MNF,

		distinguish between built-up vegetation and natural vegetation, likewise sand from soil.	GLCM variables. I.e. entropy, dissimilarity etc., plus shape indicators improved classification by between 0.5% to 3%. RBF parameterization in SVM improved on the classification accuracy. Future works include; testing same workflows on similar landscapes, Multi-season and Multi-annual datasets to be used in the thematic classification of wetlands. Use of Post classification approach on RF and ANN algorithms .
Gasparovic and Dobrince, 2020.	Sentinel-1(5m), Sentinel-2MSI(10m) used to characterize wetlands in Prague, Cologne and Lyon both in ascending and descending orbit (year,2019)	Machine Learning SVM, RF, XGB, AB and ELM on Multitemporal and Single date imageries. Accuracy assessment using Kappa coefficient, F-Score measure, McNemar's test and Figure of Merit(FOM). SAR-C band (~5.0 cm) is less suitable for distinguishing urban vegetation(forest confused with water or soil) in Prague, Cologne (low vegetation mistaken with forest), and Lyon (built-up confused with low vegetation) (Patel.P,et al.,2006)	SVM on Single date speckled S-1 had an OA (61.6%), Single date S-1(non-speckled) at OA (80.2%), 3-Date Multitemporal S-1 and 5-Date MT Sentinel -1 produced an OA (90%) in both cases. Using MT-3 and MT-5 increased the OA by 8.6% and 13.6% respectively. Future works should engage GLCM texture to distinguish class borders on both optical and SAR images together. use of Sentinel-1 Multi-temporal SAR with CNN Deep Learning models. Use of Cross-validation (k-fold) recommended.
Long et al., 2014	Radarsat-2(SAR) 2009, ENVISAT(ASAR)2012-2013. Landsat5TMused to characterize river Zambezi and Lake Liambei wetlands in Zambia. Landuse include agricultural , urban and Impervious surface.	Methods used include; Image differencing, Histogram thresholding to remove dark pixels, Change Detection(CD). Gamma filtering for removal of speckles (post-processing). Random Forest and Decision Tree(DT) classifiers. Problems noted include; Landsat5TM not suitable for reference in flood mapping. Moderate pixel error observed due to cloud cover on the pixel based Landsat5TM image.30%-90% of non-matching pixels occurred in the	The pixel % in error (non-matching pixels) increase with the image spatial resolution (60m reduced to 6 .25m). Pixel based Landsat5TM classification correlated to SAR based flood classification maps except for few errors due to cloud cover in the time series. Change Detection and Threshold(CDAT) maps correlated well with SAR based flood maps. Lack of Quantitative information in the results except visual assessment on the flood maps. This technique has been successful at mapping the extents of seasonal

		non-flooded areas, yet they were considered as flooded.	floods in Caprivi, Namibia in 2009, 2011, 2012 and 2013 and answers the work of Pricope (2013).No suggestions for future works found.
(Fabio Cian et al., 2018)	Ascending and Descending, Cosmo-Sky-Med (X-band-HH). Terra- SAR-(X-band-HH), ASAR (C-HH+VV+VH). All were captured in ascending and descending modes. These bands were used to characterize wetlands in different regions i.e. swampy landscape (Nsanje,Uganda), flooded urban area(Veneto, Italy), and Northern Uganda(Teso district) in year 2010	Thresholding using Difference Flood Index (NDFI) and Normalized Difference Flood in brief Vegetation-index Thresholding (NDFVI). Change Detection, Cross-validation fold. The method did not detect class, ‘short vegetation in water’. Secondly mixture of pixels belonging to the ‘flooded water’ class and the ‘short vegetation in water’ class. Inconsistency in the Sentinel-1 pixel geometry.	Cross comparisons with the e-GEOS reference image resulted in overall accuracy of 85%. Using the Copernicus EMS image (CIMA) as a reference (Pulvirenti et al., 2011)resulted in a specific agreement on flood areas of 75.7 % and an overall agreement of 96.7 %. NDFVI was able to recognize shallow vegetation in water. The same workflow can be applied in other landscapes to retrieve ’short vegetation in flood areas. The use of Sentinel1(SAR),Single Look Complex (SLC) datasets can be used to further improve the results of this study.

2.6 SCOPE OF THE STUDY

The study investigates how Object-Based Image Analysis (OBIA) approach when integrated with machine learning is able to enhance target feature extraction in heterogeneous riparian landscapes. Several steps were involved including but not limited to the following: i) Collection of remote sensing datasets i.e., Landsat 5 TM, Landsat 7 ETM from USGS and Dual SAR Sentinel-1 (GRD and SLC) and Sentinel-2 optical imageries from Copernicus sci-hub. ii) Due to the challenge in detection and characterization of Acacia tree on the datasets, OBIA and Machine Learning approaches are embraced in order to allow for easy detection of the target feature using Sentinel Products from 2014-2020. iii) Since OBIA can't work as a standalone tool, GIS and remote sensing are integrated in order to come up with maps of high integrity, accuracy and clarity. iv) In order to capture phenology metrics for tree health assessment, the Landsat times series images captured between 2008-2017 consisting of before and after flood events imageries were used. A novel approach was used to run time series on different seasonal datasets hence coming up with temporal profiles depicting disturbance of the Acacia Forest over the years. v) Spatio-temporal information about the Acacia in relation to the flooding lake was carried out using correlation studies engaging the relationships between the area covered by the lake against the area covered by Acacia strands around the lake in the period 2014-2020. The range of years described in this study depended solely on data availability.

Figure 2.3 shows the relationships of some of the algorithms used in this study whereby under Machine Learning we have classical learning which involves supervised classification which was adopted using SVM, K-NN, Naïve Bayes and Decision Tree(DT). Under Unsupervised classification, several algorithms were embraced in the study such as K-means clustering and dimensionality reduction such as Principal Components (P.C.A). Application of ensemble learning into the datasets include; Random Forest with bagging on image stacks. The Artificial Neural Network (ANN) group involves the use of Convolutional Neural Networks (CNN) and Multi-Layer Perceptron(MLP).

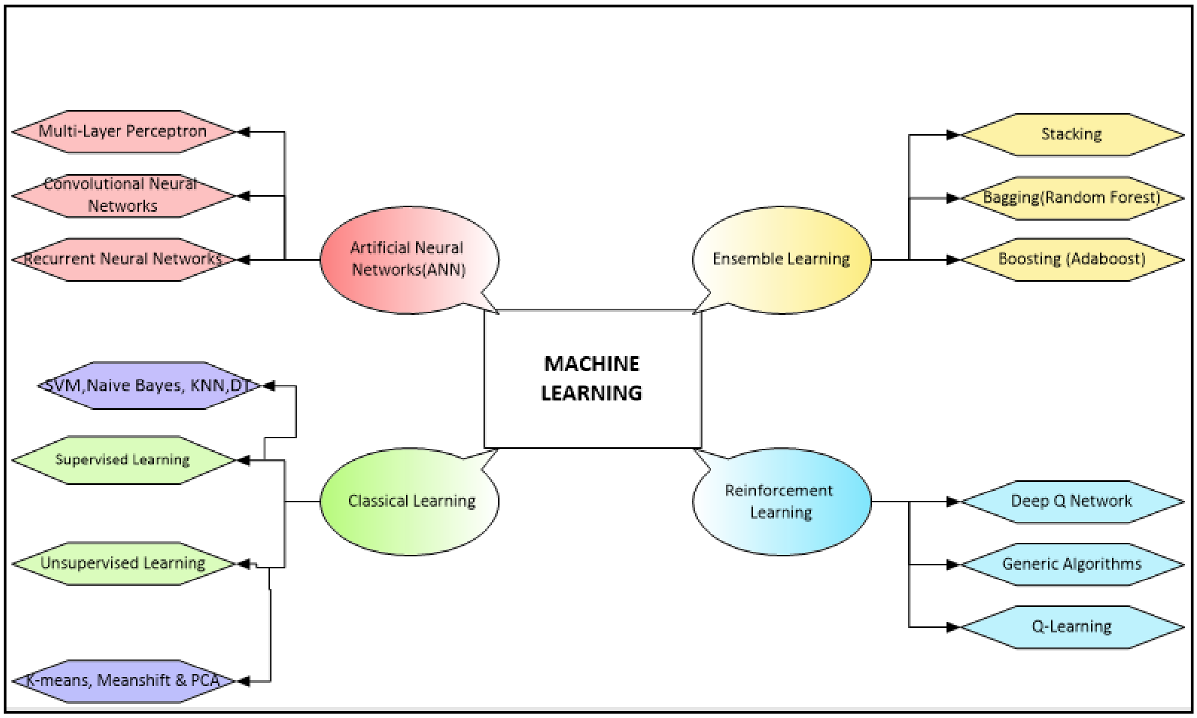

Figure 2.4: A schematic diagram showing variables used in the study **Source**: Zaheer Ch Zee

2.7 PROBLEM STATEMENT

Due to unsustainable development, 87% of the world's wetlands have been lost over the past 300 years, and 80% of the world's untreated waste water has been dumped into wetlands. These are fragile environments that suffer from the invasion of alien species, which can be very harmful to local species. Wetlands are suffering from environmental changes brought on by climate change. The largest threat to these places is the draining of wetlands to make room for agriculture or settlement. Wetlands are frequently used as landfills for the disposal of sewage, domestic trash, and industrial effluents.

Lake Nakuru is a Ramser site of international importance (Avni, 2020).It is a home of herbivorous animal population including the Rothschild giraffe (*Giraffa camelopardalis rothschildi*), vervet monkeys and a sanctuary for some endangered animal species i.e. Black rhinoceros (*Diceros bicornis*) which depend on *Acacia xanthophloea* tree species for their fodder. Massive degradation of Acacia has been witnessed over the last 13 years Mangi et al., (2022) due to the effect of pollutants from Agricultural farmlands and industries (Alvin,2020; Mwanzia et al.,2013). Moreover, untreated sewage effluents from the surrounding heavily populated Nakuru Town (Avni, 2020) is also emptied into the lake.

Due to the fact that Lake Nakuru is a closed hydrological ecosystem without outlets, bioaccumulation of toxins within the system poses a great risk to both the flora and fauna within the park, hence interference with the whole food chain. Despite the existence of the laws governing sustainable use of wetland resources (Maithya, 2021), Kenya wildlife services (KWS) as the key player has been unable to implement them due to unavailability of financial resources.

Lake Nakuru has been expanding beyond it's designated boundary based on the 2000 Land Use Land Cover map Ng'weno et al., (2010) and hence risks being deregistered from the list of wetlands of international Importance due to it's unsustainable use. Ecologists and wildlife managers lack knowledge on the extent of damage on Acacia, thus unable to fulfil policies as engraved in the Ramser convention of1971(Maithya, 2021). Previous studies in LNNP have engaged optical-based imagery Mangi et al., (2022) but none has used RADAR to characterize Acacia xanthophloea as a unit of study. Knowledge on engaging deep learning (R-CNN & Retina-net) and Machine learning (i.e. RF, DT) frameworks and algorithms into the workflow is also lacking. Inadequate knowledge calls for the creation of a new algorithm that enable detection of spatial and spectral aspects of time series BIG DATA on existing historical data from spaceborne and airborne sensors. Researchers gaps inherent in their previous research on riparian vegetation characterization and scientific data on ecological functions and inter-relationships especially in the area of Remote sensing and Geosciences is also lacking in developing countries. This study aimed at assessing the rate of Acacia xanthophloea degradation around Lake Nakuru National Park using an Object based Image Analysis (OBIA) Approach, hence providing policy makers and Park Managers with a decision-making tool.

2.8 JUSTIFICATION FOR STUDY

Although lakes are the world's most popular tourism attractions, increased pressure from tourism and recreation, impact of climate change, environmental change and increased competition for land and water has made sustainable development of lake tourism problematic (Hess & Kelman, 2017; Gössling et al., 2012). In 1955 Lake Nakuru was observed to have dried up completely and only reappeared in 1959; in line with reports from World Lakes Water watch (KWS et al., 2004). Since it's gazettment in 1968, Lake Nakuru National Park was expanded from its original area of coverage (63.5sqkms) to the current 188sqkms (Mwasi, 2002), 42sqkms of which was covered by the Lake. In recent times the lake was noted to have been drying due to the drying streams that fed the lake, namely; enderit, makalia and njoro.

The rivers became permanent in 1982, but recently became sporadic and heavily laden with silt during the rainy seasons (KWS *et al.*, 2004).The siltation was attributed to deforestation that took place in the upper Mau Complex and catchment basin that feed Lake Nakuru (Iradukunda et al., 2020). In 1987 a reinforcement along its perimeter using electric cables with an aim of protecting the then newly introduces Black Rhinoceros. In 1990, Lake Nakuru wetland was registered as Ramser site (Mbithi, 2016) and later in 2011 recognized as designated UNESCO world heritage site (Hausmann et al., 2019). The primary Act governing wildlife conservation and management in Kenya is the Wildlife Conservation and Management Act Cap 376 of 1976 and the 1989 Amendment (Otianga-Owiti et al., 2021).

Kenya Wildlife Services (KWS) which is the lake's management authority, is governed by this Act. It's duties include creating and carrying out management plans for National Parks and National Reserves, as well as exhibiting animals and plants in their natural habitats to promote tourism and benefit and educate Kenyans. The Act also empowers the director to collaborate with other authorities to ensure that animal migration corridors, which are crucial to the survival of National Parks, are preserved. Despite the existence of these legislative laws, implementation of such requires proper design, planning and resources which might not be available. The major phenomena that has disturbed ecologists and which needs to be addressed by KWS is the degradation of Acacia woodlands around lake riparian reserve. Since the year 2010 most of the Rift valley lakes (Lake Nakuru included) have been experiencing surging water levels (Chrisphine et al., 2016). Siltation (Iradukunda et al., 2020) is one of the factors that has attributed to the swelling of the lake, hence the degradation on the *A. xanthophloea* on the lake's riparian reserve. This tree species is an important habitat to a number of bird species in the park and fodder for the black Rhinoceros and Rothschild giraffe (Kiffner et al., 2017).

Object Based Image Analysis (OBIA) approaches have been used in change detection studies (Paliwal et al., 2019 ; Ma et al., 2016). Object features include properties such as color, texture, shape, area and scale. Previously studies have shown that the common pixel-based algorithm that has drawbacks and hence the need for OBIA's exploration on riparian vegetation characterization (Keshtkar et al., 2017). There is an existing gap that need to be understood about the effect of the flood waters on the riparian vegetation. The workflow used in this study could help lead mapping agencies to revise the Topographical map (Scale: 1:50,000) of Lake Nakuru National Park (LNNP) in order to adapt to the current state of Land use patterns as inscribed in Kenya's Vision 2030. Quantitative information on the number of degraded trees forms a basis for planning onto which clearing of tree logs on wild animal corridors could be implemented (Kenya Vision 2030 , 2007).

The study aimed to use Object-based approach to describe relationships between the dynamism of the lake and its effect on Acacia xanthophloea in terms of several categories of characteristics each of which are assigned certain weightings. The methods used in this research will be used by future researchers as a basis of tree monitoring and characterization on complex riparian reserve. It gives researchers a baseline onto which they can improve the current deep learning networks to handle objects (degraded trees) on complex riparian landscape. The results of this study will be valuable to a wide range of stakeholders including Cartographers, ecologists, hydrologists, wildlife managers and conservationists.

2.9 GENERALOBJECTIVE

To determine the distribution of *Acacia xanthophloea* around Lake Nakuru using OBIA and machine learning approaches on time series datasets.

2.9.1 Specific Objectives

i. To evaluate the capability of OBIA in characterization of Acacia Xanthophloea along Lake Nakuru riparian reserve.

ii. To evaluate the integration of object-based approach into remote sensing and GIS.

iii. To determine the spectral changes on Acacia xanthophloea tree spp using OBIA approaches (2008-2020).

iv. To determine Spatio-temporal changes on Acacia xanthophloea tree using OBIA approaches (2008-2020).

2.9.2 Research Questions

i. What is the performance of object-based approach in characterizing Acacia Xanthophloea on Lake Nakuru Riparian?

ii. What is the effect of integrating object-based approach into remote sensing and GIS?

iii. What are the spectral changes that have occurred on Acacia xanthophloea spp along Lake Nakuru Riparian using OBIA approaches? (2008-2020)

iv. What are the spatio-temporal changes that have occurred on Acacia xanthophloea spp along Lake Nakuru Riparian using OBIA approaches? (2008-2020)

2.10 DESCRIPTION OF THE STUDY AREA

Lake Nakuru National Park is located in Nakuru County, 170 kms from Nairobi. Its bottom initially before the recent flooding was about 1756 meters above sea level while the surface of the water at 1758.5m above sea level. The altitude ranges from 1760-2080m above sea level. Mean annual rainfall ranges between 876mm and 1050mm and has an inherent bimodal pattern. The long rains start in March and end in June while the short rains occur between October and December. Mean daily minimum and maximum temperatures fluctuate between 8.2◦C and 25.6◦C. Lake Nakuru has no outlets and hence evaporation is the only factor that accounts for water loss.

Four seasonal rivers feed the lake, i.e., Lamurdiak, Enderit, Makaila and Enjoro. The soils are volcanic and shallow in nature. Underneath the open grasslands were soils and ashes which were well drained, friable to sandy clay loams that supported the grasslands in the park. Siltation from sand harvesting contributes to the fluctuation of the water depth in the lake. According to previous studies by Iradukunda et al., 2020, the depth of Lake Nakuru has was 2.18m in 1972 but increased to 4.18m hence recording a 47% increase. Multi-spatial and Multispectral datasets were used in this study i.e. Sentinel 1 and 2, Landsat TM and ETM+, ALOS, Pleiades-1A and UAV. A total of four (4) training and testing sites were established for each study, except for the UAV study which had 6 designated plots around the lake. Sentinel-1(GRD) involved Training site 1 on the northwestern side and corresponding test site 1 on the northeastern part. In the other hand Train site 2 was established on the southern part of the lake and test site 2 on the southwestern part of the Lake. Figure 2.4 depicts the Locational Map of the study area.

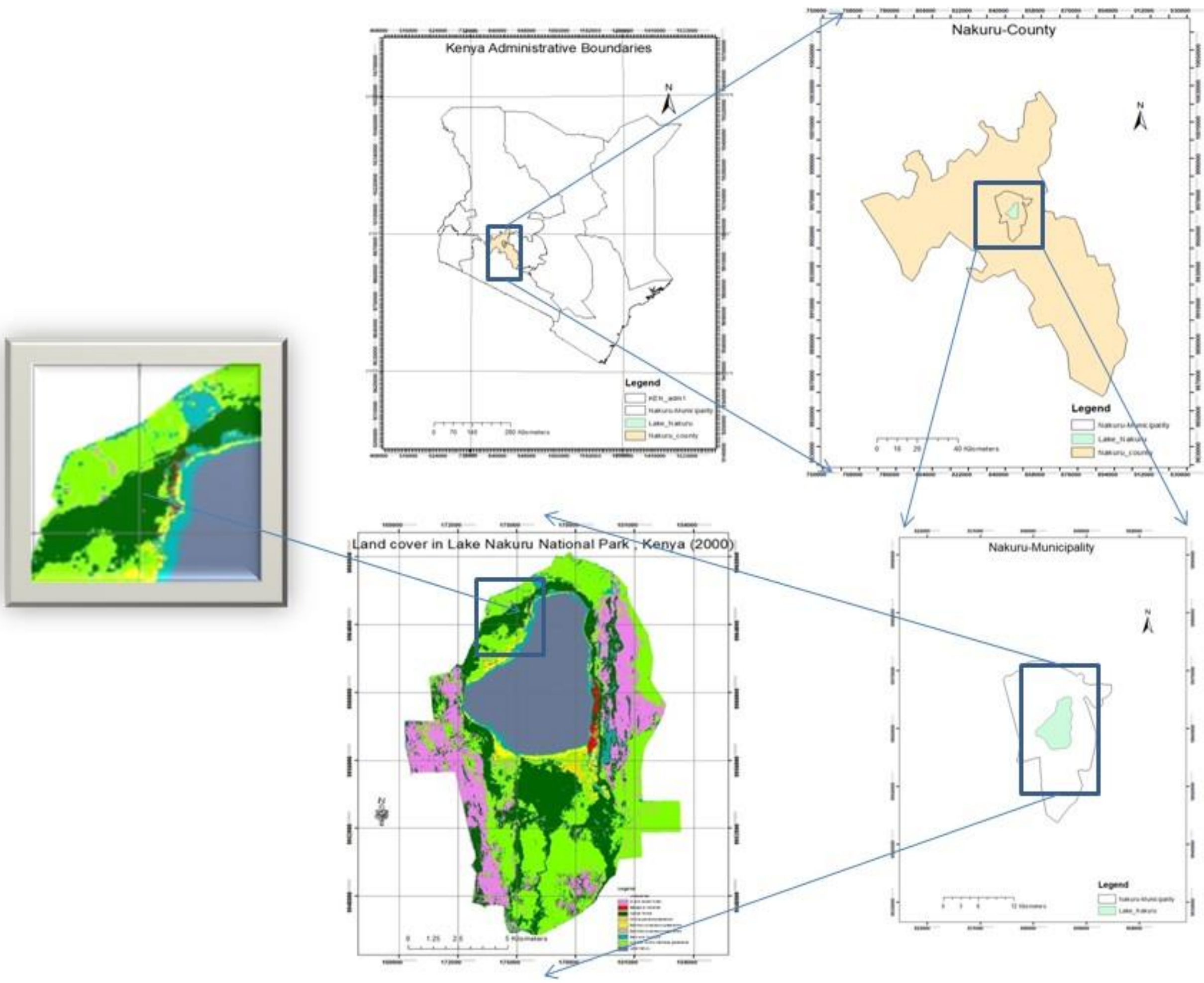

Figure 2.5**:** Study Area, located in Nakuru County within Nakuru Municipality (0◦18’S → 0◦27’S, 36◦1.5’E → 39◦9.25’E), Kenya.

2.11 ORGANIZATION OF RESEARCH STUDY

The Research is organized into 9 (Nine) chapters as follows:

Chapter 1: General Introduction.

Due to the effect of the overflow of saline waters on Lake Nakuru riparian, Acacia xanthophloea tree species have been suffering from moisture stress. This Chapter introduces the importance of wetlands as kidneys of nature and the role they play in regulating closed and fragile ecosystems such as in the case of Lake Nakuru basin. In addition, it explains how external drivers have contributed to pollution in Lake Nakuru leading to the flooding of the Lake. It further explains the role of existing policies in sustainable management of the wetlands, key players and inherent challenges. In addition, this chapter highlights the problem inherent in the study area being *Acacia xanthophloea* degradation experienced over time. Justification which includes the importance of Lake Nakuru being one of the wetlands of international importance and hence needs to be monitored. The main and specific objectives act as guide into the next chapters.

Chapter 2: Literature Review of the study

This chapter begins by introducing the context therein. It gives a detailed approaches used by several authors to tackle the problem in different depths and context. Their study areas are specifically wetland landscapes situated in different parts of the globe namely United States of America (U.S.A), United Kingdom (U.K), Germany, France, Italy, Russia, Greece, Brazil, Ecuador Turkey, Kenya, Uganda, Zambia and Zimbabwe. The gaps inherent in these studies were captured and engaged further in this study.

Chapter 3: OBIA-SAR hybrid classification with machine learning approaches in mapping A. Xanthophloea along Lake Nakuru, Kenya.

This Chapter is related to the paper that was presented in ISPRS 2021 Congress and published in the Annals of International Society for Photogrammetry and Remote Sensing (ISPRS). In this section the importance of *Acacia xanthophloea* tree species is emphasized, one of them being to protect the Lake from siltation and pollution. The challenge of mapping flooded *Acacia xanthophloea* and related species is inherent in this study while the goal of this study was to use a Time Series of Sentinel-1(VV and VH) of Single Look Complex (SLC) orbit, in detecting Acacia *xanthophloea* degradation along Lake Nakuru Riparian Reserve. The Specific objectives outlined herein aims to answer to the following objectives: i) To determine the spectral changes that have taken place along the riparian reserve using co-registered Sentinel-1(SLC) time series. ii) To explore the capability of C2 Covariance matrix derivatives (C11, C22 and RVI) to characterize the condition of *Acacia xanthophloea*. iii) To explore the Spatio-temporal changes that have occurred on Acacia strands. To answer specific objective (i), Sentinel-1(SLC) polarimetric bands that had the highest spectral response were C11, C22 and RVI. In response to objective(ii), the best performing bands (C11, C22 and RVI), were used in *Acacia xanthophloea* detection. Several Models were used in running the classification. Results obtained realized high detection rates >90% with OBIA-Random Forest approach.

Chapter 4: Integration of OBIA into G.I.S and Remote Sensing in characterizing the distribution of the fever trees.

The findings in this Chapter are related to a published Conference paper, currently archived in the HAL repository (https://hal.univ-reunion.fr/hal-01960341/file/geobia2018osio). In this chapter, Integration of OBIA into Remote Sensing and G.I.S is demonstrated. The motivation behind this approach is to enable data transfer, cleansing and re-organization across different softwares that were used. Since there was no single software that could handle data pre-processing, processing and post processing, Object Based Image Analysis (OBIA) paradigm existing in eCognition Developer 9.2 was used due to availability of a range of segmentation algorithms therein. The results obtained from eCognition Developer environment were then transited to ARCMAP environment for post-processing. Furthermore, the .csv files were exported to WEKA machine Learning Environment for further analysis.

Chapter 5: Spatio-Temporal Monitoring of Acacia xanthophloea

This Chapter is related to the journal paper that was presented in ISPRS 2020 Congress and published in the Annals of International Society for Photogrammetry and Remote Sensing (ISPRS). Detecting and mapping flooded vegetation remains a challenge, especially when the target vegetation is immersed in flood waters. The study demonstrates how Sentinel-1 Level 1C ground range detected in conjunction with Sentinel-2 optical imageries can be used to characterize and detect the spatial distribution of Acacia xanthophloea in time and space. The motivation behind this study was to extract Attribute profiles (AP) from Sentinel-1(GRD) polarimetric bands i.e., VV and VH and use them to detect the condition of *Acacia xanthophloea* tree species. As a comparative measure, conversion of the VV and VH Polarimetric bands to GLCM bands and Attribute Profiles (AP) was embraced. The study aimed to fill the following knowledge gaps i) Identify a reliable method that can be used in tree condition and health detection. ii) Produce reliable maps validated using up-to-date temporal reference maps and machine learning approaches. iii) Explore the capability of σ_{db}VV and σ_{db}VH backscatter and their haralick features in Acacia xanthophloea health condition and health. iv) Explore the capability of morphological attribute profiles (AP) in discriminating Acacia trees. To answer to the knowledge gaps in sequence, the most reliable method involved the use of attribute profiles in characterization of *Acacia xanthophloea.*

Chapter 6: A Novel Approach of detecting and mapping Acacia xanthophloea phenology metrics on Landsat Time Series

This chapter contain a manuscript expected to be published in the Journal of Remote Sensing of Environment (MPDI). In this chapter a novel algorithm OBIA.py (see appendix VI) was developed with the aim of detecting *Acacia xanthophloea* patterns along Lake Nakuru riparian reserve. The significance of producing different clusters was to detect the health condition of *Acacia xanthophloea on* the Fragmented riparian reserve. The motivation behind this study was to generate clusters based on the condition of the riparian reserve. A Very High Resolution (V.H.R) image at 10cms spatial resolution was used as a reference image as a basis for the generation of clusters. The clusters produced as a result were then used in running 68-time series on Landsat 5TM and Landsat 7ETM captured between 2008 (before the floods) and 2017 (after the floods). Research questions inherent in this study were; Does the newly developed OBIA.py algorithm able to run Big data of NDVI in its processing chain? ii) Does Acacia forest phenology metrics described by both the Landsat 7ETM+ and Sentinel 2 MSI NDVI datasets allows for the detection of forest degradation? iii) What are the differences in phenological parameters of the degraded, non-degraded and degraded-submerged forest? NDVI time series derived from the datasets were used in the production of temporal profiles (graphs) in TIMESAT software environment. Application of OBIAT.py code based on SLICK-K Means algorithm was able to produce clusters along the riparian reserve, hence the production of temporal profiles and phenology metrics associated to vegetation health.

Chapter 7: Detection of Acacia xanthophloea using Deep Learning techniques on UAV imageries.

This chapter is related to the journal paper that was presented in ISPRS 2022 Congress and published in the Annals of International Society for Photogrammetry and Remote Sensing (ISPRS). In this section the capability of deep networks, i.e., Region Based Convolutional Neural Networks (R-CNN) and RetinaNet on imageries derived from Unmanned Aerial Vehicles (UAV) based flight missions are explored. The motivation behind this study was to use Very High Resolution (~5cms) imageries to detect *Acacia xanthophloea* at Individual scale. Detection of flooded riparian vegetation at individual scales was made possible through the application of deep learning techniques on 256*256-pixels image patches in combination with their respective annotations in form of .xml files. These datasets are injected into the R-CNN and RetinaNet channels for the purpose of detection and classification of individual trees and their environmental background. Different Metrics were used to measure the capability of different Networks in the detection and classification of individual tree species at local scale. The study aimed to answer two knowledge gaps: i) Determine the capability of the R-CNN network in detection of Acacia xanthophloea at individual scale? ii) Determine the capability of the Retina-Net Model in characterizing Acacia xanthophloea at individual scale. In this study the R-CNN and Retina-Net are used in comparison, in order to determine the better option.

Chapter 8: Object Based Time Series using Pleiades imageries.

This chapter is a manuscript expected to be published in the Journal of Remote Sensing of Environment (MPDI). In this section, the capability of Pleiades imageries in detection of Acacia xanthophloea is demonstrated. The Areas of Interest (AOIs) corresponding to each UAV mission were created in ARCMAP to enable extraction of the same areas as covered by the UAV flight missions in four different years i.e., 2012, 2016, 2018 and 2020. The motivation behind this study is to generate time series maps for the purpose of detecting thematic changes that took place nine years. In addition, the imageries were used to generate Landuse Landcover (LULC) and NDVI maps of the same regions. The study sought to fulfill the following objectives; i) To test the capability of OBIA analysis on VHR Time series of Pleiades -1A imageries ii) To analyze the importance of machine learning on OBIA classification scheme iii) and to quantify their contribution to classification accuracy iv) To quantify change by implementing post classification comparisons on the target classes.

Chapter 9.0 GENERAL DISCUSSION, CONCLUSION AND RECCOMENDATION

In this Chapter, the General discussions are captured from the summary of the results by giving a brief outlook of the results presented herein. In the conclusion part, the author gives an overall conclusion about the various approaches used in the study and the inherent research gaps. Final recommendation is also given at the end of this section, followed by the reference section. The Appendix consists of important documents in form of Approval letters, Conversion Tables and License that were necessary for carrying out the entire Research study. Figure 2.6 describes the statistical tests implemented on parametric and non-parametric datasets. The assumptions made in the workflow is that the dataset used are independent, continuous and needs parametric approach in finding the differences between the algorithms and metrics used. In the case of this study continuous data (satellite and airborne) were used, which underwent subsequent classification using the various machine Learning (ML) and Convolutional Neural Networks (CNN). The differences in the means of the results were dependent on the number of treatments (number of algorithms) used. In this study, the least minimum number of algorithms used were two (2) while the maximum was four (4) hence fulfilling the parametric assumptions required in the workflow. Since this factor was fulfilled, the workflow allows for the use of ANOVA one-way analysis to carry out tests on the differences between means as used in this study. In order to determine the significance differences between specific algorithms then further tests (Post-Hoc analysis) were carried out using Tukey's test

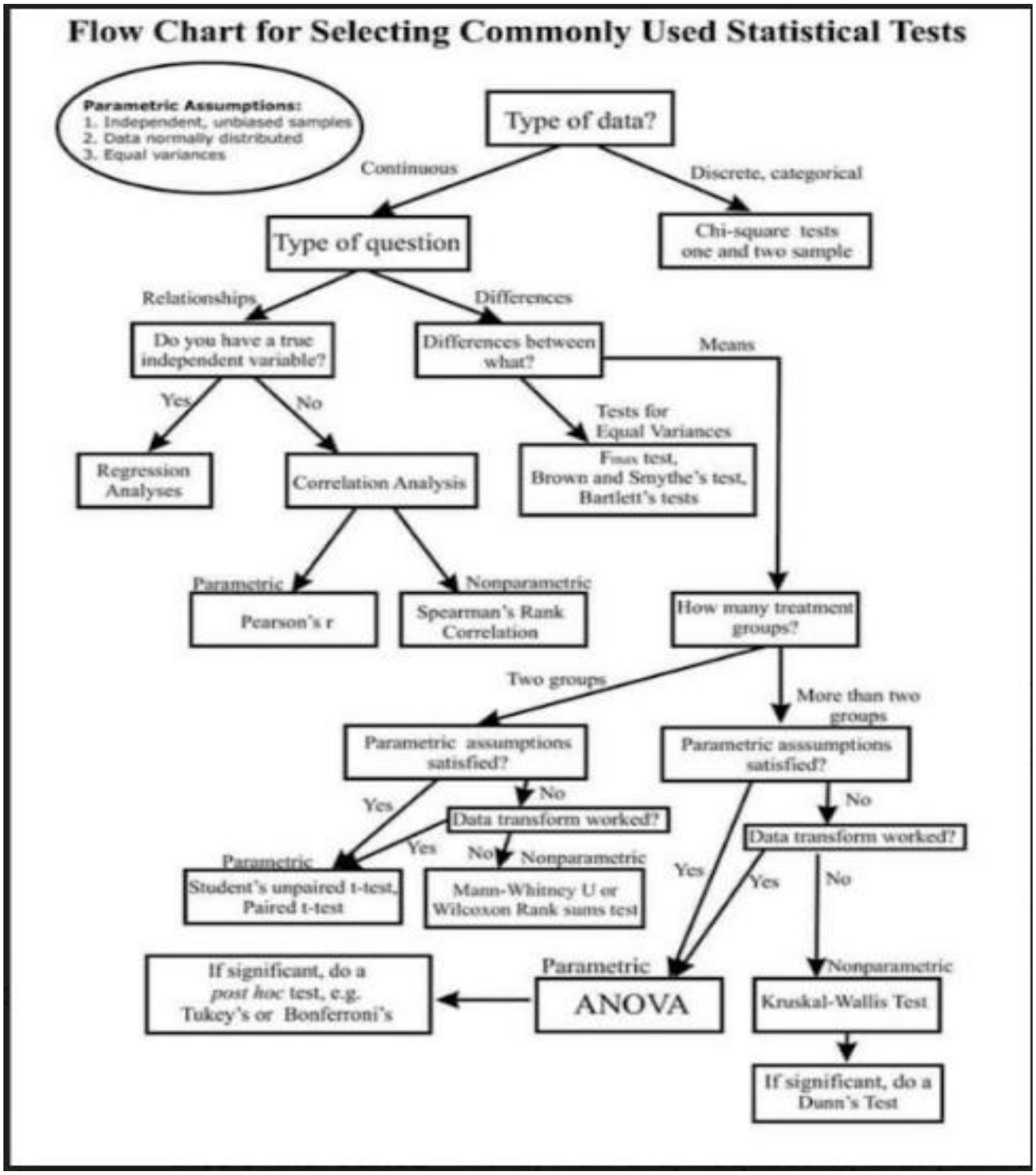

Figure 2.7: A Flow chart depicting the selected statistical test in this study **Source**: Abhishek Singh.

CHAPTER THREE:

OBJECT-BASED CHANGE DETECTION ON ACACIA XANTHOPHLOEA SPECIES DEGRADATION ALONG LAKE NAKURU RIPARIAN RESERVE

This chapter is based on, Osio, A., & Lefèvre, S. (2021). Object-based change detection on acacia xanthophloea species degradation along lake Nakuru Riparian reserve. *International Archives of the Photogrammetry, Remote Sensing and Spatial Information Sciences, 43,* 347-352.

Presented at the 2021 Congress of the **International Society for Photogrammetry and Remote Sensing,** held virtually in Nice, France, on 6th July, 2021.

ABSTRACT

Automated mapping of heterogeneous riparian landscape is of high interest to assess our planet. Still, it remains a challenging task due to the occurrence of flooded vegetation. While both optical and radar images can be exploited, the latter has the advantage of being independent from acquisition conditions. However, and despite their popularity, the threshold-based approaches commonly used present some drawbacks such as not taking into account the spatial context and providing mixed pixels within class boundaries. In this study, a novel methodology using Covariance Matrix (C2) generated bands C11, C22 and RVI from SAR-C Single Look Complex (SLC) was proposed. A total of 84 classifications were realized using an Object Based Image Analysis (OBIA) in conjunction with classical machine learning algorithms i.e. Naïve Bayes (NB), Decision Tree (D.T) and Random Forest (RF). Replacing RVI with PCA-I improved the K-NN classifier performance by 15.4%. OBIA-RF model had the highest average performance in the whole series of datasets achieving an OA of 90.5% and Kappa: 0.88 using the cross-validation (10-fold) approach. Significant differences using One Way Analysis of Variance (ANOVA) were noted amongst the algorithms used with two cross-validation approach yielding desirable results at p-value 0.02 and p-value 0.03 respectively, based on $\phi<0.05$. Other significant differences were noted using the 2/3train and 1.3 test split approach at p-value 0.027 and p-value 0.017 respectively, based on $\phi<0.05$. Reduction in the areas covered by the healthy Acacia xanthophloea was observed across all training and testing sites. There was a strong negative correlation (R^2=-0.94) between the areas covered by the remnants of healthy Acacia xanthophloea against the water surface area over the years, meaning that the swelling lake had a negative impact on the Acacia xanthophloea tree strands along lake Nakuru riparian reserve.

3.1 INTRODUCTION AND LITERATURE REVIEW

Wetlands are important in regulating both the aquatic and benthic ecosystems. In recent time, Lake Nakuru situated along Kenya's great Rift valley has been facing challenges due to the rising water levels hence causing destruction of the National Park's natural and cultural features (Onywere et al., 2013). Amongst the natural features that have been gradually affected by the floods, and that need to be monitored, is the Acacia *xanthophloea* tree species which is an important feed for the giraffes and vervet monkeys in the park (Pellew, 1983). However, detecting and mapping flooded areas remains particularly challenging when the target vegetation or trees are immersed in water.

Previous studies have engaged optical and Synthetic Aperture Radar (SAR) imageries and their derivatives to extract spatial information from riparian reserves. Wetland classification based on optical imagery remains limited due to heavy cloud cover (Amani & Mobasheri, 2015). Conversely, SAR sensors can provide observations irrespective of the time of the day or night, penetrating through cloud cover, hence producing imageries of high quality and integrity (Anusha & Bharathi, 2020). However, their use on the classification mostly relies on pixel-based thresholding (Schumann et al., 2010). Such a strategy does not take care of the contextual information of the pixels at the land cover class boundaries, thus leading to low classification accuracies.

Thus, the goal of our study was to use time series of Sentinel-1 (VV-VH) Synthetic Aperture Radar (SAR) with Single Look Complex (SLC) acquisition modes from 2014 to 2020 within an Object-Based Image Analysis (OBIA) framework in order to detect changes in Acacia xanthophloea degradation along Lake Nakuru Riparian Reserve. Although previous studies have already used S1 Ground Range detected products in flood mapping, few studies have involved S1 Single Look

Complex (SLC) Polarimetric SAR products together with an object-level analysis for flood mapping (Osio et al., 2020).

3.2 MATERIAL AND METHODS

3.2.1 OBIA Model Workflow

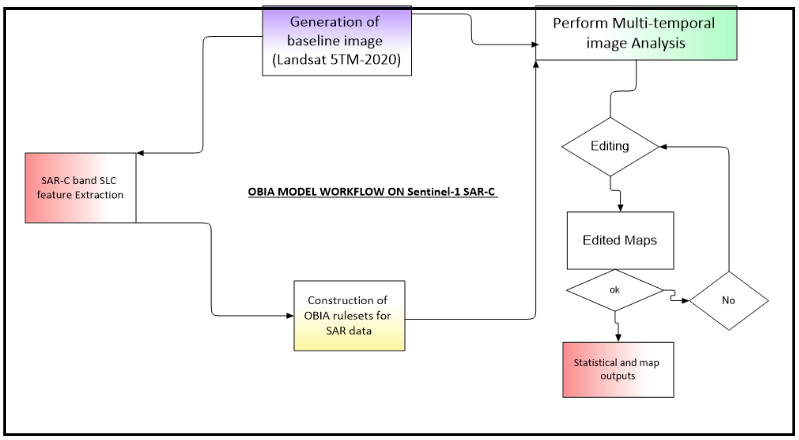

Figure 3.1: OBIA Model workflow adopted for this study

3.2.2 Data acquisition

We consider Dual Polarized Single Look Complex SAR, all from ascending orbits with phase information between two cross polarized channels, i.e., VV and VH respectively. SAR data were acquired at both wet and dry seasons, from Fall 2015 to Summer 2020 (12 dates). All the data were in the same datum and projection i.e. WGS 84 / UTM Zone 36N.

3.2.3 Sentinel-1 SLC Pre-processing

Time Series of Single Look Complex (SLC) level-1 datasets containing both phase and amplitude information was collected in slant range geometry from Copernicus scihub (https://scihub.copernicus.eu/dhud//home). The single date images were pre-processed using Sentinel-1 toolbox from ESA (Main et al., 2017). The single date imagery was imported into ESA SNAP environment after which the following steps were implemented, i) Identify the subswaths i.e., W1, W2 or W3 consisting of the study area ii) Using the S-1 Top split tool, extract the subswath that has the Area of Interest (AOI) from the rest of the sub swaths. iii) Application of the orbit file on each single date Sentinel-1 in order to provide accurate satellite orbit position and velocity into the processing chain. iv) radiometric calibration of SAR that converts the Sentinel-1 intensity values of polarization channels VV and VH are saved in complex output format was necessary to generate polarimetric matrix for further steps of image analysis. v) Using the Sentinel-1 tops deburst tool, the AOI with two or more bursts are debursted to remove the scan lines.

The tool is used to merge bursts in the azimuth direction to form a seamless image. vi) In this step two debursted Sentinel-1 from different subswaths are merged using the Sentinel-1 merge operator. vii) polarimetric matrix generation is appended on the merged Sentinel-1 image consisting of a single Area of Interest (AOI). The 2x2 covariance matrix generation [C2] is possible from dual-pol Sentinel-1 SLC data. viii) multi-looking was applied in order to reduce speckle noise and generate a ground range square pixel in this study a 14.04m square pixels was achieved. ix) polarimetric speckle filtering using refined Lee filter to append despeckle operation on the polarimetric matrix x) terrain correction was carried out a single date Sentinel-1 using Doppler terrain correction and geocoded to the correct co-ordinate system in the case of this study WGS84

xi) The final stage involves manual removal of the baseline information (from the metadata) in order to produce an image with header information (. hdr) which was exported in PolSARPro format for further image processing in QGIS software environment. The exported Sentinel-1 image was a single date data product in PolSARPro format with the following matrix elements stored in it; (C11, C22, C12 real, and C12 imag) individually in a binary format with header information.

3.2.4 ALOS Level 1.1 Pre-processing

The reference image used in this study was an ALOS-1 Level-1 of L-Band and HH+HV channels in ascending mode at an incident angle of 38.7◦ in September 2007 before the floods. The ALOS-1 Level 1.1 image was radiometrically corrected by converting the HH and HV into σ_{db}HH and σ_{db}HV that represents the true SAR backscatter of the objects under study. In order to achieve an image with square pixels at ground range scaling, multilooking produced a ground range square pixel using 1 look in range and 5 looks in azimuth. The resulting mean ground range pixel size was 15m. multilooking affected the original pixel size initially 9.36m squared. In order to remove noise or speckles from the image, single product speckle filtering using refined Lee filter was appended on this image.

The resultant image having been visualized as a clearer image than the initial image before filtering process was done. Since ALOS-1 Level 1.1 is distributed in squinted geometry, deskewing was implemented on the dataset in order to transfer it into a zero Doppler like geometry before applying standard SAR processing. Finally, the Image was terrain-corrected and the region of interest extracted using the land sea mask tool in ESA SNAP toolbox. Terrain correction was done using range Doppler terrain correction approach and the image geocoded to the correct co-ordinate system which is WGS84.

3.2.5 Landsat 5TM Pre-processing

Landsat 5TM collected in 2010 was used as a baseline map since it was still depicting the state of all riparian classes along the lake. The steps engaged here were: i) extraction of AOI of the study area; ii) atmospheric corrections done by conversion of DN values to TOA reflectance; iii) pan sharpening to 15m spatial resolution using ehlers fusion technique; iv) production of a false color image RGB using Band 4 (0.73-0.9um), Band 3 (0.63-0.69um) and Band 2 (0.52-0.60um). The latter combination makes deciduous trees such as acacia forest appearing bright red in color, urban area cyan while soil dark to light brown (see Figure 3.5).

3.3 DATA ANALYSIS

In this subsection different band combinations of ALOS-1 Level 1.1 and Sentinel-1 Single Look Complex data with their ratios were processed for use in this study. Spectral indices, their derivatives and their polarimetric bands were retrieved from Sentinel 1 Single Look Complex datasets collected between 2014 and 2020. The main aim was to find out which band combination realized the best class discrimination. Both supervised and unsupervised classification approach were embraced.

3.3.1 Sentinel-1 SLC data analysis

From the preprocessed S-1 SLC single date images, we generated bands C11, C22, C12REAL and C12IMAG using 2*2 (C2) matrix image in ESA SNAP toolbox (J.-S. Lee & Pottier, 2017). The spectral bands derived from C2 matrix-based single-date images consisted of radar-based vegetation indices.

3.3.2 Feature Extraction from PolSARPro based header file

The single date Sentinel-1 Single Look Complex dataset with PolSARPro header information was imported into the QGIS version 3.4 environment. The SAR plugin was used in extracting both SAR polarimetric and spectral bands from the. hdr file extension containing the C2 (2*2) covariance matrix-based bands C11, C22, C12REAL and C12IMAG. The polarimetric spectral indices produced from the C2 covariance matrices from each single date dataset were: Radar Vegetation Index (RVI), Dual Polarimetric Vegetation Index (DpRVI), Polarimetric Radar Vegetation Index (PRVI) and Degree of Polarization for Dual Polarimetric (XX, XY) SAR data where X, Y are taken from (H, V), (V, H). Time series temporal profiles were then generated from the multi-date stack S1 SLC series built from datasets ranging from 2014 to 2020 as shown in Figure 3.2 and Figure 3.3. The bands with the highest backscatter response with other additional variables were then used for further data analysis. Classifiers appended on the classification include K-NN, Naive Bayes, Decision Tree (DT) and Random Forest (RF). Training and testing areas were identified on this image and were later used on multi-date S-1 SLC image analysis.

3.3.3 Unsupervised Polarimetric classification

Raw Sentinel-1 (SLC) time series images collected between 2014 and 2020 were pre-processed in ESA (SNAP) toolbox as shown in sub-section 3.2.4. The pre-processed imageries were then exported to PolSARPro version 6.0 software for extraction of entropy, Anisotropy and Alpha bands from tree biomass. The three band combination imageries RGB (Anisotropy, Entropy, Alpha) after (Merchant et al., 2019) were again exported to ESA SNAP toolbox where each single date imagery was processed using Unsupervised polarimetric classification in a 7*7 window with

9 iterations using H-Alpha Wishart Dual Polarization algorithm. The resultant single date images consist of 9 classes inhibiting scattering charactering response in % form i.e. class 1(Dihedral reflectance), Class 2 (Dipole reflectance), Class 3 (Bragg surface), class 4 (Double reflectance), class 5 (Anisotropic surface), class 6 (Random surface), class 7(complex structures), class 8 (Random Anistropy) and class 9 (non-feasible). The single date bearing these bands with their related % scattering reflectance's are converted into a .tiff image format and exported into QGIS where the PolinSAR plugin tool after (Mandal et al., 2020) was used in the extraction of the following bands namely: C11,C12.image,C12.real and C22.bin and in addition the Vegetation Index bands i.e. Radar Vegetation Index (RVI), Dual-Pol Radar Vegetation Index (DpRVI), Polarimetric Radar Vegetation Index (PRVI) and in addition Degree of Polarization Index (DOP). All these bands were tested by plotting their scattering power through time using Sentinel-1(SLC) dataset ranging from 2014 to 2020 as shown on Figure 3.2 and Figure 3.3. The band combination considered in this classification based on their scattering power were the RGB (C11, C22, RVI). This approach was combined with an Object-based approach in eCognition Developer software and WEKA Machine Learning environments for further processing.

3.3.4 ALOS 1 Level 1.1 data analysis

The pre-processed reference image was imported into eCognition Developer 10.1 environment for further processing. The true SAR backscatter bands i.e., σ_{db}HH σ_{db}HVσ_{db}VV & σ_{db}VH were used in this case to generate FOUR (4) Principal Components i.e., PCA1, PCA2, PCA3 and PCA4. Random Forest based classification was done from two training sites using RGB (σ_{db}HH, σ_{db}HV, PCA1) band combinations. Two training and test sites were also delineated from different parts of the study area. These bands were transited to eCognition Developer 10.1 where additional variables such as the PCA1, PCA2 mean and standard deviation were added into the classification. Other variables include geometric features such as border index and ecliptic fit.

3.3.5 Landsat 5TM data analysis

Classification of the Landsat 5TM (with bands 4, 3, 2) data was conducted with the aim of visualization as shown in Figure 3.5. The following classes were considered: Acacia Forest, Bushed Themada Grassland, *Chloris gayana* Grassland, *Cynodon - Chloris - Themada* Grassland, *Cynodon niemfluensis* Grassland, Cynodon niemfluensis - wooded Acacia grasslands, *Euphorbia Candelabra*, Lake Nakuru, *Olive & Teclea* Forest, *Sand & Mudflats*, *Sedges & Marshes* and *Tachonandus* Bushland. These classes were then compared to the classified image previously generated by (Ng'weno et al., 2010a) as shown in Figure 3. 6.

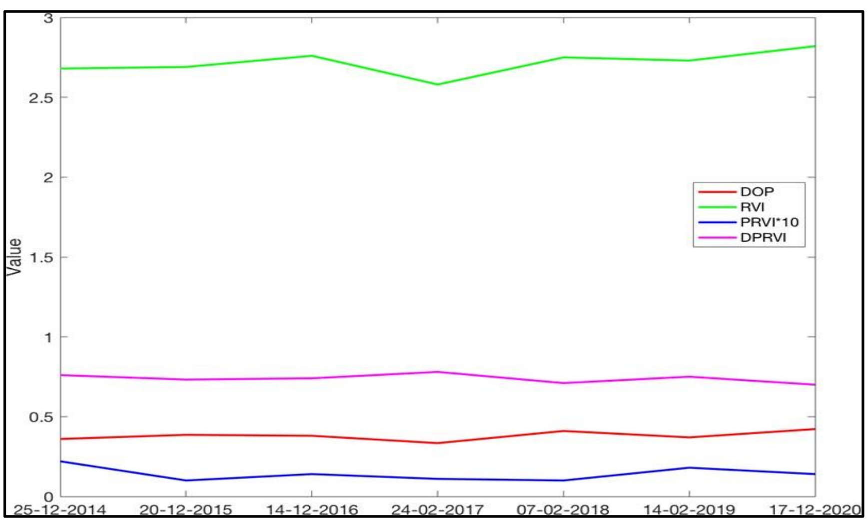

Figure 3.2: Sentinel 1 SLC spectral response of RVI, DpRVI, PRVI and DOP of the degraded Riparian Reserve 2014-2020 of Lake Nakuru, Kenya.

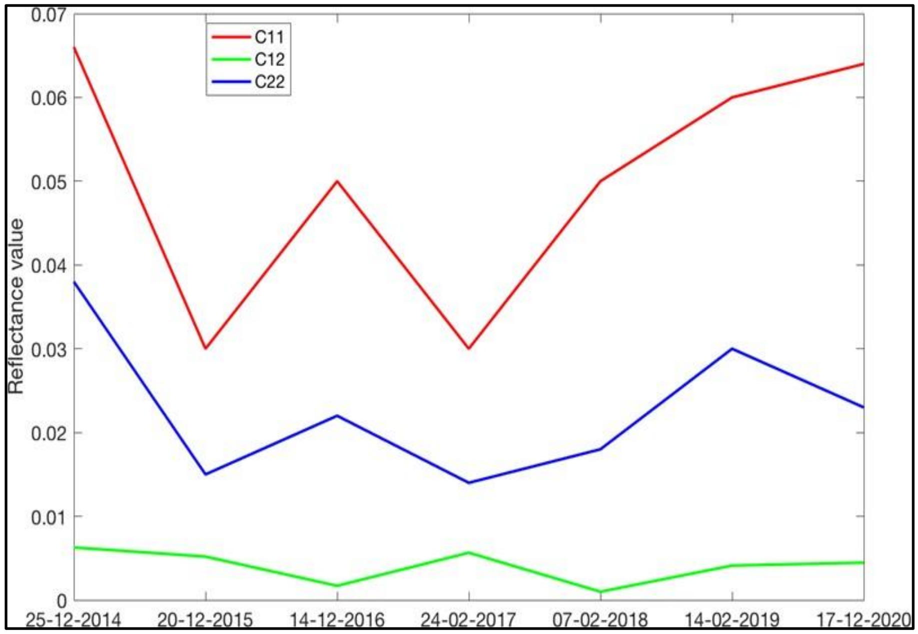

Figure 3.3: Sentinel 1 SLC covariance matrix generated band averages of C11, C12 and C22 response on the degraded riparian reserve 2014-2020 of Lake Nakuru, Kenya.

3.4 **RESULTS**

The proposed methodology was designed to fill the following knowledge gaps: i) to determine the spectral changes that have taken place along the riparian reserve by using preprocessed and co-registered multi-date stack time series images built from S-1 Single Look Complex SAR data; ii) to explore the capability of the C2 covariance matrix derivatives (i.e. C11,C22 and RVI)to characterize Acacia *xanthophloea* along Lake Nakuru riparian reserve; iii) to explore the spatio-temporal changes that have occurred on the Acacia strands from 2014 to 2020. We report here the experiments conducted to answers these questions and provide some quantitative and qualitative results.

3.4.1 Determine polarimetric spectral response on time series images detected along the riparian reserve via temporal profiles

We generate a 2*2 covariance matrix from SLC data to enhance polarimetric characterization of the target. The covariance matrix (C2) data (header and binary files) are used in the generation of C11, C22, C12-REAL and C12-IMAG bands. We derive radar-based vegetation indices, namely Radar Vegetation Indices (RVI) (Mandal et al., 2020b), Dual Pol Vegetation Index (DpRVI), Polarimetric Radar Vegetation Index (PRVI) (Mandal, et al., 2020b) and Degree of Polarization (DOP) for Dual Polarimetric SAR. The bands that had the highest backscatter response, i.e., C11, C22 and RVI were then selected for multi-date image classification across time series of Sentinel-1 Single Look Complex data captured from the period 2014-2020. Figure 3.2 and Figure 3.3 show the multi-temporal average backscatter response of the C2 (2*2) covariance matrix generated bands.

3.4.2 The capability of C2 covariance matrix and spectral derivatives in detecting the changes on the riparian vegetation

In this section, the C11, C22 and RVI bands of each imagery captured after the floods between 2014 and 2020 are classified in eCognition Developer 10.1 environment. For further class refinement, the shape files consisting of the resulting classes, namely Acacia Forest, Acacia undergrowth, Acacia crown gap and Other were exported to ARCGIS 10.5. Later the tabular CSV files consisting of multi-date Sentinel-1 SLC datasets were transited to WEKA, an open-source machine learning environment. The results were then reported in the preceding subsections depicting OBIA classification conducted on the Acacia Strands along the different parts of Lake Nakuru (i.e., north-western and southern) at three different dates, namely December 2015, February 2017 and February 2019.

3.4.3 North- Western Acacia strands, 2015

We considered both a multi-resolution segmentation with parameters set to scale=5, shape=0.6 and compactness=0.8 (Kavzoglu & Tonbul, 2017), and a spectral difference segmentation with scale=10 (J. Yang et al., 2017). Indeed, using multiple segmentation algorithms has proven to to yield better results (Tonbul & Kavzaoğlu, 2019). Features included in the classification were the mean and standard deviation of C11, C22 and RVI. As far as geometric features are concerned, we selected shape index, rectangular fit, roundness and ecliptic fit (Kaplan & Avdan, 2019). The default K-NN classifier yielded an overall accuracy (OA) of 87% and a Cohen’s Kappa score of 0.78. Using Random Forest with bagging and 100 iterations out of 737 instances, 2.3% attributes with a 2/3-1/3 train-test split yielded higher values, with 96.1% of OA and 0.93

of Kappa. Cross-validation with a 10-fold approach improves further the results, with an OA of 96.7% and a Kappa of 0.94. Out of the 737 instances in the classification, 67% were detected as Acacia Forest class while less than 1% recorded as class Other.

3.4.4 Southern Acacia strands, 2015

For this second experiment, we rely on multi-resolution segmentation with scale=10, shape=0.6 and compactness=0.8, and give more weight to bands C11 and RVI. The mean and standard deviation of C11, C22 and RVI were also included in the classification. Geometric features such as shape index, ecliptic fit, roundness and rectangular fit were completing the set of features. The default K-NN algorithm in eCognition environment yielded an OA of 83% and a kappa of 0.76. Comparatively, the Random Forest classification with a 10-fold cross validation yielded an OA of 96.3% and a Kappa of 0.94, this time lower than the 2/3-1/3 train-test split yielding an OA of 96.8% and a Kappa of 0.95. Out of the 2491 instances used in the classification, 29% instances were classified as Acacia Forest while 1% instances were confused as class Other. True positive rate (TPR) and false positive rate (FPR) for Acacia Forest were measured as 99.7% and 0.3% respectively.

3.4.5 North-Western Acacia strands, 2017

Again, we used multi-resolution segmentation with scale=10, shape=0.6 and compactness=0.8 (yielded 1014 objects), as well as spectral difference segmentation at scale 10, and consider the mean and standard deviation of C11, C22 and RVI, and integrate a set of geometric features (shape index, rectangular fit, roundness, border index and ecliptic fit). We obtain an OA of 97% and a Kappa of 0.95 with the default K-NN classifier, while Random Forest classification carried out in WEKA environment using baggings with 100 iterations and 10-fold cross-validation yielded an OA of 94.4% and a Kappa coefficient of 0.91. Out of the 1,140 instances used in this classification, 0.2% instances were classified as Acacia Forest while less than 1% instances confused as class Other. TPR for the Acacia forest target class was 91% while FPR reaches 2.5%. Using the 2/3-1/3 train test split lowers the results, with an OA of 91.5% and Kappa 0.86. Out of the 388 test instances, less than 1% were classified either Acacia Forest or class Other.

3.4.6 Southern Acacia strands, 2017

We continue to use C11, C22 and RVI bands, but also apply a Principal Component Analysis (PCA) leading to 3 principal components, i.e. PCA1, PCA2 and PCA3. We then replace C22 by PCA1 and reorder the bands as C11, RVI, and PCA1, before applying a multi-resolution segmentation with scale=10, shape=0.6 and compactness=0.8, and a spectral difference segmentation at scale 10 to separate class Acacia Forest from Sporobolus Spicatus and Chloris gayana grasslands. K-NN classifier yielded an OA of 98.7% and a Kappa of 0.97. The positive role played by the PCA features in the classification process was emphasized, because it contributed to an improvement of 15.4% on the North-western, 2015 (where no such features were used). Comparatively, Random Forest classification with 10-fold cross-validation yielded an OA of 97.4% and a Kappa of 0.96. Out of the 2668 instances used in this approach, 46.9% were classified as Acacia Forest and less than 1% belonging to class Acacia undergrowth, and class Other respectively. TPR stood at 97.8% while FPR was 2.2%. Finally, the 2/3-1/3 train-test split yielded an OA of 98.1% and a Kappa of 0.97. 46.8% of test instances were classified as Acacia Forest while less than 1% confused as either Acacia undergrowth or Other respectively. TPR and FPR were measured to 98.8% and 1.2%, respectively.

3.4.7 North-Western Acacia strands, 2019

Similarly, to the previous case, we consider C11, C22, RVI, and the Principal Components that can be derived from them. Here, we give more weight to C11, RVI, PCA1 and PCA2 according to their importance as determined by their correlation coefficient (e.g. R = 0.91 between PCA2 and RVI, R = 0.97 between C11 and PCA1, and R = 0.96 between C22 and PCA2). Some geometric features, namely ecliptic fit, shape index, rectangular fit, roundness, border index and shape index were used. The best results were obtained with super-pixel segmentation (SLICO) (Mi & Chen, 2020) and spectral difference segmentation. The default K-NN classifier in eCognition Developer 10.5 yielded perfect results (OA of 100%, Kappa of 1.0). Random Forest bagging with 100 iterations and 10-fold cross-validation yielded an OA of 97.9% and a Kappa of 0.96. However, TPR of the target class (Acacia Forest) achieved stood at 85.4% while FPR stood at 1.3%. Out of the 1634 instances, less than 1% were classified as Acacia Forest, Acacia undergrowth or Other respectively. The 2/3-1/3 train-test split yielded an OA of 98.3% and a Kappa of 0.97, leading to TPR and FPR for the Acacia Forest class measured at 79% and 0.5%, respectively. Out of the 624 test instances, 1% was classified as Acacia Forest and Acacia undergrowth respectively.

3.4.8 Southern Acacia strands, 2019

The same approach and parameters used in the previous setup were considered here: bands C11, C22, RVI, PCA1, PCA2, PCA3; their mean and standard deviation; super-pixel (SLICO) and spectral difference segmentation. K-NN achieves again perfect results. Random Forest with baggings, 100 iterations and 10-fold cross-validation realized an OA of 86.1% and a Kappa of 0.78. Out of the 1014 instances, 0.1% were correctly classified as Acacia Forest, while less than 1% incorrectly classified as Acacia undergrowth and Other respectively. TPR for the target class (Acacia Forest) was 90% and FPR was 4%. Random Forest with a 2/3-1/3 train-test split resulted in OA of 86.7% and Kappa of 0.79. Out of the 345 instances involved in this classification, 0.2% instances were assigned to class Acacia Forest while less than 1% were misclassified as class Other and Acacia undergrowth respectively. TPR and FPR for this target class were then 98% and 5%.

3.5 SPATIO-TEMPORAL CHANGES ON ACACIA XANTHOPHLOEA SPP. ALONG LAKE NAKURU RIPARIAN RESERVE

Statistical change detection was carried out on the different training and test areas. This was made possible by calculating the area of the Acacia x. spp. strands not affected by the floods ranging from 2014 to 2020 as shown on the bar graphs in Figure 3.

Site 1 corresponds to the northern side of Lake Nakuru, divided in a training site (north-western, in blue in the figure) and a test site (north-eastern, in yellow in the figure). Similarly, site 2 corresponds to the southern side of the lake (with the same color code). Figure 3.3 depicts the distribution of Acacia Forest strands in the different training and test sites.

In site 1 (train), the spatial difference in Acacia x. Spp strands between year 2014 and 2020 was accounting for an area of ~123ha, corresponding to an area initially covered by the healthy Acacia

Forest that became degraded and submerged in the flooded lake. For the test area, the difference in area covered by the healthy Acacia x. Spp between year 2014 and 2020 was ~445ha as of 26th July, 2020. Similarly, the Acacia Forest transition for the training area of site 2 (southern part of the Lake Nakuru) consists in a reduction of a total area initially covered by Healthy Acacia X. Spp in 2014 of ~848ha to an area of ~405ha by the year 2020, i.e. a loss in area of ~443ha. As far as the test site is concerned, similar loss was observed from ~179ha in February, 2014 to ~19ha by July, 2020. In other words, the area covered by degraded Acacia x. Spp accounted for was ~160ha. To determine if the Acacia Forest degradation was actually affected by the floods, the area covered by the lake per each given year (2014-2020) was calculated and correlated to the area covered by the remnants of the Acacia along Lake Nakuru Riparian Reserve. To do so, we used multi-resolution and spectral difference segmentation approaches on a composite image made of C11, C22, and C11/C22 bands. We obtained the following measures: 52.2 km^2 in 2014, 54.11 km^2 in 2016, 57.24 km^2 in 2018, and 59.8 km^2 in 2020. These figures were correlated to the area covered by the Acacia Forest on train site 1 as follows: ~325ha in 2014, ~262ha in 2016, ~208ha in 2018, and ~203ha in 2020. We then use the correlation coefficient to measure strength of relationships between variables. We observed a strong negative correlation of R=-0.94 between the area of the Lake against the area covered by healthy Acacia x. per each year. The equation of the regression line in relation to this correlation being y = 57870-808.9x.This means that, as the level of the lake continued to rise over the years, the more the Acacia Forest continued to degrade, confirming reports by (Mutangah, 1994) that the main cause of stress and eventual death of the *Acacia Xanthophloea* was due to the rising water table in a closed drainage system (i.e. Lake Nakuru Basin).

3.6 DISCUSSION

The study demonstrates how S1 captured in SLC mode was used to characterize the degrading Acacia x. Spp along the shores of the flooded Lake Nakuru Riparian reserve. The bands that had the highest reflectance were C11, C22 and RVI. They were used to carry out classifications in an object-based image analysis (OBIA) pipeline using multi-date datasets ranging from 2014 to 2020. We hypothesized that SAR polarimetric bands filtered through the C2 (2*2) Covariance Matrix could improve characterization of the flooded riparian vegetation. In this study, classification was carried out on a time series of SLC products, after which they were imported into eCognition Developer software environment for object detection and classification. Rule sets where different segmentation types and scales were appended on 28 training and testing sites (Nico et al., 2000; Kavzoglu & Tonbul, 2017)

The variables that contributed well to the classifications were determined by measuring correlation coefficients. It was worth noting that there was a strong positive correlation between the ecliptic fit and rectangular fit (R = 0.91), and between border index and shape index (R = 0.95). We follow previous studies that show some improvement of classification accuracy using shape and geometric variables (Kaplan & Avdan, 2017).

Other variables that contributed to the high-classification accuracies were the standard deviation of polarimetric bands C11, C22 and RVI, and their principal components. Strong positive correlations were noted between the Standard Deviation (SD) of C11/PCA1 (R = 0.97), C22/PCA2 (R = 0.96) and PCA2/RVI (R = 0.98). The inclusion of the dimensional reduction features (here PCA) onto the classification process increased the K-NN based classification from

15.4%. These results corroborates well with previous research by (Chatziantoniou et al., 2017) where PCA predictor variable improved their classification accuracy. Other studies that used P.C.A to improve their classification accuracy include (Granata et al., 2020; Osio et al., 2020; Pham et al., 2017).

The average results derived from the 84 classifications using 10-fold cross-validation approaches were as follows; Naive Bayes OA (76.5%) Kappa (0.77), Decision Tree (DT) an OA (87.8%), Kappa (0.85) and Random Forest (RF) an OA (90.5%), Kappa (0.88). The results achieved using cross-validation approach on Sentinel-1 SAR-C band fills in the gap left by (Gašparović & Dobrinić, 2020) who suggested that improvement on the OBIA-RF model accuracy required the use of cross validation approach as demonstrated in this study. On the other hand, the average results achieved using 2/3-1/3 train-test split approach were as follows; Naive Bayes OA (76.6%) Kappa (0.73), Decision Tree (DT) OA (88.6%) Kappa (0.85) and Random Forest (RF) OA (88.9%) Kappa (0.87).

The overall average results obtained from both approaches i.e., 10-fold cross-validation and the 2/3-1/3 train-test split consisting of the 84 classifications using the three classification algorithms were as follows; Naive Bayes OA (76.38%) Kappa (0.73), Decision Tree (DT) OA (88.2%) Kappa (0.84) and Random Forest (RF) OA (89.7%) Kappa (0.88) as shown on the results in Table. 3.1, Table. 3.2, Table. 3.3 and Table. 3.4 respectively. The average True Positive Rate (TPR) of the target vegetation i.e. Acacia Forest class was achieved using different classifiers as follows; Naive Bayes (0.78), Decision Tree (DT) (0.86) and Random Forest (0.88) respectively.

On the other hand, the average results derived from pre-processed and classified reference image, an ALOS 1 level 1.1 image of L-Band captured in September 2007 before the flood events, was as follows: Naive Bayes OA (90.7%) Kappa (0.89), Decision Tree (DT) OA (93.4%) Kappa (0.90) and Random Forest (RF) OA (93.8%), Kappa (0.92) respectively. These were the average results derived using the same approaches as were used on the test and training sites on the Sentinel 1 SLC based imagery of the study area, confirming that ALOS 1 Level 1.1 image with HH and HV polarization and L-band was suitable for use as reference image in this study.

The difference in the performance of classification algorithm have been demonstrated using different methods. (Gašparović & Dobrinić, 2020) used McNamara's χ^2 test to compare the performance of classifier algorithms, including XGB, SVM and Random Forest (RF). In this study we also compare the performance of the three classifiers, namely Naive Bayes, Decision Tree (DT) and Random Forest (RF) in a total of 84 classifications carried out across the multi-date images as reported in Table 3.5 and Table 3. 6.

To test if there are any significant difference between the different classification outcomes based on the algorithms, statistical inferences have to be used such as One Way Analysis of Variance (ANOVA). The resultant outcome was used to determine if there was any significant difference between the outcome of the classifications based on the algorithms used. The results on the one-way ANOVA has different variables including the mean, standard deviation and standard error of the datasets being compared against each other.

Important parameters that were used included Degrees of Freedom (DF), Sum of Squares (SS) within and between groups. The F-statistic and the P-value related to this value were also realized. Using the F-distribution table (See Appendix 1) based on α=0.05, the F-critical value is located using the DF1 and DF2 values being the Degrees of Freedom (DF) between and within groups. In the F-Distribution table (See Appendix 1), DF1 is the numerator while DF2 is the denominator.

Results achieved through the inter-group comparisons were demonstrated via the relationship between F-statistic and F-critical values. When the F-stat based on α=0.05 and degrees of freedom (DF1) and (DF2) is greater than the F-critical value, then the outcome becomes statistically significant.

Results achieved through inter-group comparisons using one-way ANOVA reported a statistical significant difference between the three classifiers namely Decision Tree (D.T), Random Forest(RF) and Naive Bayes in all the training sites used in this study using both cross-validation and the 2/3-1/3 train-test split approaches. Two group combinations had a statistically significant difference between their group which was between Naive Bayes (NB) and Decision Tree (DT) from Train site 2 using the 2/3-1/3 train-test split approach as depicted on Table 3.6. On the other hand, three group combinations had statistically significant difference achieved amongst them i.e. Naïve Bayes (NB), Decision Tree (DT) and Random Forest (RF), using both cross-validation and 2/3-1/3 train-test split approaches on Train site 1 and Train site 2 as reported on Table 3.5.The quantitative results achieved through inter-group comparisons using one-way ANOVA depicted statistically significant difference between the three classifiers in all the training sites that were used in this study using both cross-validation and 2/3-1/3 train-test split. Random Forest was confirmed as the best performing classifier.

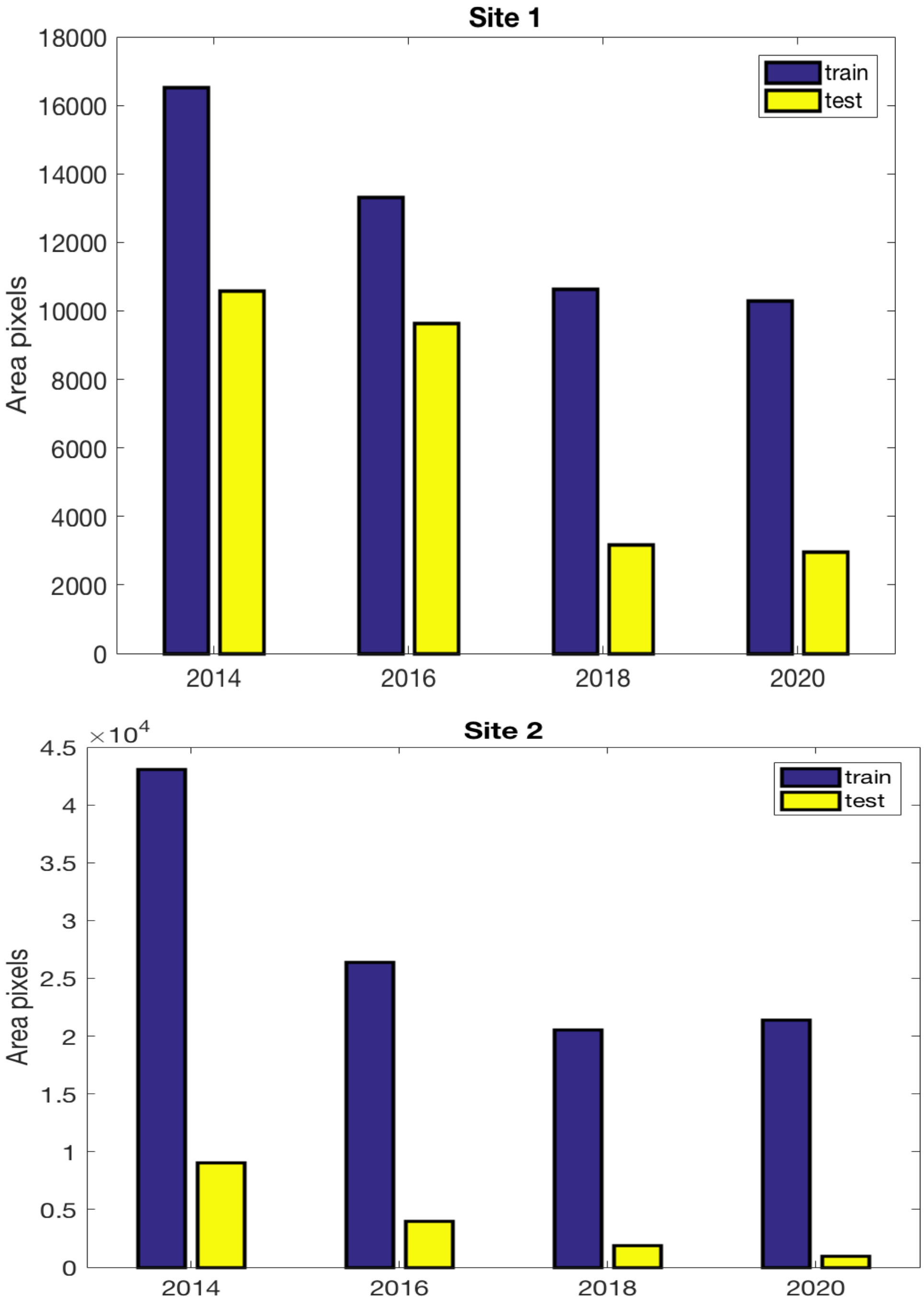

Figure 3.4: Spatio-Temporal Change Detection on Acacia x. spp on Training and Test sites 1 (Top) and 2 (Bottom)

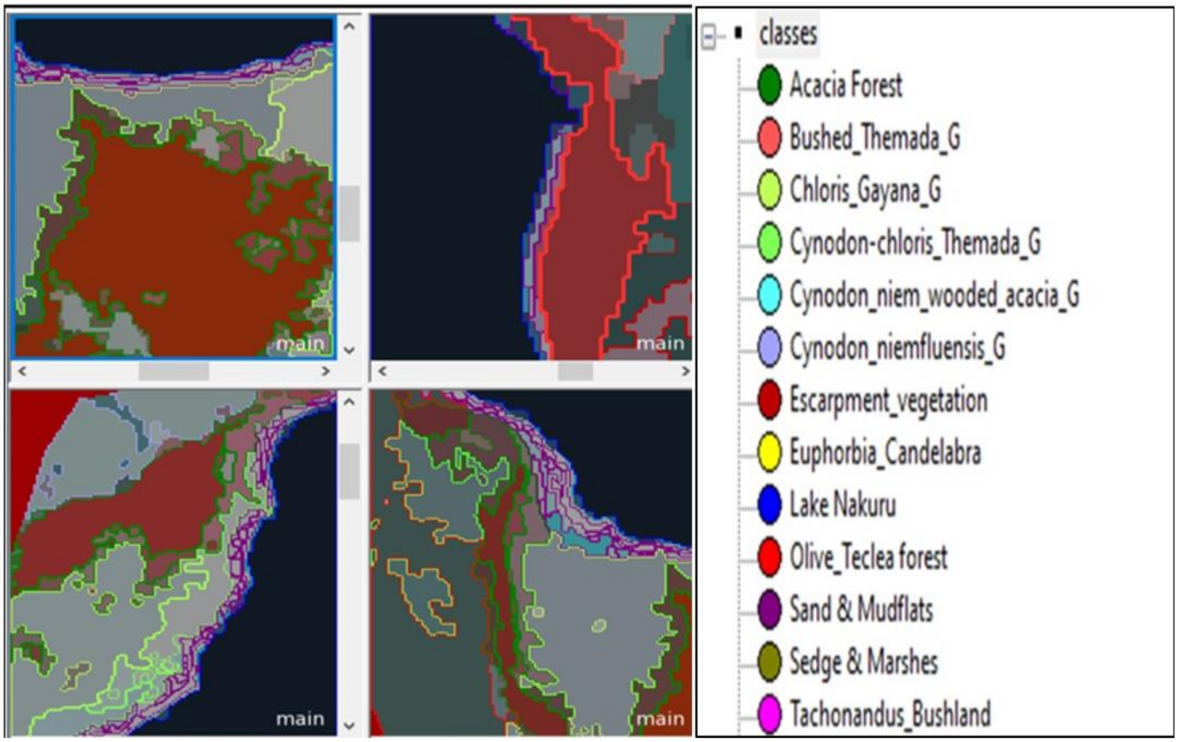

Figure 3.5: The state of Acacia forest patches clockwise from upper left corner: Southern part, North-Eastern part, Southern-Western part, & North-Western part of the study area where Acacia Forest patches (in red) existed before the onset of floods.

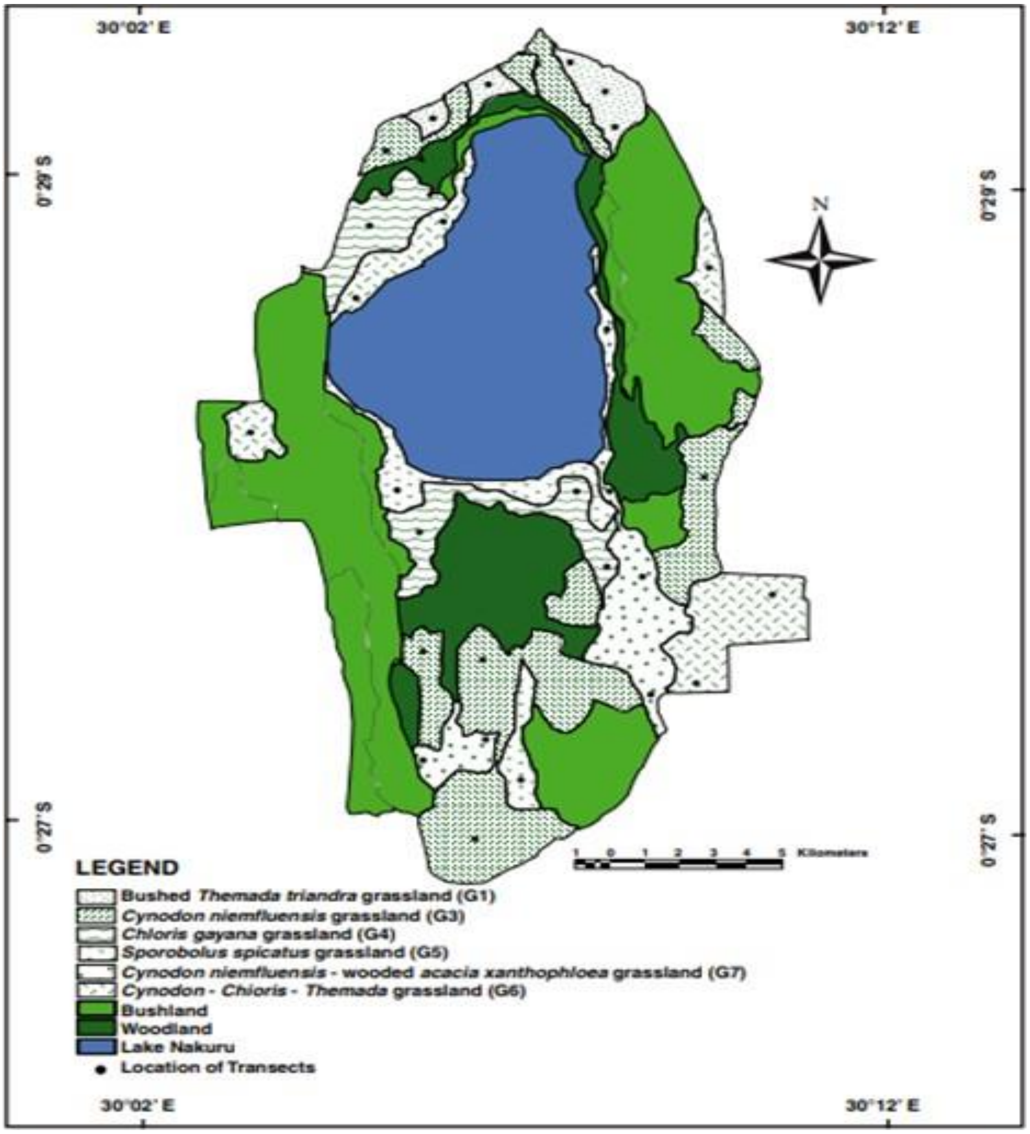

Figure 3.6: Distribution of vegetation classes in Lake Nakuru National Park (illustration from (Ng'weno et al., 2010b)**.**

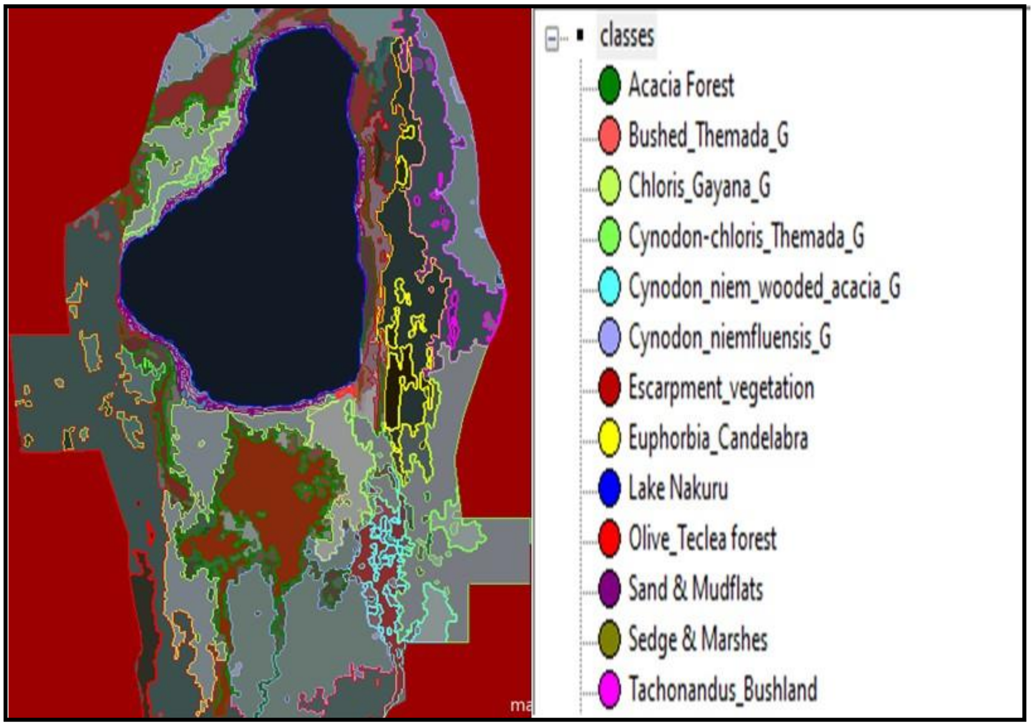

Figure 3.7: Land cover classification in the study area, before the onset of flooding

Table 3.1: Train site 1-Northwest (10-fold cross-validation).

Classifer	25/12/2014			20/12/2015			29/06/2016			24/02/2017			19/06/2018			14/02/2019			26/07/2020		
Metrics	OA	Kappa	TPR	OA	Kappa	TPR	OA	Kappa	TPR	OA	Kappa	TPR	OA	Kappa	TPR	OA	Kappa	TPR	OA	Kappa	TPR
Naïve Bayes	58.1	0.49	0.58	70.7	0.68	0.64	77.8	0.74	0.83	51.1	0.45	0.93	67.3	0.62	0.88	82.9	0.78	0.75	72.2	0.68	0.75
Decision Tree	67.0	0.64	0.65	64.4	0.62	0.65	83.4	0.79	0.88	93.4	0.9	0.96	79.4	0.73	0.89	86.0	0.84	0.91	89.0	0.86	0.85
Random Forest	69.3	0.67	0.69	96.6	0.96	0.92	84.7	0.82	0.88	97.4	0.97	0.99	79.6	0.74	0.9	81.9	0.78	0.79	89.1	0.88	0.79

Table 3.2: Train site 1-Northwest (66% Train, 34% Test).

Classifier	25/12/2014			20/12/2015			29/06/2016			24/02/2017			19/06/2018			14/02/2019			26/07/2020		
Metrics	OA	Kappa	TPR	OA	Kappa	TPR	OA	Kappa	TPR	OA	Kappa	TPR	OA	Kappa	TPR	OA	Kappa	TPR	OA	Kappa	TPR
Naïve Bayes	75	0.72	0.7	70.7	0.69	0.65	77.8	0.73	0.83	66.5	0.63	0.91	94.6	0.91	0.97	99.1	0.94	0.96	93.9	0.90	0.94
Decision Tree	92	0.91	0.92	96.4	0.94	0.95	83.3	0.79	0.78	91.5	0.86	0.87	96.8	0.92	0.83	99.2	0.94	0.96	96.8	0.93	0.79
Random Forest	92	0.91	0.89	96.4	0.94	0.92	84.8	0.82	0.84	91.5	0.86	0.86	79.9	0.76	0.94	98.3	0.97	0.79	96.9	0.94	0.96

Table 3.3: Train site 2-Southern (10-fold cross-validation).

Classifier	25/12/2014			20/12/2015			29/06/2016			24/02/2017			19/06/2018			14/02/2019			26/07/2020		
Metrics	OA	Kappa	TPR	OA	Kappa	TPR	OA	Kappa	TPR	OA	Kappa	TPR	OA	Kappa	TPR	OA	Kappa	TPR	OA	Kappa	TPR
Naïve Bayes	58.1	0.49	0.58	70.7	0.68	0.64	77.8	0.74	0.83	51.1	0.45	0.93	67.3	0.62	0.88	80.0	0.78	0.75	72.2	0.68	0.75
Decision Tree	67.0	0.64	0.54	64.4	0.62	0.65	83.4	0.79	0.88	93.4	0.90	0.96	79.4	0.73	0.89	86.0	0.84	0.91	89.0	0.86	0.85
Random Forest	69.3	0.67	0.69	96.6	0.96	0.92	84.7	0.82	0.88	97.4	0.97	0.99	79.6	0.74	0.90	81.9	0.78	0.79	89.1	0.88	0.79

Table 3.4: Train site 2-Southern (66% Train, 34% Test).

Classifier	25/12/2014			20/12/2015			29/06/2016			24/02/2017			19/06/2018			14/02/2019			26/07/2020		
Metrics	OA	Kappa	TPR	OA	Kappa	TPR	OA	Kappa	TPR	OA	Kappa	TPR	OA	Kappa	TPR	OA	Kappa	TPR	OA	Kappa	TPR
Naïve Bayes	63.3	0.59	0.62	73.2	0.69	0.72	78.0	0.75	0.79	54.5	0.52	0.92	70.2	0.67	0.90	80.0	0.76	0.76	75.4	0.72	0.68
Decision Tree	64.4	0.63	0.65	95.9	0.94	0.92	81.8	0.78	0.87	89.2	0.79	0.93	79.3	0.71	0.93	84.9	0.82	0.98	89.1	0.88	0.83
Random Forest	69.3	0.65	0.68	96.8	0.95	0.94	82.9	0.81	0.84	98.1	0.97	0.99	79.9	0.76	0.94	86.7	0.87	0.98	90.9	0.90	0.95

Table 3.5: The between groups (NB, DT & RF) One Way ANOVA results on train site 1&2

ANOVA SUMMARY (10-fold Cross-Validation) Train site 1					
Source	**Degrees of Freedom (DF)**	**Sum of Squares (SS)**	**Mean Squares (MS)**	**F-Statistic**	**P-Value**
Between Groups	**1**	483.69	483.69	4.33	0.059
Within Groups	**12**	1339.36	111.69		
Totals	**13**	1823.05			
ANOVA SUMMARY (66% Train & 34% Test) Train site 1					
Source	**Degrees of Freedom (DF)**	**Sum of Squares (SS)**	**Mean Squares (MS)**	**F-Statistic**	**P-Value**
Between Groups	**2**	489.11	244.56	2.98	0.076
Within Groups	**18**	1477.23	82.07		
Totals	**20**	1966.34			
ANOVA SUMMARY (10-fold Cross-Validation) Train site 2					

Source	**Degrees of Freedom (DF)**	**Sum of Squares (SS)**	**Mean Squares (MS)**	**F-Statistic**	**P-Value**
Between Groups	**2**	1054.12	527.05	4.67	0.023
Within Groups	**18**	2033.03	112.95		
Totals	**20**	3087.14			
ANOVA SUMMARY (66% Train & 34% Test) Train site 2					
Source	**Degrees of Freedom (DF)**	**Sum of Squares (SS)**	**Mean Squares (MS)**	**F-Statistic**	**P-Value**
Between Groups	**2**	979.77	489.88	5.18	0.017
Within Groups	**18**	1702.46	94.58		
Totals	**20**	2682.22			

Table 3.6: ANOVA (one way) results achieved in inter-classifier comparisons per training site and approach

Classifier	Statistics 1		Statistics 2		Statistics 3	Statistics 4		Remarks
	F-Stats	**P-Value**	**Df1/Df2**	**F-Critical**	**Fstats>F-Critical**	**Approach**	**Train site**	
NB, DT	4.336	0.0594	1/2	4.747	4.336<4.747	Cross-valid	Site 1	Not significant
NB,RF,DT	4.335	0.0291	2/8	2.849	4.335>2.849	Cross-valid	Site 1	Significant
RF,DT	0.0451	0.8355	1/12	4.747	0.0451<4.747	Cross-valid	Site 1	Not significant
NB,DT	4.3971	0.0579	1/12	4.747	4.3971<4.747	Train & Test	Site 1	Not significant
NB,RF,DT	2.9799	0.0762	2/18	2.849	2.9799>2.849	Train & Test	Site 1	Significant
RF,DT	0.4961	0.494	1/12	4.747	0.4961<4.747	Train & Test	Site 1	Not significant
NB,DT	4.030	0.0678	1/12	4.747	4.030<4.747	Cross valid	Site 2	Not significant
NB,RF,DT	4.667	0.0233	2/18	3.555	4.667>3.555	Cross valid	Site 2	Significant
NB, DT	0.8533	0.3738	1/12	4.747	0.8533<4.747	Cross valid	Site 2	Not significant
RF, DT	6.362	0.0268	1/12	4.747	6.362>4.747	Train & Test	Site 2	Significant
NB,RF,DT	5.180	0.0167	2/18	2.849	5.180>2.849	Train & Test	Site 2	Significant
RF, DT	0.280	0.061	1/12	4.747	0.280>0.061	Train & Test	Site 2	Not significant

Table 3.7: Pearson's correlation between the shape variables

Correlation	**Border Index**	**Ecliptic fit**	**Rectangular fit**	**Roundness**	**Shape Index**
Border Index	1.0				
Ecliptic fit	-0.89	1.0			
Rectangular fit	-0.84	0.91	1.0		
Roundness	0.82	-0.87	-0.84	-1.0	
Shape Index	0.95	-0.78	-0.82	0.78	1.0

Table 3.8: Pearson's correlation between the Pol. Bands & PCA variables

Correlation	C11	C22	PCAI	PCA2	PCA3	RVI
C11	1.0					
C22	0.85	1.0				
PCA1	0.97	0.83	1.0			
PCA2	0.84	0.96	0.79	1.0		
PCA3	0.89	0.90	0.83	0.88	1.0	
RVI	0.87	0.92	0.82	0.98	0.87	1.0

Table 3.9: Confusion matrix on training site 2 using 10-fold cross-validation approach (S1-February,2017)

		PREDICTED					
		Others	A. Crown Gap	A. Undergrowth	A. Forest	Total	UA
ACTUAL	Others	137	4	20	18	179	77%
	A. Crown Gap	7	624	0	0	631	99%
	A.Undergrowth	3	0	542	3	548	99%
	A.Forest	7	3	4	1251	1272	98%
	Total	154	631	566	1272	2623	
	PA	89%	99%	96%	98%		
	OA	97.3%					

Table 3.10: Confusion matrix on training site 2 using 10-fold cross-validation approach (S1-February, 2015)

		PREDICTED					
		Others	A.Crown Gap	A.Undergrowth	A.Forest	Total	UA
ACTUAL	Others	**403**	41	0	5	**449**	90%
	A. Crown Gap	31	**1059**	0	0	**1090**	97%
	A.Undergrowth	0	0	**236**	0	**236**	100%
	A.Forest	0	2	0	**711**	**713**	99%
	Total	**434**	**1102**	**236**	**716**	**2488**	
	PA	93%	96%	100%	99%		
	OA	**96.8%**					

Table 3.11: Confusion matrix on training site 2 using 10-fold cross-validation approach (S1-February, 2019)

		PREDICTED					
		Others	A.Crown Gap	A.Undergrowth	A.Forest	Total	UA
ACTUAL	Others	**488**	20	8	9	**525**	93%
	A. Crown Gap	25	**230**	6	1	**262**	87.7%
	A.Undergrowth	6	24	**141**	8	**179**	78.7%
	A.Forest	1	14	21	**14**	**50**	28%
	Total	**520**	**288**	**176**	**32**	**1016**	
	PA	94.2%	79.8%	80.1%	44%		
	OA	**86.1%**					

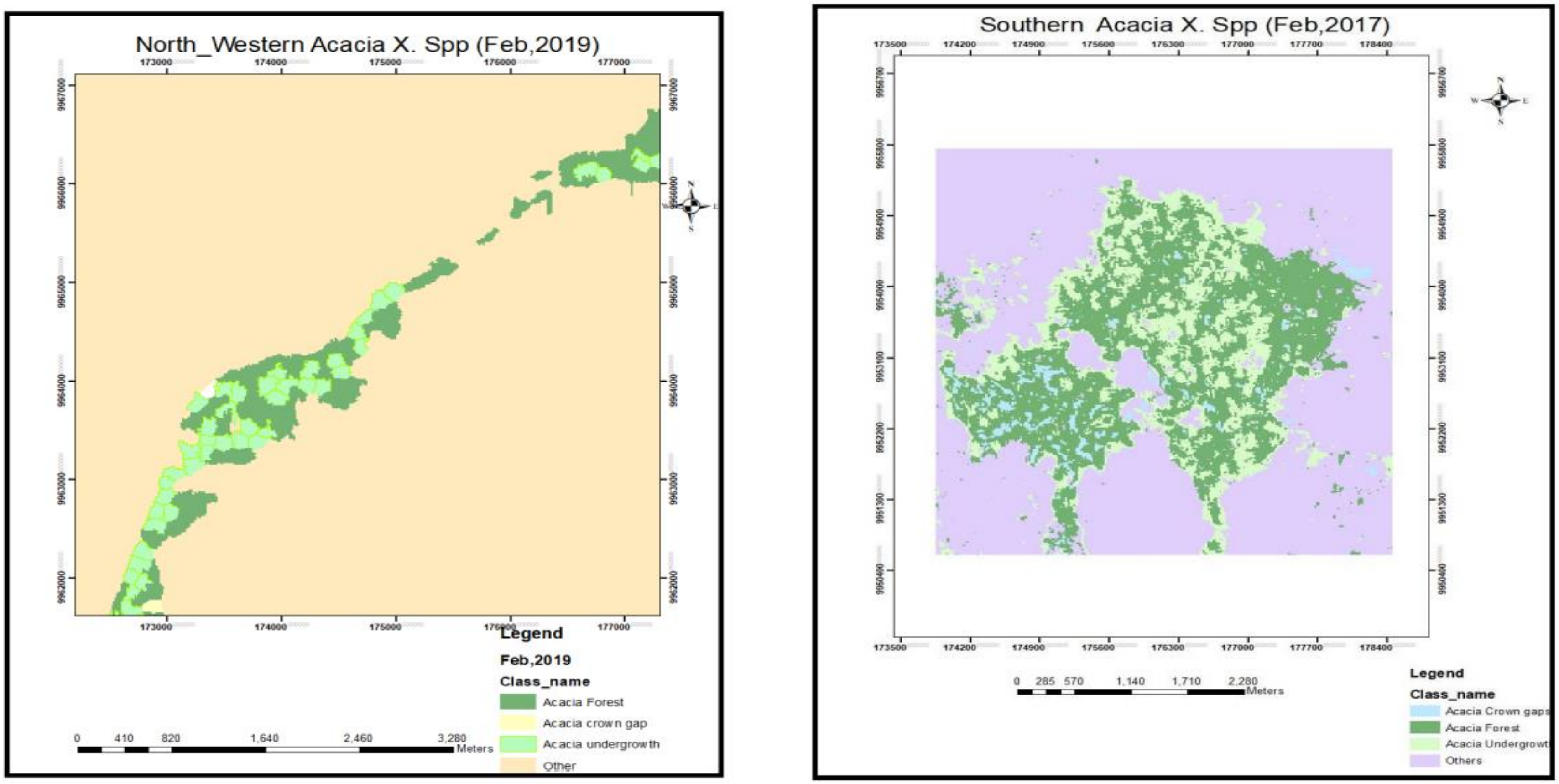

Figure 3.8: OBIA classification on train sites 1 & 2 based on RGB (C11, C22 & RVI)

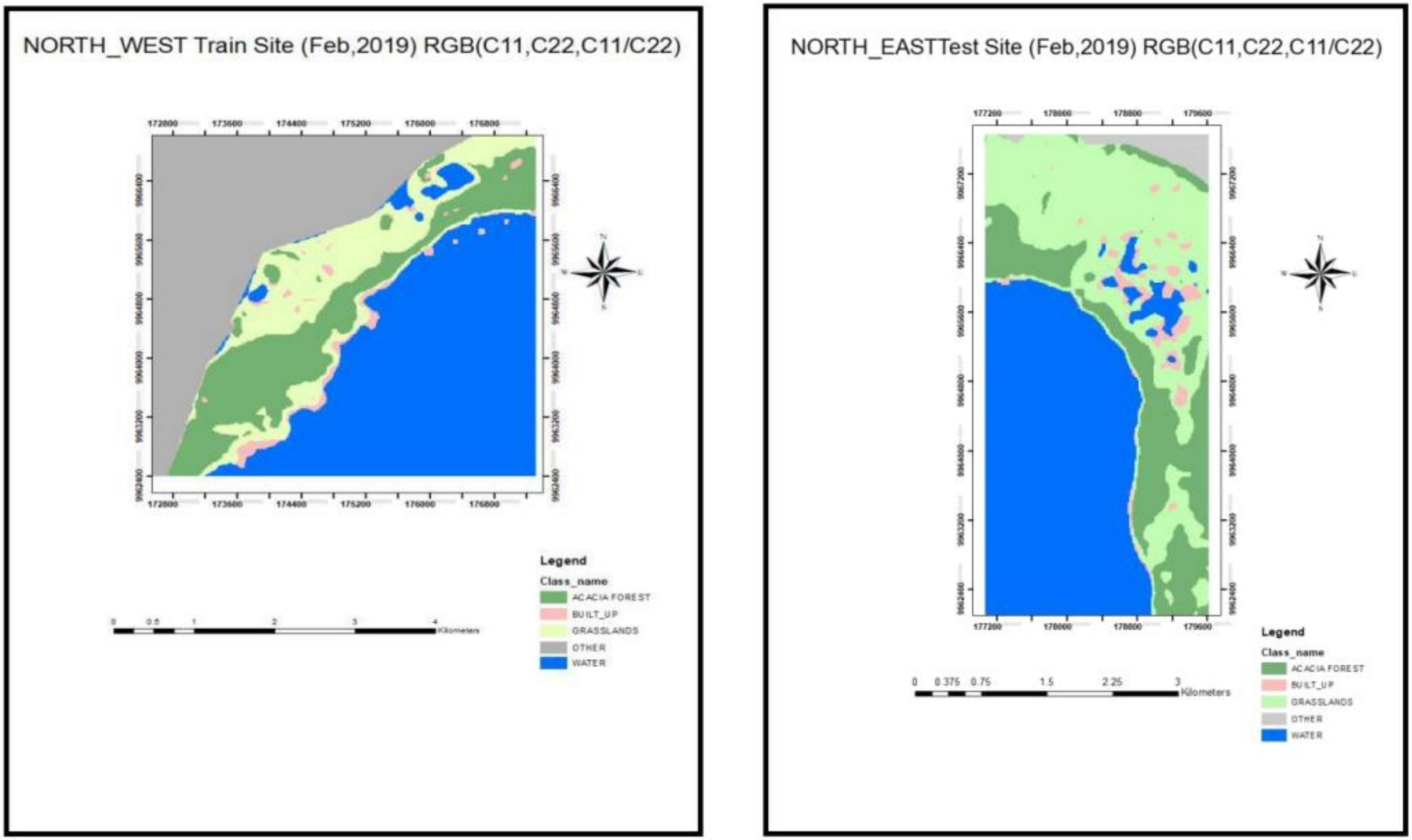

Figure 3.9: OBIA classification on train site 1 and test site 1 based on RGB (C11, C22&C11/C22)

3.7 CONCLUSION

This study demonstrates how Sentinel-1 SLC polarimetric bands σ(VV) and σ(VH) filtered through covariance matrix could improve wetland classification. We consider an OBIA-based approach coupled with PCA derived features, as well as geometric and shape features. Numerous experiments were conducted on several datasets and several dates, assessing the effect of all components in the pipeline: input bands for the segmentation, segmentation algorithm and parameters, features to describe the objects, and classifier settings. We have observed that the optimal selection was specific to each image (area, date) under study. The average results achieved by ALOS PALSAR with Random Forest (OA of 93.8%, Kappa of 0.92) makes it a suitable choice as a reference image in this study. Out of 84 classifications carried out, Random Forest (RF) (Fawagreh et al., 2014) achieved the highest average score (OA of 90.0%, Kappa of 0.88). However, in some instances, Acacia forest was either confused as class Acacia undergrowth or Other, hence confirming reports by (Moskal et al., 2011a) on confusion between classes in wetland-based land cover classification.

Other studies by (Gašparović & Dobrinić, 2020) also confirmed confusion between Forest and water or soil class, in addition between built-up and low vegetation. Significant differences were reported between and amongst group members (Naïve Bayes, Decision Tree and Random Forest) as reported on Table 3.6 using One Way Analysis of Variance (ANOVA). However, (Camargo et al., 2019) reported contrary results from the OBIA in conjunction with RF on Multi-temporal SAR –C bands. The gaps left by the authors is fulfilled in this study, whereby PolinSAR techniques was used in the pipeline, hence realizing desirable results.

Between 2014 and 2020 the area covered by the degraded Acacia xanthophloea spp trees on the north western side of the lake was ~123ha, on the southern part where the largest strands of acacia forest were existing ~444ha, and on the south western side (~160ha) were degraded. There was a strong negative correlation (R = -0.94) between the area covered by the lake against the area covered by the Acacia Forest remnants on the riparian reserve, confirming reports by (Mutangah, 1994) that the flooding lake could have been the cause of the death of the Acacia Trees within the closed ecosystem. Future studies should look into the possibility of using Quad Polarized Sentinel SLC product to characterize riparian reserves.

CHAPTER FOUR:

OBIA-BASED MONITORING OF RIPARIAN VEGETATION, APPLIED TO THE IDENTIFICATION OF DEGRADED ACACIA XANTHOPHLOEA ALONG LAKE NAKURU, KENYA

This Chapter is based on, Osio, A., Lefèvre, S., Ogao, P., & Ayugi, S. (2018, June). OBIA-based Monitoring of Riparian Vegetation Applied to the Identification of Degraded Acacia Xanthophloea along Lake Nakuru, Kenya. In *GEOBIA 2018-From pixels to ecosystems and global sustainability* (pp. 18-22).

Presented at the **7th, GEOBIA 2018 Conference** dubbed, 'From pixels to ecosystems and global sustainability', in Montpellier, France on 18th-22nd, June 2018

ABSTRACT

The Lake Nakuru (Kenya) faces flooding since 2010, thus interfering with the growth of riparian vegetation, and requiring automated image analysis to monitor the effect of flooding on the Lake Nakuru Riparian Reserve vegetation species. The vegetation specie that was affected by the flooding lake is Acacia Xanthophloea, i.e. a habitat and feed for many animal species within the National Park. In this study, we explore how *an OBIA methodology can provide* riparian vegetation classification, *thus* eas*ing* the detection of degraded *Acacia xanthophloea spp*. Our study shows that: i) from a thematic point of view, GEOBIA was able to identify Acacia xanthophloea from Landsat satellite imagery, and comparing the resulting classification maps allows us to achieve monitoring of this specie through time; ii) from a software point of view, it might be necessary to involve several different tools (both proprietary or open source) since there are still some missing functionalities in the existing GEOBIA software solutions.

4.1 INTRODUCTION AND LITERATURE REVIEW

Object-based image analysis has been used in various change detection studies (Lunetta et al., 2006; Ma et al., 2016). Object-oriented classification describes relationships in terms of several categories of characteristics, each of which being assigned certain weightings. Object features include properties such as color, texture, shape, area and scale. Previous studies have also shown that the common pixel-based approach used in remote sensing imagery classification has drawbacks, in that it causes noise in the output image, otherwise known as the 'salt and pepper' effect (Oke et al., 2012). The OBIA approach to image classification has been used on land use and riparian studies (Dupuy et al., 2012; Tormos et al., 2012).

The method has been applied over wide areas covered by High and Very High Spatial Resolution satellite imageries. It provides an effective computer-assisted classification technique whose results are close to the manual photo-interpretation. According to research carried out by Durieux et al., (2008) and Lang, (2014), this method is faster, cheaper and more reproducible than pixel-based approach.

The basis of OBIA is the traditional segmentation method, where pixels containing the object to be studied are measured against the spatial extent of the object. The underlying principle of the system uses a region growing technique, which starts with regions of one pixel in size based on the spectral and spatial characteristic of the pixels under study (Baatz et al., 2004). The local homogeneity criteria are then used to make decisions about merging regions of interest by taking into account the image analyst's expertise. The goal of multiscale segmentation is to build a hierarchical set of image object primitives at different resolutions by appending multi-resolution segmentation maps in which objects are subject of coarse structures. The parameters controlling the algorithm include scale, homogeneity criteria, shape and color.

Object-based image analysis (OBIA) allows for use of variables such as texture, shape, context and other cognitive information provided by the image analyst to segment and classify image features thus improving classification. OBIA method of classification improves the accuracy results and allows mapping of very small urban features, such as mature individual trees or small clusters of shrubs (Platt & Rapoza, 2008; Hay et al., 2005).

Other studies have shown that pixel-based classification approaches, although appropriate on Landsat imagery, are outperformed by OBIA approaches on hyperspectral images in urban, sub-urban and agricultural landscapes and in urban-wildland interface, especially in instances where tree cover is complex and heterogeneous (Platt & Rapoza, 2008 ; Tuominen & Pekkarinen, 2005). OBIA algorithm is capable of extracting the indices of various land cover features. Satellite imagery of high or very high spatial resolution has been used in various studies to extract indices assuming presence of channels with Top of the Atmosphere (TOA) reflectance (see equation 4.3). The first step involves conversion of raw data into TOA spectral radiance, then converting the spectral radiance into spectral reflectance. TOA bands include Red, Green and Near-Infra-Red (NIR) bands. The feature view tool in eCognition enables calculation of Vegetation, Water and Soil index. According to (McFeeters, 1996), vegetation indices range between 0 and 1. Normalized Difference Vegetation Index (NDVI) closer to 1 indicates healthy vegetation while negative NDVI indicates stressed vegetation. Measuring of NDVI is made possible through thresholding in eCognition (Ma et al., 2016). The threshold map is then exported to ArcGIS 10 for thematic re-classification (Sakamoto et al., 2007) .

There is dire need on the improvement of classification methods using the recently developed classification algorithms and classifiers such as random forests, J48 decision tree, CART and Naïve Bayes in order to achieve a better classification model. Accuracy of classification being a method of classification stability has been applied in recent research studies. Accuracy assessment carried out on OBIA is known to be high (>85%) compared to non-OBIA approaches.

It compares how each element (e.g., pixel) is classified against the definite land cover condition obtained from the corresponding ground truth data. *Specificity* and *Sensitivity* are two aspects in accuracy assessment where results are determined by the classification of specific terrain classes of the predicted elements against the observed ones. The *sensitivity* of the model is the proportion of positive pixels correctly predicted (*i.e.*, the probability that a pixel belonging to a particular category is correctly identified).

The *specificity* of the model is the proportion of negative pixels correctly predicted (*i.e.*, the probability that a pixel not belonging to a particular category is correctly identified). Thus, models with high sensitivity can correctly predict positive pixels (pixels belonging to the category of interest) and models with high specificity can correctly predict negative pixels (pixels not belonging to the category of interest). High sensitivity is usually associated with poor specificity, which manifests as an overestimate of area in the category of interest.

An optimum classification model would be one with the highest possible value of sensitivity and specificity, minimizing omission and commission errors at the same time. Since this ideal situation is usually not the case, there is a need to make a compromise, and the Receiver Operator Characteristics (ROC) curve is an appropriate tool to make such a choice.

4.2 MATERIAL AND METHODS

In this section, we successively present the data capture, preprocessing, processing, and analysis. Figure 4.1 shows vegetation distribution around Lake Nakuru National Park(LNNP) in year 2000 before the onset of the floods.

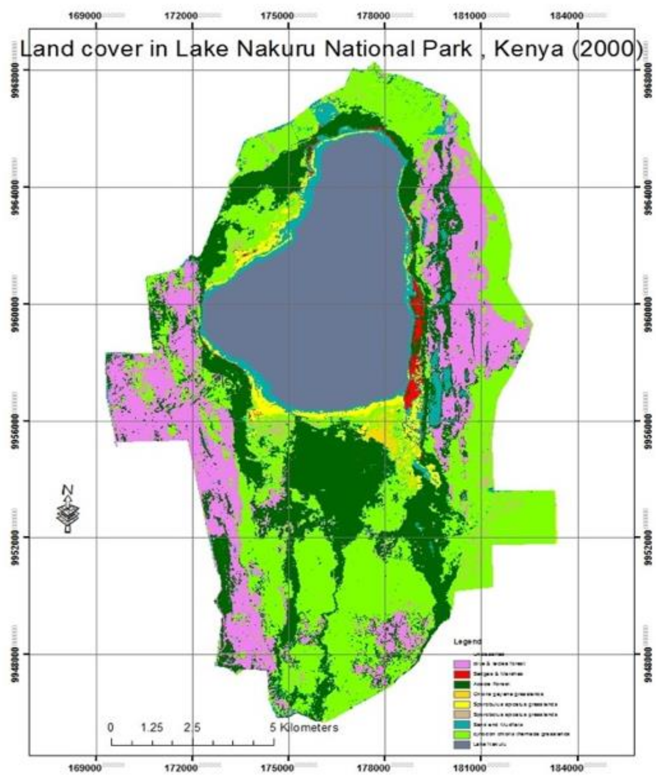

Figure 4.1: Vegetation Distribution around Lake Nakuru before the onset of the floods

4.3 DATA CAPTURE

Raw satellite data were downloaded from the USGS site. The study area fell specifically within path 169 and row 060.The datasets were of the same datum and projection, *i.e.*, WGS 84/UTM Zone 36N. Datasets were as follows: Landsat 5 TM collected on 17.01.2011, Landsat 8 OLI dated 2014, and Landsat 8 OLI dated 16.12.2016.

4.4 DATA PRE-PROCESSING

Preprocessing of datasets was carried out on the imageries in order to remove noise and enable uniformity between datasets. Band compositing was carried out followed by sub setting of the four imageries, using Erdas Imagine. Each image was pan- sharpened to 15m resolution using Ehlers fusion technique. The panchromatic bands that came with each dataset have been used in each case. The final products were Landsat imageries of false colors with band combination RGB (4, 3, 2).

4.4.1 Radiometric Calibration

Top Atmospheric corrections of the bands 4, band 3 and band 2 of Landsat5TM & Landsat7ETM was required to avoid the noise due to satellite path radiance. The technique converts the Digital Numbers (DN) in an image to atmospheric radiance using the following equation:

$$L\lambda = \frac{SR_k - DN}{DN(max)} \quad \ldots\ldots 4.1$$

Where SR_k is the saturation Radiance of the K^{th} band, DN is the digital Number, while *DNmax is* the maximum possible value of a pixel. The resultant Atmospheric Radiance is converted further to at Sensor Atmospheric Reflectance using the following equation:

$$R_{sensor} = \frac{L\lambda * \pi * d^2}{ESUN*Cos(SZ)} \quad \text{……4.2}$$

Where π = 3.141593, d^2 = Square of the Earth to Sun distance in astronomical units of the specific date of image capture. SZ is the Sun Zenith angle in degrees, *ESUN* is the Solar Exo-atmospheric spectral Irradiances for the specific TM bands in use. Radiometric corrections on Landsat 7 ETM include the removal of scan lines from the bands in use. The Landsat 7 ETM+ SLC-off data and which refers to all Landsat 7 images collected after May 31st, 2003, after the Scan Line Corrector (SLC) instrument failed, hence creating some data gaps. To remove these data gaps, the Landsat 7 ETM+ files have additional GEOTIF products (Gap masks) in GZIP format, which is meant for Gap filling. This procedure was carried out on Landsat 7 ETM+ before the procedures in equation 4.2 was done.

4.4.2 Atmospheric Corrections

To convert raw values (DN) to Top of the Atmosphere (TOA) reflectance (see equation 4.3), the images were uploaded in ArcGIS 10.4 whereby procedures were carried out using the spatial analyst tool in Arc Toolbox using the following equation:

$$\rho\lambda = M_\rho Q_{cal} + A_\rho \quad \text{……4.3}$$

where $\rho\lambda$ is the TOA planetary reflectance, without correction for solar angle (NB does not contain a correction for sun angle), $M\rho$ and $A\rho$ the band-specific multiplicative rescaling factor and additive rescaling factor from metadata (Reflective_Add_Band_X, where X is the band number), and Q_{cal} the quantized and calibrated standard product pixel values (DN). In case a correction for the sun angle is needed, the computation becomes

$$\rho\lambda = \rho\lambda'/\cos\theta_{SZ} - \rho\lambda'/\sin\theta_{SE} \ldots\ldots\ldots\ldots\ldots(4.4)$$

with θSE the local sun elevation angle and θSZ the local solar zenith angle ($\theta SZ = 90° - \theta SE$). The scene center sun elevation (SE) angle in degrees is also provided in the metadata i.e. MTL file. The three Landsat images were then cropped to the shape of the study area in ArcGIS in readiness for export into eCognition Developer (Cordeiro & Rossetti, 2015). The scene size was (936 x 1520) pixels in spatial extent.

4.5 DATA PROCESSING

The images were then uploaded into eCognition Developer (Cordeiro & Rossetti, 2015) of which the first step was to convert the pixels into image objects by the use of multiresolution segmentation algorithm. The layer weights adopted on the 2011 Landsat 5 TM image prior to classification were scale = 5, shape = 0.2, and compactness = 0.7. The Green, Red, NIR and SWIR bands were useful in the calculation of Normalized Difference Vegetation Index (NDVI) on each dataset. NDVI values were calculated and captured in eCognition database link tables which were exported to ArcMap environment for post classification. The values that were captured through the customized tool in eCognition (Cordeiro & Rossetti, 2015) were mean Red, Green and NIR. Rulesets were thus formed in the feature view section so as to come forth with NDVI values which were calculated from eCognition customized tool (Cordeiro & Rossetti, 2015). Supervised classification by sample selection was carried out on each image using the K-NN Algorithm. Initially, from the 2011 imagery it was possible to extract vegetation classes using the previous studies by (Mutangah, 1994). Using a sample selection method, the following classes of vegetation were thus created: *Acacia Xanthophloea*, *Chloris Gayana* grasslands, *Bushed Themada Triandra* grasslands, *Cynodon Niemfluensis* grasslands, *Cynodon Niemfluensis* wooded *Acacia Xanthophloea* grasslands, *Cynodon Chloris Themada* grasslands, Lake Nakuru, *Sedges & Marshes*, *Sand & Mud flats*, *Sporobolus Spicatus* grasslands, *Tachonandus bush land*, *Euphorbia candelabra* and the highland vegetation.

4.6 DATA ANALYSIS

Several aspects were observed in this study, namely: i) the classification scales used on each image; ii) pan-sharpening methods and type of sensors used; iii) type of classification used (thresholding or sampling); iv) procedures used in atmospheric, radiometric, and geometric corrections; v) classification algorithms and modes used.

Classification scales varied across the different images, thus giving rise to different number of instances per imagery. These instances were then used to measure the significance of the number of instances on classification accuracy. Pan-sharpening methods used on the imagery were Ehlers fusion and IHS. Type of classification in eCognition Definiens can either be through sampling or thresholding using the feature view tool (Cordeiro & Rossetti, 2015). In this study the sample selection technique was used. Procedures used in atmospheric corrections involve the conversion of raw DN values to at sensor reflectance. Using the MTL files that come in handy with the downloaded images, values can be inserted into equations (4.1) and (4.2) to come up with spectral radiance bands and into equations (4.3) and (4.4) to come up with Top of the Atmosphere reflectance (TOA) of each band. The main goal is to be able to calculate vegetation indices from the same images. NDVI values were calculated in eCognition and NDVI related shape files (image objects) exported to ArcGIS 10.4 environment for re-classification. Finally, the .CSV files and the shape files of the imageries were exported to Weka Machine Learning software for further analysis (Camargo et al., 2019)

The classifier that was used on the datasets in eCognition was K-Nearest Neighbor (K-NN) algorithm since it has the ability of retaining all it's training data, while the ones used in Weka were J48, Random Forest, Binary Support Vector (SMO) and Naïve Bayes. We looked at the classifier performance on each dataset which was initially generated in eCognition Developer 9.2 (Cordeiro & Rossetti, 2015). The classification modes explored were full training, data split in 2/3 for training and 1/3 for testing, and 10-fold cross-validation. OBIA supervised classification was appended on the different datasets from different dates in order to find out the best classification models. It was worth investigating the effect of classification scales and sample size on classification accuracy.

4.7 RESULTS AND DISCUSSION

4.7.1 Segmentation Parameters

The process used in segmenting the images into objects was multiresolution segmentation algorithm in eCognition Developer 9.2 (Cordeiro & Rossetti, 2015). Major features that were incorporated into the image segmentation routine when setting segmentation parameters were:

- *Layer weights*: there are layers with more important information about particular features for segmentation process; they are thus given higher weight.
- *Scale parameters* that measure the maximum change of heterogeneity when merging image objects.
- *Composition of homogeneity criterion* that prioritizes the drivers for object creation such as "color has preference to shape".

The outlined parameters were set in eCognition Developer 9.2 which used multiresolution segmentation (Table 1) and divides the image into homogenous image objects based on how close is the value of the neighboring pixel in relation to the class under study. In eCognition developer 9.2 (Cordeiro & Rossetti, 2015), the band mixing tool was used in generating false positive image with RGB {5, 4, 3} band combination for Landsat 8 OLI 2014 (*i.e.*, NIR, R, G) while RGB {4, 3, 2} for Landsat 5 TM 2011 and Landsat 8 OLI 2016 (*i.e.*, NIR, R, G). The following segmentation scales were then set as shown in the aforementioned table.

Table 4.1: Segmentation scales appended in eCognition Definiens

Image	scale	shape	compactness	Red	Blue	Green	NIR
Landsat5TM_2011	5	0.2	0.7	1	1	1	1
Landsat8OLI_2014	40	0.5	0.5	1	1	1	1
Landsat8OLI_2016	20	0.2	0.7	1	1	1	1

4.7.2 Appending rulesets in eCognition Definiens

Rulesets were developed within the eCognition feature view. This involved the calculations which were made possible through the use of the customized toolbar. The ruleset (Figure 2) includes NDVI which was used to measure vegetation vitality. Per pixel area was also important in measuring the spectral information of vegetation species within Lake Nakuru National Park. Figure 2 depicts the type of indices that were appended on Landsat5TM_2011 imagery.

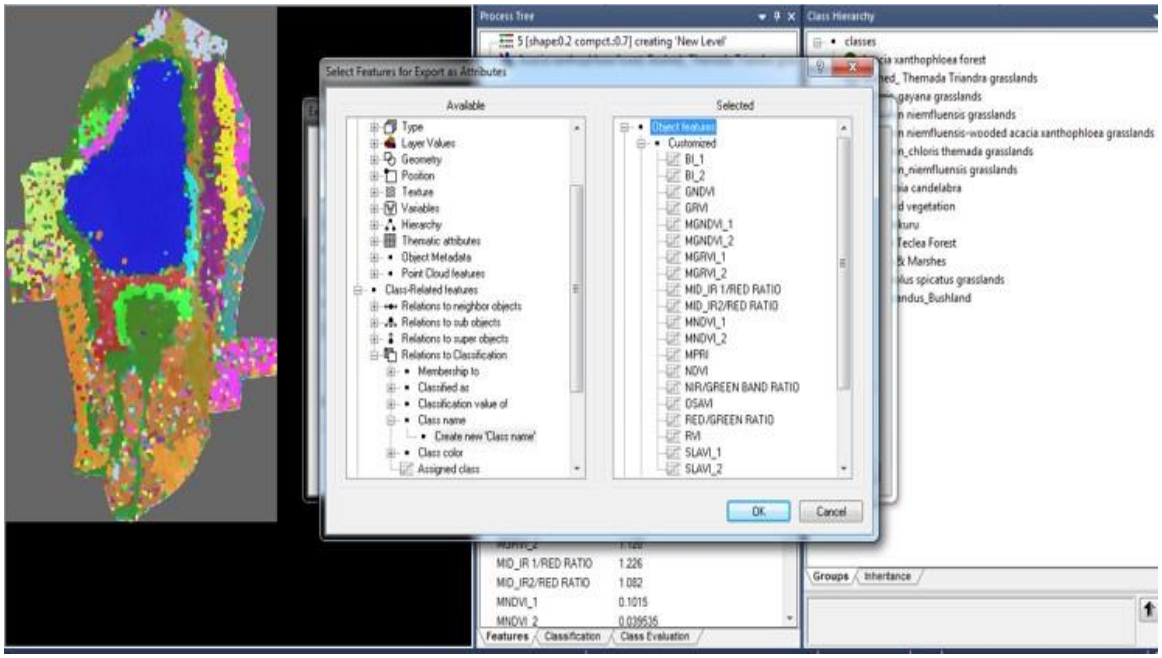

Figure 4.2: Appending Rulesets in eCognition Definiens

4.7.3 Accuracy Assessment on the datasets

The link tables associated with the classification (CSV files) and the shape file of the mapped image was exported to ArcGIS 10.5 for thematic re-classification which is a process that entails editing of datasets (Kumsa et al., 2019). It was observed that the re-classification was only possible through the use of isodata classifier in ArcGIS. Thematic reclassification was done in order to add sub-vegetation species such as Acacia xanthophloea re-growth (Acacia Saplings). The process of object-based supervised classification on each image was then carried in Weka software(Camargo et al., 2019). This process led to poor classification results on Landsat 8 OLI 2014 except for the Random Forest classifier which recorded a kappa coefficient of 1.0 and J48 with a kappa value of 0.72 (Muñoz et al., 2019b). Landsat 5 TM 2011 and Landsat 8 OLI 2016 did not undergo thematic re-classification which is why excellent classification results were realized such as on Landsat 5 TM 2011 where Random Forest (Muñoz et al., 2019b) and J48 (Zarkami et al., 2020) had the highest kappa statistic of 1.0. Landsat 8 OLI 2016 realized a kappa value of 1.0 from Random Forest and of 0.92 from J48. However, the near perfect agreement obtained from Landsat 5TM of 2011 and Landsat 8OLI of 2016 could have been caused by hyper-parametrization. For the sake of illustration, confusion matrices obtained for classification with Random Forest(Muñoz et al., 2019b) on the 3 images are provided in Tables 4.2-4.4.

Table 4.2: Confusion Matrix, Random Forest classification on Landsat 5 TM 2011. FID: (a) Lake Nakuru, (b) Acacia Xanthophloea, (c) Euphorbia Candelabra, (d) Cynodon Chloris Themada grassland, (e) Chloris Gayana grasslands, (f) Bushed Themada Triandra grass g) *Niemfluensis woodlands*

FID	a	b	c	d	E	f	g	h	i	j	k	l	m	n	Total
a	860														860
b		891													891
c			311												311
d				264											264
e			172												172
f						88									88
g							211								211
h								87							87
i									203						203
j										396					396
k											202				415
l												394			230
m													415		415
n														230	230
Tota	860	891	311	264	172	88	211	87	203	396	415	230	415	230	4724

Table 4.3: Confusion Matrix, Random Forest classification on Landsat 8 OLI 2014. FID: (a) Acacia forest, (b) Acacia saplings, (c) Acacia savannah, (d) Acacia woodlands, (e) Chloris Gayana grasslands, (f) Cynodon Chloris Themada grasslands, (g) Cynodon Niemfluensis woodlands

FID	a	b	c	d	e	f	g	h	i	j	k	l	m	n	Total
a	119														119
b		421													421
c			431												431
d				154											154
e					190										190
f						10									10
g							70								70
h								45							45
i									30						30
j										25					25
k											108				108
l												10			10
m													4		4
n														1	1
Tota	119	421	431	154	190	10	70	45	30	25	108	10	4	1	1618

Table 4.4: Confusion Matrix, Random Forest classification on Landsat 8 TM 2016. FID: (a) Cynodon Niemfluensis grasslands, (b) Sporobolus Spicatus grasslands, (c) Lake Nakuru, (d) Acacia Xanthophloea, (e) Euphorbia Candelabra, (f) Cynodon Niemfluensis woodlands

FID	a	b	c	d	e	f	g	h	i	j	k	l	Total
a	2717												2717
b		121											121
c			1024										1024
d				465									465
e					280								280
f						175							175
g							193						193
h								128					128
i									122				122
j										149			149
k											157		157
l												10	10
Total	2717	121	1024	465	280	175	193	128	122	149	157	10	5541

4.7.4 Change detection on Land cover

The main vegetation specie under investigation was Acacia xanthophloea. Post classification change detection was possible through observing the per pixel area of the vegetation under study. The Lake Nakuru area was observed to have increased from 860 pixels in 2011 to 1024 pixels in 2016, thus confirming reports by Onywere et al., (2013) that the lake has been flooding its banks. The area covered by *Acacia xanthophloea* was noted to have reduced by 47.8% between year 2011 and 2016. Thus, the difference in spatial coverage (~9.6ha) of Acacia xanthophloea was covered by the flooded lake.

Other vegetation species closer to the lakes which were affected by the flooding were sedges and marshes whose area was ~2.0 ha and Cynodon Chloris Themada grasslands with area of ~6.0ha on Landsat 5 TM 2011 but were not detected on the Landsat 8 OLI 2016. Cynodon Niemfluensis grasslands seem to have thrived in the flooded plain and thus an increase in their spatial coverage by ~31% between year 2011 and 2016. Other vegetation species whose area reduced during the study period are as follows: Chloris Gayana (~25.6%), Bushed Themanda Triandra (~88.6%), Tachonandus Bush land (~0.9%)), Sporobolus Spicatus grasslands (~40%), highland vegetation (~54.3%) and Olive & Teclea forest (~58.3%).

4.7.5 Spectral Change Detection on Vegetation Distribution

Spectral characteristics were observed on the classified baseline image i.e., Landsat 5 TM 2010 (Figure 4.3). Sand & Mudflats reflected more seconded by Chloris Gayana. The lowest reflectance was depicted by the Lake Nakuru whose graph indicated that the waters were clear. Normalized Difference vegetation index (NDVI) is a method used in

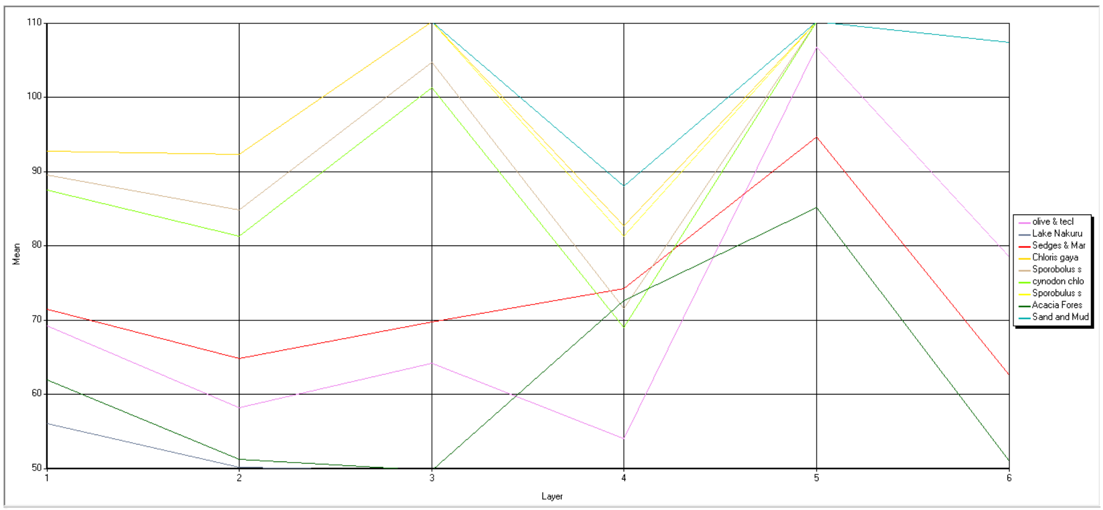

Figure 4.3: Spectral signatures of Land Use Land cover (LULC) in Lake Nakuru Park

detection of vegetation vigor. Vegetation reflects more in the Near Infra-Red bands and less within the visible range of Electromagnetic Spectrum (Grishkin & Karimov, 2022).The formulae used to derive Normalized Difference Vegetation Index (NDVI) is as follows:

$$NDVI = \frac{NIR - RED}{NIR + RED} \quad \ldots\ldots 4.1$$

For the general NDVI presentation, the classification scheme used by (Southworth et al., 2004) was adopted, having a given range of NDVI spectral values as follows; <0 (Non-vegetated area), 0-0.2 (Low vegetated area), 0.2-0.5 (Moderate vegetated) area, 0.5-0.8 (Healthy vegetated area) and 0.8-1.0 (Very Healthy vegetated area).From the NDVI maps (Figure 4.4) generated from Landsat 7 ETM+ 2000 NDVI ranged from -0.34 to +1.0 , Landsat 5TM, 2011 ranged from -0.12to +0.68 while on Landsat 8 OLI 2014 the range was from -0.64 to +0.87.

On Landsat 8OLI, 2016, NDVI values ranged from -0.42 to +0.87 while on the Landsat8 OLI 2020, the values were ranging from -0.45 and +0.87. In the earlier year (2000) before the onset of the floods, the NDVI around the Park (Max=1.0) was at its peak, meaning that the health of the Acacia xanthophloea was at its best i.e., "Very Healthy Vegetation" according to (Southworth et al., 2004) as shown on Figure 4.4. The NDVI of Lake Nakuru ranged between (0) and (0.25) where the "Low vegetation" class exists, meaning that there was a possibility that of the existence of the green blue algae in the Lake that contributed to this specific value (Schagerl et al., 2022).

However, because of the change in salinity levels in the flooded lake, the blue green algae have suddenly become scarce. Due to the impact of pollution from industrial effluents dumped into the rivers that feed the lake, there are additional causes that could have contributed to the depletion of the algae. According to (Kaiser, 2009), NDVI ranges from –ve (-1) to +ve (+1), where the healthy vegetation tends towards value +ve(1) and the unhealthy or non-vegetation tends towards value (0) and –ve(1).

Visualization and comparative assessment of Figure 4.4 against the vegetation classes produced by (Ng'weno et al., 2010b), the following vegetation classes were at their peak in the year 2000, i.e., Acacia xanthophloea Forest, Cynodon_niemfluensis grasslands, Chloris gayana grasslands, Tachonandus bushland, Cynodon niemfluensis wooded acacia grasslands, Olive & Teclea Forest, Riverine vegetation, Euphorbia candelabra and Sporobolus spicatus grasslands.

In the year 2011 just after the onset of the floods, the NDVI of the vegetation around the lake was 0.68 at its maxima, hence reducing by 0.32 with reference to the state of health of vegetation in year 2000 (Onywere et al., 2013). Figure 4.5 (Top Left) depicts the state of vegetation health in Lake Nakuru in year 2011, where class "Very Healthy vegetation" ceased to exist. However, in the year 2014, class "Very Healthy vegetation", re-emerged, this time not with a maximum of +ve (1) but with a maximum of +ve (0.87).

The observations made on Figure 4.5 (Top-Right) depicts the state of health of vegetation in year 2014, where the following vegetation were affected by the flooded lake, i.e. areas covered with Acacia xanthophloea tree species, Chloris gayana grasslands, Sedges & Marshes, Cynodon Chloris themada grasslands, Sporobolus spicatus grasslands had been affected by the flooded Lake Nakuru waters. Other non-riparian vegetation whose health were degraded by year 2014 include Euphorbia candelabra and the Escarpment vegetation as shown on Table 4.9.

In the year 2016, the NDVI maxima value remained the same (0.87) as depicted on the lower left corner of Figure 4.5. However, the values in class "moderate vegetation" and class "low vegetation" were higher (0.57) and (0.40) than those on the year 2014 image which depicted NDVI value of 0.51 on class, "moderate vegetation" and 0.26 on class, "low vegetation" respectively.

In the year 2020, the same maxima NDVI value (0.87) depicted on the 2014 and 2016 imageries was achieved on class "Very Healthy Vegetation". However, within class variability was noted as in the previous case with the 2014 and 2016 NDVI values. The class "Moderate vegetation" (mostly grassland species) on the 2020 map depicted a lower maximum NDVI value (0.54) than the same class on image 2016 which had an NDVI value (0.57). The same pattern was observed with class, “Low vegetation”, whereby on the 2016 image the NDVI value (0.4) while the same class on image 2020 achieved an NDVI Value (0.3).

These results depict an overall state of vegetation health as “Very Healthy”, but the existence in alternative patterns of “increase” and “decrease” between and within classes along the NDVI time series confirms the existence of vegetation species disturbance (degradation) and re-vegetation (re-generation).

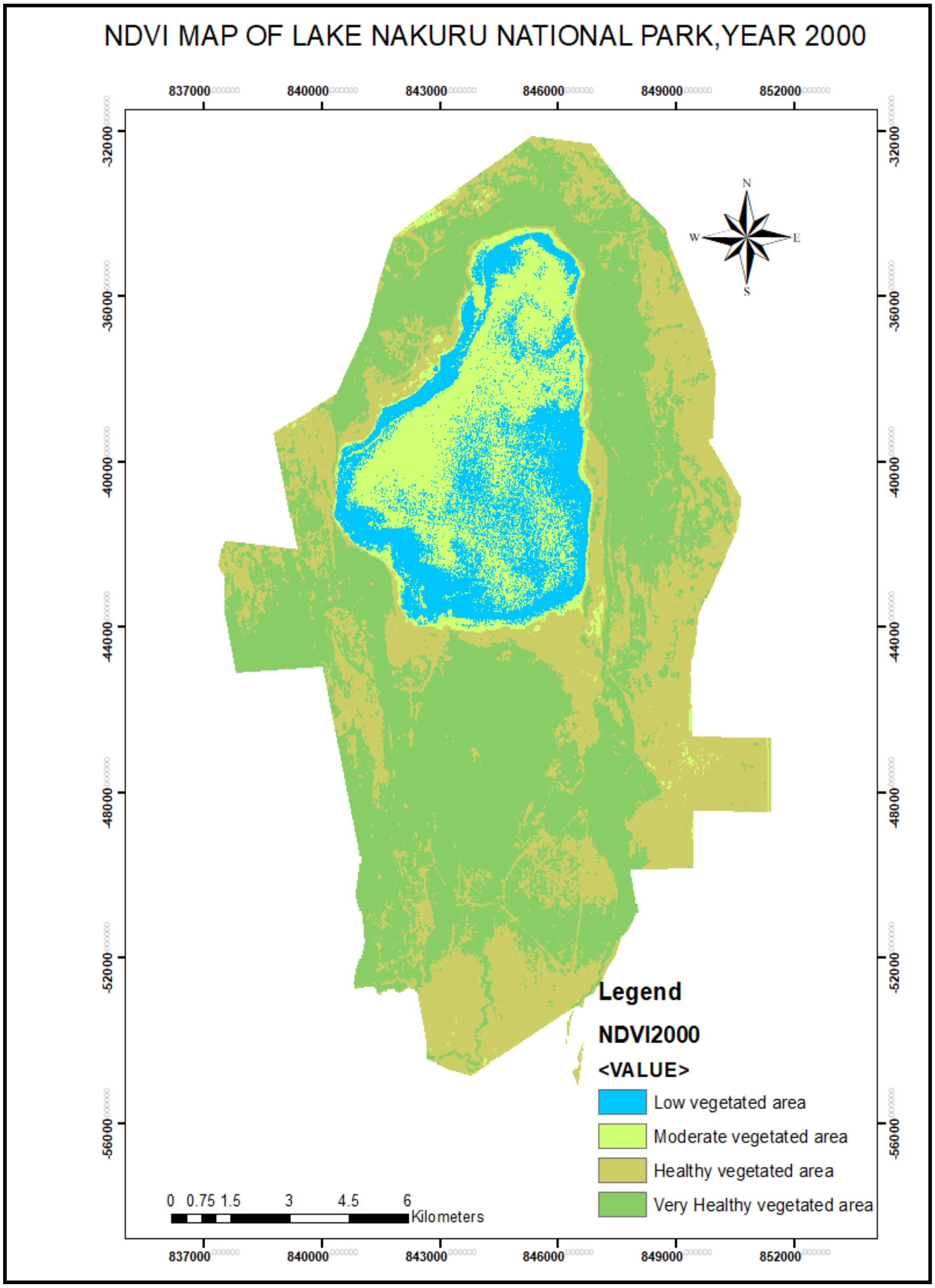

Figure 4.4: NDVI Map of Lake Nakuru National Park (Year 2000)

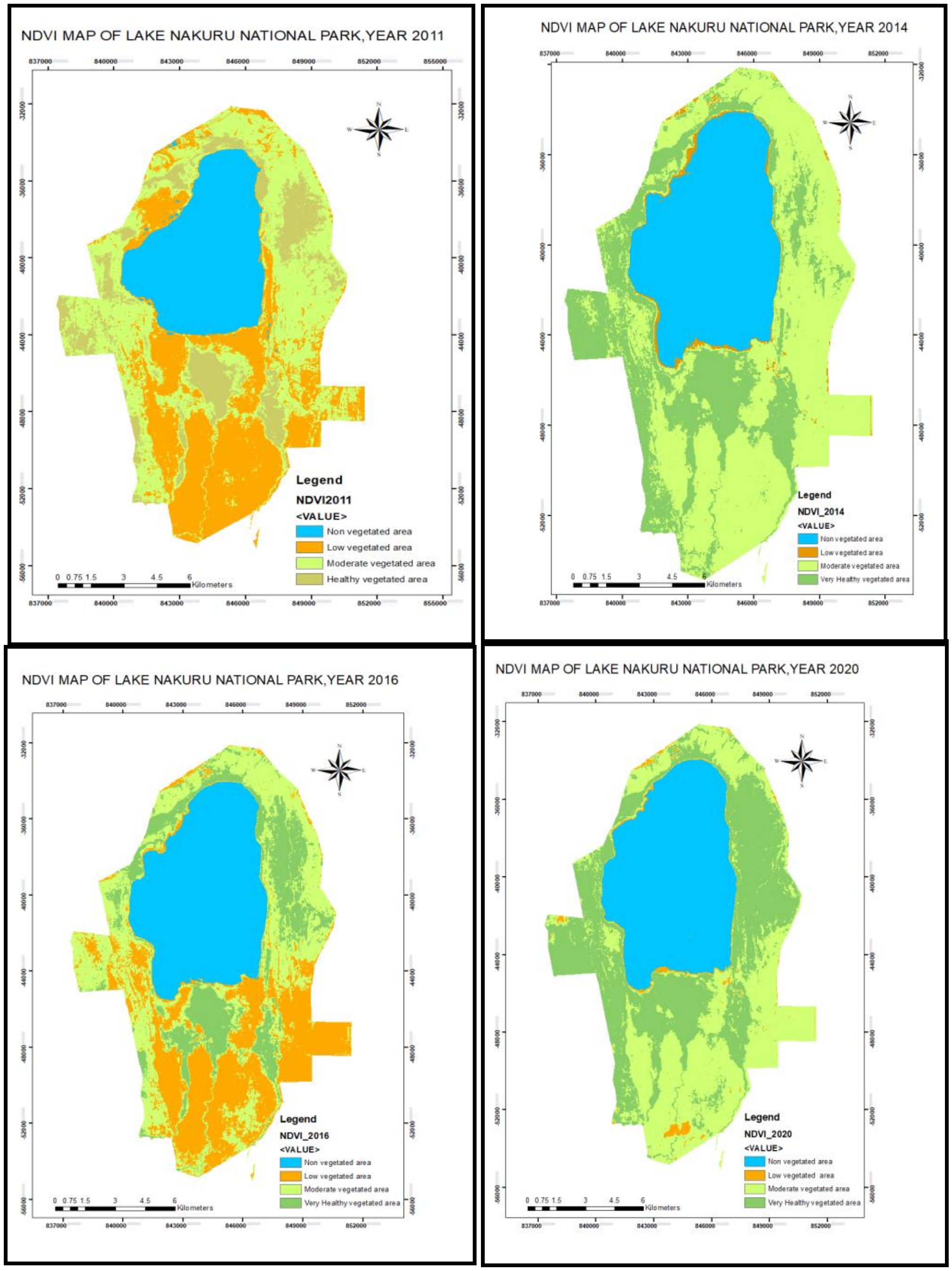

Figure 4.5: NDVI Time Series of Lake Nakuru Land Use Land Cover

4.8 CONCLUSION

The spatial and spectral changes that were detected in this study indicate the degradation of a variety of vegetation species in the National Park. Since the study focuses on *Acacia xanthophloea*, it was worth noting that by the year 2016, areas covered by healthy Acacia xanthophloea had reduced by 47.8%. NDVI around the park was at it's peak (+1.0) in the year 2000 but reduced drastically to +0.68 by 2011.

However, due to re-vegetation around the lake, NDVI values of the vegetation around Lake Nakuru park were noted to have increased to +0.87 between 2012 and 2020. Re-vegetation was noted on some of the grassland species (Cynodon niemfluensis) whose increase in the area was observed at ~31%. Accuracy assessment (Congalton & Green, 2019) on different datasets in Weka software revealed that J48 classifier achieved 0.72 (substantial agreement) while Random Forest classifier achieves a kappa statistic of 1.0 (near perfect agreement) on Landsat 8 OLI 2014. It was also noted that accuracy of supervised object-based classification in Weka using OBIA-J48 model was attributed by the number of instances (classes) as earlier observed in studies by Camargo et al., 2019. Random Forest was the best performer on all the datasets using Full Training classification approach. There was a significant difference achieved between and within the classifiers at p-value 0.0043 and $\phi<0.05$ derived from the analysis on Landsat 5 TM and Landsat 8 OLI multi-date images as reported from Table 4.7. Comparing the areas covered by healthy acacia using year 2011 imagery as a baseline, it was noted that in 2011 the area covered by Acacia xanthophloea (see Figure 4.6) was (~20ha) which was noted to have reduced to (~10.5ha) in year 2016 (see Figure 4.8). This confirms reports by

(Onywere et al., 2013) that indeed the Lake Nakuru had flooded it’s banks. Future studies should apply deep learning techniques on UAV imageries in order to detect individual tree species on the flood inundated areas. Another observation made from this practical study is the need of various software to conduct the GEOBIA-based analysis. It is thus calling for a unified, open-source solution.

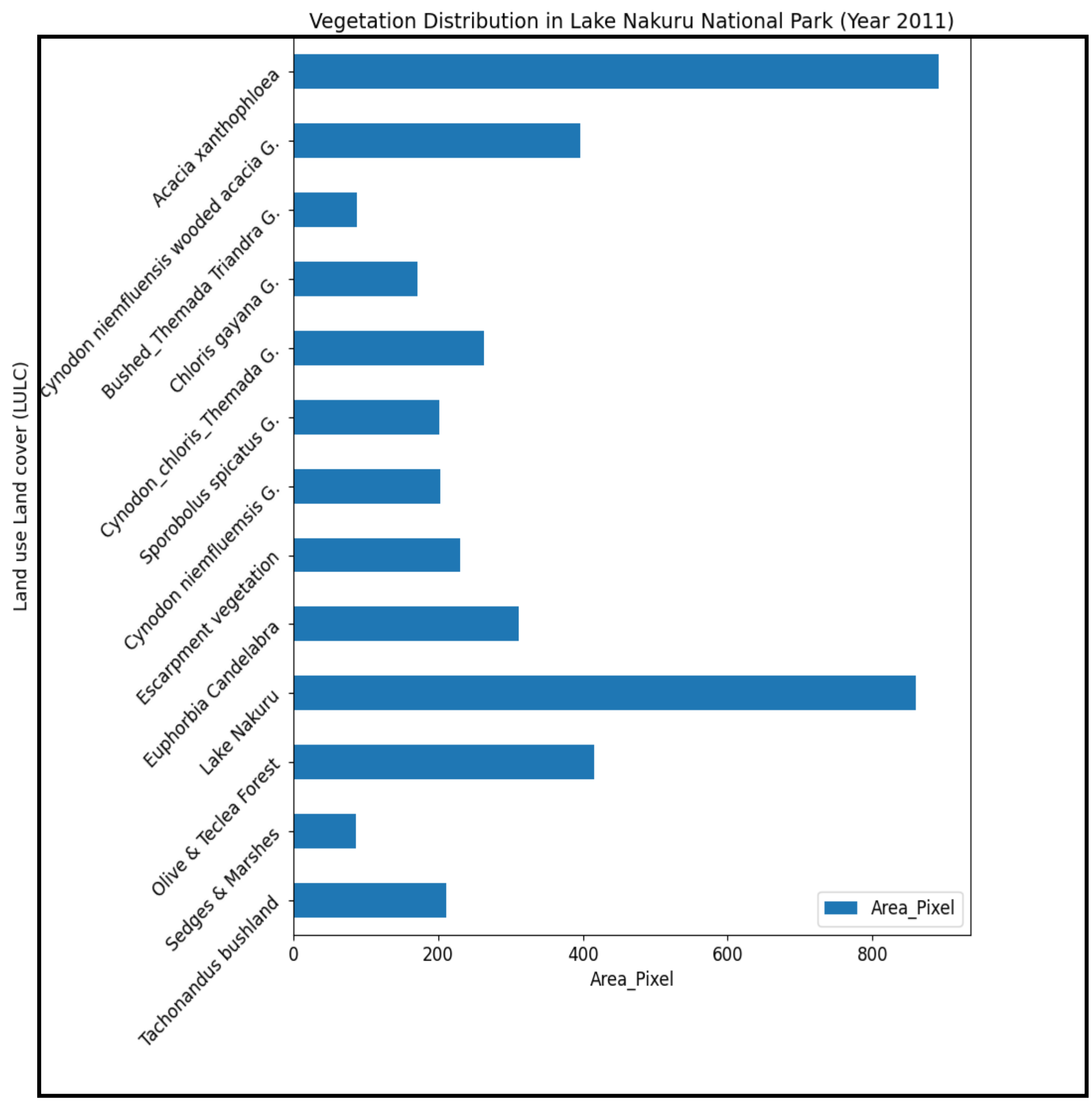

Figure 4.6: Spatial Distribution of Land Cover classes in Lake Nakuru Park (year 2011)

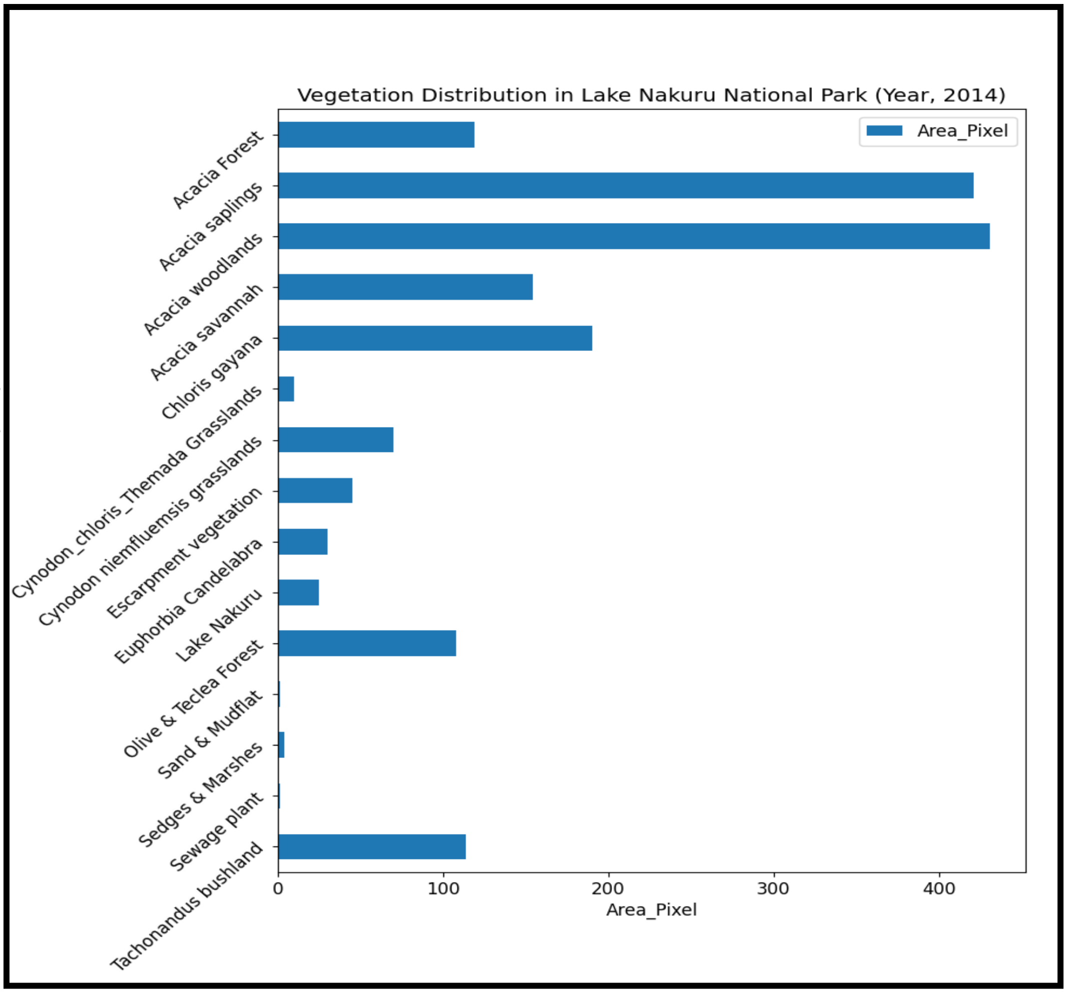

Figure 4.7: Spatial distribution of Land Cover classes in Lake Nakuru Park (year 2014)

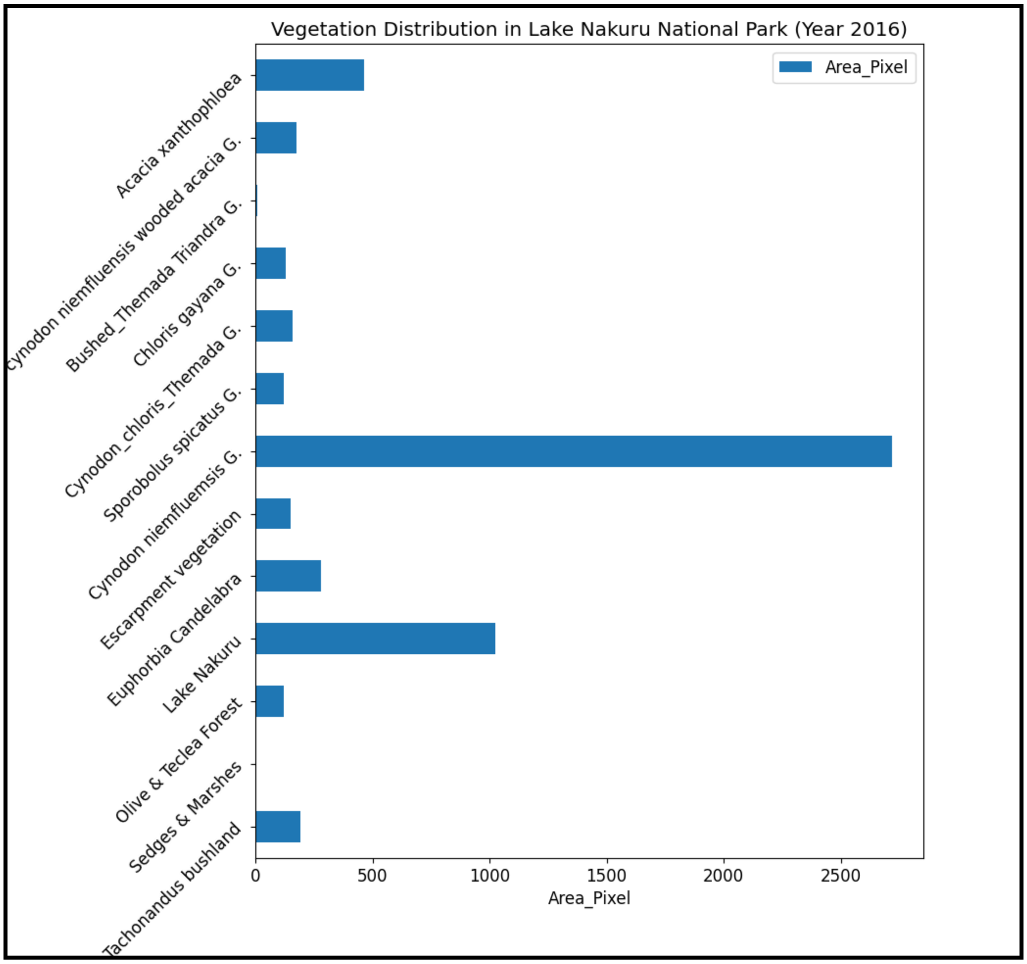

Figure 4.8: Spatial Distribution of Land Cover classes in Lake Nakuru Park (year 2016)

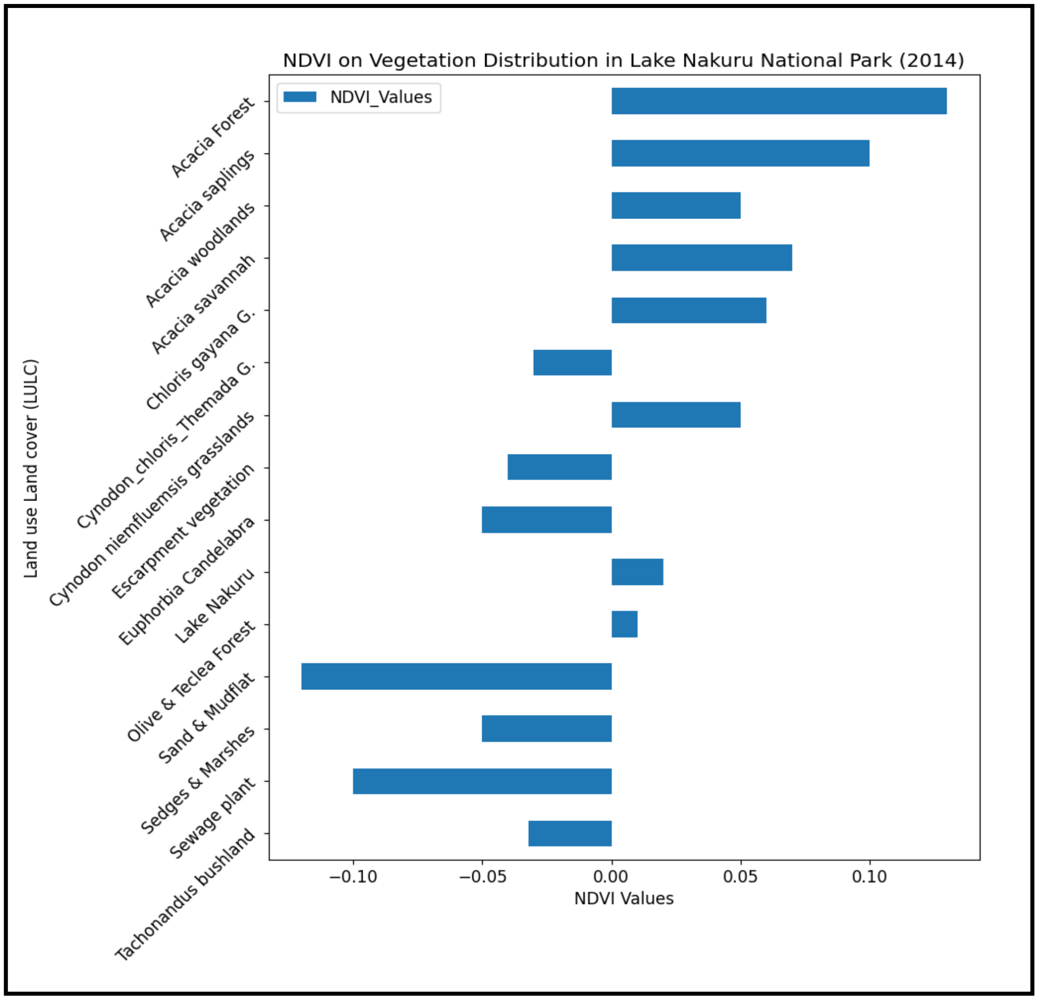

Figure 4.9: NDVI of Land Cover classes in Lake Nakuru Park (Year 2014)

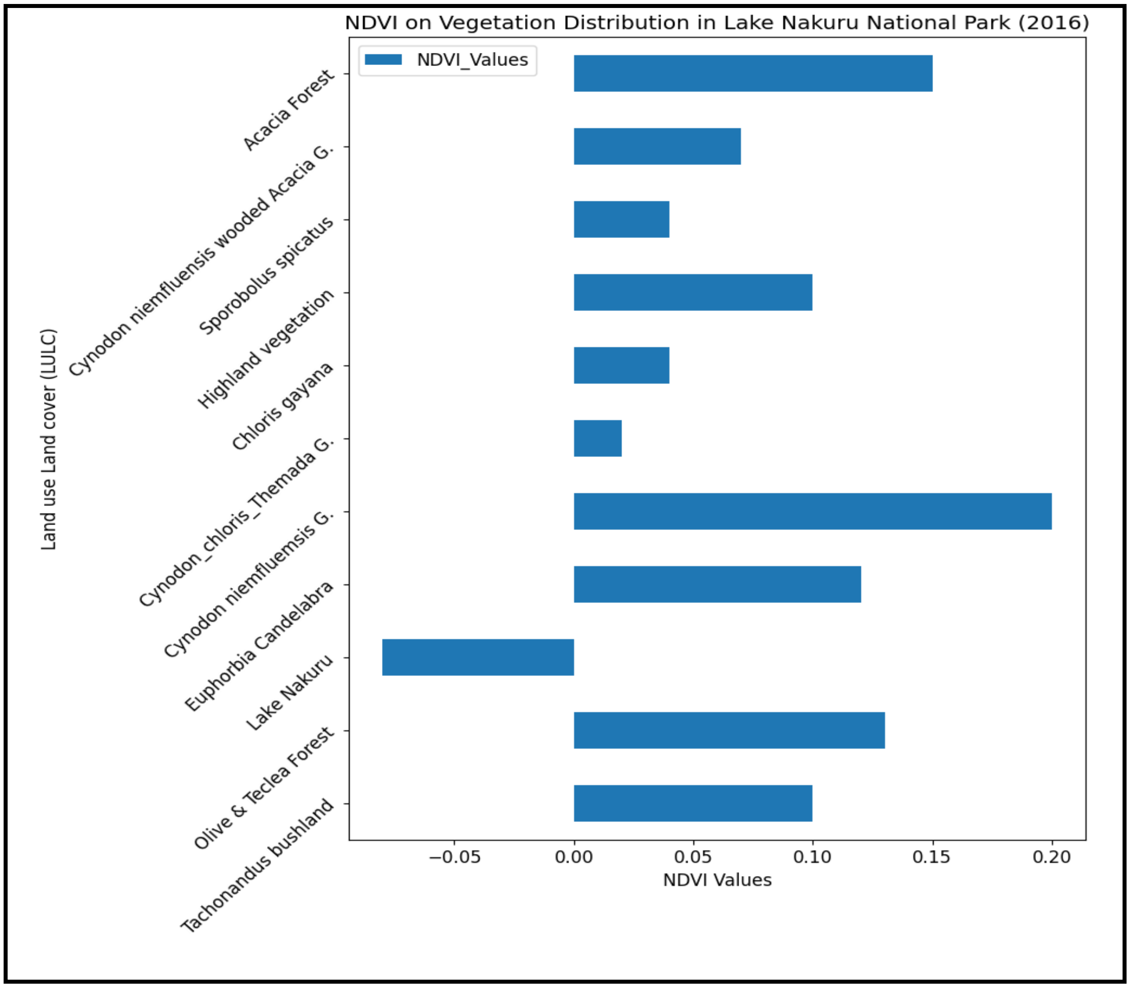

Figure 4.10: NDVI of Land Cover classes in Lake Nakuru Park (Year 2016)

Table 4.5: Accuracy Assessment results based on Lake Nakuru Land Cover distribution (2011-2016)

Classifier	Random Forest	Random Forest	Random Forest	Tree J48	Tree J48	Tree J48	SMO	SMO	SMO	Naïve Bayes	Naïve Bayes	Naïve Bayes
Approach	Cross-validation (10-fold)	2/3-1/3 train-test	Full Training	Cross-validation (10-fold)	2/3-1/3 train-test	Full training	Cross Validation (10-fold)	2/3-1/3 train-test	Full training	Cross Validation (10-fold)	2/3-1/3 train-test	Full training
Landsat 5TM-2011	0.99	0.99	1.0	0.99	0.99	1.0	0.76	0.76	0.76	0.82	0.80	0.86
Landsat 8OLI-2014	0.69	0.67	1.0	0.65	0.63	0.9	0.63	0.62	0.63	0.57	0.55	0.57
Landsat 8OLI-2016	0.73	0.73	1.0	0.71	0.69	0.92	0.62	0.62	0.62	0.55	0.71	0.71

Table 4.6: Kappa statistics rating criteria by Landis and Koch, 1977

S/No	Kappa statistics	Strength of Agreement
1	<0.00	Poor
2	0.00-0.2	Slight
3	0.21-0.4	Fair
4	0.41-0.6	Moderate
5	0.61-0.8	Substantial
6	0.81-1.0	Almost Perfect

Table 4.7: The between groups (RF, NB, J48 & RF) One Way ANOVA results achieved from Landsat 5TM and 8OLI

ANOVA SUMMARY (Groups Random Forest, Naïve Bayes, J48 and Binary SMO)					
Source	**Degrees of Freedom (DF)**	**Sum of Squares (SS)**	**Mean Squares (MS)**	**F-Statistic**	**P-Value**
Between Groups	**3**	0.2770	0.0923	5.3308	0.0043
Within Groups	**32**	0.5542	0.0173		
Totals	**35**	0.8311			

CHAPTER FIVE

SPATIAL PROCESSING OF SENTINEL IMAGERY FOR MONITORING OF ACACIA FOREST DEGRADATION IN LAKE NAKURU RIPARIAN RESERVE

This Chapter is based on, Osio, A., Pham, M. T., & Lefèvre, S. (2020). Spatial Processing of Sentinel Imagery for Monitoring of Acacia Forest Degradation in Lake Nakuru Riparian Reserve. *ISPRS Annals of Photogrammetry, Remote Sensing and Spatial Information Sciences, 3*, 525-532.

Presented at the 2020 Congress of the **International Society for Photogrammetry and Remote Sensing,** held virtually in Nice, France, on 31st August -2nd, September, 2020.

ABSTRACT

Tree degradation in National Parks poses a serious risk to the birds and animals and to a larger extent the general ecosystem. The essence of forest degradation mapping is to detect the extent of damage on the trees over time, hence providing stakeholders with a basis for forest rehabilitation and intervention. The study proposes a workflow for detection and classification of degrading acacia vegetation along Lake Nakuru riparian reserve. Inspired by previous research on the use of Dual Polarized Sentinel-1 Ground Range Detected (GRD) data for vegetation detection, a set of six Sentinel-1 GRD and Sentinel-2 MSI of corresponding dates (2018-2019) were used. Our study confirms the existing correlation between vegetation indices derived from optical sensors and the backscatter indices from S1 SAR image of the same land cover classes. Factors that were used in validating the results include some comparisons between pixel wise and object-based classification, with a focus on the underlying segmentation and classification algorithms, the polarimetric attributes (VV+VH intensity bands) and the reflectance bands (NIR, SWIR & GREEN), the Haralick features (GLCM) vs. some geometric attributes (area & moment of inertia). Classification carried out on the temporal datasets considering geometric attributes and the Random Forest classifier yielded the highest Overall Accuracy (OA) with 94.25 %, and a Kappa coefficient of 0.90.

5.1 INTRODUCTION AND LITERATURE REVIEW

Wetlands are the most productive ecosystems hosting different types of insects, birds, and large mammals. Lake Nakuru being amongst the Kenya Rift Valley Lakes listed amongst wetlands of international importance hence needs to be preserved. On the shores of Lake Nakuru thrives Acacia Xanthophloea whose occurrence is associated with the high water table. Recently, the lake has been flooding its banks as shown in Figure.5.1, thus destroying the yellow barked Acacia whose leaves provide fodder for the Rothschild giraffe and its pod important feed for the Vervet monkeys in the Park (Onywere et al., 2013). Since the acacia provides a buffer against siltation in the lake, their degradation could be one amongst other reasons behind the flooding lake.

In order to monitor degrading wetlands, microwave sensors using radar technology are appealing since they capture ground information during the day and night independent of changing weather conditions (Woodhouse, 2017), conversely to the optical-based sensors. Quantifying the physical characteristics of the backscatter mechanism and relating it to the biophysical properties of vegetation canopies in relation to the radar signals can give leads to the health and structural condition of the riparian vegetation. The capability of backscatter σ° coefficient correlated to the angle of inclination at the time of capture have been used to give qualitative information about terrain features. Although wetland classification falls under land cover mapping, classes related to riparian reserve and their product utility for various applications still remain uncertain (Krankina et al., 2010). SAR-C polarimetric intensity bands (VV+VH) have been used in previous studies to map land use and land cover, and further in conjunction with Haralick features (Jardine et al., 2018) to map sea-ice-type (Liu et al., 2015) and in ice water discrimination

(Zakhvatkina et al., 2017). The main purpose of this study is to explore the capability of Sentinel-1 SAR-C polarimetric features in discriminating flooded riparian vegetation. We hypothesized that SAR-C band of Sentinel-1-time series stacks analyzed through their Haralick features could be a reliable solution for discriminating flooded vegetation along the degrading Lake Nakuru riparian reserve. Furthermore, following a recent study (Pham, Lefèvre, & Merciol, 2018) demonstrating the relevance of Attribute Profiles (APs) in relation to the Haralick features on optical images, we also hypothesized that these profiles can be used for SAR-C backscatter intensity bands to help discriminating the flooded vegetation classes. Finally, we also hypothesized that the OBIA framework could be successfully applied on temporal stack of Haralick features extracted from Sentinel-1 images in order to increase wetland classification accuracy.

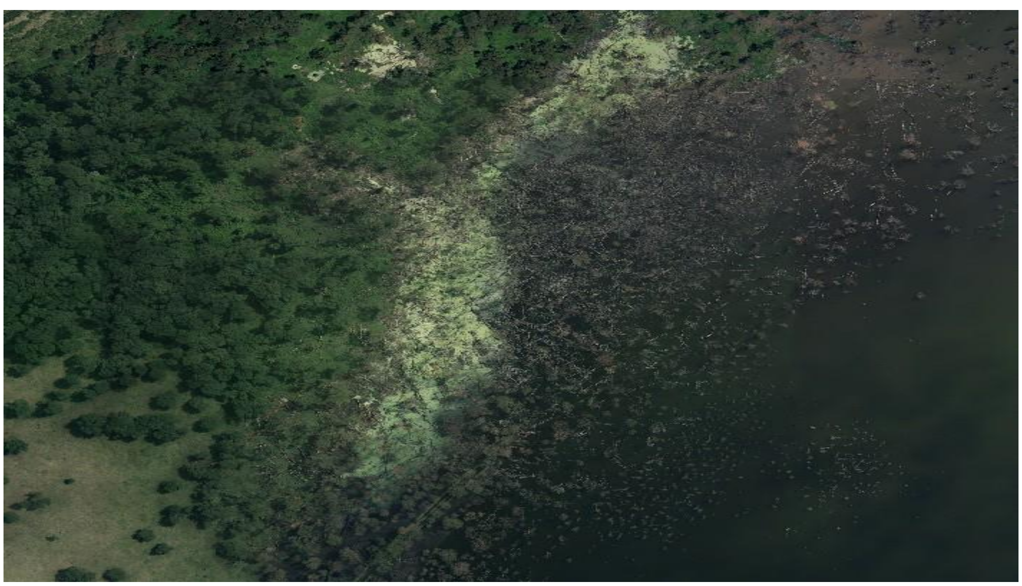

Figure 5.1**:** Aerial image depicting the flooding problem on the North-western part of Lake Nakuru. **Source**: Survey of Kenya

5.2 MATERIAL AND METHODS

5.3 DATA PRE-PROCESSING

In this study, we consider both SAR and optical images provided by S1 and S2 missions respectively, considering the following acquisition dates: 26/05/2018, 25/07/2018, 10/11/2018, 12/12/2018, 02/02/2019, 05/05/2019 and 13/08/2019 for S 1;27/05/2018, 16/07/2018, 23/11/2018, 12/01/2019, 02/05/2019 and 10/08/2019 for S2. All the data were in the same datum and projection i.e. WGS 84 / UTM Zone 36N.

5.3.1 Sentinel-1 data pre-processing

Raw S1 time series data acquired in different seasons (i.e., both rainy and dry seasons) in the years 2018 and 2019 were imported into the ESA open-source software SNAP, with the following pre-processing steps: i) Application of the orbit file on each single date Sentinel-1 in order to provide accurate satellite orbit position and velocity into the processing chain. ii) Thermal noise removal application provided a look up table into the chain to enable the elimination of noise from the SAR imageries mainly caused by the background energy from the Satellite receiver.

iii) Radiometric calibration converted the Intensity VV+VH bands into decibel units. iv) Lee sigma 7*7 Speckle filter (Lee et al., 1999) for the purpose of removing speckles (salt and pepper) effects initially caused by coherent interactions during image capture. v) Terrain correction converted the back-scatter indices from Terrain to Ground Range using an auto-downloaded DEM (STRM 3 sec) with the terrain pixels resampled to 10*10 meters ground resolution using bilinear convolution. The importance of this application was to normalize the back-scattered rays which were affected by the nature of the terrain. vi) Importing a (ROI) shape file that subsets the region of interest from the larger image. vii) Application of the land-sea mask to the ROI in order to mask out the smaller Area of Interest which is target of the study. viii) Appending texture according to Haralick features namely GLCM Mean, Variance and Contrast into the processing chain.

ix) Apply the band merge which incorporates all the selected Haralick features into one single stack of Sentinel-1 dataset. The imageries that lacked orbit information were earlier removed from the original sets of selected Sentinel-1 data. The whole process chain took 28.3 minutes to run with a batch-processor in SNAP version 7.0 (ESA, 2018) using a computer with the following specifications: Intel CORE 17-6700CPU @ 3.40 GHZ with a memory of 15.6GB. Modelling SAR backscatter indices (Kaplan & Avdan, 2018c) for their use on riparian vegetation requires conversion of VV and VH bands into decibel units, i.e. $\sigma_{db} = 10 \log_{10}(\sigma^{\circ})$, where σ° and σ_{db} are respectively the digital number values and the backscattered values (in dB).

5.3.2 Extraction of Attribute Profiles

Among a great number of spatial-spectral feature extraction techniques applied to pixel-level classification of remote sensing data, morphological attribute profiles (APs) have been widely exploited thanks to their capacity to model multilevel spatial information of the image content (Mura et al., 2010), (Pham, et al., 2018) . By well preserving significant spatial properties of regions and objects such as contours, shape, etc., APs become effective to characterize the contextual information of the observed scene, hence relevant for a classification purpose. Following the recent suggestion from for optical imagery, we replace the extraction of GLCM textural features with AP extraction for better characterization of structural and textural information within the observed zones from S1 intensity images after the above pre-processing step (Pham et al., 2018a).

The generation of APs from an image can be summarized as a four-step process: 1) construct a morphological hierarchy (a.k.a. tree) from the image; 2) compute some relevant attributes (area, moment of inertia, standard deviation, and so on) from each region associated with each node of the tree; 3) filter the tree by keeping/removing nodes according to their attribute values; and 4) reconstruct the image from the filtered tree. Steps 3) and 4) can be done for different attributes (with different threshold values) to finally produce a set of filtered images (by stacking them) to form APs.

5.3.3 Sentinel-2 data pre-processing

Beyond S1 data, we also rely on Sentinel-2 Multispectral Imagery for the purpose of training polygon extraction to be used in the corresponding S1 classification (Kaplan & Avdan, 2018b). The SNAP toolbox is also exploited to pre-process raw S2 data. Raw data of corresponding Sentinel-2 Multispectral Imager (MSI) collected from Copernicus data hub (https://scihub.copernicus.eu/dhus/home) were preprocessed for the purpose of training polygon extraction to be used on the Sentinel-1 classification. The raw Sentinel-2 datasets were atmospherically corrected independently using Sen2cor Processor that applies atmospheric corrections on the raw Sentinel-2 dataset. This processor was earlier installed as a plugin tool from the SNAP library and played the role of converting the Sentinel-2 raw bands from Top of the Atmosphere reflectance to Bottom of the Atmosphere reflectance. Cloud masks were then created for each single date S2 image using a conditional statement within the band-math tool in SNAP toolbox. Cloud masks were thus retrieved from each atmospherically corrected Sentinel-2 image in relation to each of the three band spatial resolutions of 10, 20 and 60. The masks were then saved as virtual bands with other bands of interest in this study i.e., Band 3 (Green), Band 8A (NIR), Band 11 (SWIR) and Band 12 (SWIR). Seven sets of natural color imageries, each of band combination (8A, 11, 12), were resampled independently using Sentinel-2 MSI band 3 (10m resolution) using nearest neighbor re-sampling algorithm in ESA SNAP tool version 7.0 for Sentinel-2 processing. After resampling each of the imagery, they were then re-projected to WGS'84 using WGS'84 Automatic tool in SNAP version 7.0. After resampling all the S2A imageries, each image was uploaded in the subset extraction window in SNAP. The extent of the specific area of interest with regard to this study was extracted using geo-coordinates as follows; North Latitude bound (-0.307), West Longitude bound (36.053), South Latitude bound (-0.343) and East Longitude bound (36.098). The specific area was on the North-Western area where part of the lake with massive damage of trees on the lake riparian has been observed in recent times.

5.4 DATA ANALYSIS

Once both S1 and S2 image time series are pre-processed, we conduct a data analysis procedure that makes use of both sources as follows.

5.4.1 Sentinel-1 data analysis

From the pre-processed S1 products were derived eight bands per date: σ(VV), σ(VH), σ(VV) mean, σ(VV) contrast, σ(VV) variance, σ(VH) mean, σ(VH) contrast and σ(VH) variance. Stack averaging was then performed for each band, allowing to project all temporal information into a single, representative image. We then apply a supervised Random Forest algorithm to classify the wetland classes on the NW part of Lake Nakuru wetland. Due to the dynamism of the lake riparian reserve, training polygons to be used for the classification were derived from S2 data of the corresponding S1 image of the same month (see next subsection). The reference images used for validation come from some high spatial resolution (~50cms) aerial images captured in 2015 on which visual mapping was achieved.

5.4.2 Sentinel-2 data analysis

For the S2 images, we extract training polygons by relying on color composition (RGB band combination: 8A, 11, 12) as suggested by (Kaplan & Avdan, 2018b). Furthermore, to ease visual assessment, we also derived spectral indices i.e., Normalized Burnt Ratio Index (NBR) and Normalized Difference Water Index (NDWI) values, since the study area is a wetland. These additional bands allow us to get a clear map or image of the study site (see Figure.5.3) which can be subsequently used as a reference image for each corresponding classified S1 image. We recall that NBR and NDWI are computed as follows:

$$NBR = \frac{B8A - B12}{B8A - B12} \ldots\ldots\ldots\ldots\ldots\ldots\ldots\ldots\ldots\ldots\ldots\ldots\ldots\ldots\ldots\ldots\ldots\ldots\ldots\ldots. 5.1$$

$$NDWI = \frac{B3 - B8A}{B3 - B8A} \ldots\ldots\ldots\ldots\ldots\ldots\ldots\ldots\ldots\ldots\ldots\ldots\ldots\ldots\ldots\ldots\ldots\ldots\ldots\ldots. 5.2$$

The main reason for using NBR and NDWI indices was to distinguish between the dry land and the flooded areas.

In order to investigate the correlations between S1 reflectance values (σ_{db}) in dB and the NBR reflectance values on the various wetland classes, a correlation analysis was conducted. The cross-correlation analysis derived from the time series data on Table 5.1 and results of inter-class correlations measured with Pearson's correlation coefficient are shown on Table 5.2 where relationships between the backscatter index (Borah et al., 2018) σ_{db} (VH) from Sentinel-1 and the NBR reflectance from Sentinel-2 are emphasized.

The NBR values for each corresponding date and land-cover class were derived from the SNAP toolbox during image post-processing. Vegetation reflects more in the Near Infrared (NIR) section of the electromagnetic spectrum but less in the Short-Wave Infrared (SWIR) region and thus the NBR mostly used for pre-fire and post-fire studies can also be used to measure the health of the trees or vegetation in general. According to previous studies, higher NBR values indicate healthy vegetation while low NBR values indicate degraded one.

5.5 RESULTS

Our study exploited S1 and S2 data to characterize the condition of the degrading Acacia Forest along Lake Nakuru National Park and further used SAR backscatter coefficient σ_{db} (Borah et al., 2018) to map the effect of SAR returns on the Acacia xanthophloea spp. To the best of our knowledge, no studies have used SAR backscatter indices in discriminating the condition of tree degradation along Lake Nakuru riparian reserve (Chen et al., 2020). Our research aims at addressing the following knowledge gaps:

1) Identify a robust and reliable method that can be used in tree condition and health detection especially on Acacia Xanthophloea strands along Lake Nakuru riparian reserve.
2) Produce clear and reliable mapping products validated using up-to-date temporal reference maps and machine learning approaches.
3) Explore the capability of σ_{db} (VV) and σ_{db} (VH) backscatter and their Haralick features in detection of the condition of Acacia trees along Lake Nakuru riparian reserve (Borah et al., 2018).
4) Explore the capability of the morphological attribute profiles in the discrimination of wetland classes along Lake Nakuru riparian reserve.

In the sequel, we address these questions in some dedicated subsections.

5.5.1 Characterization of condition and health of Acacia Xanthophloea using Sentinel 1-time series datasets

The NBR values emanating from SITS captured between May 2018 (0.76) and May 2019 (0.42) revealed that the yellow barked Acacia have been degrading. To characterize the health of the riparian vegetation, S1 SAR time series with the C-band were used as shown by previous studies.

Tree condition and health were characterized by generating the spectral signatures and the backscatter indices σ_{db} (VV) and σ_{db} (VH) as shown in recent studies by Chen et al., (2020). Figure 5.5 shows the capability of the backscatter indices for detecting the condition and health of riparian vegetation along the flooding lake. The land-cover backscatter returns from the highest to the lowest were captured as urban, non-degraded forest, degraded forest, degraded submerged forest, and lastly Lake Nakuru. High backscatter response from the urban class was due to double bounce scattering inherent in built up areas. Specular reflectance from Lake Nakuru caused low backscatter response as shown by previous research (Mahdavi et al.,2018). The backscatter indices (Chen et al., 2020) i.e.σ_{db} (VV) and σ_{db} (VH) had the capability of detecting four classes: degraded submerged forest, degraded forest, non-degraded forest and urban. Tree strands consist of crown and the bark.

Ground observation revealed massive destruction involving the degrading trees (see Figure 5.1), where some of the trees have dried up and standing while others had fallen off the ground. The backscatter response of tree trumps which falls under degraded submerged forest class were captured both in σ_{db} (VV) and σ_{db} (VH) polarization modes (see Figure 5.4). According to previous studies (Richards et al., 1987), the backscatter response emanating from the water surface undergoes double bounce phenomena to and from the flooded vegetation which in this case consists of dead tree trunks in water. Finally, the backscatter signals are relayed back to the antennae of the SAR instrument. The degraded forest and urban classes were captured in VV polarization mode, non-degraded forest was best captured in VH polarization mode since healthy tree strands experience volume scattering on the tree crown and double bounce from their bark. It is known that the backscatter response can be captured from vegetation only in the early phenological stages. Acacia xanthophloea strands on the riparian reserve are mature trees that have been in existence for many years. The backscatter response patterns as observed in (Santos et al., 2021) were evident in this study as shown on Figure 5.5 where the increase in backscatter response signals was observed at growing levels for the open water (OW), dry land (DL) and flooded vegetation (FV). However, according to (White et al., 2015) the patterns are influenced by several factors such as radar wavelength, polarization, angle of incidence, open water surface roughness, topography, vegetation type and phenology.

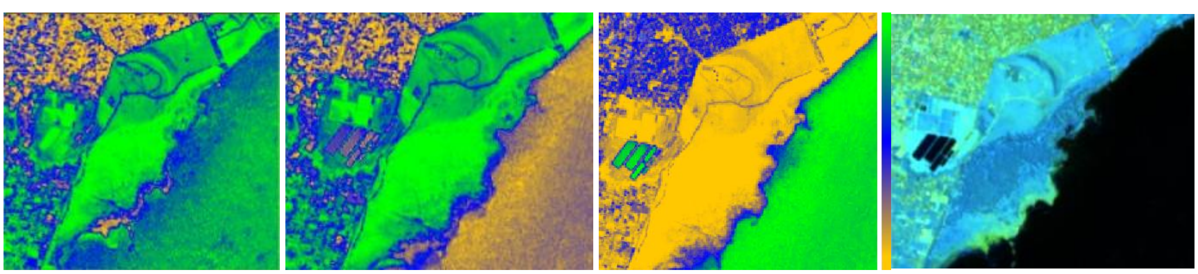

Figure 5.2: Spectral indices on Sentinel-2 (10/08/2019): Left to Right: NBR, NDWI (NDWI-NBR) and Sentinel-2 MSI natural image (spectral bands 12, 11 and 8A).

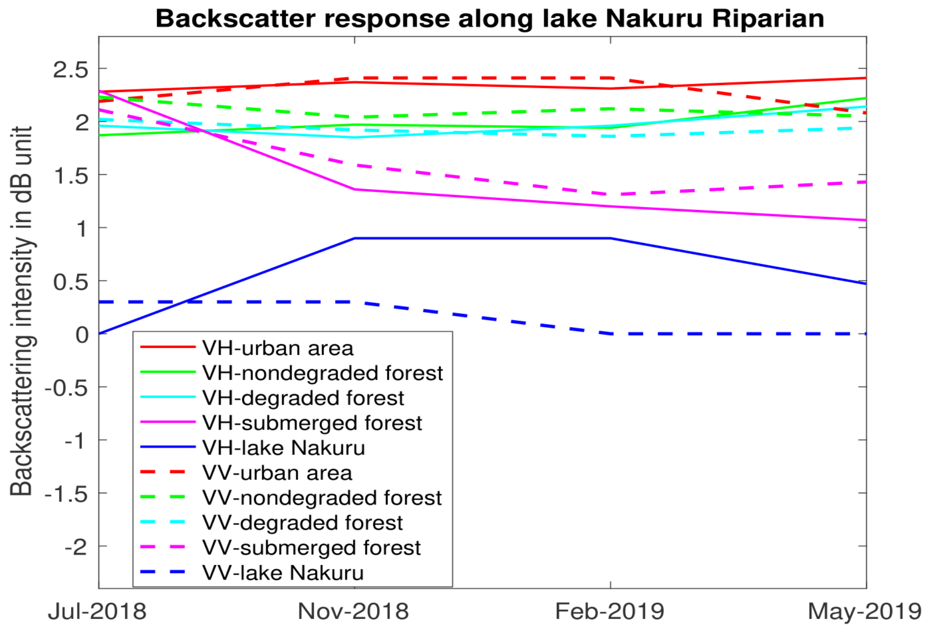

Figure 5.3: Time series of Sentinel-1 backscatter coefficient

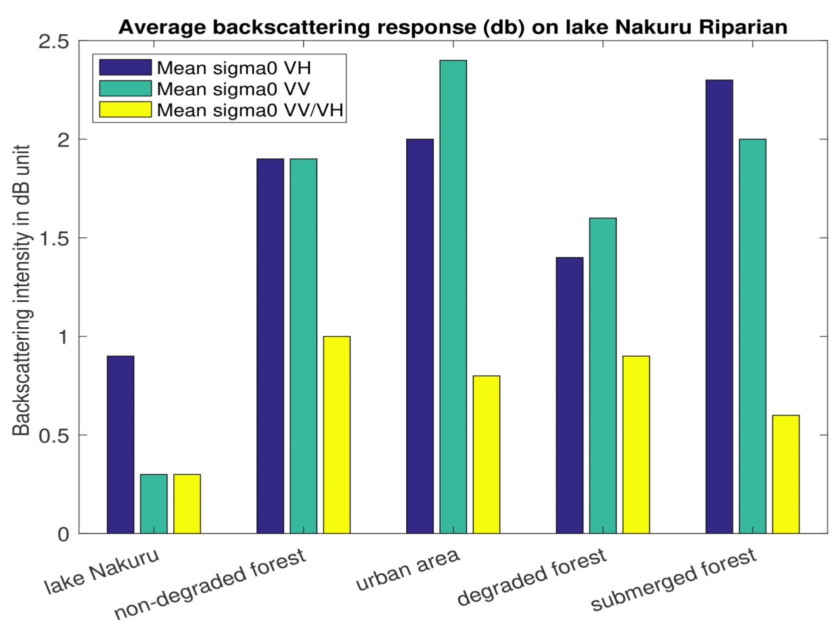

Figure 5.4: Average backscatter σ_{db} response on Lake Nakuru Riparian classes**.**

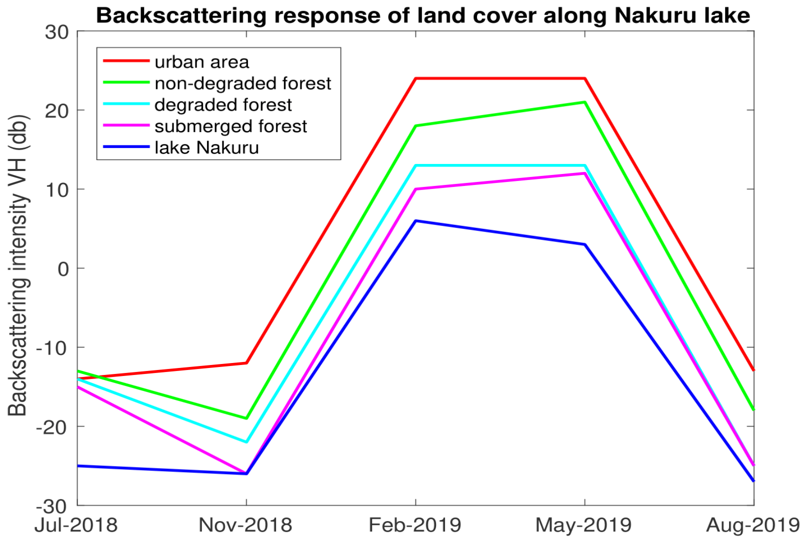

Figure 5.5: Time series of the backscatter response (db.) on riparian land cover classes

Table 5.1: Time series backscatter response from Sentinel-1 (σ_{db}(VH)) and spectral values from Sentinel-2 (NBR).

Date	S1 Lake	S1 Forest non deg	S1 Deg sub forest	S1 Deg forest	S1 Urban	S2 (NBR)
July, 2018	-14	-15	-25	-14	-13	0.69
Nov, 2018	-12	-26	-26	-22	-19	0.60
Feb, 2019	24	10	6	13	18	0.5
May, 2019	24	12	3	13	21	0.42
Aug, 2019	-13	-25	-27	-25	-18	0.66

Table 5.2: Synergy between Sentinel-1 (σ_{db}(VH)) and Sentinel-2 (NBR).

Correlations	S1 Lake	S1 Forest non deg	S1 Deg sub forest	S1 Deg forest	S1 Urban	S2(NBR)
S1 Lake	1.0					
S1 Forest non deg	0.964	1.0				
S1 Deg sub forest	0.996	0.975	1.0			
S1 Deg forest	0.971	0.996	0.983	1.0		
S1 Urban	0.988	0.993	0.990	0.991	1.0	
S2(NBR)	-0.933	-0.854	-0.901	-0.868	-0.902	1.0

Ground observation revealed massive destruction involving the degrading trees, where some of the trees have dried up and standing while others have fallen off the ground. The backscatter response of tree trumps which falls under degraded submerged forest class were captured both in σ_{db} (VV) and σ_{db} (VH) polarization modes.

5.5.2 Production of reliable mapping products validated using up-to-date temporal reference maps and machine learning approaches

In this section, the Sentinel-1 capability in the classification of riparian vegetation classes was tested. In order to determine the effect of Haralick features on classification accuracy, the inclusion of the Haralick features in VV and VH SAR intensity bands was embraced. Object-based and pixel-wise supervised classification were carried out on the different datasets as follows:

1) The test dataset was a Very High Resolution imagery (VHR) at 10-cm spatial resolution captured in the year 2015 when the lake was already flooding its banks (Figure 5.1). Sample-based classification was carried out to produce four classes namely degraded acacia, degraded submerged acacia, non-degraded acacia, and Lake Nakuru. Multi-resolution segmentation was appended, setting scale parameters at scale 73, shape 0.6 and compactness 0.8. In order to promote class separation, four Haralick features were appended namely GLCM-Mean, GLCM-Contrast, GLCM-Homogeneity and GLCM-Correlation. The user-defined test dataset was processed using Random Forest yielding 99.7%, Multi-Layer Perceptron 91.6%, and Binary Support Vector (SMO) at 75% accuracy respectively.
2) The second test dataset was made of 8 pre-processed S1 Ground Range detected (GRD) imagery and their corresponding Haralick features captured between May 2018 and August 2019. The images of different temporal dates were combined to form a single stack image consisting of 32 master and slave images. Stack averaging was performed giving rise to an image with eight features. Super-pixel segmentation (SLICO) with minimum region size of 25 was used. For further class refinement, a spectral difference segmentation at scale 10 was applied in order to create distinct boundaries between classes. Classification accuracy yielded the following results: Random Forest 82.3%, Multilayer Perceptron 80.3%, and Binary Support Vector (SMO) 76.6% respectively.
3) Pixel-wise supervised classification was carried out on three datasets which consist of Sentinel-1 Level-1 Ground range (GRD) detected of VV and VH intensity bands. The Haralick features included in the classification were GLCM-mean, GLCM-contrast and

GLCM-variance hence giving rise to a total of 8 bands per each image. Random Forest (500 trees) classification was used with 5000 samples used for training and 500 samples for validation. This procedure was carried out in ESA SNAP environment. The Overall Accuracy (OA) achieved from the classified image of the study area captured on July 2018 was 96%, November 2018 94% and May 2019, 95% respectively.

4) Supervised object-based classification on lake riparian classes was done using a different approach. Since the riparian classes were dynamic due to the persistent flooding, S2 images of the corresponding S1 SAR images were used in collection of training sets as demonstrated from recent studies by (Kaplan & Avdan, 2018c) while the in-situ dataset was a VHR aerial imagery of 10cm ground resolution (Figure 5.1). Random Forest classification appended on three S1 datasets captured in February 2019, May 2019 and August 2019 yielded overall classification accuracy of 89.2%, 87.9%, and 94% respectively (Table 5.3).

5.5.3 Exploring the capability of σ VV+VH polarimetric indices and their Haralick features in the detection of condition and health of Acacia xanthophloea along Lake Nakuru riparian reserve

S1 polarimetric features are suitable for the detection of riparian vegetation classes along Lake Nakuru riparian reserve. This can be observed in Table 3 with Random Forest classification results of 87.7%, 84.93% and 92.45% for the 3 dates. Furthermore, incorporating the Haralick features improved by 1% to 3% the classification result. This improvement is consistent for all images, leading even to a 93.95% overall accuracy.

5.5.4 Exploring the capability of Attribute Profiles in the discrimination of wetland classes along Lake Nakuru riparian reserve

The final objective of this study was to investigate the capability of engaging attribute profiles derived from the 8 bands coming from Sentinel-1 SAR imagery and compare the results with different datasets and different attributes. The eight bands included σ_{db}(VV), σ_{db}(VH), σ_{db}(VV) GLCM-mean, σ_{db}(VV) GLCM-variance, σ_{db}(VV) GLCM-contrast, σ_{db}(VH) GLCM-mean, σ_{db}(VH) GLCM-variance, and σ_{db}(VH) GLCM-contrast.

Attribute profiles were derived from these 8 bands and used in the classification of Lake Nakuru riparian reserve, mainly on the North Western part where flooding has caused tree degradation. Visual comparison between Haralick features and AP is given in Figure 5.6. The results of the classification using Random Forest algorithm are shown in Table 5.3. The overall accuracy (OA) reached 90.88%, 90.48% and 94.25% for the 3 dates. It was obtained using the self-dual APs with two geometric attributes including area and moment of inertia. Manual setting of attribute thresholds has been done based on the spatial resolution of Sentinel-1 images.

Four thresholds were set for each attribute: λ_a=100, 500, 1000, 5000for area and λ_i = 0.2, 0.3, 0.4, 0.5 for moment of inertia, following the parameter setting guide provided in (Pham et al., 2017), (Pham, Lefèvre, & Aptoula, 2018). The generation of APs was performed on each band of VV and VH, then all profiles were stacked to form the AP feature vector and perform Random Forest classification.

Table 5.3: Comparative results

Approach	02/02/2019			05/05/2019			13/08/2019		
	OA	AA	kappa	OA	AA	kappa	OA	AA	kappa
Intensity	87.76%	72.77%	0.7917	84.93%	69.17%	0.7918	92.45%	76.97%	0.8699
GLCM	89.22%	75.42%	0.8159	87.89%	73.58%	0.7958	93.95%	82.55%	0.8962
AP	90.88%	78.18%	0.8435	90.48%	76.98%	0.8362	94.25%	85.40%	0.9019

5.6 DISCUSSION

The study demonstrates how Sentinel-1 backscatter coefficient σ_{db}(VV) and σ_{db}(VH) can be used to characterize wetland degradation. While it is well-known that SAR polarimetric analysis of electromagnetic waves enables discrimination of different scattering mechanisms emanating from the ground, we have found σ_{db}(VV) and σ_{db}(VH) to be less sensitive to the scattering mechanisms (+0.9db) emanating from Lake Nakuru riparian mainly because Acacia xanthophloea are mature trees that have been in existence on the riparian reserve for a long time. It was worth noting that the SAR C-band response in the σ_{db}(VH) was sensitive to moisture content in the leaves of the healthy trees as captured in the peak season (June, 2019) when average rainfall distribution was at its peak in the study area (Figure 5.5) as captured in previous research (Koppe et al., 2013).

The backscatter σ_{db}(VH) had the lowest average response on class Lake Nakuru (+0.3) in σ_{db}(VV). This was confirmed by existing studies (Muster et al., 2013) that report small lakes reduce the backscatter response due to their smooth surfaces. The degraded submerged forest had equal average backscatter response (+1.9 db) in σ_{db}(VV) and σ_{db}(VH), as shown on Figure 5.4. This part of the wetland consists of dead and semi-dead biomass lying on the mudflats on the riparian reserve. SAR-C polarimetric electromagnetic waves have short wavelengths i.e. ~5.0cms and hence are unlikely to penetrate through the biomass and only represent a few centimeters of signals emanating from the surface of the degrading biomass, thus excluding the response from the wet soils beneath the mass. Another aspect which could contribute to the higher average backscatter was the presence of biomass in open water (Lake Nakuru), meaning that the response was a mixture of specular reflectance from the open water and double bounce from the biomass in water (degraded-submerged forest) as confirmed by previous studies by Santos et al., 2021. From the class forest degraded, the highest average backscatter response (+1.6) was achieved by σ_{db}(VV). Most of the biomass was in class degraded submerged, hence the difference in backscatter response between the class degraded submerged and forest degraded. This report corroborates with previous studies stating that low biomass presence on wetlands caused low backscatter response while higher volumes of biomass caused higher backscatter response.

Forest non-degraded class which consisted of healthy acacia xanthophloea had the highest average backscatter response σ_{db}(VH) of value +2.3db which was higher than the previous classes i.e., forest degraded and degraded submerged, hence confirming reports that the dynamic range of the cross-polarized VH component renders it suitable for measuring the backscatter mechanisms of vegetation. Due to the short wavelength inherent in Sentinel-1 SAR C (~5.0cms), volume scattering occurs on the tree crowns without penetrating the understory vegetation (Nairn & Brisco, 2004).

The highest mean backscatter σ_{db}(VH) (+2.4db) emanated from the urban class that has double bounce response due to the buildings in the neighboring Nakuru Town. Limitations on the backscatter response can be pointed out on the fact that the values were obtained from user defined polygons from each class, meaning that the values vary across different sites on each class. Future research should engage collection of backscatter values across each class. However, accessibility to different parts of the affected areas is difficult and thus in-situ data from a Very High Resolution aerial imagery at 10cm (see Figure 5.1) ground distant resolution was used. The baseline aerial image at GRD of 10cm was used as input of a multiresolution segmentation with subsequent classification with Random Forest, yielding 99.7% accuracy. This was due to the fact that VHR imageries have distinct class boundaries.

The averaged stack of 32 master and slave imageries yielded 82.3% overall accuracy. These results could have been influenced by the number of training instances, as well as the number of trees used in the parameterization; 100 trees yielded 100% overall accuracy on the dataset and hence the number of trees that was set was 30 with the main aim of dealing with overestimation issues. The effect of SAR-C polarimetric intensity bands on classification accuracy was tested. It was worth noting that pixelwise Random Forest classification of Sentinel 1 SAR-C dataset considering VV, VH, and ratio yielded a high overall accuracy of 92.45% on the August 2019 image of the study area. Stacking Haralick features on the intensity bands namely GLCM-mean, GLCM-contrast and GLCM-variance improved the classification on the same image by 1.5% meaning that engaging the GLCM-Haralick feature bands contributed slightly to the improvement of classification accuracy.

A further slight improvement of classification accuracy at 1.8 % was noted when Attribute Profiles were extracted from the Sentinel-1 bands. The highest commission error was noted with class degraded forest considering both the Haralick and attribute profile-based classification. This could have been due to the fact that the degraded forest class lies in the middle of classes degraded submerged forest and the non-degraded forest, thus causing confusion between class boundaries. Pixelwise Random Forest on the single date (8 bands, VH, VV and their respective 3 Haralick features) yielded higher 94.0% overall accuracy. Attribute profile-based classification by Random Forest working on 62,067 instances and 200 trees yielded 94.25% overall accuracy.

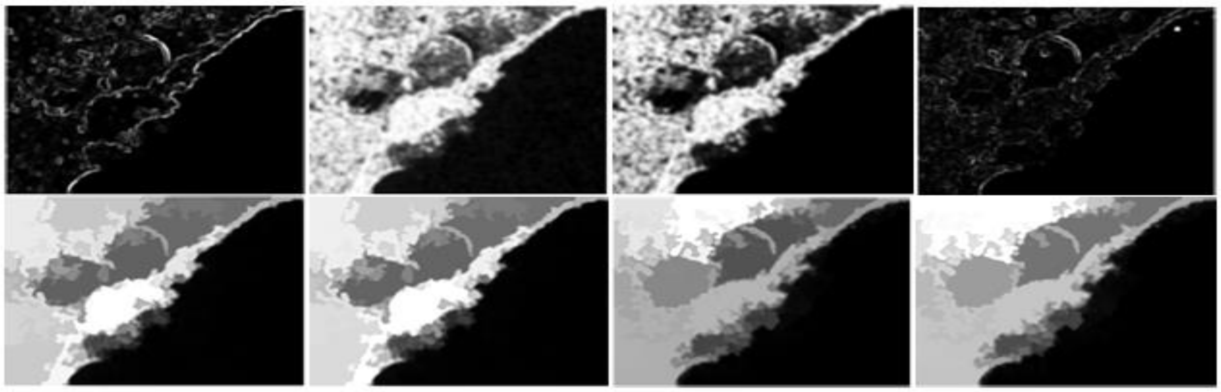

Figure 5.6: An Illustration of Haralick textural features (top line) produced by GLCM method and Multi-level AP features (bottom line)

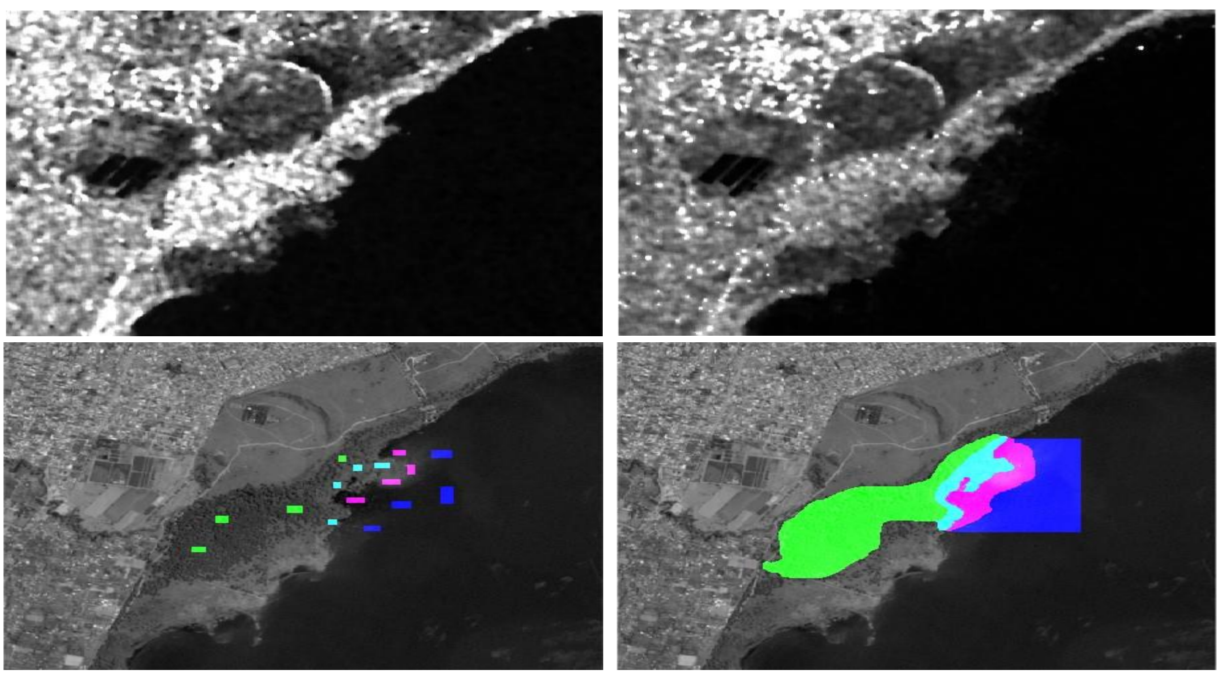

Figure 5.7: Sentinel-1 VV and VH images (13/08/2019) on the studied area (filtered by 7* 7 Lee filter) together with the train and validation sets (shown on the corresponding Sentinel-2 image). Color codes: Green: healthy forest; Cyan: damaged forest; Magenta: submerged tree, Blue: water.

5.7 CONCLUSION

This study demonstrates how Sentinel-1 Synthetic Aperture Radar (SAR-C) imagery, Ground Range Detected (GRD) with a wavelength of ~5cms can be incorporated with Haralick features to discriminate wetland classes along the North Western part of Lake Nakuru riparian reserve. Identifying the various classes and confirming their different backscatter response across different polarimetry opens up new perspectives on their response to vegetation health and structures. The Sentinel-2 datasets corresponding to the Sentinel-1 datasets were helpful in providing training polygons used for the Haralick and Attribute-Profile-based feature extraction and classification, hence avoiding errors due to the dynamism of the flooding lake over time. The highest classification accuracy received from the different datasets came from the attribute profiles at 94.25%. However, there was no significant difference between the Haralick features (93.95%) and the outcome of the Attribute Profiles. Haralick features embedded on the Synthetic Aperture Radar SAR-C bands could have some limitations due to the short wavelength associated with the electromagnetic spectrum (EMS).

Future research should explore the capability of radar imagery with longer wavelengths such as the L-band to collect the backscatter response values from the wetland classes. Application of OBIA on Attribute Profiles should also be tested in future. Decomposition of quad-polarized Synthetic Aperture Radar polarimetric bands could give leads to structure of the biomass along Lake Nakuru riparian. Given the heterogeneous nature of the study area in comparison with the level of accuracy achieved in this study, we can conclude that the procedures and attributes used in this study could be also used elsewhere where the landscapes are similar.

CHAPTER SIX:

OBJECT BASED SPATIO-TEMPORAL ANALYSIS ON ACACIA FOREST DEGRADATION BY PHENOLOGY ALONG LAKE NAKURU WETLAND, KENYA.

ABSTRACT

Seasonal patterns captured from terrain feature phenology provides information about forest degradation and disturbances. The main aim of this study was to find out if vegetation phenology could be used to study the effects of flooding on the acacia degradation along Lake Nakuru riparian reserve. We compared the phenological parameters of degraded, non-degraded and degraded submerged forest derived from 68 Landsat 7 ETM+ Time series of NDVI data on the North Western part of Lake Nakuru National Park, Kenya from 2008-2017. Use of different softwares in the workflow was necessary since tools inherent in particular software was not available in other softwares. NDVI of Landsat 7 ETM+ time series were pre-processed using ORFEO band math tool and post-processed in the user developed python code (OBIATS.py). The data was later transmitted to QGIS version 3.4 to enable extraction of OBIA Time series using shape files of segments were derived from SLIC-K means algorithm in GRASS GIS environment. The Object-based times series of datasets for each class were filtered in TIMESAT 3.3 software using a 4*4 window Savitsky Golay filter algorithms in order to remove noise from the data. The phenological parameters used in the detection of forest degradation include start of the Season and end of the Season (SOS), Length of the season (LS), Peak value, Base value (BV) and Small Integral values (SI), and were extracted from each land cover. The non-degraded forest exhibited the higher NDVI values across all seasons compared to the NDVI values captured in the degraded and degraded submerged forest categories. The highest base value was captured in one season due to bush and thicket regeneration. The OBIATS.py code was able to provide 68 Landsat 7 ETM+ based NDVI time series in 7 seconds within a 15G.GB RAM computer environment, hence providing a robust method of time series data clustering. Sentinel-2 NDVI time series exhibited a stable distribution across the three seasons that were captured. A strong positive correlation of determination atR^2 = 0.84 was noted between length of the season and the base value, meaning that Sentinel-2 NDVI temporal profile could provide a suitable option in capturing vegetation health assessment. Regression analysis carried out between the base values of Landsat 7 ETM+ phenological parameters against Sentinel-2 base values yielded a correlation of determination value of $R^2 = 0.95$ meaning that Landsat 7 ETM+ and Sentinel-2 MSI phenology metrics are suitable for forest degradation studies.

6.1 INTRODUCTION AND LITERATURE REVIEW

Optical Remote sensors using aerial and satellite imageries such as Landsat and Sentinel-2 provide a good basis of vegetation ecosystem studies such as agriculture, urban tree strands and forests in general. Through these images, variables such as pattern, texture, size, shape, tone and association in forest studies could be derived to give information of distribution of forest species and their state of health. Flooding along riparian reserves can cause forest strands damage through the process of waterlogging hence affecting the leaf nutrient concentration which in turn affects the spectral signatures in the VNIR and SWIR portion of Electromagnetic Spectrum. Optical remote sensing sensors are also affected by noise due to clouds and dusts in the atmosphere (Kuntsevich et al., 2018).

Several studies have also engaged NDVI in measuring the health of tree and vegetation foliage (Wilson et al., 2013).Some studies have also engaged the use of OBIA and NDVI time series to capture vegetation health. To remove noise from the NDVI series of datasets, Timesat Software initially developed by Eklundh & Jönsson, 2015 has been used in previous studies to eliminate inconsistencies in the NDVI time series datasets.

According to studies by Cai et al., (2017) , models of phenology used in TIMESAT software are highly competitive and preserve signal integrity. Since its inception, several studies have used TIMESAT in modelling phenology metrics e.g., (Liu et al., 2018;Lin et al., 2022) as demonstrated on their time series of MODIS NDVI dataset. Although MODIS NDVI has been used in modelling of crop phenology metrics, the problem of mixed pixels in heterogeneous agriculture landscapes was experienced. The problem was later resolved by delineating specific crop boundary parcels and using pure pixels within these boundaries to analyze specific crop phenology. The aspect of

Object-based Image Analysis (OBIA) (Blaschke, 2010) occurs in the use of hierarchical network of homogeneous objects (croplands) where each object refers to an individual crop parcel. Studies by Wang and Atkinson, 2018,have demonstrated the suitability of phenology metrics in mapping forest disturbance in Mexico using MODIS NDVI datasets. Landsat 8 NDVI time series of the same phenology period were used to validate their results.

The main purpose of this study was to explore the capability of Landsat 7 ETM+ time series datasets in discriminating the three forest classes namely: degraded forest, non-degraded forest and degraded submerged forest.

We hypothesized that Landsat 7 ETM+ NDVI time series could be used to extract phenology metrics from the degrading acacia tree strands along the flooding North Western part of Lake Nakuru riparian reserve. We demonstrated that the user-defined OBIATS.py code (see Appendix VI) could be used to extract NDVI values from Landsat and Sentinel-2 datasets. Further we demonstrated that SLIC K-means clustering algorithm for image segmentation in GRASS GIS environments in collaboration with the OBIATS.py code (see Appendix VI) could be used to discriminate Riparian reserve into different clusters resulting in a given pre-set number of land cover classes. We also hypothesized that Sentinel-2 optical data can be used to derive NDVI which could be used for validation of the Landsat 7 ETM+ OBIA-based NDVI time series results due to the differences in ground resolutions of the two datasets. This research study aims to answer the following questions: i) Does the newly developed OBIA.py algorithm able to run Big Data of NDVI in its processing chain? ii) Does Acacia forest phenology described by both the Landsat 7 ETM+ and Sentinel-2 MSI NDVI datasets allows for the detection of forest degradation? iii) What are the differences in phenological parameters of the degraded, non-degraded and degraded-submerged forest?

6.2 MATERIAL AND METHODS

6.2.1 Adaptive Savitsky-Golay filter

One way of smoothing data and suppressing disturbances is to use a filter, and replace each data value as follows:

$$y(i), i = 1 \dots \dots \dots N \text{...} 6.1$$

by a linear combination of nearby values in a window

$$f(x) = \sum_{n=1}^{n} (C_j y_j + \mathrm{j}) \text{..} 6.2$$

In the simplest case, referred to as a moving average, the weights are

$$C_j = \left(\frac{1}{2n+1}\right) \text{..} 6.3$$

and the data value $y(i)$ is replaced by the average of the values in the window. The moving average method preserves the area and mean position of a seasonal peak but alters both the width and height. The latter properties can be preserved by approximating the underlying data value, not by the average in the window, but with the value obtained from a least-squares fit to a polynomial. For each data value points in the moving window and replace the value y(i)with the value of the polynomial polynomial (Pan et al., 2015) at position t_i.

We quote a quadratic polynomial as follows:

$$y(i)\ ; i = 1,2 \dots \dots \dots N \text{...} 6.4$$

$$f(x) = C_1 + C_3\ t_2 \dots \dots \dots \dots . . 2n + 1 \text{....................................} 6.5$$

6.2.2 Extracting Seasonal Parameters

In Timesat 3.3, a number of key seasonality parameters were retrieved, namely start and end of the season, the base value, and the amplitude are computed for each of the full seasons in the time-series as shown in Figure 6.1 below. After fitting the function, more stable measure was achieved after noise removal. A number of consistency checks were carried out on the parameters for purpose of error checks. Please note, once again, that a time series spanning t years will give seasonality parameters for the t-1 center-most seasons. The definitions of all the extracted seasonality parameters are listed herein as described by Timesat 3.3 manual (Touhami et al., 2022). Procedures of extracting and validating these parameters was dependent on previous research done on phenology. However, the importance of these parameters lies in the possibility to map out spatial or temporal changes in the vegetation cover resulting from climatic or land use changes.

The definitions according to TIMESAT 3.3 Manual (Jönsson & Eklundh, 2004) are as follows: (1) time for the start of the season; time for which the left edge has increased to a user-defined level (often a certain fraction of the seasonal amplitude) measured from the left minimum level. (2) time for the end of the season; time for which the right edge has decreased to a user-defined level measured from the right minimum level. (3) length of the season; time from the start to the end of the season. (4) base level; given as the average of the left and right minimum values. (5) time for the mid of the season; computed as the mean value of the times for which, respectively, the left edge has increased to the 80% level and the right edge has decreased to the 80 % level. (6) largest data value for the fitted function.

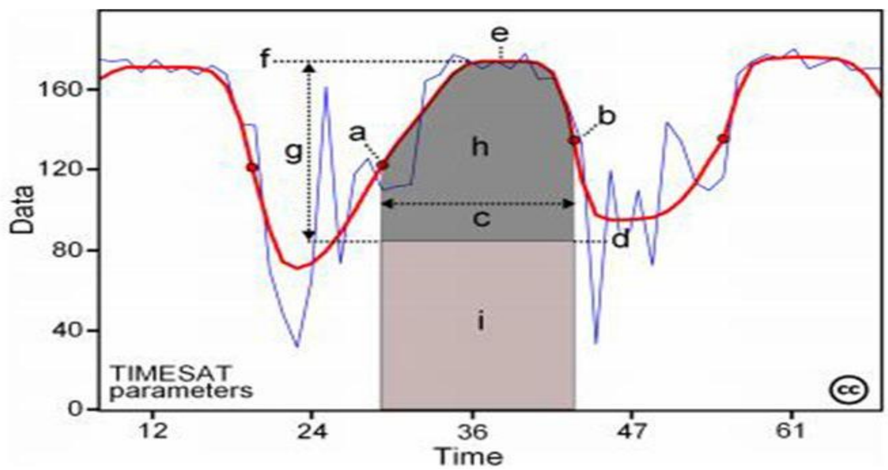

Figure 6.1: Graph illustrating phenological parameters, adopted from Timesat 3.3 manual [18]. The phenological characteristics are the following: (a) start of season, (b) end of season, (c) length of season, (d) base value, (e) peak value, (f) time of peak value, (g) amplitude, (h) small integral values.

During the season; may occur at a different time compared with (5) and (7) seasonal amplitude; difference between the maximum value and the base level. (8) rate of increase at the beginning of the season; calculated as the ratio of the difference between the left 20% and 80% levels and the corresponding time difference. (9) rate of decrease at the end of the season; calculated as the absolute value of the ratio of the difference between the right 20% and 80% levels and the corresponding time difference. The rate of decrease is thus given as a positive quantity. (10) large seasonal integral; integral of the function describing the season from the season start to the season end. Note that the large integral has no meaning when part of the fitted function is negative. (11) small seasonal integral; integral of the difference between the function describing the season and the base level from start of season to end of season.

6.2.3 Tree Health Assessment

Tree cover assessment studies are integrated in Land Use Land Cover studies where supervised or unsupervised classification procedures are carried out on satellite or aerial images in the detection of spatial characteristics on tree crowns by using spatial metrics (Huang et al., 2014). Tree cover forest pattern metrics are useful in quantifying tree cover status which can then be used for tree health assessment (Kotaridis & Lazaridou, 2022;Turner & Gardner, 1991). Some studies have engaged LULC studies in ecosystem service assessment (Yu, et al.,2022).

Corine Land Cover datasets have been used to assess ecosystem services and the benefits it provides for the people and to quantify the impacts of land cover change on ecosystem service provision and has also been used to identify the vulnerability of wetland ecosystem to drivers of change (Rahman et al., 2017; Kaya and Görgün, 2020)

In their quest to subdivide the dataset into segments, the authors used the bottom-up approach of segmentation to divide the study area into specific Minimum Mapping Units (MMU) hence embracing the concept of vector-based OBIA. More studies have further involved OBIA technology that makes use of spatial, spectral and contextual information to process change metrics on the tree crown or tree strands over a given period of time (Castro et al., 2018;Özcan et al., 2018). Studies on vegetation surface phenology have been used to characterize tree health (Bejarano et al., 2022; Galiano et al., 2015).

6.2.4 Object Based Image Analysis (OBIA)

Object Based Image analysis (OBIA) studies has taken a central stage in the field of deep learning. The OBIA paradigm is implemented in different software such as eCognition Developer. The underlying algorithms which are also found in other software environments such as Python and R have been used in image segmentation and classification. According to (Blaschke, 2010), OBIA-based classification yields higher classification on Very High Resolution (VHR) imageries. Galiano et al., 2012 used OBIA applications on their forest mapping studies while (Kaushik et al., 2015)applied OBIA on debris cover mapping. (Dronova, 2015) did a review of 73 studies on OBIA on wetland classification and noted an improvement on the overall accuracy by 31%. Further suggestions by (Wang et al., 2016) pointed out the need of carrying out OBIA on different satellite based sensors ranging across different physical environments. Previous studies have engaged OBIA on different types of satellite imageries for example on crop type mapping using Sentinel-2 and Random Forest (Huo et al., 2019), on crop type mapping using a combination of Very High Resolution (VHR) Pleiades, Sentinel-2 times series datasets and SPOT Digital Elevation Model (Immitzer et al., 2016) on small scale agricultural fields, on wetland mapping using Sentinel-1 and Sentinel-2 MSI (Kaplan & Avdan, 2017) and on land cover mapping using Sentinel (Gutman et al., 2008).

6.2.5 OBIA and Time Series

The integration of OBIA and time series studies have also been engaged in remote sensing studies in recent times. MODIS NDVI Time Series datasets have been used in crop monitoring studies engaging OBIA using vector-based segmentation (Liu et al., 2013; Dong et al., 2020) . Landsat OBIA time series datasets have also been used on cropland mapping (Yan andRoy, 2014; Liu et al., 2013). Sentinel-2 MSI Time Series recently developed by European Space Agency (ESA) provide High Resolution Imagery suitable for Object Based Image Analysis. Gumma et al., 2022 in their studies on cropland monitoring used Sentinel-2 of time series datasets to model crop monitoring using a combination of OBIA and Time Warping Dynamic Time Warping (TWDTW) method yielding an overall accuracy of 93.4% and a kappa index of 0.92 respectively. Li et al., 2010 in their studies on annual cropland mapping in central Asia used Reference time series Based Mapping method (RBM) on different agricultural landscapes using Landsat time series datasets ranging from 2001 to 2016. Integration of OBIA on the different time series of 30M resolution Landsat imagery stacks yielded both producers and users accuracy >85% per each land cover across different landscapes and an overall classification of >90% per landscape.

6.3 DATA PRE-PROCESSING

Our objective was to build a map representing the trees depending on their health level. The key idea is to locate the trees before they were affected by the floods. Then we associate this spatial information with the temporal information provided by a time series covering the flooding period. In our case, we ran SLIC-K Means segmentation on a very high resolution image of the study area, which has been acquired before the beginning of the floods. This segmentation results in the creation of a shape file containing georeferenced polygons, which are further used to delineate different kinds of land cover. Then, we retrieved a time series of 68 Landsat 7 ETM+ images, before computing a NDVI band for each image. The next step was to compute each polygon temporal profile. A polygon is associated with its temporal profile, which is composed of 68 values. These values correspond to the mean value of the pixels that are covered by this polygon, for the 68 images. Finally, we classified the temporal profiles using SLIC K-Means, an unsupervised clustering method (see Appendix VI). Using the results of this classification, we were able to group the polygons depending on the class of their temporal profiles, resulting in the creation of a representative map by associating a specific color for each group of polygons.

6.3.1 Pre-requisites

Before using the OBIATS.py tool (see Appendix VI), there are two prerequisites' steps to be done: the segmentation of a VHR image, and the construction of a NDVI dataset.

6.3.2 Segmentation of a VHR image

We ran SLIC super-pixel segmentation on a VHR picture of the lake prior to the floods period, using its implementation on GRASS GIS. We have determined the segmentation parameters manually, to ensure that one polygon is covering only one type of land cover at the same time. Thus, each object of interest (i.e. trees, water or soil) are delineated by at least one polygon as shown in Figure 6.2. This process creates a shape file containing all the georeferenced polygons, that will be used in the next step to classify the evolution of the land surface they cover during the floods period.

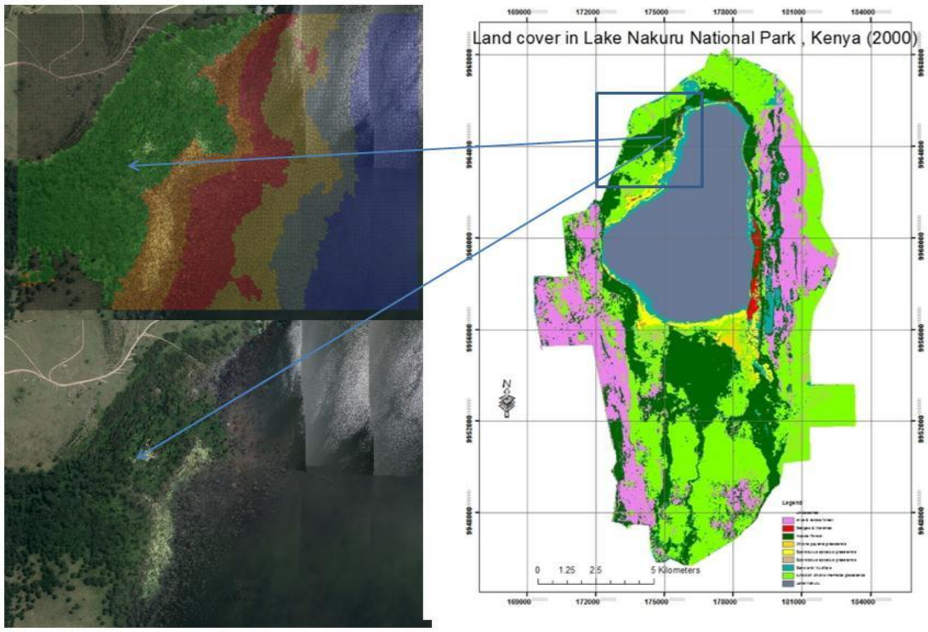

Figure 6.2: SLIC K-Means segmentation algorithm applied on the North-Western part of the Lake: From the inset on the top left corner, green (non-degraded forest); Dark brown (Degraded-forest); Red (Degraded-submerged while dirty green, dirty blue and Navy blue colors consist of areas initially covered by sand, mudflats and grasslands before the onset of the floods.

6.3.3 Construction of time series

The second prerequisite is the construction of the time series that will be used to follow the evolution of the floods. We retrieved 68 Landsat 7 ETM+ images, ranging from 2008 (before the floods) to 2017 (after the floods). Then we computed NDVI on each picture using the Orfeo Toolbox band math tool (Karasiak et al., 2020). As a result, we obtained a time series of 68 NDVI images of one spectral band (i.e. NDVI band). The bands used for generating the NDVI spectral bands were Band 3 (Red) and Band 4 (NIR) (Xie et al., 2010).

6.3.4 Validation of temporal profiles

Validation of the temporal profiles is carried out using pre-processed sentinel 2 NDVI time series datasets of the same study area and segmented polygons in one of the classes created herein. Sentinel-2 Multispectral Imager (MSI) was atmospherically corrected using SEN2COR (Fernerkundung, 2017)in SNAP Tool (Dubois et al., 2020) before being subjected to cloud masking. Since Sentinel-2 MSI was first launched in 2015, the datasets available for the validation engaged in this study ranges from September 2015 to July 2018. The bands used in the generation of NDVI per every image were Band 4 (Red) and Band 8A (Narrow-Near-Infra-Red) respectively. Each band was resampled to 10-metre spatial resolution using nearest neighbor resampling technique in ESA SNAP tool. To create uniformity in the dataset, each image in the dataset was reprojected to the same projection i.e., WGS 84 UTM Zone 36N.

6.4 DATA ANALYSIS

In this section we export the Landsat 7 ETM+ NDVI values from the 68 dates to form temporal profiles in QGIS 3.4 and later to TIMESAT 3.3 software for further processing.

6.4.1 Computation of segment temporal profiles

In order to capture the temporal profile for each land cover, namely degraded forest, non-degraded forest and degraded submerged forest, NDVI values from .IMG files are imported into QGIS 3.4 software where the average values of NDVI per each given date are computed using the value tool. The final temporal averaged NDVI values are exported into MS Excel to create CSV files and later converted to ASCII files which are later exported to TIMESAT 3.3 software for filtering and further presentation of phenological metrics. All the three filtering algorithms are tested on the

NDVI Time series in order to determine the best fit per each land cover. If the time series is smooth, but with a plateau indicating that the underlying signal is composed of two vegetation signals, then the more local Savitzky-Golay filter is the preferred method (Eklundh & Jönsson, 2015) . For noisy time series the Savitzky-Golay method sometimes yields undesirable results. In these cases, fits to the asymmetric Gaussian or double logistic functions may be the better choice.

6.5 RESULTS

Table 6.1: Phenological parameters of submerged degraded forest for Landsat 7 ETM+ NDVI time series

SEA	start t	end t	length	Base value	Peak t	Peak value	Amp	L. derv	R. derv	L. int	S. int	Start val	End val
S1	2.268	7.48	5.21	50.35	4.49	53.17	2.81	2.49	1.38	368.0	15.48	52.49	51.02
S2	12.16	16.06	3.91	50.49	14.14	55.94	4.45	1.86	1.49	325.4	22.43	52.41	54.02
S3	20.09	24.98	4.89	51.89	22.60	56.10	4.21	1.40	1.53	330.0	18.66	54.10	53.89
S4	0.00	0.00	0.00	0.00	0.00	0.00	0.00	0.00	0.00	0.00	0.00	0.00	0.00
S5	32.67	38.66	5.98	48.95	36.33	55.89	6.94	6.94	2.34	428.6	37.01	52.76	52.08
S6	42.03	46.40	4.37	50.69	44.36	56.90	6.31	6.31	2.18	330.5	26.90	52.58	54.91
S7	0.00	0.00	0.00	0.00	0.00	0.00	0.00	0.00	0.00	0.00	0.00	0.00	0.00
S8	51.90	58.30	6.40	50.29	55.55	57.54	7.46	7.46	4.42	489.9	48.37	56.11	51.92
S9	62.21	65.81	3.60	47.43	63.86	54.43	7.00	7.00	2.17	262.3	25.12	50.27	51.59

Table 6.2: Phenological parameters of non-degraded forest for Landsat 7 ETM+ NDVI time series

SEA	start t	end t	length	Base value	Peak t	Peak value	Amp	L. derv	R. derv	L. int	S. int	Start val	End val
S1	5.43	9.28	3.84	48.82	7.08	51.79	2.97	1.48	0.90	304.3	11.36	50.92	49.69
S2	13.56	16.50	2.94	49.82	15.43	54.21	4.39	2.43	2.17	260.7	11.60	50.90	53.12
S3	19.80	24.15	4.35	53.54	22.11	55.61	2.07	1.18	0.29	383.3	8.529	53.83	55.33
S4	25.50	28.92	3.42	52.33	26.45	56.00	3.68	0.96	2.59	273.9	12.30	55.53	52.80
S5	30.58	37.13	6.55	48.37	33.52	52.06	3.69	2.13	0.99	457.9	22.61	50.83	49.60
S6	41.58	45.85	4.26	50.27	44.22	55.63	5.36	2.15	1.15	321.5	19.95	51.38	54.51
S7	0.00	0.00	0.00	0.00	0.00	0.00	0.00	0.00	0.00	0.00	0.00	0.00	0.00
S8	52.47	57.49	5.02	52.67	55.47	57.36	4.69	0.37	2.38	390.4	21.74	56.50	53.52
S9	60.55	64.75	4.20	48.85	62.31	51.84	2.99	1.18	1.04	305.1	12.00	50.76	44.93

Table 6.3: Phenological parameters of degraded forest for Landsat 7 ETM+ NDVI time series

SEA	start t	end t	length	Base value	Peak t	Peak value	Amp	L. derv	R. derv	L. int	S. int	Start val	End val
S1	4.054	8.245	4.191	45.22	5.652	51.67	6.454	1.968	1.343	300.5	29.16	49.38	44.38
S2	0.00	0.00	0.00	0.00	0.00	0.00	0.00	0.00	0.00	0.00	0.00	0.00	0.00
S3	0.00	0.00	0.00	0.00	0.00	0.00	0.00	0.00	0.00	0.00	0.00	0.00	0.00
S4	25.02	26.58	1.561	45.17	26.14	56.76	12.60	5.039	6.942	159.7	24.91	52.81	52.81
S5	32.50	36.46	3.964	42.52	33.03	53.65	11.13	5.045	0.978	303.3	48.2	50.50	49.77
S6	0.00	0.00	0.00	0.00	0.00	0.00	0.00	0.00	0.00	0.00	0.00	0.00	0.00
S7	0.00	0.00	0.00	0.00	0.00	0.00	0.00	0.00	0.00	0.00	0.00	0.00	0.00
S8	50.65	55.63	4.99	44.79	55.01	60.76	15.97	1.267	8.625	386.1	72.61	54.08	53.79
S9	61.43	64.12	2.685	42.08	61.96	54.14	12.06	5.43	1.513	251.9	41.47	50.45	50.01

Time series profiles were generated from Timesat version 3.3 using NDVI datasets imported from QGIS version 3.4 and converted to ASCII files. The peak values, base values and small integral values depicted in the phenological parameters table (Table. 6.3, Table. 6.2, Table. 6.1) represent the NDVI values captured in each specific season. In each year, only one season was captured per year. The Salvitky-Golay filter in a 4*4 window was used for fitting the time series curve. The data range was fixed between -100 and +100, while the median 2*2 filter was used in fixing the spikes. Seasonal amplitudes for the start and end of the season were set at 0.5. The number of seasons derived for the 10-year period (2008-2017) were nine (9).

6.5.1 Temporal profiles on Non-Degraded Forest against Degraded Forest on Landsat-7 ETM NDVI Time Series

In this section, the class non-degraded forest consists of acacia forest which has not suffered any effects due to flooding during the year under review (2008-2017). As for the class degraded forest, it consists of the acacia forest which was initially healthy but due to the flooding of the lake the trees suffered massive degradation. Time series Landsat 7 ETM+ NDVI for non-degraded and degraded forest are presented in Figure 6.3 and Figure. 6.4. Generally, NDVI values captured across the eight seasons are higher in Figure. 6.3 than NDVI values captured on Figure 6.4 across the five seasons. Time series phenology derived from Table. 6.2 shows that the start of the season (SOS) for the degraded forest was sooner than the non-degraded across all the eight seasons. As for the length of the season (LS), the degraded forest had a shorter length than the non-degraded one. The peak value (PV) and base value (BV) for the non-degraded were greater than the degraded across the corresponding seasons.

The non-degraded forest recorded the highest peak value (57.36) during the eight season and a shorter length of season (5.021) against season 5 which recorded a pick value (52.06) and a longer length of season (6.551). The degraded forest recorded the highest peak value (60.76) during the eighth season and the longest length of season (4.988). Pearson's correlation coefficient between the peak values and base value on the non-degraded forest class depicted a strong positive correlation at R=0.87 meaning that the NDVI values achieved during the period under review were higher for the non-degraded than the one achieved with the degraded forest class at R=0.29. Moreso, the NDVI values were not determined by the length of the growing season upon the acacia forest.

6.5.2 Temporal profiles of Degraded Forest against the Degraded submerged Forest on Landsat 7 ETM+ NDVI Time series

The degraded forest consists of acacia forest which was once healthy in the earlier years before flooding (2008-2010) but due to the effect of flooding, the leaves of the trees and other undergrowth vegetation began to experience stress, hence lacking chlorophyll pigment. The degraded submerged forest captured in Figure. 6.5 consisted of healthy acacia which were submerged in water hence during 2012-2015 period, the leaves of acacia trees had begun to deteriorate gradually as confirmed by (Osio et al., 2018b).

During the period under review (2008-2017), 9 seasons were captured for the degraded forest, four of which had no phenological parameters (See Table. 6.2). As for the degraded submerged forest, seven out of nine seasons were captured and their phenological parameters presented (See Table. 6.1) using time series for Landsat 7 NDVI for degraded forest and degraded submerged forest (See Figure 6.4 and Figure 6.5). Generally, NDVI values presented in Figure. 6.5 are higher than Figure. 6.4 across all the corresponding seasons, however the eighth season on Figure. 6.4 recorded the highest NDVI value against Figure. 6.5.

Time series phenology metrics derived from Table. 6.2 shows that the start of the season (SOS) for the degraded forest was later than the start of the season (SOS) for the submerged degraded forest except for seasons seven and eight which came sooner. As for the length of the season (LS), the degraded submerged forest had a longer length of season (LS) than the degraded forest across the corresponding seasons. As for the base value (BV), the degraded submerged Forest had higher values than the BV for the degraded forest class. Higher peak values (PV) were recorded for the degraded submerged forest than the degraded forest. The small integral (SI) values were higher in the degraded forest class than in the degraded submerged forest category. The degraded forest class recorded a higher peak value (60.76) during the eighth season with a seasonal length of 4.988. As for the degraded submerged forest, the highest peak value (57.74) was also captured during the eighth season with length of season at 6.40. There was a weak positive correlation between the base values (BV) and the peak values(PV) on the degraded submerged forest category at R=0.33

meaning that the NDVI values on the submerged forest category were slightly higher than those on the degraded forest category at *R*=0.29.

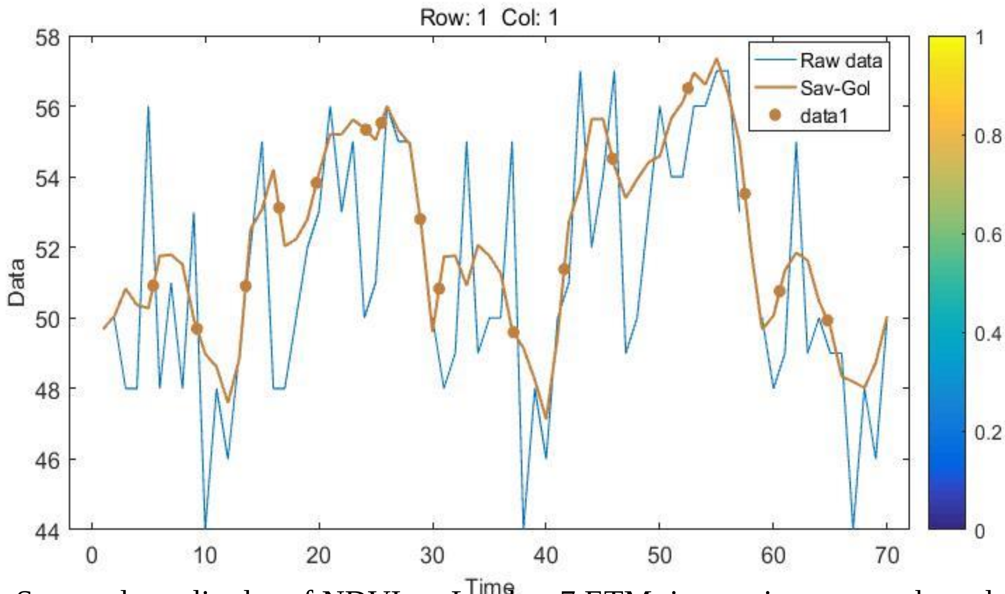

Figure 6.3: Seasonal amplitudes of NDVI on Landsat 7 ETM time series on non-degraded forest (2008-2017)

In mid-2015 the acacia trees began to experience regrowth and hence an increase in the peak value during the eighth season (60.76) and then experiencing some reduction in the ninth season (54.14). The eighth season had the highest length of season at 4.988 reflecting no phenological parameters. As for the degraded submerged forest category, Season 8 captured the highest peak value (57.74) with the length of season being 6.40. In the subsequent season (9^{th} season), the peak value dropped to 54.43 with a shorter length of season at 3.601.

There was a weak positive correlation (R = 0.24) between the length of the season and the base values for the submerged degraded forest (see Table. 6.3) meaning that the length of the season was not determined by the base values derived from the seven seasons captured from the degraded submerged class. There was a weak positive correlation (R = 0.075) between the length of the season and the base value for the degraded forest (see Table 6.2), meaning that the length of the season captured during the period under review did not determine the base value of the degraded forest class.

6.5.3 Temporal profile of degraded forest derived from Sentinel-2 MSI NDVI time series

To test the validity of the results, a time series of Sentinel-2 MSI NDVI captured between September 2015 and July 2018 were used in this case. Another polygon falling under class degraded forest was used to create temporal profiles using Sentinel-2 MSI NDVI time series. The temporal profiles of the degraded forest based on Sentinel-2 NDVI time series were generated in Figure. 6.6. The same filter (Salvitsy-Golay) with a 4*4 passing window was used on this dataset as was used on Landsat 7 ETM+ NDVI time series.

Three seasons were captured during the four-year period (2015-2018). The length of the season values achieved for the 4 seasons was correlated against the Base values and hence a correlation of determination R^2= 0.84 was achieved. The correlation results obtained for the forest degraded using Sentinel-2 MSI NDVI series portrays a more stable NDVI of time series against the Landsat 7 ETM+ NDVI time series as shown on Figure 6.4 and Figure 6.6 respectively. A series of three plateaus are observed on the graphs representing degraded forest category on Landsat 7 ETM+ and Sentinel-2 MSI NDVI time series confirming reports by (Jönsson & Eklundh, 2004) meaning that there are two types of vegetation. These plateaus represent the degraded acacia together with bush and thicket category.

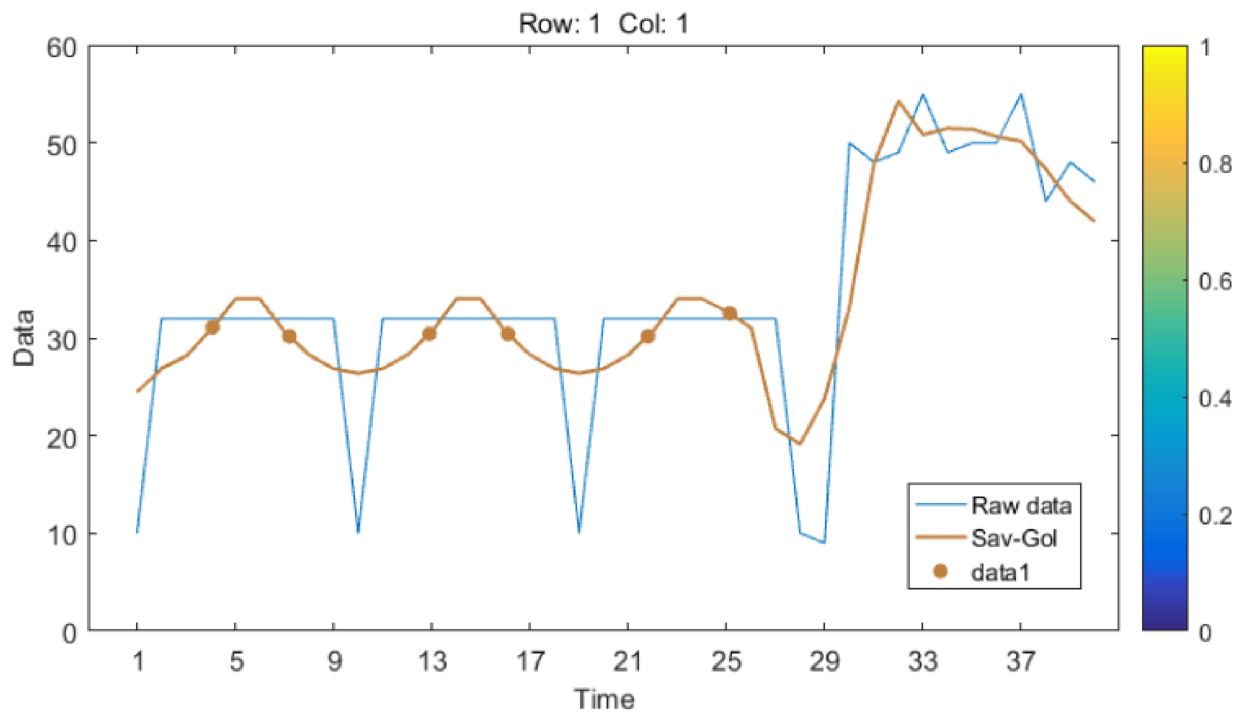

Figure 6.4: Seasonal amplitudes of degraded forest with Sentinel-2 MSI NDVI time series (2015-2018).

6.5.4 Unsupervised classification of temporal profiles

In this study, segmentation of SLIC-K algorithm is implemented on a time series stack of 68 Landsat 7 ETM+ NDVI images. The robustness of this methodology lies with the fact in the newly developed OBIATS.py code (see Appendix VI), K-values can be adjusted in order to come up with the required number of classes along the riparian reserve (Figure. 6.2). A separate file that consists of shape files promoting averaging of pixels within each polygon in the time series stack is provided. The shape files are then superimposed on the time series stack in QGIS 3.4 software. The SLIC-K algorithm (see Appendix VI) provides a more stable approach than multi-resolution segmentation that uses hierarchical segmentation for example (Csillik et al., 2019). Estimation of scale parameter tool has been used in several OBIA studies for example (Vamsee et al., 2018).

ESP2 tool has been used in the extraction of greenhouses using Worldview 2 (Aguilar et al., 2016), on urban Land Use Land Cover applications using Big data (Fallatah et al., 2018), on forest strands delineation using multispectral IKONOS image (Dong et al., 2015), in scale parametrization that leads to region merging of objects (J. Yang et al., 2015) and in the optimization of scale parameters used in delineating buildings from remote sensed imageries . Despite the fact that ESP tool parameterization has been used in previous studies to segment pixels of similar spectral signatures into objects, the problem of over-segmentation was experienced. Over-segmentation occurs when small objects are produced which are smaller than the object under study.

At times under-segmentation occurs where big objects are produced, bigger than the object under study. To overcome the problem inherent in the ESP2 parameterization (Vamsee et al., 2018) , super-pixel segmentation approach (Song et al., 2020) has been implemented in previous studies using SLIC K-Means algorithm as demonstrated by (Csillik et al., 2018). The novelty of the SLIC-KM algorithm lies with the fact that it picks the pixels of the same spectral signatures and group them into objects. A region merging algorithm (Dong et al., 2015) was then used to merge the objects that belonged to the same land cover e.g. Degraded Forest. After merging the objects per each land cover, the merged objects were then superimposed on 68-time series image stack of Landsat 7 ETM+ collected between 2008 and 2017. Validation of the unsupervised temporal profiles are then carried out using pre-processed Sentinel-2 MSI collected between 2015 and 2018. Seasonal phenological parameters of the temporal profiles revealed that non-degraded forest had the highest NDVI values.

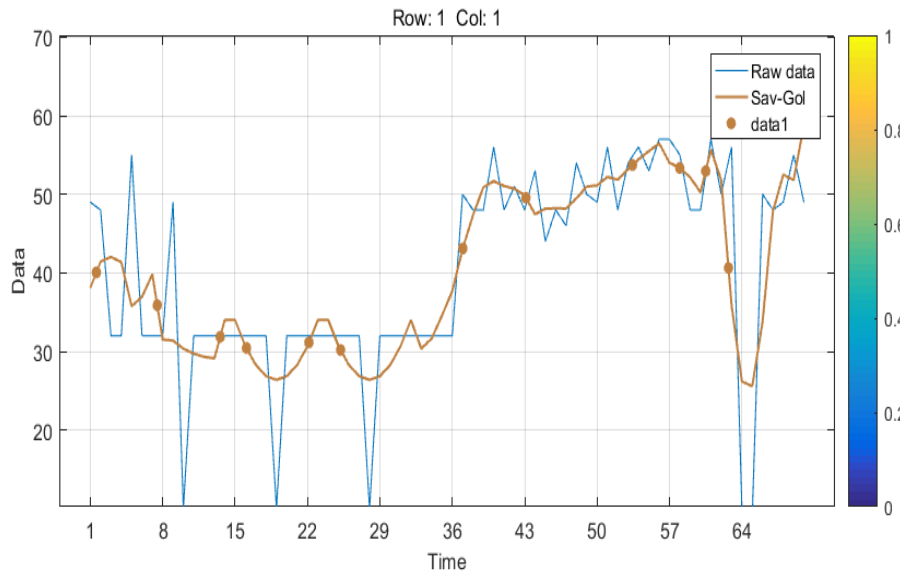

Figure 6.5: Seasonal amplitudes of Degraded Forest on Landsat 7 ETM + NDVI time series (2008-2017).

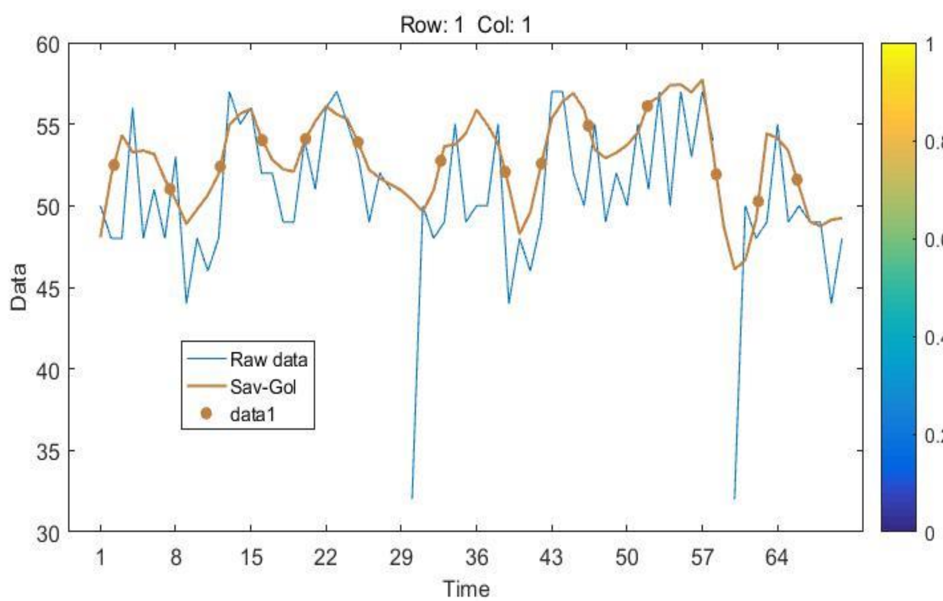

Figure 6.6: Seasonal amplitudes of degraded submerged forest on Landsat 7 ETM+ NDVI time series (2008-2017)

6.6 DISCUSSION

The study revealed that phenological metrics from the NDVI time series based on Landsat 7 ETM+ were different from Sentinel-2 MSI phenological metrics (on the degraded forest category) but depicted the same phenological patterns as shown on Figure. 6.4 and Figure. 6.6. (Sola et al., 2018). Differences in phenological metrics could have possibly been caused by several factors namely, cloud cover, satellite sensors (band specifications for NDVI generation on Landsat 7 ETM+ and Sentinel-2 MSI), differences in land cover category, calibration accuracy on different sensors (scan lines with no data (Digital Numbers) values on Landsat 7 ETM+) and atmospheric corrections as described in studies by (Geng et al., 2016). According to studies by Sola et al., 2018, these patterns are attributed to the uniform standard deviations that occurs during green-ups and senescence between the sensor systems which are consistent with the natural variance of phenology.

Previous studies by Sola et al., 2018 also used regression analysis to validate the results of their studies by relating the phenological metrics of MODIS with the other sensors and hence realized high correlation of determination results of $R^2 > 0.90$. In this study the correlation of determination results yielded between Landsat 7 ETM+ and Sentinel-2 MSI stood at $R^2 = 0.95$ meaning that phenological metrics can be used to characterize vegetation health along Lake Nakuru riparian. SLIC-KM algorithm (see Appendix VI) provided a basis of running object-based time series analysis of the NDVI datasets for both Landsat 7 ETM+ and Sentinel-2 MSI. This segmentation algorithm has an advantage in that it overcomes both the problem of over segmentation and under segmentation by incorporating region merging algorithm (Torres et al., 2021) that allows for merging of smaller objects with similar reflectance into one bigger object e.g., one land cover with similar spectral characteristics such as shown in Figure. 6.2. These objects were saved as shape files that were used in creating clusters using the newly developed OBIATS.py code (see Appendix VI) which was run in Anaconda python environment to come up with the number of required classes along Lake Nakuru Riparian.

The OBIATS.py algorithm (see Appendix VI) is robust since it could be able to run time series of NDVI values from a series of Landsat 7 ETM+ bands 3 (Red) and band 4 (NIR) using band math tool in Orfeo toolbox (Karasiak et al., 2020) exported to the same folder where the SLICK-KM means segments had been stored. Incorporating the shape files from SLIC K-Means and NDVI image files from Orfeo toolbox and importing them into OBIATS.py algorithm (See Appendix VI) enabled linear interpolation to be carried out on these image files, hence coming up with averaged NDVI values per given date on the 68 Landsat time series imageries.

This study demonstrates how the newly developed OBIATS.py code was able to provide a robust environment offering a reference provision service in running the big data in form of 68-time series of NDVI dataset in its environment, hence providing readily available clustered NDVI of Landsat 7 ETM+ and Sentinel-2 MSI for phenology metrics studies. Salvitsky-Golay filter in Timesat 3.3 had the best results against all the other filters inherent in Timesat 3.3 and thus fitted the NDVI reflectance values well producing time series profile and phenological metrics which were used in interpreting the seasonal parameters in terms of NDVI values, land cover type and composition.

Small integral values, base values, peak values, start & end of the season and the length of the growing season were the most preferred parameters to distinguish between non-degraded, degraded and degraded submerged class categories. The highest NDVI values were captured across 7 out of 8 seasons in the non-degraded forest category. For the degraded forest and non degraded forest, the length of the season was a good indicator to distinguish non-degraded and degraded forest categories. The start of the season for the degraded forest was sooner than the start of the season for the non-degraded.

According to (Cuba et al., 2018), degraded forest has other undergrowth vegetation such as bush and thicket which responds faster to shallow water and which could have contributed to it adopting early start of the season than the non-degraded conserved acacia forest. This factor could have contributed to the highest NDVI peak noted on the degraded forest category observed in Figure. 6.4 on date 2013/06/23 on the Landsat 7-time series of data.

However, the length of season for the non-degraded was longer than that of the degraded forest. It was important to note that Landsat 7 NDVI time series have inherent errors due to the scan lines (missing DN values) and heavy cloud cover in the study area during the period under review. This aspect could have contributed to the noise observed in the temporal profile of the non-degraded forest in Figure. 6.3. According to previous studies by (Bezerra et al.,2022), cloud cover affects phenology parameters.

6.7 CONCLUSION

This study demonstrates the robustness of the newly developed OBIATS.py algorithm (see Appendix VI) in retrieving big data in terms of 68 Landsat 7 ETM+ NDVI of time series to be used in phenology metrics retrieval. The act of running 68-time series of NDVI time series dataset confirms its robustness and ability to provide big data in the shortest time possible (7 seconds) using a computer with a RAM of 15GB. Its robustness provided us with clustered NDVI datasets which enabled us to come up with results about the state of health of the vegetation along Lake Nakuru Riparian Reserve. Furthermore, the resultant NDVI img files were able to be converted to ASCII files which enabled production of land cover temporal profiles which produced time series graphs in Timesat 3.3 software.

It was possible to retrieve NDVI data (base values) (Torres et al., 2021)from the phenological parameters generated from the NDVI time series initially generated from OBIATS.py code. There were some phenological similarities between Landsat 7 ETM NDVI temporal profiles and Sentinel-2 MSI NDVI based on class degraded forest temporal profiles as shown in Figure. 6.4 & Figure. 6.6. The three plateaus observed on the preceding graphs indicate the presence of two vegetation categories i.e., degraded acacia and bush/thicket (Phiri et al., 2019).

Regression analysis carried out on the base values of Landsat 7 ETM+ against Sentinel-2 base values yielded a strong positive correlation of determination at R^2 = 0.95 meaning that both Landsat 7 ETM+ and Sentinel-2 MSI phenology metrics can be used in forest degradation studies. This study confirmed that Sentinel-2 MSI derived NDVI could provide validation to the results on Landsat 7 ETM+ NDVI temporal profiles. The research confirms previous reports by (Osio et al., 2020) that Lake Nakuru Riparian reserve has been degrading. This was confirmed by the high small integral values achieved from the Degraded Forest category (Torres et al., 2021). Future studies will look into application of the newly developed OBIATS.py code in generating time series of different climatic or meteorological parameters such as temperature from thermal bands on Landsat imagery.

This aspect occurs during the retrieval of Perpendicular Vegetation Index (PVI) and other related indices which are important in eliminating the effect of underlying soil reflectance on the NDVI of vegetation cover, hence improving the quality of the phenology metrics. Further studies could also engage the use of backscatter indices generated from Sentinel-1 Ground Range Detected (GRD) SAR Time Series in the characterization of the various land covers by running backscatter index σ_{db}(VV) and σ_{db} (VH) time series in OBIATS.py code.

CHAPTER SEVEN:

DETECTION OF DEGRADED ACACIA TREE SPECIES USING DEEP NEURAL NETWORKS ON UAV DRONE IMAGERY.

This Chapter is based on, Osio, A. A., Lê, H.-Â., Ayugi, S., Onyango, F., Odwe, P., and Lefèvre, S.: DETECTION OF DEGRADED ACACIA TREE SPECIES USING DEEP NEURAL NETWORKS ON UAV DRONE IMAGERY, ISPRS Ann. Photogramm. Remote Sens. Spatial Inf. Sci., V-3-2022, 455–462, https://doi.org/10.5194/isprs-annals-V-3-2022-455-2022, 2022.

Presented at the 2022 Congress of the International Society for Photogrammetry and Remote Sensing on 6th-11th June, 2022 in Nice, France.

Abstract

Deep learning approach to image detection and classification have been applied with great success to tree monitoring. However, most of the existing studies focus on tree crowns and analysis of fallen tree trunks, especially on flood inundated areas, remains largely unexplored. Moreover, detection of degraded tree trunks on different natural environments such as water, mudflats, and natural vegetated areas poses a challenge to the deep learning framework. This is due to mixed color signals from the image background or when the target object needs to be localized by fitting a bounding box. In this chapter, Unmanned Aerial Vehicles (UAV), or drones, with embedded RGB Camera were used to capture the fallen trees from six designated plots around Lake Nakuru, Kenya. Motivated by the need to detect the fallen trees around the lake, two well-established deep neural networks, i.e., Faster Region-based Convolution Neural Network (Faster R-CNN) and RetinaNet were used for fallen tree detection and classification. A total of 7,590 annotations belonging to three classes and derived from 256×256 image patches were used for this study. 80% of the sample annotations were used for model training and validation while 20% for testing. Three classes of trees were quantitatively identified according to their location on the environment i.e. Mudflat (2077), Land (2514) and water (2,999). Results obtained shows that RetinaNet had slightly higher detection rate, with an Average Precision (AP) of 38.85% and Recall 57.9%, while Faster R-CNN had a slightly lower AP of 37.21% and Recall 53.2% respectively, pegged on IoU ≥ 0.5.

7.1 INTRODUCTION AND LITERATURE REVIEW

Forest detection has been embraced in many studies using different types of remotely sensed datasets, captured from different aerial and satellite sensor platforms. Assessment of fallen trees is an important step to characterize forest health. According to (Torres et al., 2021), most of the studies have been applied mainly in America and Europe with the most frequently used data being multispectral imageries from Landsat sensors (She et al., 2015).

The recently launched Sentinel-2 have shown less capability in detecting individual vegetation species (Nzimande et al., 2021). UAV remotely-sensed images are ideal for forest health assessment since they provide optical imagery with high geometric spatial resolution i.e. 10-40cm (Naik et al., 2021). Conversely, coarse ground resolution satellite imagery from optical sensors does not allow to capture the geometric structure of fallen trees and hence remains mainly used for classification at local and regional scales (Naik et al., 2021; Gorelick et al., 2017).

Other studies have also shown that incorporating LiDAR data with multispectral imagery improved the prediction of tree height estimation and canopy detection models within natural forests (Manzanera et al., 2016). Despite the reliability of LiDAR data, it remains expensive and can only cover small areas of study. Moreover, models based on LiDAR data (especially in relation to above ground biomass or fallen trees) highly depends on the type of forest under study and the level of tree degradation on site (Galidaki et al., 2017).

Synthetic Aperture Radar (SAR) data with longer wavelengths and cross-polarization capabilities have also been used in fallen tree studies. Models created using SAR data produce uncertainty and variance in modelling accuracy of above ground biomass Dalponte et al., (2018), Naik et al., (2021). On the contrary, confirmed that the use of SAR-C channels captured in Single Look Complex

(SLC) mode in conjunction with machine learning models and object-oriented approach yielded the best results with an OA of 98.1% and a Kappa of 97.0%, hence improving the above ground biomass classification on the Acacia strands around Lake Nakuru, Kenya (Osio & Lefèvre, 2021). Despite achieving results at local scale, such a model was not suitable to capture individual degraded target tree species that are fallen around the lake. In recent times, the deep learning paradigm with models tailored at image classification and detection has become a standard methodology in remote sensing studies (Neupane et al., 2021). The main advantage provided by deep learning over classical machine learning approaches is that models created using deep learning can learn and extract information directly from input data, not requiring a costly feature engineering step. These models can then be used to detect and predict similar features on the entire scene under investigation.

Deep learning has been used in many studies in recent times including automatic extraction of ice-wedge polygons using Mask R-CNN framework on both high-resolution imagery and UAV, producing F1 Scores of 72% and 70% respectively (Zhang et al., 2020). Santos et al., 2019, made a comparison of three different deep learning frameworks, namely YOLOv3, Faster Region Based Convolutional Neural Networks (Faster R-CNN), and RetinaNet to assess a time series of RGB images in the context of tree crown detection achieving an overall Average Precision of 92% (Jiang et al., 2019).

Other studies have used object-based image analysis (OBIA) approach to detect Coarse Wood Debris (CWD) from Unmanned Aerial Systems (UAS) in conjunction with LiDAR point clouds (Thiel et al., 2020). The authors reported an overall average precision of 85% and a recall of 69.2%. However, they pointed out that the results achieved using Very High Resolution (VHR) imagery and their line detection algorithm over CWD areas could be improved using deep learning approaches (Jiang et al., 2019). Further concerns by the authors involved controversy about the application of deep learning frameworks on tree species, pointing out the challenge in model transferability onto similar scene.

In this chapter, we evaluate off-the-shelf deep architectures in detecting fallen trees of the Acacia xanthophloea species around Lake Nakuru National Park, Kenya. The wetland was designated amongst wetlands of international importance (Odada et al., 2004) as Ramser site number 476 on 5th June, 1990. Kenya, being a signatory to the Conference of Parties (COP) based on the Ramser convention in 1971, is required to actively conserve and make wise use of Lake Nakuru wetlands in a sustainable manner (Davidson et al., 2019).

The acacia forest used to play an important ecological role of preventing siltation in the lake. It is also an important feed and habitat for various animals within the conservation area including the Rothschild giraffe, Vervet monkeys, and Black rhinoceros. However, the Acacia trees are on the verge of extinction due to the flooding lake.

Unmanned Aerial Vehicles (UAV) missions around the lake revealed massive destruction of the trees, especially inside the water body and on the mudflats. Therefore, the purpose of this study was to provide a state-of-the-art model based on the detection and classification of fallen trees around the lake, hence enabling the wildlife and forest conservation managers to make informed decision on the fallen Acacia trees. More precisely, our main goal was to subdivide the UAV/RGB Images into 256*256 image patches, annotate the trees to form a corresponding file (. json) which were then used to train two off-the-shelve deep learning frameworks i.e. Faster R-CNN and Retina-Net with an aim of detecting fallen trees around Lake Nakuru, Kenya.

7.2 MATERIAL AND METHODS

In this section the 6 designated areas under study around lake nakuru as shown on figure 7.4. Other sub-sections depict how the data was captured, pre-processed and analyzed for the production of the results.

7.2.1 Data Capture

Table 7.1**:** Da-Jiang Innovations Science & Technology Co. Ltd (DJI) Real Time Kinematic (RTK) of Phantom 4 Specifications according to (Phantom, 2018).

UAV Features	DJI Phantom 4 RTK
Frequencies used	GPS:L1/L2; GLONASS:L1/L2
Positional Accuracy	H: 1.5cm; V:1cm; Both +1ppm (RMS)
Image Sensor	CMOS 1”
Maximum resolution	4864×3648 (4:3); 5472×3648 (3:2)
Field of View	84◦
Mechanical Shutter	8-1/2000s
Data Format	Photo (JPEG), Video (MOV)

UAV drone images were captured across six sites around the lake in the early September 2021 for 5 consecutive days, see Figure. 7.4. The drone used for the ground surveys was a DJI Phantom 4 RTK SDK, all its specification is reported in Table. 7.1. Images with a mean Ground Sampling Distance (GSD) of 4.84cm and covering approximately 6.1 square kilometers were captured across six designated sites around the Lake Nakuru National Park. The surveyed areas were mainly near the lake shorelines where a large number of degradations were observed during the flight planning stage. A total of 9,056 training image patches were generated from the six images (see Figure 7.3) with 7,590 tree samples annotated from the training set. The fallen trees are classified into 3 classes according to their background namely Water (W), Land (L), and Mudflat (M) as shown in Figure. 7.3.

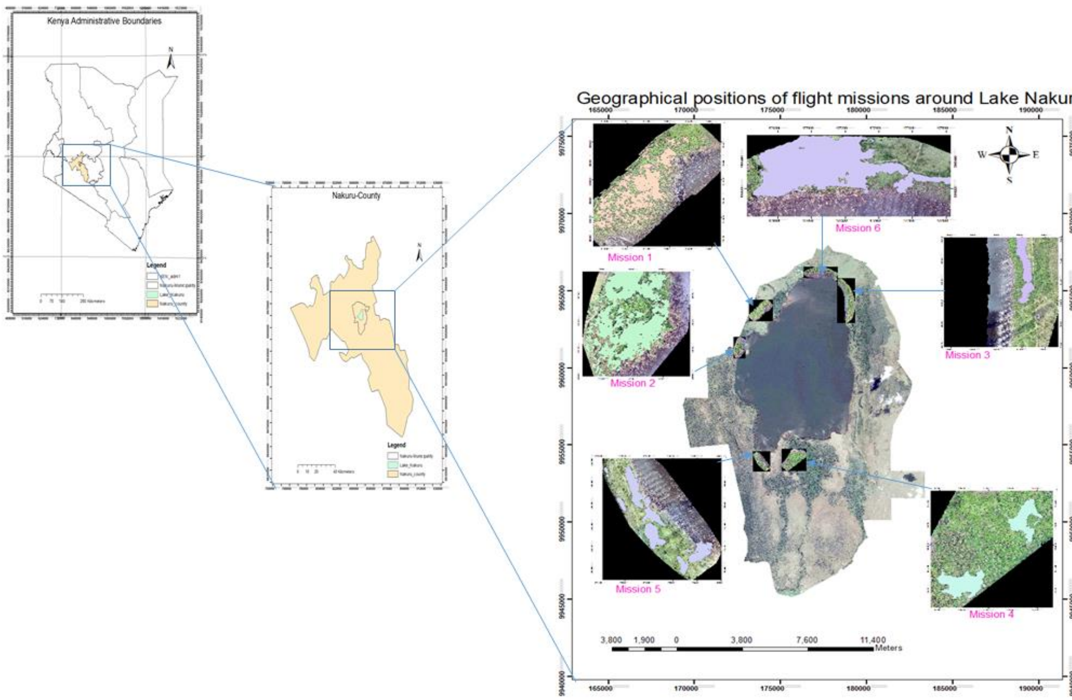

Figure 7.1: The geographic position of the 6 flight mission areas around Lake Nakuru, projected at WGS84, UTM Zone 37S.

7.3 GENERAL WORKFLOW

The study consisted of 4 steps. On the first step, images are acquired from a UAV/RGB drone platform. Then, patches of non-overlapping 256-pixel squares are extracted from the acquired images and randomly sampled to training and test set. The fallen trees from the image patches are annotated with bounding boxes using the Labelimg tool. Finally, the training image patches with their annotations are used to train a deep convolutional neural network (CNN) while the mutually exclusive test set is used to report the performance of the network on unseen data. Figure 7.2 shows the general workflow engaged in this study.

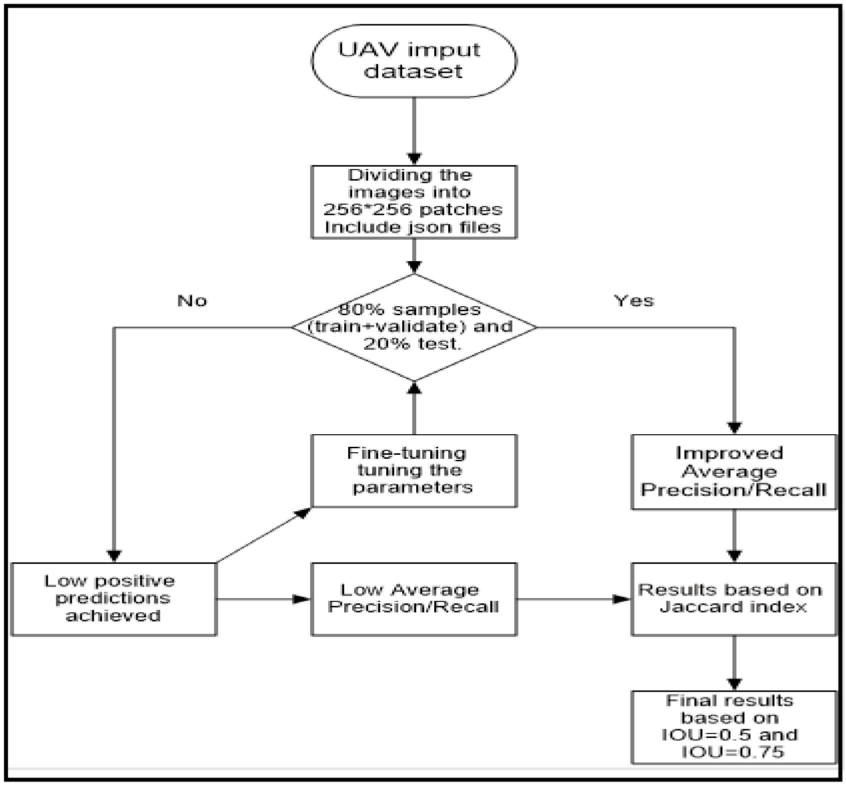

Figure 7.2: The general workflow engaged in this chapter: **Source**: Author

7.3.1 Deep Learning for Object detection

Object detection is made of 2 subtasks, (1) localizing an object of interest in an image with a bounding box and (2) categorizing the box with the correct class. The tasks could be performed in a 2-step process, with the bounding boxes first proposed then classified, or all at once, leading to the so-called 1-stage detectors. The exemplar model for each type of architecture include Faster RCNN Ren et al., (2018) and RetinaNet Lin, et al., (2017), respectively. In this study, we evaluate these two models for detecting fallen trees around the Lake Nakuru.

7.3.2 Faster R-CNN

The Region-based CNN (R-CNN) laid the groundwork for deep-learning-based object detection (Girshick et al., 2014) with bounding boxes proposed by Selective Search (Uijlings et al., 2013). Fast R-CNN speeds up the process by introducing the ROI pooling layer and inputting the full image instead of just the proposals to the deep network. Significant acceleration is achieved by Faster R-CNN when a sub-network, called Region Proposal Network (RPN), is used to generate the proposal boxes in place of Selective Search and both 2 stages can be trained end-to-end (Berkeley et al., 2017).

The vanilla Faster R-CNN architecture extracts low-level image features by passing an input image through several convolutional blocks, called a backbone (sub-)network. The features are then shared between both the region proposal network (RPN) and region-of-interest (ROI) head. The RPN generates a number of proposal boxes, 2000 by default, from which the corresponding features are obtained and classified by the ROI head (sub-)network. The classifier is a multi-layer perceptron (MLP).

7.3.3 RetinaNet

RetinaNet is an improvement over the Single Shot Detector (SSD) (Lin, et al., 2017). RetinaNet has four main components which include: i) Classification sub-network which predicts the probability of an object occurrence at each spatial location for each annotated box and object class. ii) Regression sub-network that regresses the offset for the bounding boxes from the annotated boxes for each ground-truth object. iii) Bottom-up pathway which consists of the backbone network (ResNet) whose role is to calculate the feature maps at different scales. iv) Top-down pathway that up-samples the spatially coarser feature maps from higher pyramid levels. Lateral connections are included to merge top-down layers and bottom-up layers with the same spatial size. The RetinaNet architecture includes Feature Pyramid Networks for feature extraction through upsampling or downsampling approach and relies on the “Focal Loss” objective function, both concepts that are recalled below (Yongqiang Zhao et al., 2019).

FPN are feature pyramids in an image used to detect objects using different scales. The outlook of FPN consists of image layers existing on different parts of the pyramid whose samples and sub-samples can be used for object detection across the pyramid layers. Since its inception, the hand engineered pyramids have since been replaced by CNN. FPN behave in similar way as CNN, since in both architectures the output size of feature maps decreases after each successive block of convolution operations. Pyramidal feature hierarchy has been utilized by models such as Single Shot detector (SSD), but the only weakness is lack of its ability to recycle the multi-scale feature maps from different layers across the pyramids.

Focal Loss (FL) is an enhancement over Cross-Entropy Loss (CE) and was introduced to handle the class imbalance problem with single-stage object detection models. According to (Lin, et al., 2017), single-stage models suffer from some adverse effects of foreground to background class imbalance due to dense sampling of annotated bounding boxes. In RetinaNet, at each pyramid layer, there can be thousands of anchor boxes but only a few will be assigned to a ground-truth object leaving majority as background class. Sometimes detection with high probabilities may lead to small loss values thus overwhelming the model. Focal Loss reduces the loss contribution from easy examples and increases the importance of correcting misclassified cases.

7.4 EXPERIMENTAL SET-UP

In relation to this experiment, all the annotations from the three classes, namely Dead Tree Land, Dead Tree Water and Dead Tree Mudflat were sampled into two parts consisting of training/validation and testing set. From each given class of the dataset, 80% of the samples across all the missions were used for training/validation while 20% remained for testing. This particular design was adopted to cater for imbalances within the datasets across the 6 missions (Figure. 7.4). Missions 3 and 4 had less annotations compared to the rest of the missions and hence we couldn't adopt the within dataset approach popular with deep learning object detection.

Figure 7.3: The three sample classes and numbers of annotations in the dataset: from left to right, dead trees on land (2,514 boxes), dead trees on mudflat (2,077 boxes), and dead trees on water (2,999 boxes).

The metrics used in these experiments are taken from **'**Common Objects in Context' i.e.,(COCO) (Lin, et al., 2017) challenge for quantitative assessment. The challenge employs the standard definition of precision (P) and recall (R) based on the notion of true positive (TP), false positive (FP), and false negative (FN) (Eq. 7.1, Eq. 7.2 and Eq.7.3) as follows:

$$\mathrm{P} = \frac{TP}{TP+FP} \qquad \text{Eq. 7.1}$$

$$\mathrm{R} = \frac{TP}{TP+FN} \qquad \text{Eq. 7.2}$$

$$\mathrm{F1} = 2\,\frac{\mathrm{P} \times \mathrm{R}}{\mathrm{P} + \mathrm{R}} \qquad \text{Eq. 7.3}$$

The COCO metric differs in the definition of a positive box prediction, for which the intersection over union (IoU, or Jaccard index) of it with ground truth boxes are computed. IoU measures the ratio between the overlapping area of the two boxes divided by the area covered by their union. As such, the number of positive boxes changes according to the IoU level: higher IoU threshold (max of 1 or 100%) results in fewer positive predictions and thus, lower measurement.

At an IoU threshold, the boxes with at least (or higher than) the given level are considered positive, true or false depending on the predicted class, and are used to computed precision and recall. In this paper, the precision is computed for each of pre-defined recall values (101 values from 0 to 1 with step of 0.01), which are used to plot the precision-recall (PR) curve. We also report the average precision (AP), average recall (AR), and subsequently F1-score using Eq. 7.3 for 2 IoU levels, 0.50 and 0.75. The average precision is taken across all recall levels and equal to the area under the PR-curve (Eq. 7.4).

$$\sum_{j=1}^{N} \mathrm{p(k)}\Delta\mathrm{r(k)} \qquad \text{Eq 7.4}$$

where N is the total number of images in the collection, p(k) is the precision at a cut off of k images, and Δr(k) is the change in recall that happened between cutoff $k - 1$ and cut off k.

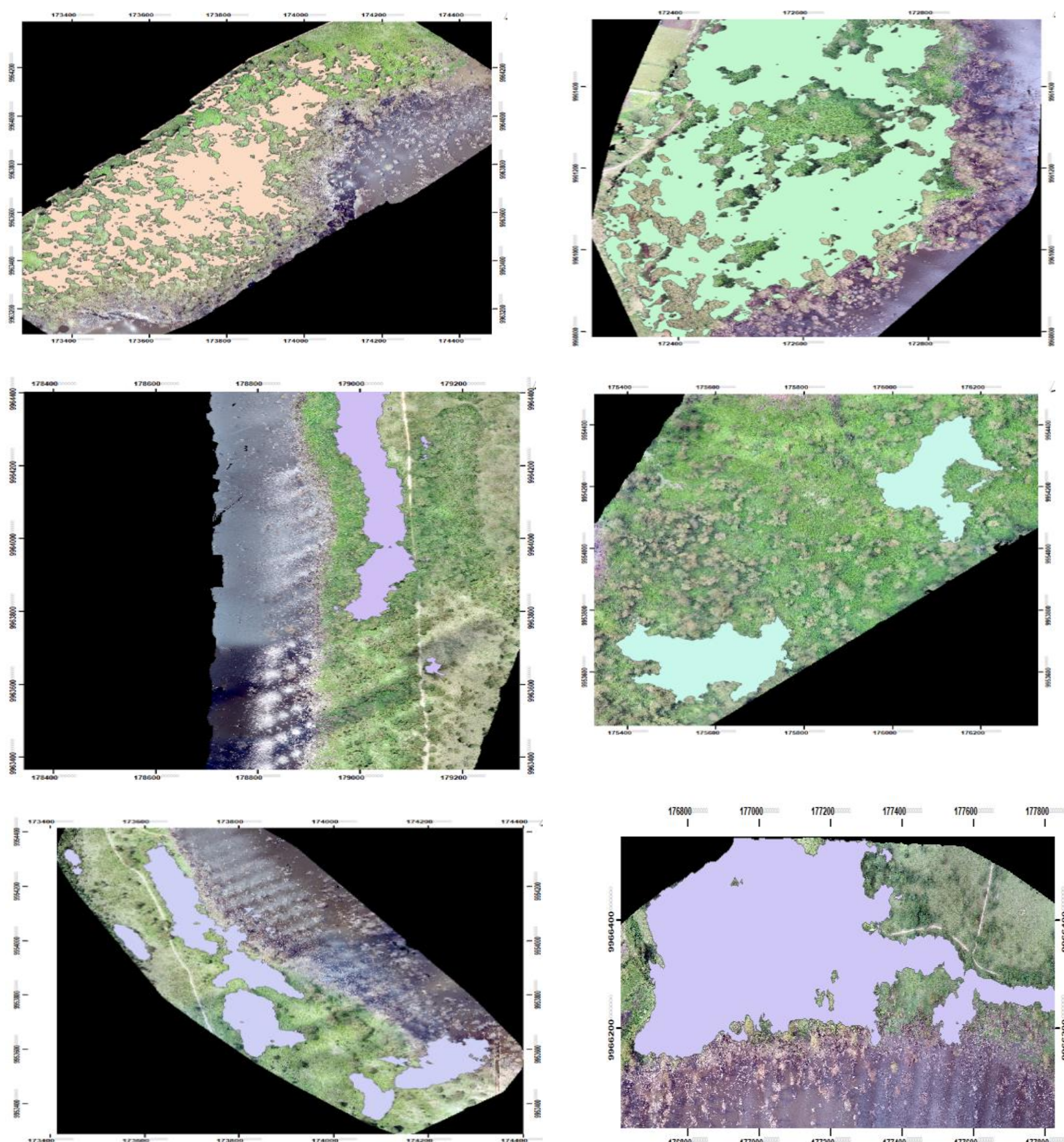

Figure 7.4: The six flight missions captured from different sites around the Lake using DJI Phantom 4, SDK Drone. The overlay vector polygons were derived from QGIS-based forest detection plugin, Mapflow.ai representing the detected trees on each imagery

7.5 **RESULTS**

We report here quantitative results measures with the metrics reviewed in the previous section, namely Average Precision, Average Recall, Area Under Curve, F1 score and the general accuracy between classes. We provide in Figure. 7.7 and Figure. 7.8 the Precision-Recall curves for the two deep neural networks considered in our study. When comparing RetinaNet and Faster R-CNN, one can observe that the former delivers higher average AP results (38.85%) than the latter (37.21%) considering an IoU threshold of 0.5. Nevertheless, the difference remains within a small margin. In terms of Average Precision per class, RetinaNet performs best for both classes “Land” and “Water” (with improvement of 2-4%) but worse for class “Mudflat” (degradation of 2%). Considering a higher IoU threshold of 0.75, the methods reach lower APs. Again, RetinaNet performs better than Faster R-CNN (also with a small margin). A class wise analysis leads to somehow different conclusions, with RetinaNet achieving better results for classes “Mudflat” and “Water”, Faster R-CNN for “Land”. The margin being very small, one should take these results with caution. We then show in Figure. 7.5 and Figure. 7.6 some visualization results achieved by RetinaNet and Faster R-CNN per each given class. All classes were predicted with a high confidence level as shown at the edge of the bounding boxes. Illustrations also include the average AP reported per class and mean Average Precision on all the bounding boxes of a specific class (shown in red values). The low Average Precision values achieved in this chapter were mainly due to the background noise from the UAV/RGB datasets.

7.6 DISCUSSION

The model that achieves the best performances (Precision and Recall) was the RetinaNet with a setting IoU ≥ 0.5, as shown in Table. 7.2. These results corroborate with recent studies carried out by (Santos et al., 2019) where RetinaNet outperformed two other variants, namely YoloV3 and Faster R-CNN. Similar studies (Alon et al., 2019) involving tree crown detection with UAV orthophotos and LiDAR point clouds had promising results with RetinaNet as well. The overall AP reported with RetinaNet was 43.85%. Usually AP or Area Under the Curve are normally used on imbalanced datasets. Datasets with low True Positive Rates (TPR) and high False Positive Rates (FPR) / False Negative Rates (FNR) usually produce low Precision and Recall.

In the case of our UAV dataset, annotations were carried out on the fallen trees which exhibited different backgrounds, i.e. mudflat, water and land. Class “water” had the highest detection rates (AP=43.85%) due to uniformity of their background, while class “mudflat” shows the opposite behavior dues to the background non-uniformity.

The other factor which could have influenced the performance of the deep networks is the number of annotations and image patches derived from the UAV dataset, as already shown in recent studies (Hägele et al., 2020). A case in point is whereby in this study, 9,056 image patches and 7,590 tree sample annotations were used. Compared to the number of image patches used in pre-training the Faster R-CNN network using the COCO dataset, the number of samples in our dataset is very low. The COCO dataset that was used to pre-train Faster R-CNN had 385,000 image patches and 2.5 millions of annotations (Lin et al., 2014). In some studies, using RetinaNet in tree crown detection (Santos et al., 2019), encouraging results (AP=92.64%) were achieved using only 392 image patches. In our study, we rely on a far much larger number of image patches, while not achieving the same scores. Let us observe that two different areas might come with very different visual features and landscapes, so problems with varying difficulty to tackle. More precisely, the tree crown detection problem is much simpler (thus leading to higher detection rates) thanks to the tree crown uniformity (shape factor) than our use case, where we have to deal with coarse wood debris (tree biomass) which come in different shapes and backgrounds, hence the creation of noise within networks.

Finally, let us comment the complexity of the proposed approaches. Both networks are trained on a cluster node with 2 CPU x 20 E5-2687W v3 @ 3.10GHz, 396G RAM, and 1 NVIDIA GeForce GTX Titan-X of 12.2GB VRAM, which are shared among cluster users. The Faster R-CNN with ResNet50 backbone and FPN contains 17,260,319 parameters while the RetinaNet model with the same backbone contains around 14,460,660 parameters.

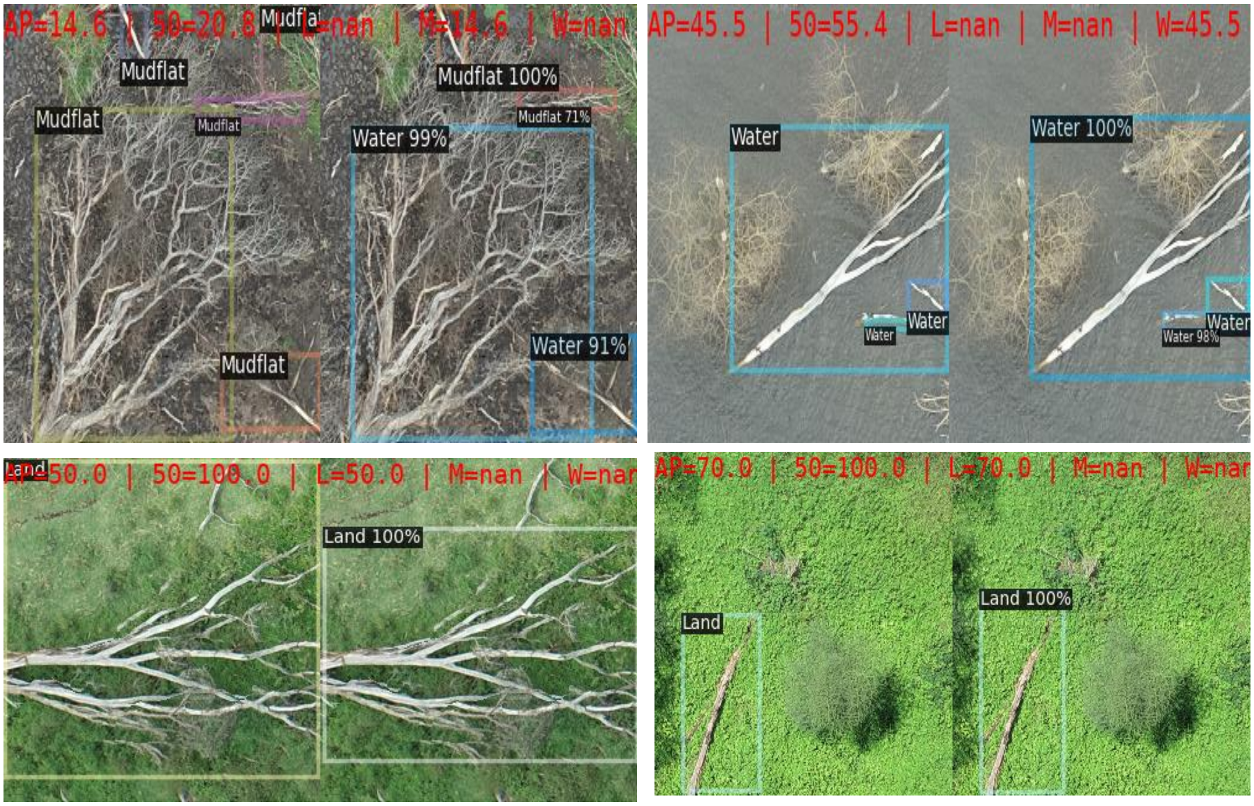

Figure 7.5: Sample results from different scenes using Faster R-CNN, with average precision (AP) averaging over all IoU levels in [0.5, 0.95], step size 0.05 and (50) precision at IoU $\geq$ 0.5) on three classes: Dead Tree in Water (W), on Land (L), and on Mudflat (M). The confidence levels (%) are shown on the bounding boxes.

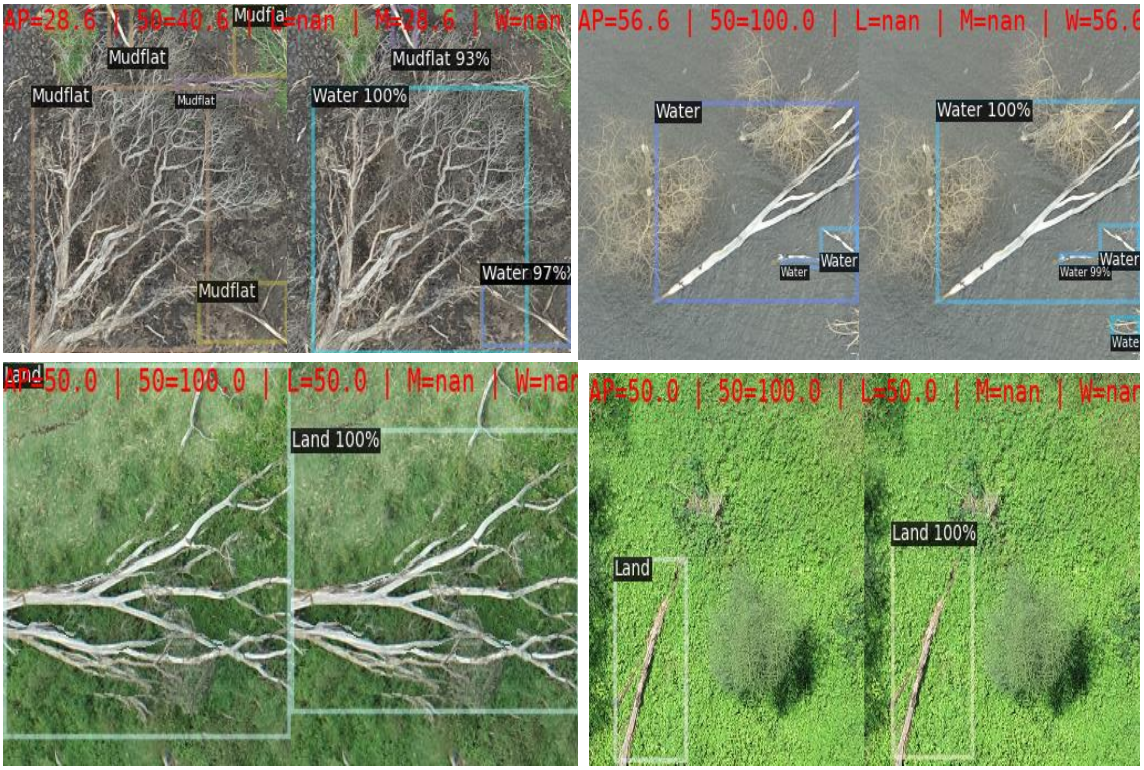

Figure 7.6: Sample results from different scenes using Faster R-CNN, with average precision (AP) averaging over all IoU levels in [0.5, 0.95], step size 0.05 and (50) precision at IoU ≥ 0.5) on three classes: Dead Tree in Water (W), on Land (L), and on Mudflat(M). The confidence levels (%) are shown on the bounding boxes.

Table 7.2: Quantitative results obtained with the two deep neural networks and two IoU thresholds.

IoU	RetinaNet			Faster R-CNN		
	Precision	Recall	F1 Score	Precision	Recall	F1 Score
0.50	38.9%	57.9%	46.5%	37.2%	53.2%	43.8%
0.75	14.1%	29.0%	19.0%	14.0%	27.7%	18.8%

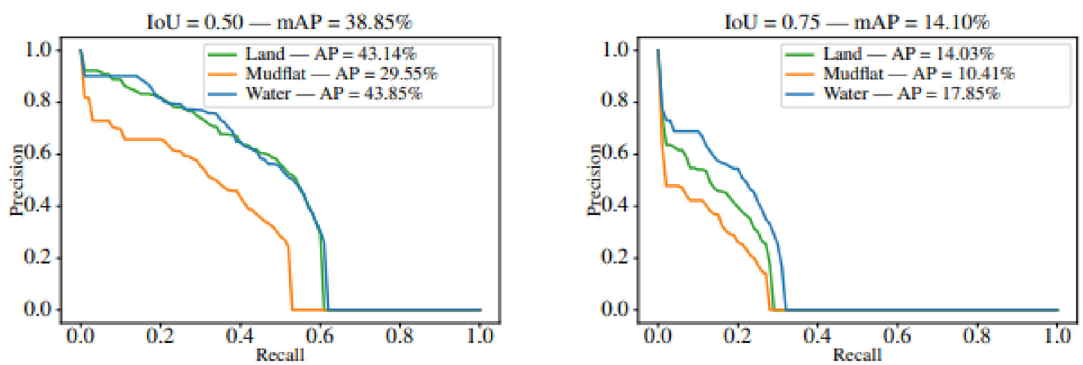

Figure 7.7: Precision-Recall curves for Retina-Net and two IoU thresholds.

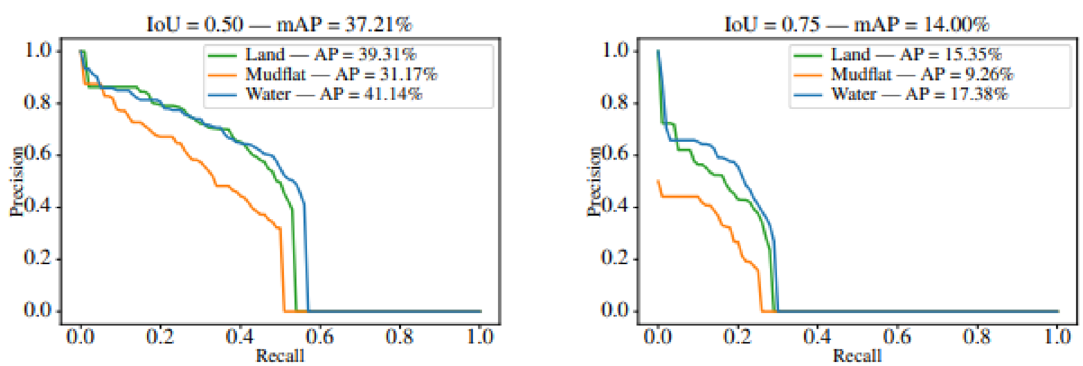

Figure 7.8: Precision-Recall curves for Faster R-CNN and two IoU thresholds.

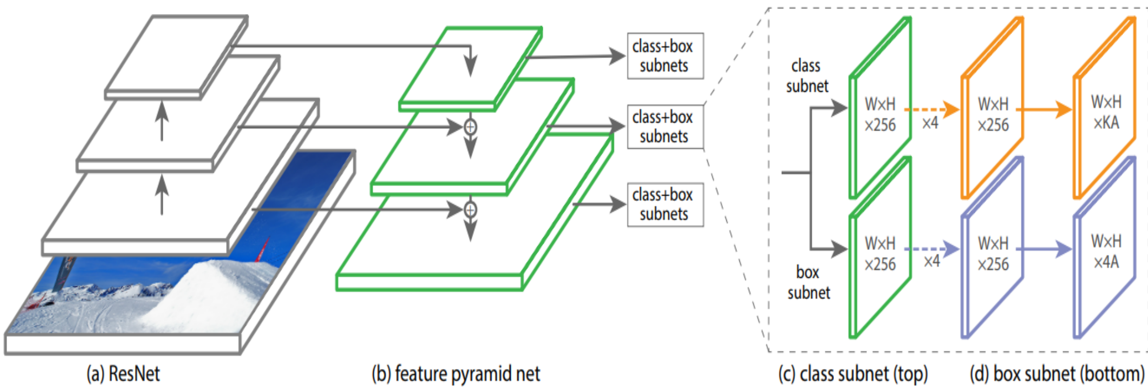

Figure 7.9: A cross sectional diagram of RetinaNet Network Architecture based on the FPN backbone (Lin,et al., 2017)

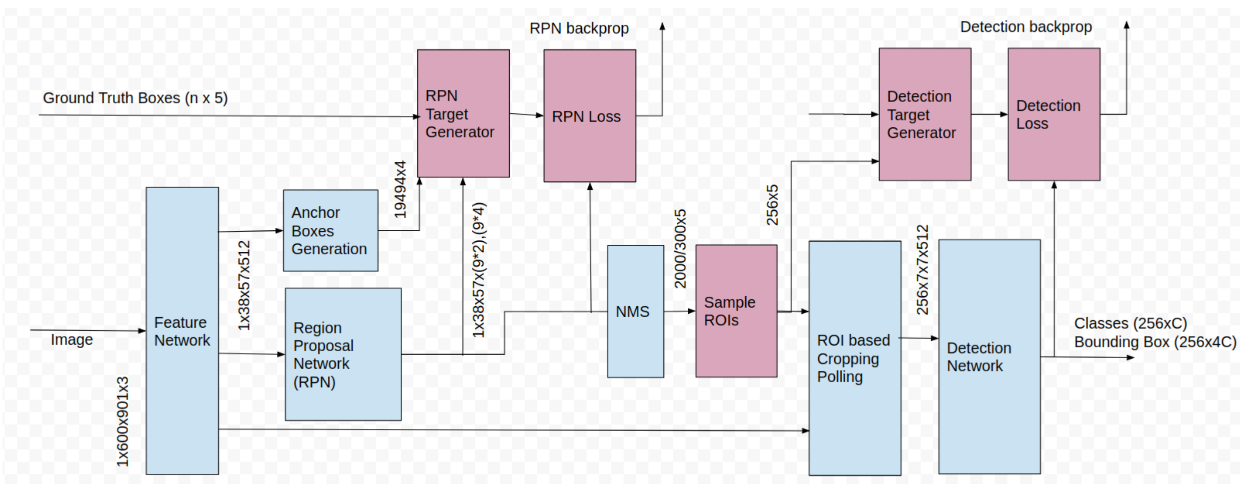

Figure 7.10: A schematic diagram of Faster R-CNN Object Detector Architecture, based on ResNet Backbone

7.7 CONCLUSION

In this study, we dealt with the detection of fallen acacia trees, on which we evaluated two competitive CNN models, i.e. Faster R-CNN and RetinaNet using images captured by UAV with RGB Cameras on board. The networks were trained and assessed using a dataset made of 9,056 image patches and 7,590 annotations on bounding boxes. RetinaNet achieved overall Precision of 38.9% and Recall of 57.9%.

These results indicate that RGB Cameras embedded on UAV in conjunction with deep neural networks could possibly lead to the development of operational tools for the detection of fallen trees on different environmental backgrounds. This could also help in carrying out demographic surveys of fallen trees around the Park and in similar environments.

Fallen tree demography could help ecologists and conservationists in quantifying the magnitude of Acacia Tree degradation around Lake Nakuru. This model can be applied on other areas with similar characteristics such as fallen trees along the riparian reserve of other Rift valley lakes. Future studies should look into combining UAV-based images and their point clouds for tree detection and classification using deep networks.

CHAPTER EIGHT:

INTEGRATED OBIA AND MACHINE LEARNING CLASSIFICATION SCHEME FOR MAPPING ACACIA XANTHOPHLOEA USING PLEIADES_1A TIME SERIES

Abstract

Pleiades-1A optical imagery is expected to improve riparian vegetation classification due to spatial integrity measured at ~50cms, hence it's ability to distinguish submerged vegetation species on flood inundated areas. The target vegetation under study was *Acacia xanthophloea* tree species on the verge of extinction along Lake Nakuru, Kenya. To overcome the constraints associated with mapping flooded riparian vegetation, Object Based Image Analysis/Machine Learning approaches were implemented on high spatial resolution Pleiades time series. OBIA was implemented in eCognition Definiens, with further image post-processing done in ArcGIS environment. Further processing was done on 3 different plots selected from different locations around Lake Nakuru National Park. Experiments were then carried out as follows: i) To test the capability of OBIA analysis on VHR time series of Pleiades-1A imagery. ii) To analyze the importance of machine learning on OBIA classification scheme and iii) to quantify their contribution to classification accuracy. iv) To quantify change by implementing post classification comparisons on the target classes. Multiresolution segmentation was used to segment each Pleiades image but with variation in vegetation types given to the different plot locations in the park. Machine Learning algorithms appended on all classification scheme include Naïve Bayes, Binary Support Vector, J48 and Random Forest. Three types of approaches were used i.e. Full Training, 2/3 Train - 1/3 Test and the (10-Fold) cross-validation. One Way Analysis of Variance (ANOVA) was used to test if there was a significant difference between and amongst the four Machine Learning algorithms and three approaches used. The results achieved revealed that there was a significant difference amongst the algorithm used, since the value of the F-statistic (3.039) greater than F-Critical (2.901) at p-value (0.04). There was also a significant difference amongst the three approaches used, determined by the F-statistic (6.3004) greater than the F-Critical (2.892) at p-value (0.005). Post-Hoc analysis using Turkey's HSD Q-stat F-statistic sample test revealed a significant difference between Random Forest (RF) and Binary Support Vector Machine (SVM) with F-static value (3.846) significant at p-value 0.04. Random Forest (RF) had the highest score with an overall Accuracy (OA) of 88.0% and Cohen Kappa (0.83).

8.1 INTRODUCTION AND LITERATURE REVIEW

Remote sensing approaches have been used to characterize wetlands using different low flying airborne camera sensors embedded on UAV Drones (Román et al., 2022) achieving promising results with Support Vector Machine (SVM) i.e. 93.2% against the Random Forest (Raczko & Zagajewski, 2017) which yielded an Overall Accuracy of 90.8%. Other studies have integrated UAV and Lidar techniques approach (Zhu et al., 2019) in mapping mangrove within sub-tropical estuarine ecosystems, hence improving their detection rate by > 90%.

The availability of Sentinel products by the Copernicus programme through the European Space Agency (ESA) have enabled the availability of free access mid-resolution optical multispectral and radar-based imageries (Val et al., 2022) which have also been used for flooded vegetation detection. (Lebourgeois et al., 2017) used a combination of High Spatial Resolution (HRS) time series of Sentinel-2, Very High Resolution DEM and in addition some spectral and textural indices to map small holder agricultural systems using Random Forest ensemble algorithm.

The authors achieved high overall accuracy 91.7% on croplands and 64.4% on cropland sub-classes. In another study, (Nzimande et al., 2021) used Sentinel-2 Multispectral Imager to map the yellowwood tree (*Podocapus henkelii*) in Wezangele forest, South Africa. The authors generated 5 classes using spectral bands and indices, with the combined features realizing 80% Overall Accuracy against the single spectral band image which yielded an OA of 67%.

Amani et al., 2019, used Landsat 8 Multispectral imagery to create a new Canadian Wetland Inventory (CWI) considering five wetland classes outlined in the Canadian Wetland Classification Systems (CWCS) namely bog, fen, marsh, swamp and shallow water. The authors provided a comprehensive updated CWI with location and spatial extent of features, citing that an estimated

36% of Canada is covered by wetlands. The classification accuracy achieved over an area coverage of ~10square kilometers was 71%, with producer (66%) and user (63%) accuracies respectively. (Muñoz et al., 2019b) used an Object Based Analysis in conjunction with Random Forest (RF) hyper parameter adjustments to map complex salt marsh ecosystems in different wetlands across the United States of America (USA), namely weeks bay (Alabama), Savanna estuary (Georgia) and Fire Island (New York) hence yielding an OA of 91%, 97% and 95% respectively.

Time series on wetlands involve detection and monitoring of biophysical, spectral and spatial changes observed over time. The integrity of the final results would always depend on the underlying classification accuracy derived from the single date imageries. The term 'time series' in the context of vegetation monitoring relates to change detection over time of a discrete entity in space and time. Land cover changes can be related to natural processes such as floods and landslides. The rate of change and nature of land cover transition are also bound to change in space and time. Land cover transformation and transition are different due to the fact that some areas such as permanent forests remain intact while others such as urban and flooded vegetated areas undergo dynamic change over short periods of time.

According to (Kennedy et al., 2014), identifying spatial and temporal patterns through analysis and interpretation of frequent land cover maps provide insights into underlying processes and drivers of change. Maps relating to change between two dates would rarely give information on persistent of change (Panigrahi et al., 2019), hence more than two dates need to be engaged to enable insights into the transformation involved in the target area of study. Previous findings by (Lambin et al., 2003) emphasized the importance of considering rapid change transformation such as inter-annual change. This is confirmed by other studies carried out by National and International

Agencies that produced CORINE cover map of Europe and the EOSD Land Cover Map, Canada based within temporal periods of 1-3 year intervals using Landsat SITS. These national land cover maps programs have been operational since the early 1990's and 2000's (Feranec et al., 2016; Wulder et al., 2003).

Time series have been engaged in many studies, demonstrating trends on both discrete and environmental phenomena using both optical and radar-based datasets such as detection of salinity stress on rice crops using MODIS V1 datasets (Paliwal et al., 2019), assess vegetation dynamic change in tropical arid ecosystem using MODIS time series (Reddy et al., 2020), monitoring land disturbance using Landsat datasets (Zhu et al., 2020), forest disturbance trends using Landsat time series datasets (Masek et al., 2013), spatial-temporal dynamics of water surface change using Landsat time series datasets (Tulbure andBroich, 2013), detecting forest disturbance using pixel-based (LandTrendr) temporal segmentation algorithm on yearly based Landsat datasets (Kennedy et al., 2010), detection of temporary flooded vegetation using Sentinel-1 time series datasets (Tsyganskaya et al., 2018), land cover mapping using combined time series of Sentinel-1 and Sentinel-2 datasets using multi-source deep learning architecture (Ienco et al., 2019).

In this study we investigated the issues for generating and validating temporal time series maps from the high spatial resolution (~0.5metres) Pleiades-1A datasets to support monitoring of riparian vegetation disturbance. Specifically, we focus on the time series of the *Acacia xanthophloea* tree species disturbance around Lake Nakuru National Park. In addition, we hypothesized that Pleiades-1A datasets spectral bands incorporated with OBIA and machine learning techniques, could lead to the realization of promising classification accuracy to be used for wetland ecosystem disturbance and characterization.

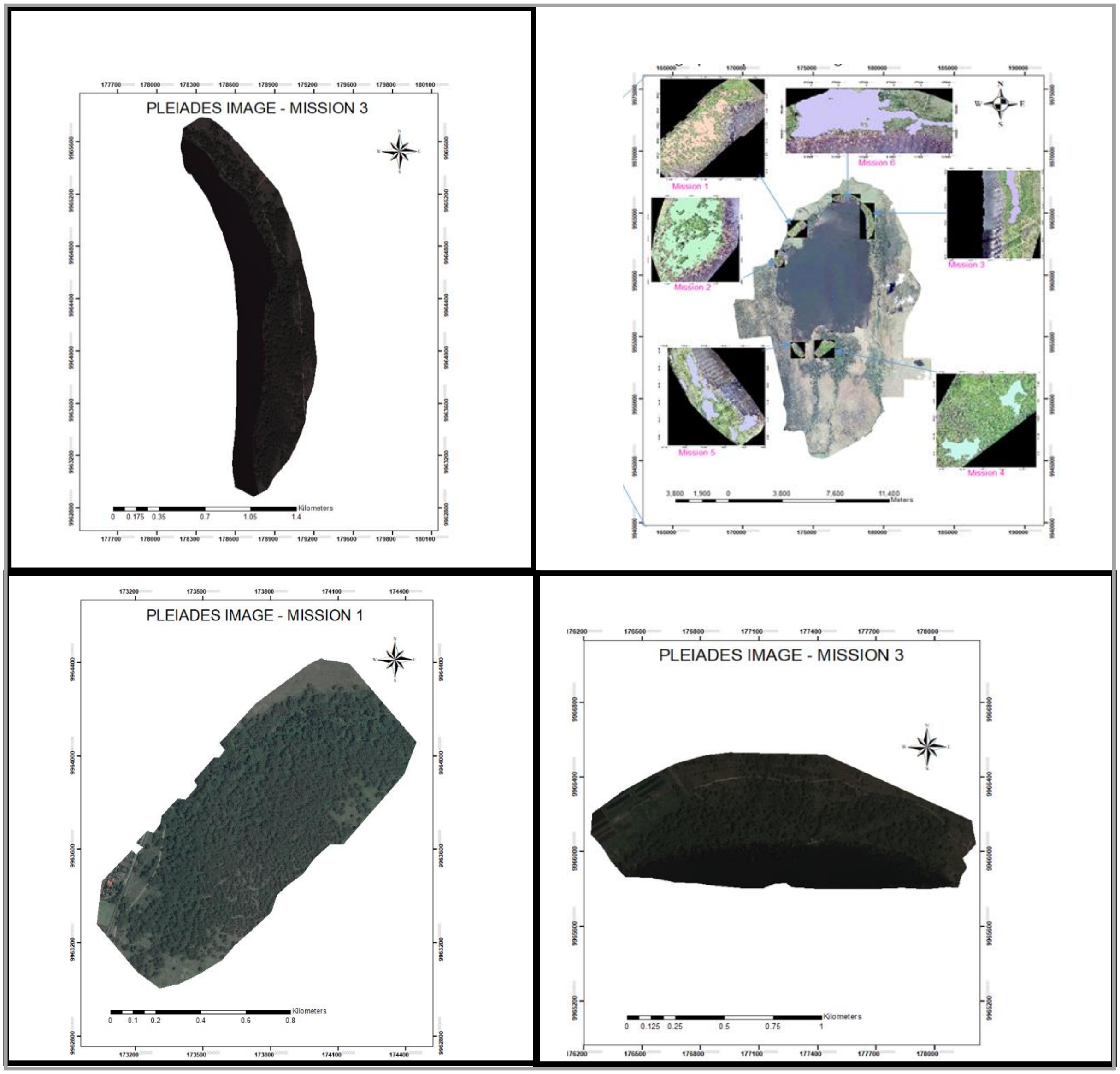

Figure 8.1: The three PLEIADES-1A Imagery based on the UAV missions around Lake Nakuru.
Source: Pléiades© CNES (27/10/2012) and AIRBUS DS

8.2 MATERIAL AND METHODS

8.2.1 Data Capture

The data used in this study was collected from https://pleiades.stoa.org/places and donated by Airbus Defense and Space Company, located at Toulouse France. Pleiades-1A is an optical sensor based satellite of sun-synchronous orbit, located at an altitude of 694kms above the earth surface. It covers a swath width of 20 kilometers with a daily revisit to any part of the globe. Four Pleiades-1A files were unzipped and added into ArcGIS 10.5 environment for the purpose of image visualization. Each file contained Multispectral Image Bands with their corresponding Panchromatic bands, dated 27/10/2012, 13/03/2016, 16/12/2018 and 21/03/2020 respectively. The imageries were projected at WGS 84 Transverse Mercator.

8.2.2 Data Pre-processing

In this subsection, data pre-processing steps are engaged on the Pleaides-1A Imageries which include i) pan-sharpening, ii) image subsetting, iii) radiometric calibration, iv) atmospheric correction.

The multispectral bands in Pleiades-1A image spectral bands had the following specifications in terms of spectral range: Blue (450nm-530nm), Green (510nm-590nm), Red (620nm-700nm) and Near-Infra-Red (775nm-915nm) with the initial Ground Surface Distance (GSD) of 2.0metres. Pleiades-1A Pan band (470nm-830nm) consisted of panchromatic imageries of 16bits pixel depth, unsigned integer being the pixel type of a 0.5m by 0.5m GSD. The 4-band Multispectral imageries were used as an input images, while the panchromatic bands used for pan-sharpening the MS imageries of the four Pleiades-1A sets of imageries, using Gram-Schmidt algorithm in ArcMap.

The second step involved sub-setting the 3 sample plots from the pan-sharpened imageries whose spatial resolution had improved from 2m to 50cm. Area of Interest (AOI) of the previously captured UAV missions around Lake Nakuru were used as shown on Figure 8.1. For the purpose of this study, the AOI's for Mission 1 (0.92sq kms), Mission 3 (1.5 sq. kms) and Mission 6 (1.3sq kms) were adopted. The choice of the three plots were purposive, meaning that the samples were chosen due to the flood dynamism around the specific areas, as noted from our previous study (Osio et al., 2022) on Acacia xanthophloea detection and classification using UAV imagery .

The second step involved the conversion of the radiance image (subset of pan-sharpened multispectral image) from the TIFF format to ENVI header file and final conversion into ASCII file. Fast-Line-of-sight Atmospheric Analysis of Spectral Hypercube (FLAASH) Module inherent in ENVI 5.3 provides a means of compensating for atmospheric effects from airborne sensors. The model estimates aerosol and haze amounts from an image with selected pixels from areas covered by Land. This method is based on observations previously made by (Felde et al., 2004) using a nearly-fixed ratio between the reflectance of such pixels at 660nm and 2100nm (ENVI, 2009).

8.2.3 Reference data

The reference data used in this study are the Very High Resolution (VHR) optical-based imageries captured by UAV flights around Lake Nakuru Riparian Reserve. The plots (UAV Missions) as used in recent works by (Osio et al., 2022) were adopted in this study for the sake of consistency on the Pleiades time series images. Training samples depicting different land uses and land covers were collected from each of the three selected UAV-related plots, which were later implemented in their corresponding AOI on Pleiades time series imageries (Effiom et al., 2019).

The GCP's collected during the UAV flights (Osio et al., 2022) were used for Ground Truth during the Accuracy Assessment steps in eCognition Developer Definiens software environment. Other reference data was the topographical map of Nakuru at scale 1:50,000 to be used for map to image registration (Yaseenet al., 2012) especially during the image differencing process in ENVI classic Software (ENVI, 2009). UAV imageries being of finer spatial resolution (~5cm) collected in September,2021 are suitable for use as reference against the Pleiades-1A whose spatial resolution was ~50cms (Effiom et al., 2019). The detailed vegetation map produced by (Ng'weno et al., 2010a) was instrumental in thematic map class visualization and comparisons.

8.3 DATA ANALYSIS

On each times series Pleiades imagery, experiments were carried out using multiresolution segmentation with scale=80, shape=0.6 and compactness=0.8, and giving more weight to the Near-Infra-Red (NIR) band. The mean of Red (1), Green (1), Blue (1) and NIR (2) bands were also included in the classification. Geometric features such as shape index, ecliptic fit, roundness and rectangular fit were completing the set of features.

The shape files and the .CSV files associated with each classified time series imageries were exported into ARCGIS 10.5 environment for post-processing. Post-classification involves fresh color coding schemes and layouting for the sake of uniformity. The .CSV files were important in the generation of results using classical algorithms in WEKA machine learning software (Camargo et al., 2019) i.e. J48, Binary Support Vector, Naïve Bayes and the ensemble Random Forest. Each of the classifier's performance was tested on each time series dataset which was initially generated in eCognition Developer 10.2. The modes of classification were also explored including full training, data split in 2/3 for training and 1/3 for testing, and 10-fold cross-validation. OBIA supervised classification was appended on the different datasets from different dates in order to find out the best classification models. This study aims to fulfil the following objectives:

i) To test the capability of OBIA analysis on VHR time series of Pleiades -1A imageries

ii) To analyze the importance of machine learning on OBIA classification scheme

iii) To quantify the contribution of (ii) to the classification accuracy

iv) To quantify change by implementing post-classification comparisons on the target classes

8.4 CLASSIFICATION ACCURACY

Random Forest classification achieved best across the three-time series datasets an OA score of 80% and a Kappa of 0.78. Other classical algorithms that follows include J48 with average OA of 73.7% and Kappa 0.69, Naïve Bayes, OA 66.2% and Kappa of 0.64, Binary SVM, OA 63.3% and Kappa 0.60 respectively (see Table 8.1).

Cross-validation (10-fold) approach achieved average OA of 92% and Kappa (0.87) across all the algorithms. The full training approach achieved 91.9% OA and Kappa (0.9), while the 2/3 train and 1/3 test approach yielded an OA of 84% and Kappa (0.81).

The average Random Forest classification achieved in Mission 3 was with OA of 87.5% and Kappa (0.86), Mission 1 yielded an OA of 79.5% and Kappa (0.77) and Mission 6 an average RF with an OA of 72.1% and Kappa (0.71) respectively.

Table 8.1: Classification Approach and Accuracy on Time Series Pleiades imageries (2012-2020)

Approach	Classification Algorithm Applied (Mission 1)							
	Random Forest		J48		Binary SVM		Naïve Bayes	
	OA	Kappa	OA	Kappa	OA	Kappa	OA	Kappa
Cross-validation	72.5%	0.70	66.4%	0.62	66.6%	0.62	69.8%	0.65
2/3 Train 1/3 Test	66.2%	0.61	60.6%	0.57	61.8%	0.60	64.3%	0.62
Full Training	100%	1.0	85.9%	0.80	67.1%	0.64	69.7%	0.66
	Classification Algorithm Applied (Mission 3)							
	Random Forest		**J48**		**Binary SVM**		**Naïve Bayes**	
	OA	**Kappa**	**OA**	**Kappa**	**OA**	**Kappa**	**OA**	**Kappa**
Cross-validation	81.94%	0.79	79.6%	0.72	75.1%	0.70	74.2%	0.73
2/3 Train 1/3 Test	80.5%	0.79	78.1%	0.75	69.7%	0.68	74.3%	0.73
Full Training	100%	1.0	87.6%	0.84	75.2%	0.72	74.0%	0.73
	Classification Algorithm Applied (Mission 6)							
	Random Forest		**J48**		**Binary SVM**		**Naïve Bayes**	
Cross-validation	60.2%	0.58	66.2%	0.63	55.4%	0.51	59.8%	0.56
2/3 Train 1/3 Test	56.3%	0.54	51.2%	0.50	43.3%	0.42	49.8%	0.45
Full Training	100%	1.0	88.2%	0.83	55.9%	0.52	60.2%	0.60

8.4.1 Algorithm Performance

The performance between and amongst the algorithms used i.e., Naïve Bayes, Random Forest, J48 and Binary SVM was assessed using One Way Analysis of Variance (One Way ANOVA). It is a technique that is used to compare whether two sample's means are significantly different or not. In this study the classifier algorithms represent the groups as shown in Table 8.2. Each group had nine samples (Overall Accuracy values), each as shown on Table 8.1. To determine whether there was a significant difference between and amongst the groups, the F-statistic value has to be greater than the F-Critical value derived from the F-distribution Table (see Appendix)

Table 8.2: One Way ANOVA between and amongst the classifier algorithms

F-statistic value 3.03					
P-Value 0.04					
Data Summary					
Groups	**# of Samples**	**Mean**	**Standard deviation**		**Standard error**
Random Forest	9	79.74	17.33		5.78
J48	9	73.76	13.19		4.39
Binary SVM	9	63.34	10.41		3.47
Naïve Bayes	9	66.23	8.40		2.80
ANOVA Summary					
Source	**Degrees of Freedom (DF)**	**Sum of Squares (SS)**	**Mean Square (MS)**	**F-stat**	**P-value**
Between groups	3	1485.51	495.17	3.03	0.04
Within groups	32	5229.38	163.42		
Total	35	6714.89			

The values used to locate the F-critical values from the F-distribution Table (see Appendix 1) are the Degrees of Freedom (DF) values shown in Table 8.2. i.e. value 3 as the DF in the numerator and value 32 as the denominator. The F-Critical value derived from interpolating DF1 against DF2 was 2.901. Since the F-Statistic value is 3.03, then F-stat>F-Critical is achieved from the values they represent, i.e. 3.03 >2.90, meaning that there was a significant difference between and amongst groups at (P = 0.04) significant at $p<0.05$.

In order to determine which two groups had some significant difference between them, One Way ANOVA with Post-Hoc test analysis was engaged using the same sample groups and sizes shown on Table 8.2. The ANOVA Post-Hoc Tukey HSD results revealed that there was a significant difference between the results achieved using Random Forest and the Binary Support Vector Algorithm ($p = 0.04$) significant at $p<0.05$.

8.4.2 Time series analysis on classified imageries

Time series analysis involves change detection in a pixel as a unity of study. Change in a single pixel (pixelwise) can be either spectral (vegetation indices) or spatial (x, y) and are able to be detected through time e.g. from Time (t1) to Time (ti) as demonstrated by (Jönsson & Eklundh, 2004). On the other hand, OBIA time series involves the detection of both spatial and spectral values of image objects through time. For example OBIA time series has been applied in mapping paddy rice as shown in studies by (Cai et al., 2019) using time series of Sentinel-1 and Sentinel-2. In another study (Csillik et al., 2019) used Dynamic Time Warping (DTW) approach to carry out OBIA based time series on a combination of Landsat-MODIS imageries.

In this study, OBIA-based classification was implemented on each image within eCognition Developer 10.2 environment. The image objects which were exported into ARCGIS 10.5 were reclassified and color coding implemented on each thematic class for the sake of uniformity. Figure 8.1 depicts the time series of classified maps using Mission 1 AOI on Pleiades-1A satellite imageries.

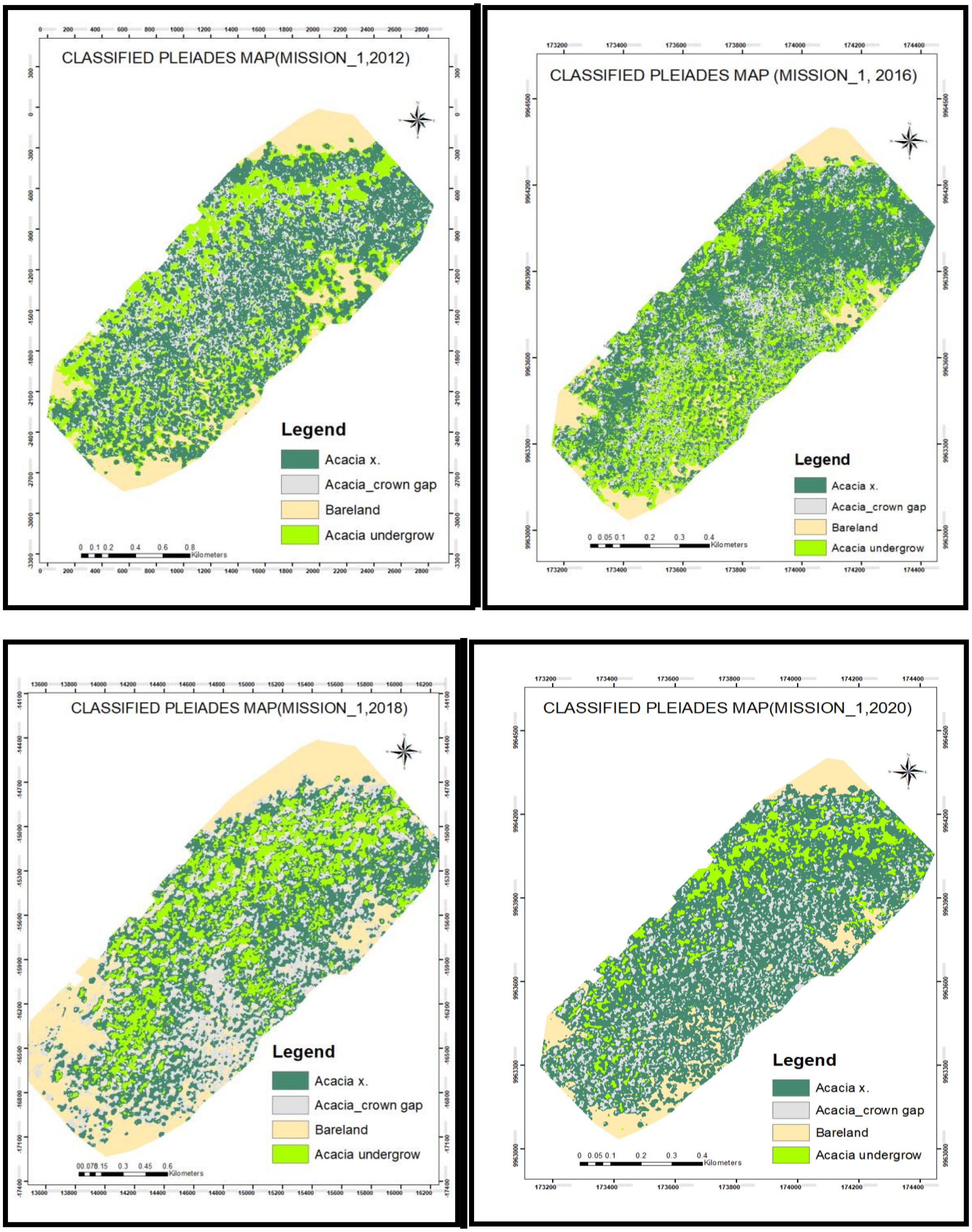

Figure 8.2: Time series on Mission 1 acquired from Pleaides-1A imagery **Source**: Pléiades© CNES (2012-2020) and AIRBUS DS

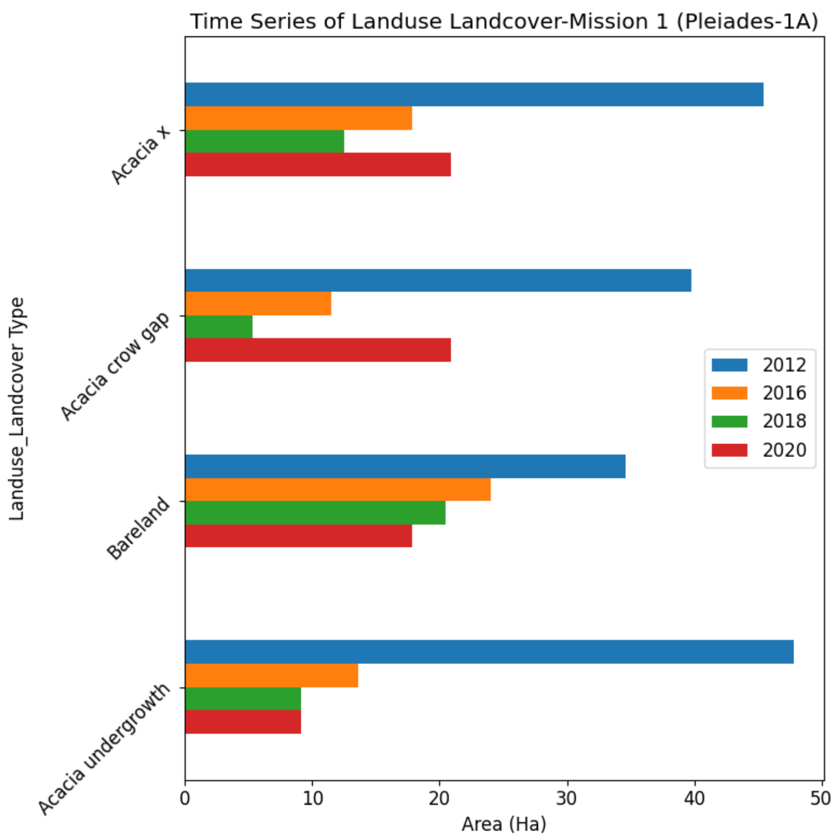

Figure 8.3: Spatio-temporal change on Acacia xanthophloea and related classes

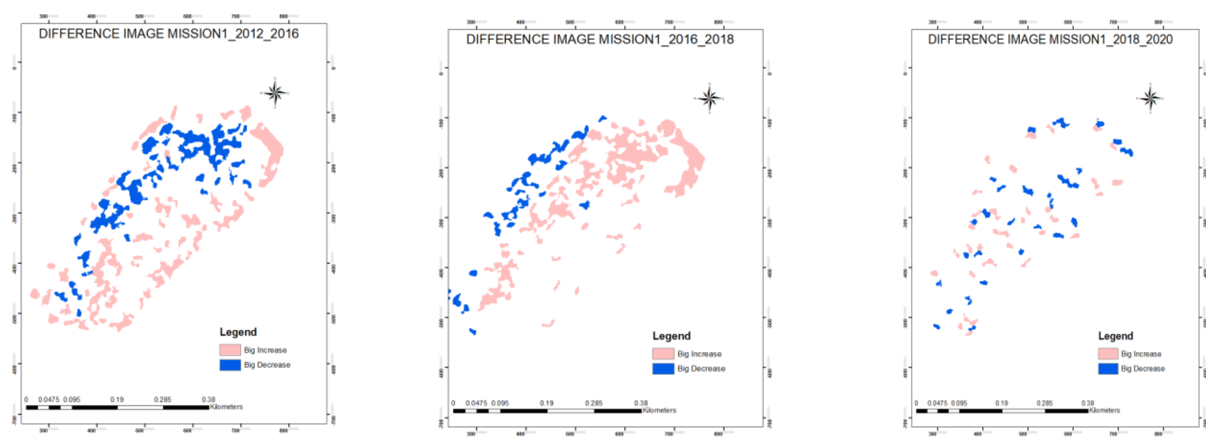

Figure 8.4: Image Differencing on Mission 1 of Pleiades imageries **Source**: Pléiades© CNES (2012-2020) and AIRBUS DS

8.4.2.1 **Spatial Temporal Analysis on Mission 1 Pleiades imageries**

Four classes were derived from Mission1 as follows: Acacia xanthophloea, Acacia crown gap, Acacia undergrowth and Bareland. Statistical counts in relation to the classes enabled calculation in hectares on each thematic land cover (post-classification comparison) as shown on the graph in Figure 8.2. The second approach used was image differencing (Yaseenet al., 2012) in ENVI classic software (ENVI, 2009) as shown with the results in Figure 8.3. According to the post-classification approach, it was evident that between year 2012 and 2016, there was a decrease in the crown area of Acacia xanthophloea by 27.7ha, Acacia crown gap (28.3ha), Acacia undergrowth (34.2ha) and Bareland (10.6ha). Between years 2016 and 2018, the same thematic land cover classes continued to decline revealing a decrease of 5.3ha on Acacia xanthophloea crown area class i.e. 'Acacia crown gap' (6.2ha), Acacia undergrowth (3.5ha) and Bare ground (4.5hac) respectively. Contrary post-classification results were experienced between 2018 and 2020. In this period an increase of 8.4ha was noted on class Acacia xanthophloea, likewise an increase noted on class Acacia crown gap by 15.6ha while the Acacia undergrowth increased by 2.7ha. The area covered by the bare ground remained the same (9.1ha) hence no increase (0ha) was experienced during the period under review i.e. 2018-2020. Figure 8.3 shows the differencing images generated from Mission 1 AOI of Pleiades time series maps.

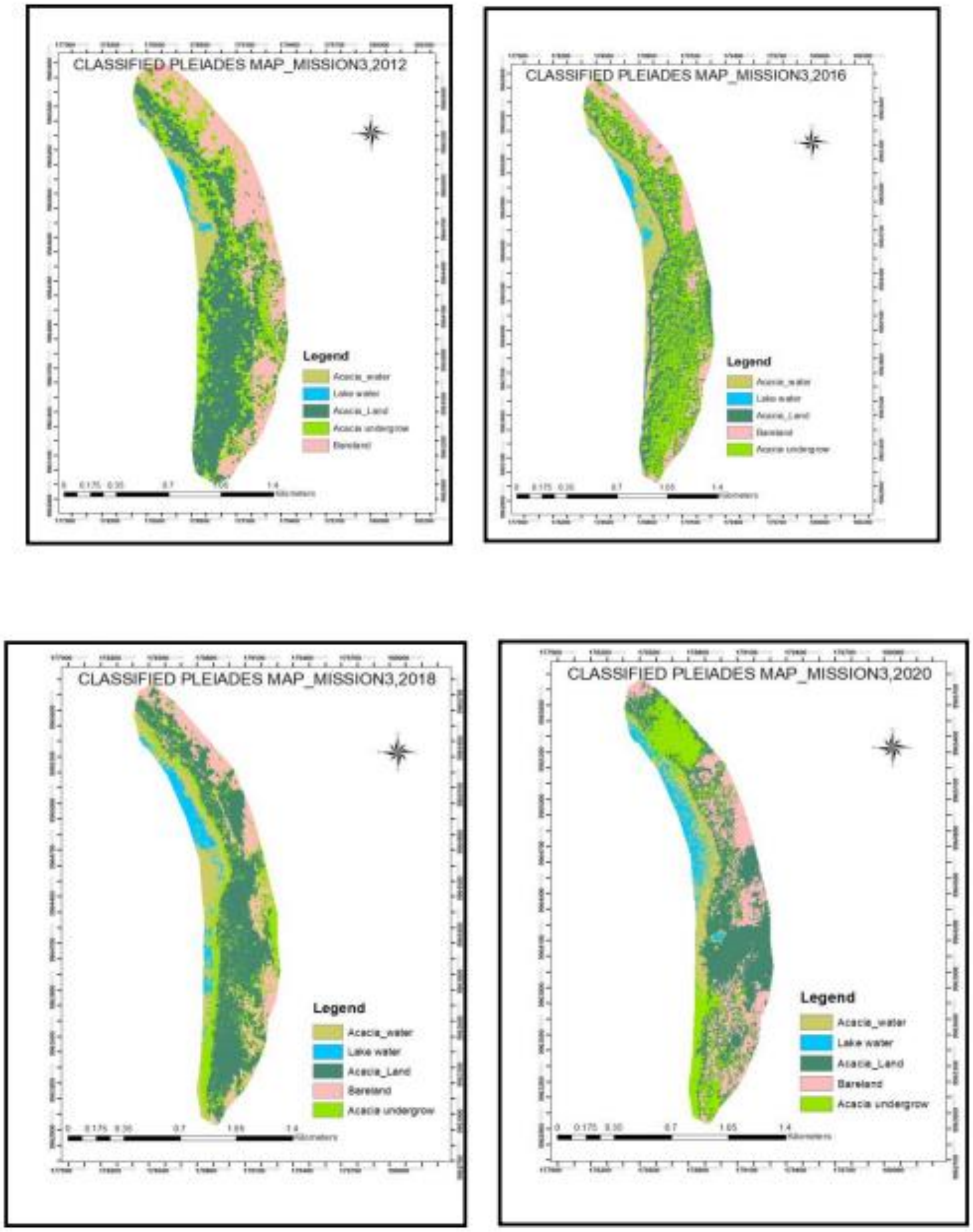

Figure 8.5*:* Time series on Mission 3 acquired from Pleaides-1A imagery **Source**: Pléiades© CNES (2012-2020) and AIRBUS DS

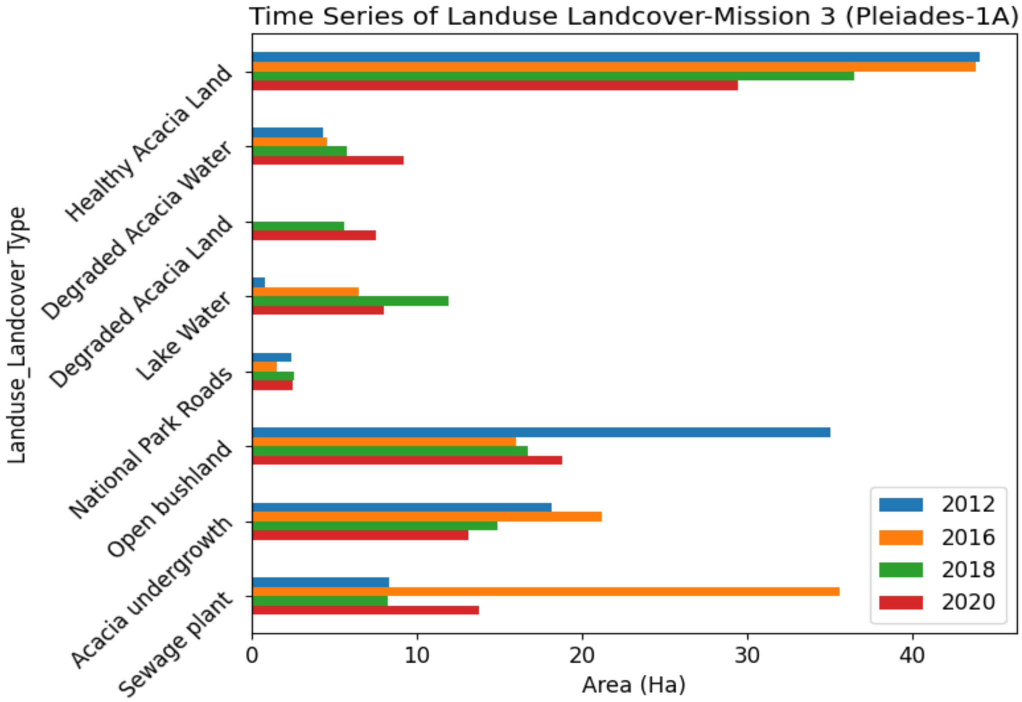

Figure 8.6: Spatial change on Acacia xanthophloea and related classes-Missio3

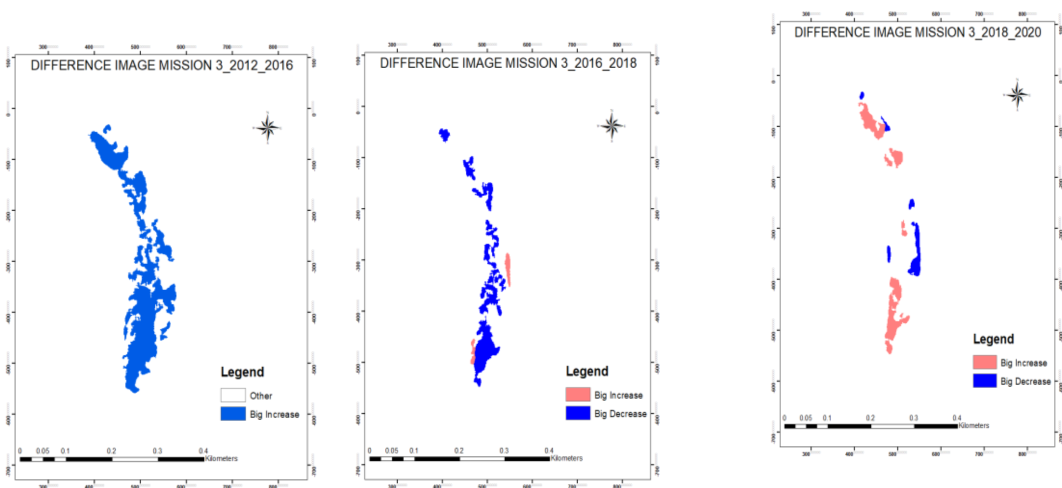

Figure 8.7: Image Differencing on Mission 3 of Pleiades imageries. **Source**: Pléiades© CNES (2012-2020) and AIRBUS DS.

8.4.2.2 **Spatial Temporal Analysis on Mission 3 Pleiades imageries**

Four classes were derived from Mission 3 as follows: Healthy Acacia Land, Acacia undergrowth, Degraded Acacia_water, Bareland and Lake water. Statistical counts in relation to the classes enabled calculation in hectares on each thematic land cover (post-classification comparison) as shown on the graph in Figure 8.6. The second approach used was image differencing (Yaseenet al., 2012) in ENVI classic software(ENVI, 2009) as shown with the results in Figure 8.7.

According to the post-classification approach, it was evident that between year 2012 and 2016, there was a decrease in the area covered by the class Healthy Acacia by 24.7ha, Acacia undergrowth an increase of 5.1ha, Degraded Acacia_water, Lake water an increase of 0.2ha and a decrease in class bareland by 18.5ha.

Between years 2016 and 2018, an increase of 13.5ha on the area covered by class Healthy Acacia Land was noted while Acacia undergrowth declined by 19.0ha. Under the same period, area covered by Degraded Acacia_water increased by 0.6ha, increase in class Lake water by 3.8ha and likewise an increase in bare land (1.4ha).

During the period 2018-2020, a decrease (5.4ha) in class Healthy Acacia Land was noted. Increase in class Acacia Undergrowth by (1.8ha) and a decrease (0.95ha) in class Degraded Acacia_water. Further increase (0.5ha) was noted on class Lake water and on class Bareland by 4.ha. Figure 8.7 shows the differencing images generated from Mission 3-time series maps.

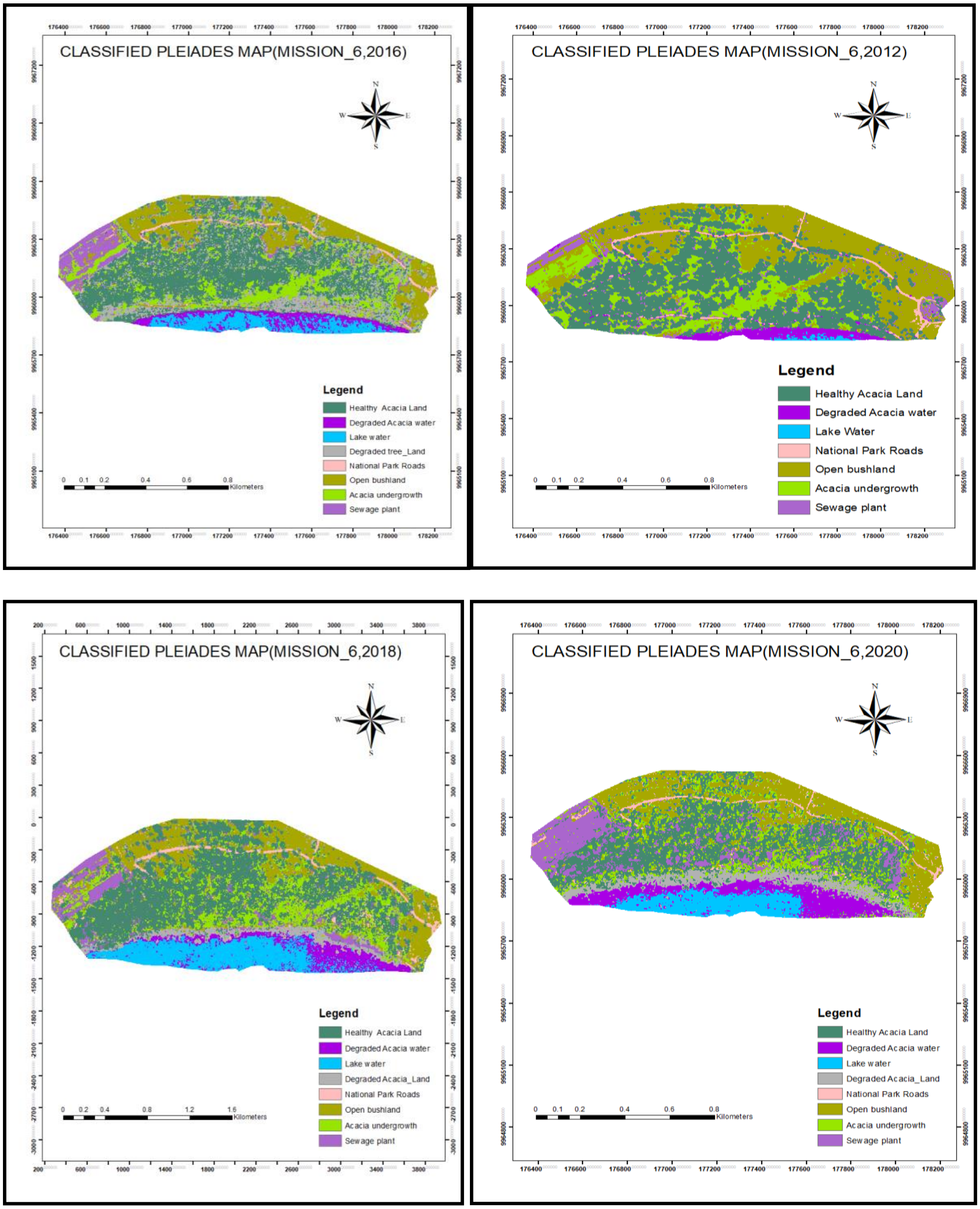

Figure 8.8: Time series on Mission 6 acquired from Pleaides-1A imagery **Source**: Pléiades© CNES (2012-2020) and AIRBUS DS

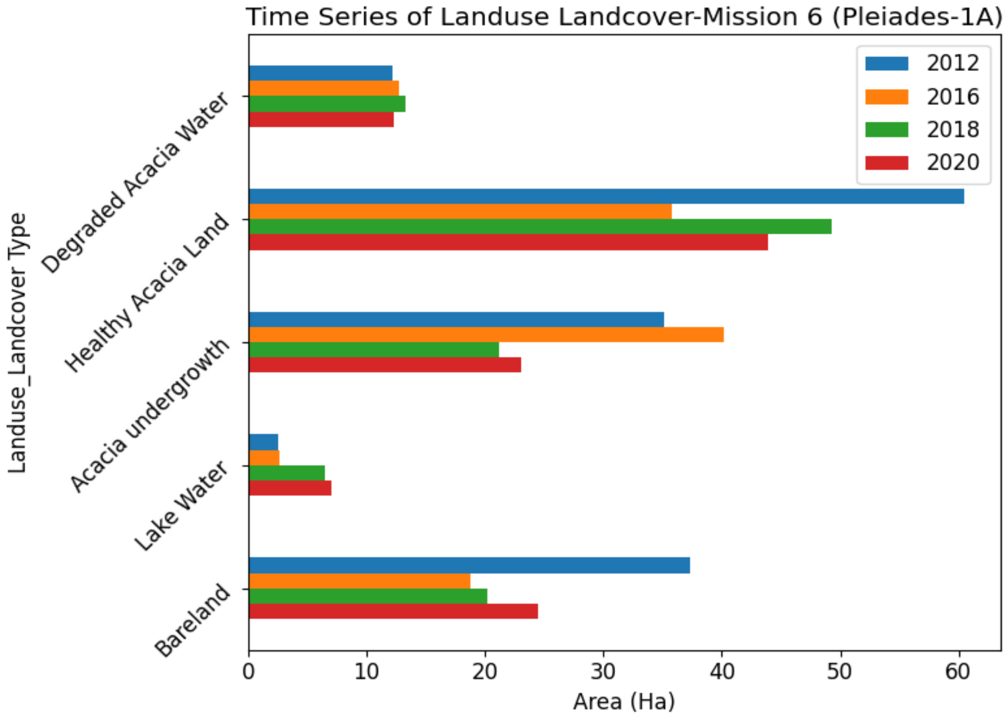

Figure 8.9: Spatial change on Acacia xanthophloea related to classes on Mission 6

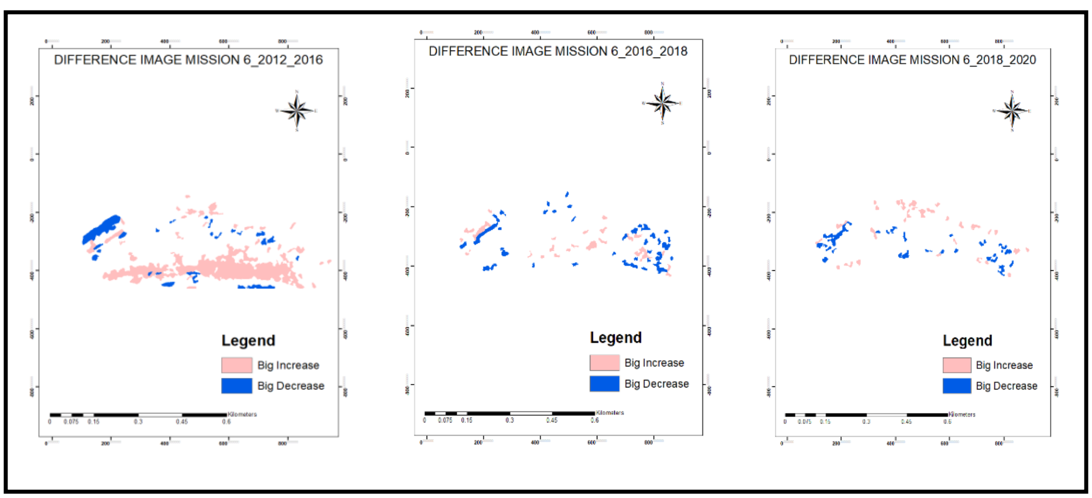

Figure 8.10: Image Differencing on Mission 6 of Pleiades imageries**. Source**: Pléiades© CNES (2012-2020) and AIRBUS DS

8.4.2.3 **Spatial Temporal Analysis on Mission 6 Pleiades imageries**

Classification carried out on the time series Pleiades imageries on mission 6 AOI revealed seven classes between 2012 and 2016 i.e. Healthy Acacia Land, Degraded Acacia_water, Lake water, National Park Roads, Open bushland, Acacia undergrowth and Sewage plant. Between 2016 and 2020, an additional class, i.e. Degraded Acacia Land was revealed. The graph on Figure 8.9 revealed the distribution of the thematic classes in hectares.

Between the year 2012 and 2016, a decrease in the class Healthy Acacia Land by 10.3ha was observed. More decrease was noted on the same thematic class by 7.3ha between 2016 and 2018. And a further decrease on the same class by 7.1ha during the 2018-2020 epoch. In the 2012-2016 epoch, degraded Acacia_water class increased by 0.3 ha and an increase (1.2ha) noted between 2016 and 2018 period of the same thematic class. A further increase of 3.4ha was noted from the same class during the 2018-2020 epoch. During the 2012-2016 period there was null (0) area covered by the class Degraded Acacia_Land, contrary to period 2016-2018 where an increase of Degraded Acacia_Land by 5.6ha was noted. Further increase by 1.5ha was noted between 2018 and 2020. The area covered by the Lake water on Mission 6 increased by 5.7 ha between 2012 and 2016. Moreover, an increase on the same class by 5.4ha was also noted between 2016 and 2018. However, a decrease of 3.9ha was noted to have occurred between 2018 and 2020.

National Parks are feeder roads within the Lake Nakuru National Park and help in park accessibility by both the park managers and tourists visiting the park. During all the period under review i.e. 2012-2020 the area covered by the park roads on mission 6 AOI remained constant at ~2.5ha. The area covered by bushland/grassland on the further northern part of the lake incurred different changes with a decrease of 19ha between 2012 and 2016. A slight increase of 0.7ha was experienced within the same thematic class. Further increase of 1.1ha was noted between the 2018-2020 epoch.

During the 2012-2016 epoch, Acacia undergrowth thematic class experienced an increase of 3.0ha. However, a decrease (6.3ha) was noted between 2016 and 2018 and a further decrease of 1.8ha during the 2018-2020 epoch. The open sewage plant located on the North Western part of Lake Nakuru National Park was noted to have increased in terms of area covered by surface water. During the 2012-2016 epoch, surface increase (27.2ha) was noted with a sharp decrease of (27.3 ha) noted between 2016 and 2018. However, an increase (5.51ha) of surface water was noted between 2018-2020 epoch. Figure 8.10 shows the differencing images generated from Mission 6 of Pleiades time series maps.

8.4.2.4 **Normalized Difference Vegetation Index (NDVI) time series on Mission 1 Pleiades**

NDVI being a measure of vegetation of vegetation health (Ozigis et al., 2018), it was implemented on all the Missions i.e. Mission 1 Mission 3 and mission 6 of Pleiades 1A Time series imageries respectively. The Red band of spectral range (620nm-700nm) and Near-Infra-Red (NIR) bands of spectral range (775nm-915nm) from the Pan-sharpened Multispectral Pleiades imageries collected between 2012 and 2020 were used to calculate NDVI’s of individual imageries as shown on Figure 8.11

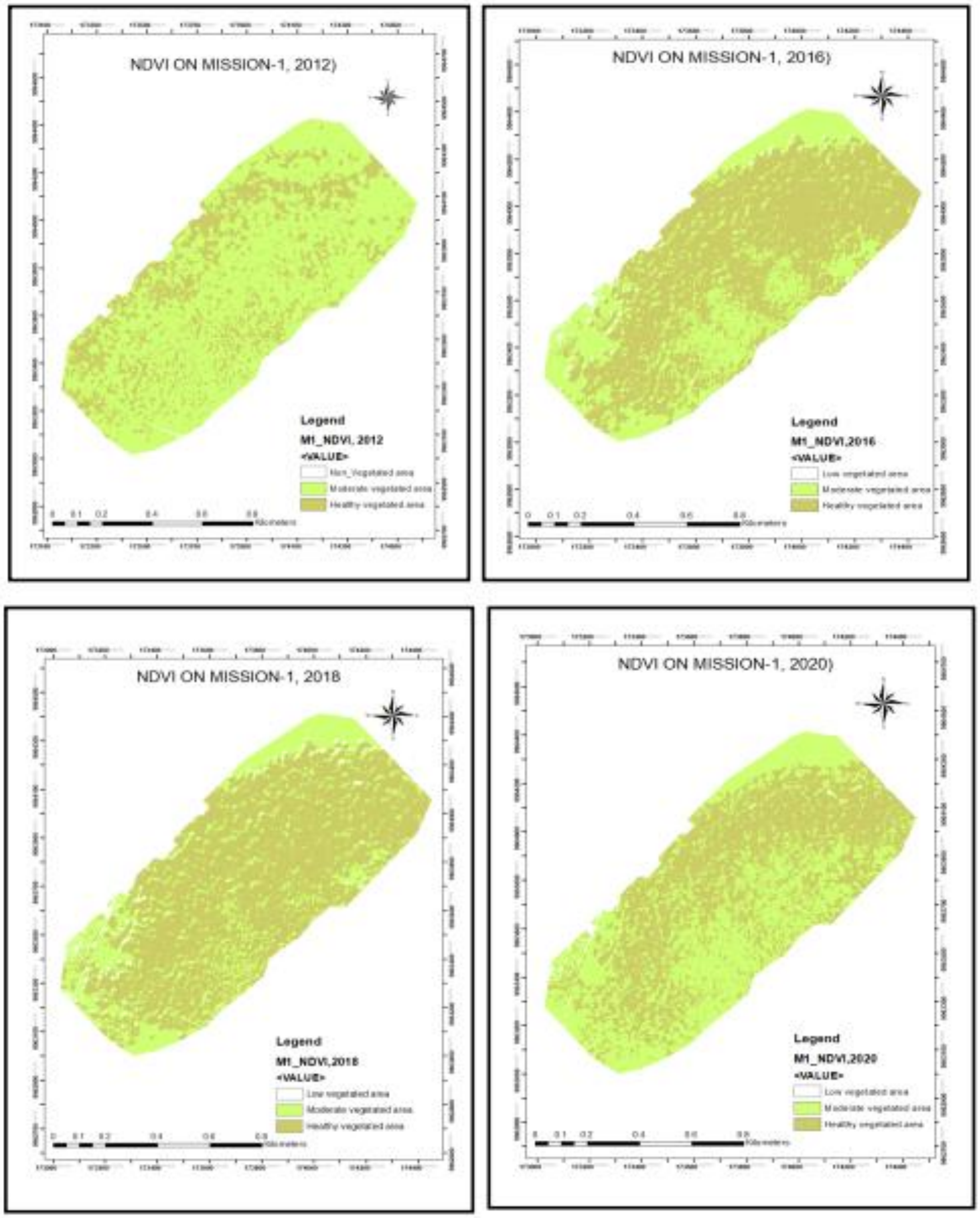

Figure 8.11: NDVI time series on Mission 1 Pleiades-1A imageries **Source**: Pléiades© CNES (2012-2020) and AIRBUS DS

The classification scheme that was used were pegged onto a range of NDVI spectral values as follows: <0 (Non-vegetated area), 0-0.2 (Low vegetated area), 0.2-0.5 (Moderate vegetated) area, 0.5-0.8 (Healthy vegetated area) and 0.8-1.0 (Very Healthy vegetated area) as demonstrated by (Southworth et al., 2004). Figure 8.11 depicts the state of vegetation health on time series of Mission 1 Pleiades imagery.

Three vegetation classes were obtained on each single date NDVI time series maps with maximum (Max) and minimum (Min) values obtained on each date i.e. 2012 (Max: 0.68, Min: -0.16), 2016 (Max:0.7, Min: -0.4), 2018 (Max:0.6, Min: -0.5) and 2020 (Max:0.74, Min -0.11).

These NDVI values relate to the land cover classes generated from Mission 1 multispectral time series imageries as shown on Figure 8.11. Acacia xanthophloea relates to the healthy vegetated area, while Acacia undergrowth which consist of a mixture of bush/thicket and grasslands relates to the moderate vegetated areas. Low vegetated areas consist of class bareland. To test if there was any relationship between the land cover classes (see Figure 8.1) and their corresponding NDVI (see Figure 8.11), Pearson's Correlation coefficient was used. The results indicated that there was a strong positive correlation (R = 0.87) between the areas covered by the Acacia xanthophloea, Acacia undergrowth and bareland against their NDVI values in the year 2012. However, in the year 2016, a negative correlation (R = -0.5) was noted between the variables, meaning that as land cover variables decreased, the NDVI values also decreased. In the year 2018, a noted increase in land cover (vegetation regeneration) led to an improvement in the relationships between these variables (R = 0.67). Vegetation degradation was noted in the year 2020, which led to the reduction as shown by the weak positive correlation at (R = 0.4).

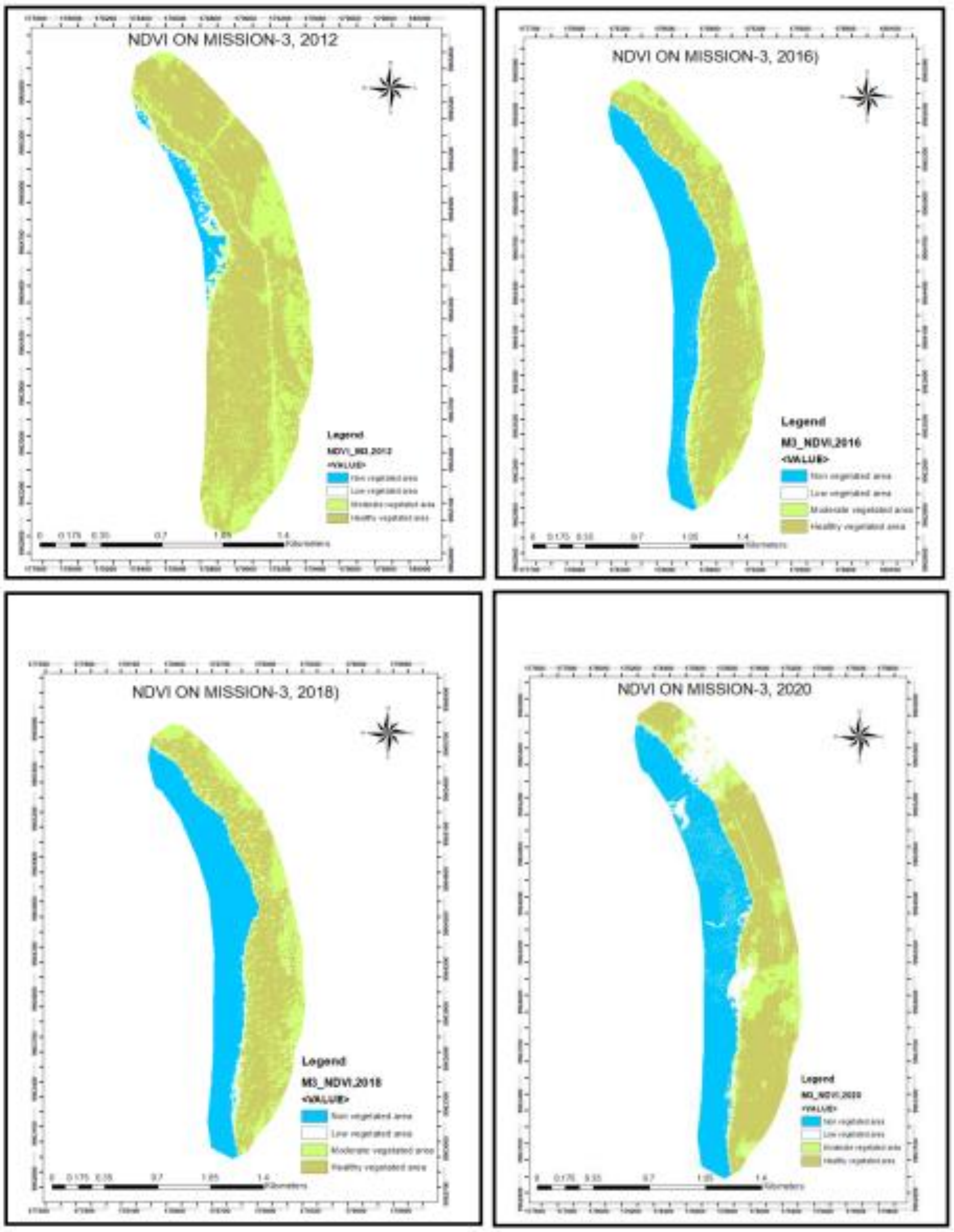

Figure 8.12: NDVI Time Series on Mission 3 Pleiades-1A Imageries **Source**: Pléiades© CNES (2012-2020) and AIRBUS DS.

8.4.2.5 **Normalized Difference Vegetation Index (NDVI) Time series on Mission 3 Pleiades**

Normalized Difference Vegetation Index (NDVI) time series was carried out on Mission 3 of Pleiades imageries captured between 2012 and 2020. NDVI has been used in remote sensing and ecology to characterize vegetation type, condition and amount including biomass (Jensen, 1996). Figure 8.12 depicts the type of classes captured based on previous studies by (Southworth et al., 2004).

The type of NDVI classes captured on Mission 3 NDVI time series include, Non_vegetated class (mainly sections of Lake Nakuru), Low Vegetated areas (mainly degraded Acacia on Water) as depicted on the land cover map in Figure 8.5, Moderate vegetated areas (mainly class Acacia undergrowth) and Healthy vegetated areas (Healthy Acacia on Land). Three vegetation classes were obtained on each single date NDVI time series maps with maximum (Max) and minimum (Min) values obtained on each date i.e. 2012 (Max: 0.65, Min: -0.44), 2016 (Max:0.65, Min: -0.16), 2018 (Max:0.60, Min: -0.48) and 2020 (Max:0.70, Min-0.97).

These NDVI values relate to the land cover classes generated from Mission 3 multispectral time series imageries as shown on Figure 8.13. To test if there was any relationship between the land cover classes (see Figure 8.5) and their corresponding NDVI (see Figure 8.13), Pearson's correlation Coefficient (Hammer et al., 2001) was used. The results indicated that there was a strong positive correlation (R = 0.97) between the areas covered by the class Healthy Acacia Land, Acacia undergrowth, bareland and lake waters against their NDVI values in the year 2012. The same scores were noted in the year 2016 where a strong positive correlation (R = 0.97) was achieved. However, in the year 2018, a slight decrease in their relationships between these variables (R = 0.89) was noted. Furthermore, in the year 2020, an improvement in the correlation between the land cover and the NDVI values was noted with a strong positive correlation (R = 0.96).

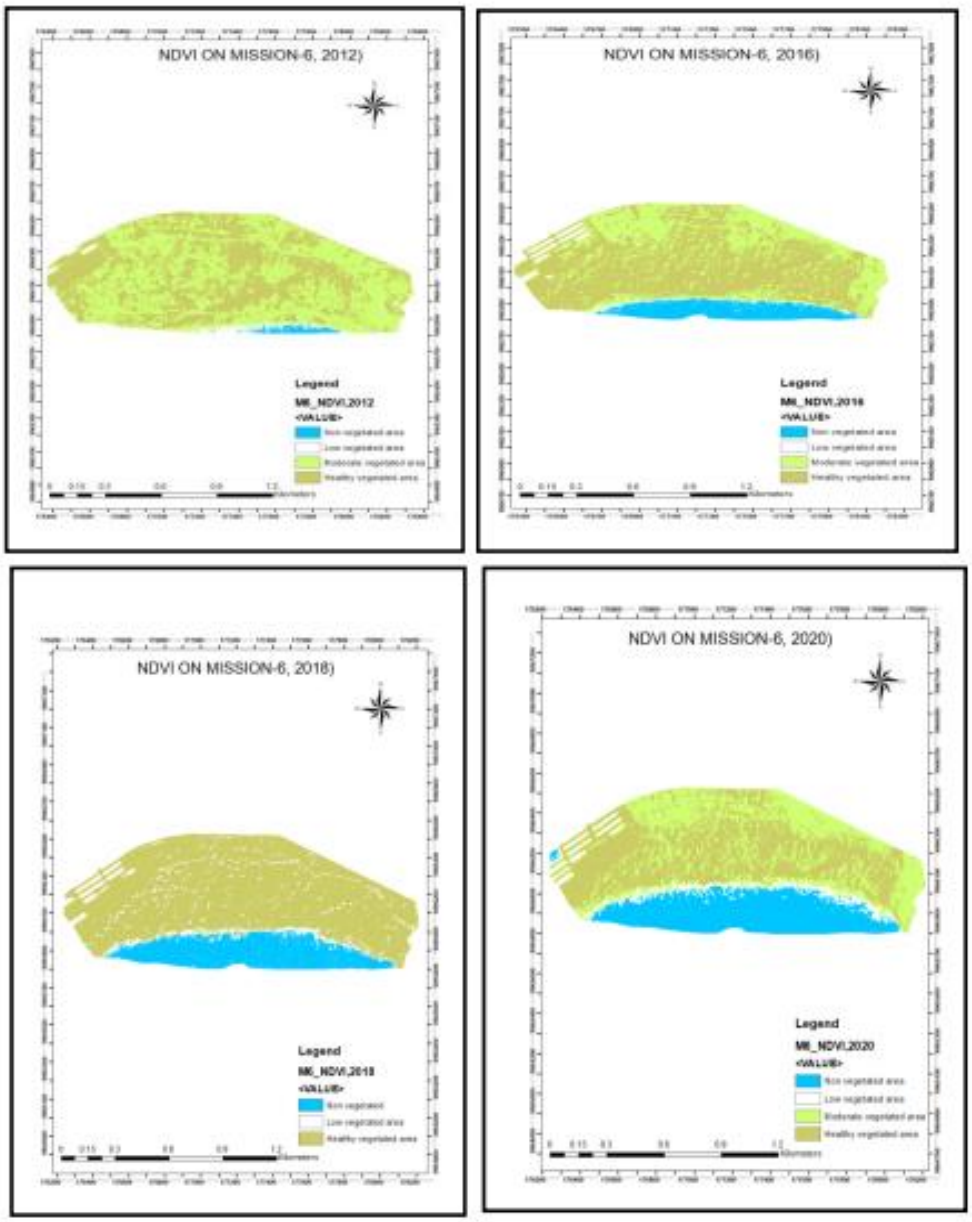

Figure 8.13: NDVI Time Series on Mission 6 Pleiades-1A Imageries **Source**: Pléiades© CNES (2012-2020) and AIRBUS DS.

8.4.2.6 **Normalized Difference Vegetation Index (NDVI) Time series on Mission 6 Pleiades**

Normalized Difference Vegetation Index (NDVI) time series was carried out on Mission 6 of Pleiades imageries captured between 2012 and 2020. This method has been applied in remote sensing studies to characterize vegetation as demonstrated by (Prasad et al., 2005). Figure 8.13 depicts the type of classes captured based on previous studies by (Southworth et al., 2004).

The type of NDVI classes captured on Mission 6 NDVI time series include, Non_vegetated class (mainly sections of Lake Nakuru), Low Vegetated areas (mainly degraded Acacia on Water) as depicted on the land cover map in Figure 8.8, Moderate vegetated areas (mainly class Acacia undergrowth) and Healthy vegetated areas (Healthy Acacia on Land). Three vegetation classes were obtained on each single date NDVI time series maps with maximum (Max) and minimum (Min) values obtained on each date i.e. 2012 (Max: 0.65, Min: -0.51), 2016 (Max:0.65, Min: -0.16), 2018 (Max:0.71, Min: -0.99) and 2020 (Max:0.71, Min: -0.69).

These NDVI values relate to the land cover classes generated from Mission 6 multispectral time series imageries as shown on Figure 8.13. To test if there was any relationship between the land cover classes (see Figure 8.8) and their corresponding NDVI (see Figure 8.13), Pearson's Correlation coefficient was used to calculate the correlation between the land cover types and their corresponding NDVI values as demonstrated by (Hammer et al., 2001). The results indicated that there was a strong positive correlation ($R = 0.89$) between the areas covered by the class Healthy Acacia Land, Acacia undergrowth, Degraded Acacia_water and lake waters against their NDVI values in the year 2012. Similar results were achieved by (Whistler et al., 1995) in the characterization of land use / land cover using Landsat time series imageries. The same scores were noted in the year 2016 where a strong positive correlation ($R = 0.89$) was achieved. However, in the year 2018, a moderate positive relationship between these variables (R = 0.68) was noted. Furthermore, in the year 2020, an improvement in the correlation between the land cover and the NDVI values was noted with a strong positive correlation (R = 0.88). The possibility of carrying out riparian vegetation characterization using Pearson's correlation to quantify the relationships between land cover and NDVI was also demonstrated by (Griffith et al., 2002b) resulting in a strong positive correlation(R = 0.80).

8.5 RESULTS AND DISCUSSION

The multispectral OBIA-RF model (T. M. Berhane et al., 2019) was the foundation onto which the time series study was laid. The most important target of study was Acacia xanthophloea tree species on the verge of extinction due to persistent flooding around Lake Nakuru, Kenya. Time series of Very High Resolution (VHR) Pleiades imageries collected from Airbus Company in Toulouse, France were used in the classification. Several classical and machine learning ensemble algorithms appended on the Pleiades-1A spectral bands and in addition some shape variables i.e., rectangular fit, Border index, Shape index and Roundness were engaged in the detection of Acacia xanthophloea tree species and their related classes.

8.5.1 OBIA-Random Forest Model

Although OBIA-RF model (Berhane et al., 2019) had excellent results in all missions by achieving an OA of 100% and Cohen Kappa (1.0) using the full training approach, these results could have been attributed to its parameterization. In each RF classification, 100 bagging and 100 iterations were involved. However, the Average Random Forest (Huo et al., 2019) classification achieved was in Mission 3 with OA of 87.5% and Kappa (0.86), Mission 1 yielded an OA of 79.5% and Kappa (0.77) and Mission 6 an average RF with an OA of 72.1% and Kappa (0.71) respectively.

In the case of approaches used, cross-validation (10-fold) approach achieved average OA of 92% and Kappa (0.87) across all the algorithms. The full training approach achieved 91.9% OA and Kappa (0.9), while the 2/3 train and 1/3 test approach yielded an OA of 84% and Kappa (0.81).

Table 8.3: Random Forest based confusion matrix table (Mission 3 Pleiades)

Classified	Predicted							
	Unclassified	Bareland	Acacia_Land	Acacia under	Acacia water	Lake water	Total	UA
Unclassified	**181**	0	0	0	0	0	181	100%
Bareland	0	**69**	65	6	10	1	151	45.6%
Acacia_Land	0	15	**837**	62	6	3	923	90.6%
Acacia Under	0	1	155	**217**	0	0	373	58.1%
Acacia water	0	0	21	0	**90**	3	114	78.9%
Lake water	0	0	0	0	3	**52**	55	94.5%
Total	181	85	1078	285	109	59	**1797**	
PA	100%	81.1%	77.6%	76.1%	82.5%	88%		
OA	**80.1%**							

Table 8.3 shows the confusion matrix of an OBIA-RF (Berhane et al., 2019) derived from a classified Mission 3 of Pleiades imagery. The highest Producer's Accuracy (PA) and User's Accuracy (UA) from the vegetation-related classes were achieved from class Healthy Acacia_Land. (n=837) instances out of (n=923) were predicted as Healthy Acacia_Land, resulting in 90.6% User's accuracy (UA) and 77.6% Producer's accuracy (PA), confirming reports by (Moskal et al., 2011b) that mature trees tend to exhibit higher Producer's and User's Accuracy than the lower vegetation species. However, 14.3%instances were confused as class Acacia undergrowth and 0.2% instances confused as class Degraded Acacia in water, confirming reports by (Heumann, 2011b) that confusion between the low lying vegetation and the degraded vegetation in water was noted in their study. In the case of Acacia Undergrowth, (n=217) instances out of (n=373) were correctly predicted, resulting in 58.1% User's Accuracy (UA) and 76.1% Producer's Accuracy (PA). However, 21.8%instances were confused as class Healthy Acacia Land (Camargo et al., 2019).

In the other hand, (n=90) instances out of (n=114) were correctly predicted as Degraded Acacia_water, resulting in 78.9% User's Accuracy (UA) and 82.5% Producer's accuracy (PA).

However, 0.6% instances were incorrectly classified as Healthy Acacia_Land and the other 0.5%as Degraded Acacia water (Camargo et al., 2019). According to (Landis & Koch, 1977), an Overall Accuracy (OA) of 80.1% achieved was accurate enough to allow for time series mapping on Mission 3 of Pleiades-1A imageries collected between 2012 and 2020.

Table 8.4: Random Forest based confusion matrix table (Mission 1 Pleiades)

Classified	**Predicted**						
	Bareland	Acacia xanth	Acacia crown gap	Acacia undergrowth	Unclassified	Total	**UA**
Bareland	**317**	50	4	9	0	380	**83.4%**
Acacia xanth	11	**887**	54	107	0	1059	**83.7%**
Acacia crown gap	5	45	**714**	141	0	905	**78.9%**
Acacia undergrowth	0	52	85	**1510**	0	1647	**91.6%**
Unclassified	0	0	0	0	**8**	8	**100%**
Total	333	1034	857	1767	8	**3999**	
PA	**95.1%**	**85.7%**	**83.3%**	**85.4%**	**100%**		
OA	**85.9%**						

Table 8.4 shows the confusion matrix of an OBIA-RF derived from a classified Mission 1 of Pleiades imagery. Highest Producer's Accuracy (85.4%) and User's Accuracy (91.6%) were realized by class Acacia Undergrowth. (n=887) instances out of (n=1059) were predicted as Acacia xanthophloea, resulting in 83.7% User's Accuracy (UA) and 85.7% Producer's Accuracy (PA), hence contracting studies by (Moskal et al., 2011b), (Heumann, 2011b) that mature trees and their crown tend to exhibit higher UA and PA than the low vegetation. However, 0.4% instances were confused as class Acacia crown gap and 0.5% instances as class Acacia undergrowth (Camargo et al., 2019).

In the other hand, 714 instances out of 905 were correctly predicted as Acacia crown gap, resulting in 78.9% User's Accuracy (UA) and 83.3% Producer's accuracy (PA). However, 0.6%instances were incorrectly classified as Acacia xanthophloea and the other 1.0% as Acacia undergrowth (Cian et al., 2018). Acacia undergrowth had (n=1510) instances out of (n=1647) correctly predicted at 91.6% User's Accuracy (UA) and Producer's Accuracy (PA) of 85.4%.

However, 0.8% instances were incorrectly classified as Acacia crown gap and 0.6%instances as Acacia xanthophloea, confirming reports by (Camargo et al., 2019) that landscape complexity and heterogeneity can lead to confusion between vegetation classes. The multispectral OBIA-Random Forest approach (Huo et al., 2019) led to an overall classification accuracy (Congalton and Green, 2019) of 85.9% which according to (Landis and Koch, 1977) is accurate enough to allow for mapping of time series on Mission 1 of Pleiades-1A imageries collected during 2012-2020 period.

Table 8.5: Random Forest based confusion matrix table (Mission 6 Pleiades)

Classified	**Predicted**										
	Unclassified	H. Acacia Land	Acacia Land	Acacia Under	Open bush	Sewer	Park-Road	Acacia-water	Lake water	Total	UA
Unclassified	**110**	0	0	0	0	0	0	0	0	110	**100 %**
H.Acacia_L	0	**2022**	19	41	2	17	1	1	0	2103	**96.1 %**
D.Acacia-L	0	153	**384**	24	2	10	1	2	0	576	**66.7 %**
Acacia_Und	0	41	8	**473**	2	13	0	0	0	537	**88.0 %**
Open bush	0	3	4	3	**157**	2	0	0	0	168	**93.4 %**
Sewer	0	63	24	13	10	**414**	2	9	0	535	**77.4 %**
Park-Road	0	13	11	0	0	6	**83**	0	0	113	**73.5 %**
D.Acacia-w	0	0	1	0	0	3	1	**112**	2	119	**94.1 %**
Lake water	0	0	0	0	0	1	0	3	**78**	82	**95.1 %**
Total	110	2295	451	554	173	456	88	127	80	**4343**	
PA	**100%**	**88.1 %**	**85.1%**	**85.4%**	**90.7 %**	**90.7 %**	**94.3**	**88.1%**	**97.5 %**		
OA	**88.2%**										

Table 8.5 shows the confusion matrix of an OBIA-RF model derived from a classified Mission 6 of Pleiades imagery. Highest Producer's Accuracy (90.7%) and User's Accuracy (93.4%) among the vegetation classes were realized by class Open bushland/ grasslands on the northern part of the lake, hence contradicting reports by (Heumann, 2011b) that mature trees and their crown tend to exhibit higher User's and Producer's accuracy than the low vegetation. However, 0.6% instances were confused as Sewage surface water and 0.1% instances each for class Healthy Acacia Land, Degraded Acacia Land and Acacia undergrowth (Cian et al., 2018).

The target vegetation i.e. Healthy Acacia_Land had the second highest Producer's (88.1%) and User's (96.1%) Accuracy. However, 0.7% instances were incorrectly classified as Degraded Acacia on Land, Acacia undergrowth 0.2%, Open Sewerage plant 0.3% and National Park roads 0.01% respectively. Previous reports by (Osio et al., 2020) confirmed the heterogeneous nature of the Lake Nakuru riparian reserve, which could be the main cause of the confusion amongst classes. "Degraded Acacia in water" class (submerged trees) became third with a Producer's Accuracy of 88.1% and 94.1% User's Accuracy. 0.7% instances were incorrectly classified as open sewer, while 0.2% instances as Lake Water. This type of error was caused by the confusion in the spectral response of class "Lake water", which was mixed with submerged degraded Acacia trees. According to studies by (Heumann, 2011b) , the heterogeneous nature of riparian vegetation causes confusion between riparian species classes, especially when degradation is involved. Acacia undergrowth which consists of a mixture of Acacia saplings and grasslands became fourth having realized 85.4% (PA) and 88% (UA). However, 0.7% instances were confused as class Healthy Acacia_Land and 0.4%instances as class Degraded Acacia_Land (Camargo et al., 2019).

The Overall Accuracy (Congalton and Green, 2019) on the multispectral OBIA Random Forest model was 88.2% with a Cohen Kappa (0.83) which confirms accurate time series analysis on Mission 6 based Pleiades imageries (Landis andKoch, 1977).

8.5.2 Post Classification Approach

The purpose of carrying out post classification is to enable change detection (spectral or spatial) between given epoch(s) of the variables under study. In this study, 3 plots adopted from the AOI of the previous UAV missions were analyzed and hence their distribution reported herein.

According to (Lark et al., 2017), change detection can be reported as 'change' or 'no change' which is binary. On the contrary, post-classification comparison approach examines the changes over time between independently classified Land Cover or Land Use (Verburg et al., 2011)

8.5.2.1 Post-classification on Mission 1 times series

OBIA-RF based multispectral classification (Table 8.4) was carried out on the time series of Mission 1 with the graphical representation of the results shown in Figure 8.2. The essence of Land Use Land cover classification is to show the difference in spatial patterns of the variables under investigation (Liu et al., 2003). The Figure 8.1 shows the information

Table 8.6: Statistical Change Detection from Mission 1-Pleiades Time series

LULC Class	LULC-2012		LULC-2016		LULC-2018		LULC-2020		Area of Change(Ha)		
	Area (Ha)	%	Area (Ha)	%	Area (Ha)	%	Area (Ha)	%	2012-2016	2016-2018	2018-2020
A.xanth	45.5	27	17.8	26.7	12.5	26.3	20.9	30.4	-18.5	-5.3	+8.4
A.crown	39.8	24	11.5	17.2	5.3	11.2	20.9	30.3	-28.3	-6.2	+15.6
Bareland	34.6	20.5	24.0	35.9	20.5	43.3	17.8	25.8	-10.6	-3.5	-2.7
A under	47.8	28.5	13.6	20.2	9.1	19.2	9.1	13.5	-34.2	-4.5	0
Total	167.7	100	66.9	100	47.4	100	68.7	100			

Table 8.6 shows the results of the Acacia xanthophloea distribution in relation to other related classes. It was evident that the Acacia xanthophloea has been on the decline from the year 2012 as noted on the change between 2012 and 2018. However, an increase of 4.1% was noted between 2018 and 2020 which could have been attributed to Acacia xanthophloea regeneration (Titus, 1990), (Barančeková et al., 2007). Acacia crown gaps also had a reduction by 6.3% which were related to the Acacia xanthophloea trees crown. Other species that grew under the Acacia

xanthophloea such as bush/thicket and grasslands were also affected by the fallen Acacia xanthophloea (Colloff andBaldwin, 2010). Acacia undergrowth reduced by 15%between 2012 and 2018 an area which could have been replaced by the flooded vegetation and the fallen Acacia xanthophloea trees (Keram et al., 2019).

8.5.2.2 **Post-classification on Mission 3 times series**

OBIA-RF based multispectral classification (Figure 8.5) was carried out on the time series of Mission 3 with the graphical representation of the results shown in Figure 8.6. The significance of Land Use Land Cover classification is to show the difference in spatial patterns (Macleod & Congalton, 1998) of the variables under investigation as shown on Figure 8.5.

Table 8.7**:** Statistical Change Detection from Mission 3-Pleiades Time series

LULC Class	LULC-2012		LULC-2016		LULC-2018		LULC-2020		Area of Change Ha)		
	Area	%	Area	%	Area	%	Area	%	2012-2016	2016-2018	2018-2020
A.xanth.L	60.5	42.2	35.8	37.9	49.3	47.5	43.9	41.7	-24.7	+13.5	-5.4
A.Water	2.7	1.9	2.2	2.3	6.5	6.3	7.0	6.6	-0.5	+4.3	+0.5
A.under	40.2	28.0	35.11	37.3	21.2	20.4	23.01	21.8	-5.09	-19.0	+1.8
Lake W.	2.7	1.9	2.5	2.6	6.5	6.3	7.0	6.6	-0.2	+4.0	+0.5
Bareland	37.3	26.0	18.8	19.9	20.2	19.5	24.5	23.3	-18.5	+1.4	+4.3
Total	143.4	100	94.4	100	103.7	100	105.4	100			

Table 8.7 shows the results of the Acacia xanthophloea distribution in relation to other related classes. It was evident that the Acacia xanthophloea has been on the decline from the year 2012 as noted on the change between 2012 and 2016. However, an increase of 9.6% was noted between 2016 and 2018 and further reduction of 5.8% during the 2018-2020 epoch. The increase could have been attributed by species regeneration (Barančeková et al., 2007), especially during the dry season, when flood waters tend to recede. There was an addition of two classes on the Mission 3, i.e., ‘Lake water’ and ‘Degraded Acacia in water’.

It is important to note that as the surface water increased, the more the Acacia Xanthophloea trees on land were getting submerged into the lake. This phenomenon caused a transition from class Acacia xanthophloea_Land to Acacia xanthophloea_water as depicted by the statistical information between 2016 and 2020. Similar spatial patterns were detected using backscatter response of Sentinel-1 SAR imageries as reported by (Osio et al., 2020).

During the same period (2016-2020), an increase in Acacia xanthophloea_water was noted, which was closely correlated to the increase in class Lake_water, meaning that the trees were submerged in water (Osio et al., 2018a). Between year 2012 and 2018, a reduction in area of class ‘Acacia undergrowth’ was also noted. Acacia undergrowth consist of a mixture of bush/thicket and grasslands that thrives as understory vegetation. During flooding, both the Acacia xanthophloea_Land and their understory vegetation (Osio et al., 2022) got submerged into the lake water as confirmed by the statistical information on Table 8.7.

8.5.2.3 **Post-classification on Mission 6 times series**

OBIA-RF based (Berhane et al., 2019) multispectral classification (Figure 8.8) was carried out on the time series of Mission 6 with the graphical representation of the results shown in Figure 8.9. The importance of Land Use Land Cover classification is to visualize the difference in spatial temporal patterns (Dewan & Yamaguchi, 2009) of the variables under study as shown on Figure 8.8.

Table 8.8: Statistical Change Detection from Mission 6-Pleiades Time series

LULC Class	LULC-2012		LULC-2016		LULC-2018		LULC-2020		Area of Change(Ha)		
	Area (Ha)	%	Area (Ha)	%	Area (Ha)	%	Area (Ha)	%	2012-2016	2016-2018	2018-2020
Sewage	8.3	7.3	35.6	27.6	8.29	8.1	13.8	13.5	27.3	-27.3	5.4
D.A.Water	4.3	3.8	4.6	3.6	5.8	5.7	9.2	9.0	0.3	1.2	3.3
D.A.Land	0.0	00	0.0	0.0	5.6	5.5	7.5	7.4	0.0	5.6	-1.9
H.A.Land	44.1	39.0	43.8	33.9	36.5	35.7	29.4	28.7	-0.3	-7.3	-7.1
Acacia.und	18.2	16.1	21.2	16.4	14.9	14.6	13.1	12.8	3.0	-6.3	-1.8
Open bush	35.0	30.9	16.0	12.3	16.7	16.3	18.8	18.4	-19	0.7	2.1
Park Road	2.5	2.2	1.50	1.2	2.5	2.5	2.5	2.4	-1.0	1.0	0.0
Lake water	0.8	0.7	6.5	5.0	11.9	11.6	8.0	7.8	5.7	5.4	-3.6
Total	113.2	100	129.2	100	102.2	100	102.3	100			

Table 8.8 shows the distribution of Acacia xanthophloea tree species and the related Land Use Land Cover classes along Lake Nakuru riparian reserve. A total of 8 classes were generated including ‘sewage plant’ and ‘Dead Acacia Land’. This was important since the open sewage plant was covered by surface water and thus had to be separated from class ‘Lake water’. The ‘Dead Acacia Land’ class included dry areas covered by Dead Acacia trees especially after water recession.

The target class in this case, i.e., the Healthy Acacia xanthophloea on Land (H.A Land) was noted to have been on the decline throughout the period under investigation, i.e., 2012-2020. As the H.A

Land declined, the Degraded Acacia in water increased during the whole period, hence creating negative correlation between the two trends at *R*=-0.7. This means that as the ‘H.A Land’ decreased, the Degraded Acacia in Water (D.A Water) increased, thus confirming reports by (Osio et al., 2018a) that Acacia xanthophloea tree species have been submerged in the Lake Nakuru waters.

The lake water experienced surface increase between 2012 and 2018. However, a decrease (recession) in the water surface was noted during the 2018-2020 epoch. The increase in the lake water contributed to the degradation of the H.A Land, mainly due to their submergence into the alkaline lake. UAV missions carried out around the plot in September 2021, revealed massive degradation of Acacia xanthophloea tree species in Lake Nakuru (Osio et al., 2022).

Degraded Acacia on Land (D.A Land) increased between 2016 and 2018 by 5.5%, only to decrease by 2.1% during the 2018-2020 epoch. The same pattern was noted with class ‘Lake water’ which increased between 2016 and 2018 by 6.6% but reduced by 3.8% during the 2018-2020 period. Class ‘D.A Land’, in the context of Pleiades-1A image analysis, consist of Degraded Acacia xanthophloea which remains on the mudflats especially during the Lake water recession. There was a strong negative correlation *R*=-0.87 between the area covered by class ‘Lake water’ against the area covered by ‘D.A Land’, meaning that as the lake water increased, the area covered by ‘D.A Land’ also decreased.

Acacia undergrowth (understory vegetation) which consists of a mixture of bush/thicket and grasslands increased by 0.3% between 2012 and 2016. However, during the 2016-2020 period, the area covered by class ‘Acacia undergrowth’ decreased by 3.6%. During 2016-2020 period, a strong positive correlation (*R*=0.8) between the area covered by ‘H.A Land’ and class ‘Acacia

Undergrowth' was noted, confirming reports by (Osio et al., 2018a) that other vegetation species such Tachonandus bushland and Bushed themada Triandra and grassland species such as sporobolus spicatus and Chloris gayana were also submerged into the flooding lake.

8.5.3 Image Differencing

Difference Image is the image prepared by subtracting the digital values of pixels in one image from those in the second image to produce a third set of pixels. This third set is used to form the difference image (Lu et al., 2004). The type of image differencing inherent in this study is the post classification Image differencing technique which was important in depicting qualitative changes over the flood inundated areas between 2012- 2016, 2016-2018, and 2018-2020 epochs generated from classified OBIA-RF Pleiades-1A multispectral imageries. The process was carried out in ENVI 5.3 classic software (ENVI, 2009) and the results attained as shown in Figures 8.3 for Mission 1, Figure 8.7 for Mission 3 and Figure 8.10 for mission 6. The % increase and decrease reported herein are in relation to the total area covered by each Mission.

In the case of Mission 1, an increase of Acacia undergrowth (1.6%), with decrease in area covered by healthy Acacia xanthophloea (0.3%) being achieved during the 2012-2016 epoch. However, 98.1% of the total area remained unaffected. During the 2016-2018 epoch a general increase of Acacia undergrowth by 6.2% was noted with a further decrease in area covered by healthy Acacia xanthophloea by 2.0%, with 91.7% of the total area remaining unchanged. Between 2018 and 2020 a general increase of 1.8% was noted on class Acacia undergrowth and a further decrease of area covered by healthy Acacia scored 10.7%, with 87.5% of the total area experiencing no change. Figure 8.14 shows that the greatest decrease was experienced during the 2012-2016 epoch, while the biggest increase experienced during the 2016-2018 epoch. Cumulatively, the overall decrease was experienced during the 2018-2020 epoch as depicted on Figure 8.14. Further visualization is shown on Figure 8.4 in relation to this experiment.

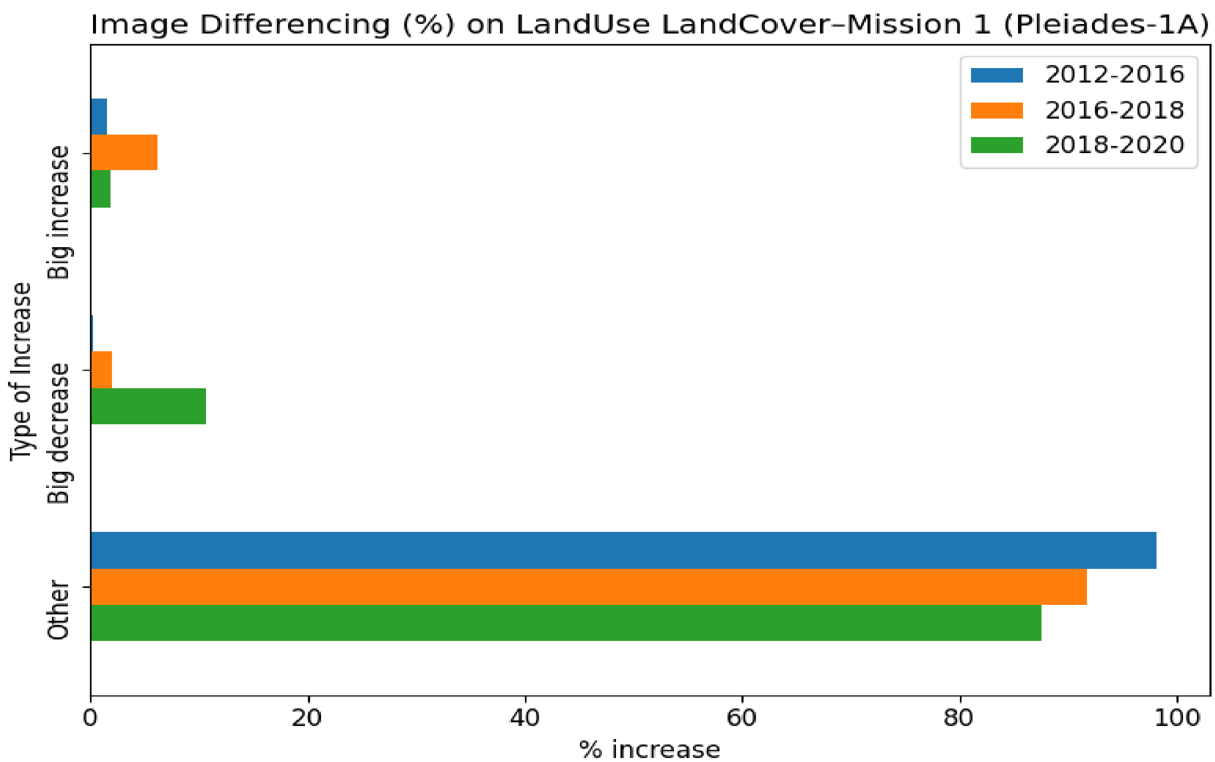

Figure 8.14: Image Differencing results on Mission 1 Pleaides imagery

In the case of Mission 3 an increase in Acacia undergrowth (3.8%) and a null increase in class healthy Acacia (0.0%) was achieved during the 2012-2016 epoch. However, 96.2% of the total area remained unaffected. During the 2016-2018 epoch an increase in area covered by Acacia undergrowth stood at 0.2% and a decrease in area covered by healthy Acacia was 1.5%, with 98.4 % of the total area remaining unchanged. Between 2018 and 2020 an increase in area covered by Acacia undergrowth was 1.0 % with a decrease in area covered by healthy Acacia stood at 0.4%, while 98.6 % of the total area experienced no change. Figure 8.15 shows that the greatest decrease was experienced during the 2016-2018 epoch, while the biggest increase experienced during the 2012-2016 epoch. Cumulatively, the biggest decrease was experienced during the 2012-2016 epoch as depicted on Figure 8.15. Further visualization is shown on Figure 8.7 in relation to this experiment.

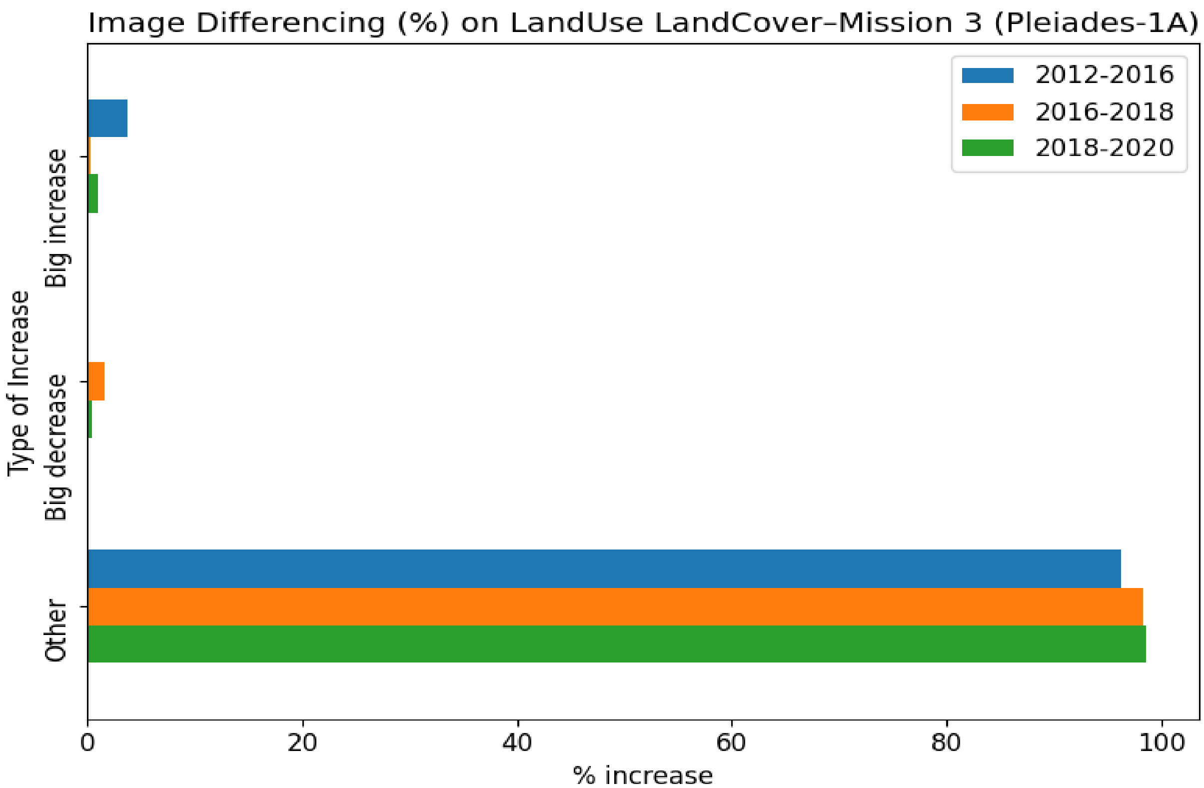

Figure 8.15: Image Differencing results on Mission 3 Pleaides imagery

In the case of Mission 6 the big increase (0.73%) and a big decrease (0.67%) was achieved during the 2012-2016 epoch. However, 98.6% of the total area remained unaffected. During the 2016-2018 epoch a big increase of 0.7% and a big decrease of 1.6%, with 97.7% of the total area remaining unchanged. Between 2018 and 2020 a big increase of 3.3 % and a big decrease of 8.3%

was noted, with 88.4 % of the total area experiencing no change. Figure 8.16 shows that both the greatest increase and decrease were experienced during the 2018-2020 epoch. Cumulatively, the biggest decrease and increase was experienced during the 2018-2020 epoch as depicted on Figure 8.16. Further visualization is shown on Figure 8.10 in relation to this experiment.

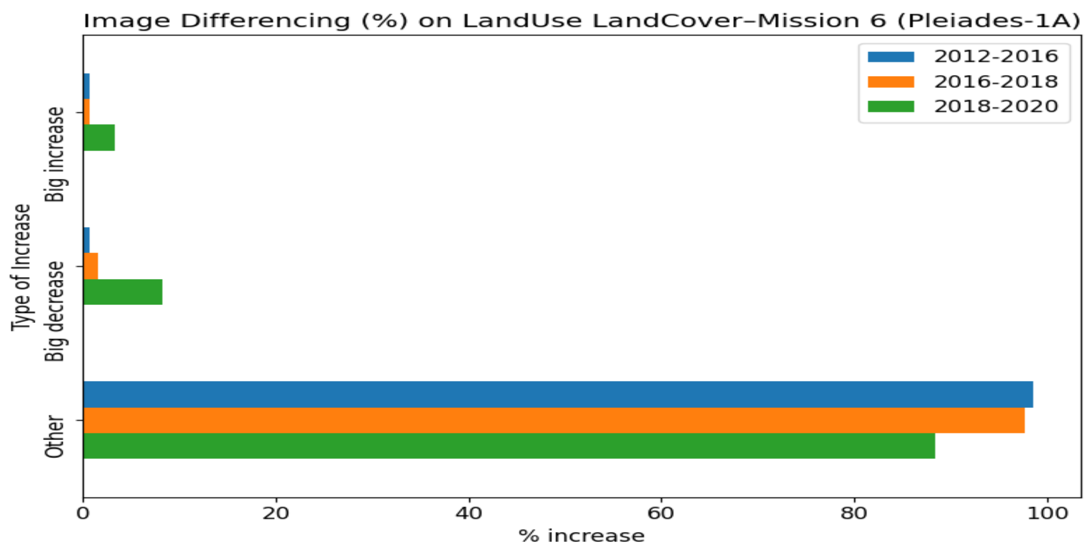

Figure 8.16: Image Differencing results on Mission 6 Pleaides imagery

8.5.4 NDVI on Land Cover Time Series

In this section, NDVI values were calculated and correlated to their corresponding land cover as shown on the graph below. The Maximum and Minimum NDVI values were collected from 3 different plots (regions) around Lake Nakuru National Park, as recommended by (Griffith et al., 2002a). The NDVI maps are shown on Figure 8.11 (Mission-1), Figure 8.12 (Mission-3) and Figure 8.13 (Mission-6). The classification scheme that was used were pegged onto a range of NDVI spectral values as follows: <0 (Non-vegetated area), 0-0.2 (Low vegetated area), 0.2-0.5

(Moderate vegetated) area, 0.5-0.8 (Healthy vegetated area) and 0.8-1.0 (Very Healthy vegetated area) as demonstrated by (Southworth et al., 2004). Post-classification approach which is used to quantify changes on landscapes was embraced. In this section, the spectral post-classification change detection between four independent were used, as reported by (Myneni et al., 1995). The advantage of this method is that, it characterizes by easy calculations the 'from and to' change information as described by (McCallum et al., 2006).

8.5.4.1 **NDVI time series on Mission 1 Land Cover**

The NDVI values were classified into different classes namely Healthy vegetated areas, Moderate vegetated areas, Low vegetated area and Non-vegetated area respectively. Each of these NDVI classes were assigned a corresponding Land Use and Land Cover, depending on their condition type or use. The choice of specific LULC classes to be used in this study was pegged to the fact that water, cloud and snow reflect more in the visible range of electromagnetic spectrum, and hence are bound to produce negative NDVI values. NDVI values range between -1 and +1, and hence thick healthy forested areas tend to exhibit NDVI values that tends towards +1 (Kaiser, 2009). Bare soil is known to reflect values closer to zero (0). In the case of Mission-1 region, only three NDVI classes were achieved, i.e., Healthy vegetated areas which corresponds to class Acacia xanthophloea, Moderate vegetated area (Acacia undergrowth) and Low vegetated area (Bareland). Maximum NDVI values were pegged to each corresponding LULC as shown on Figure 8.17.

In this region, the highest NDVI value (0.74) on class Acacia xanthophloea was recorded in year 2020, while the least value (0.68) detected on the 2012 Pleiades-1A imageries. Acacia undergrowth which consists of bush/thicket and some grassland species had the highest NDVI values (0.52) captured in 2012 and the least value (0.4) detected in 2016 and 2020 respectively. Bareland had the highest NDVI value (0.23) was detected from the 2012 Pleiades imagery, while the lowest value (0.17) achieved from the 2016 image. It is important to note that both NDVI maps of Mission 1 (see Figure 8.11) and their corresponding graphs, gives an impression of very minimal change in terms of NDVI time series.

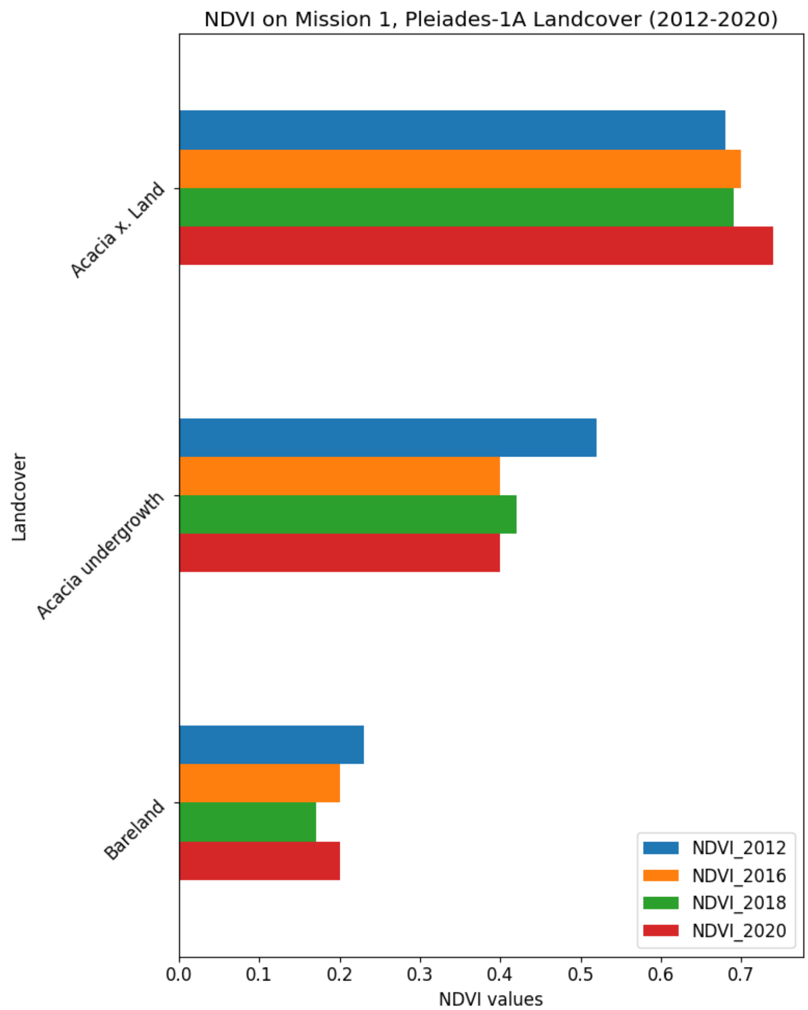

Figure 8.17: NDVI time series on Mission 1 Pleiades imagery

8.5.4.2 **NDVI time series on Mission 3 Land Cover**

The NDVI values were classified into different classes namely Healthy vegetated areas, Moderate vegetated areas, Low vegetated area and Non-vegetated area respectively. Each of these NDVI classes were assigned a corresponding Land Use and Land Cover, depending on their condition, type or use. In the case of Mission 3 region, only three NDVI classes were achieved, i.e. Healthy vegetated areas which corresponds to class Acacia xanthophloea, Moderate vegetated area (Acacia undergrowth), Low vegetated area (Bareland) and Non-vegetated area (Lake water). Maximum NDVI values were pegged to each corresponding LULC as shown on Figure 8.18.

In this region, the highest NDVI value (0.70) on class Acacia xanthophloea was recorded in year 2020, while the least value (0.60) detected on the 2018 Pleiades-1A imageries. Acacia undergrowth which consists of bush/thicket and some grassland species had the highest NDVI values (0.5) captured in 2012 and the least value (0.32) detected in 2020. Bareland depicted the highest NDVI value (0.2) which was detected from the 2012, 2016 and 2018 Pleiades imageries, while the least NDVI value (0.11) detected on the 2020 imagery.

The area covered by the Lake Nakuru (i.e. the blue part of the NDVI time series) as shown in Figure 8.12, had the highest NDVI value (-0.13) detected on the 2012 and 2020 Pleiades imageries, while the least NDVI value (-0.2) detected on the 2018 imagery. These results corroborate with previous studies by (Singh, 1989), citing that negative NDVI values indicate the presence of water, snow or cloud shadows. Each Land Cover were pegged to the corresponding NDVI values as confirmed by (Kaiser, 2009) and shown in Figure 8.18. It is worth noting that, the NDVI values of the target vegetation i.e., Acacia xanthophloea has been on the decline since year 2012 with a very slight increase observed in 2020. However, the ‘Acacia undergrowth’ experienced a steady decline from 2012-2020. Bareland had equal spectral response from 2012-2018, when a slight decline was observed.

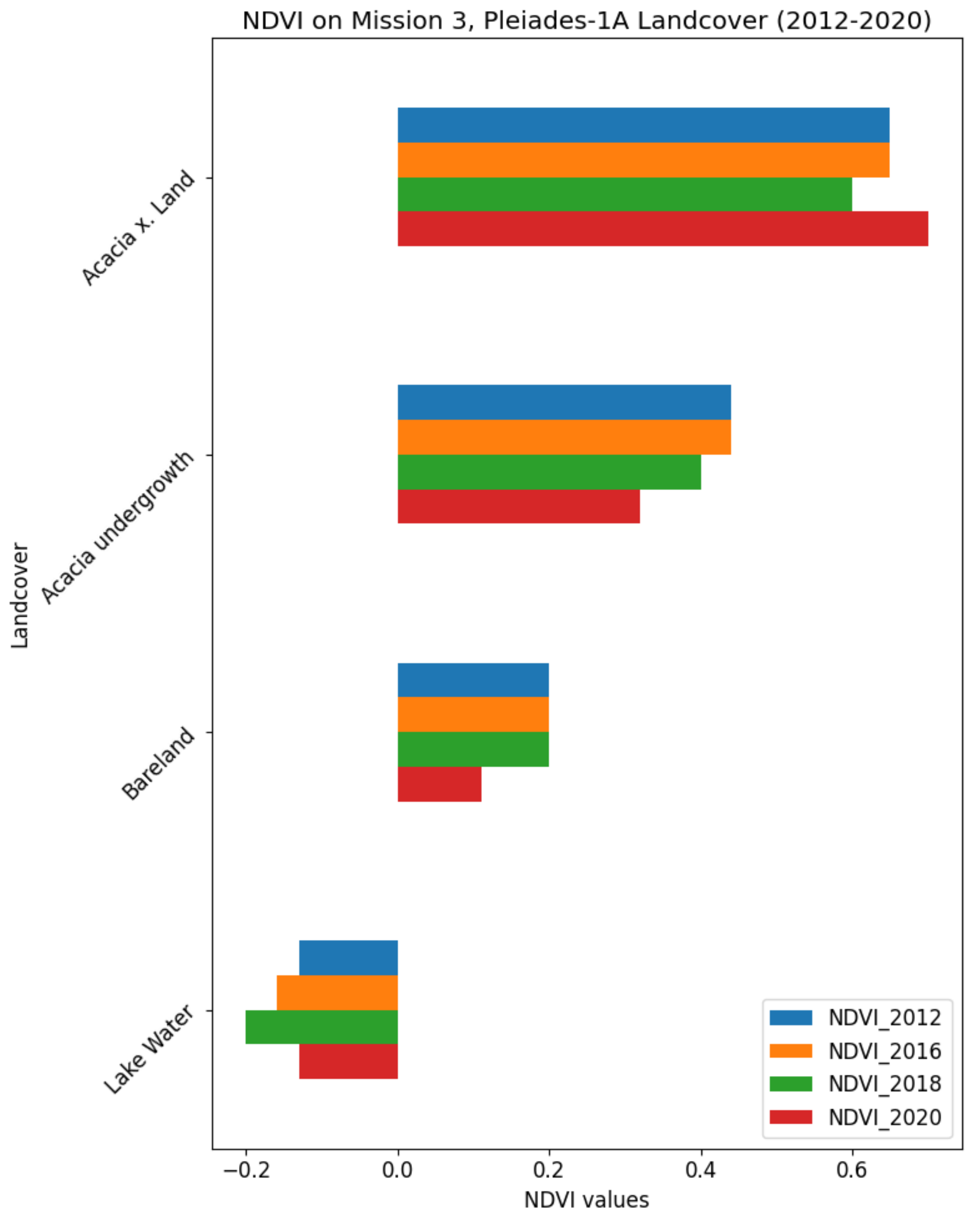

Figure 8.18: NDVI time series on Mission 3 Pleiades imagery

8.5.4.3 NDVI time series on Mission 6 Land Cover

The NDVI values were classified into different classes namely Healthy vegetated areas, Moderate vegetated areas, Low vegetated area and Non-vegetated area respectively (Southworth et al., 2004). Each of these NDVI classes were assigned a corresponding Land Use and Land Cover, depending on their condition, type or use. In the case of region covered by Mission 6, four NDVI classes were developed, i.e., Healthy vegetated areas which corresponds to class Acacia xanthophloea, Moderate vegetated area (Acacia undergrowth), Low vegetated area (Dead Acacia_water) and Non-vegetated area (Lake water). Maximum NDVI values were pegged to each corresponding LULC as shown on Figure 8.19.

In this region, the highest NDVI value (0.71) on class Acacia xanthophloea was recorded in year 2016 and 2020, while the least NDVI value (0.60) detected on the 2018 Pleiades-1A imagery. Acacia undergrowth which consists of bush/thicket and some grassland species had the highest NDVI values (0.49) captured in 2012 and the least value (0.40) detected in 2018 and 2020 respectively. Degraded Acacia_water which consisted of dead logs in water had the highest NDVI value (0.22) detected in the 2012 and 2020 imageries, while the least NDVI value (0.2) detected on the 2016 and 2018 Pleiades imageries respectively. Class 'Lake water' had the highest NDVI value (-0.11) detected on the 2012 Pleiades Imagery, while the least NDVI value (-0.2) was detected on the 2018 imagery (Singh, 1989).

The target vegetation exhibited patterns of increase between 2012 and 2016. The same pattern was noted between 2018 and 2019. Increase in the NDVI values indicates specie regeneration as cited in previous studies by (Barančeková et al., 2007). However, Acacia Undergrowth which consists of the understory vegetation was noted to have adopted a steady decline from 2012-2020, meaning that very little or no species regeneration was experienced throughout the period under review. Pearson's correlation analysis carried out between 'Degraded Acacia_water' and class 'Lake water' revealed a moderate positive correlation (R = 0.74) between the NDVI values, meaning that as the water increased, more 'healthy Acacia Land' got submerged in water which played the role of degradation. The outcome of this analysis corroborates with recent studies by (Osio et al., 2022) which revealed massive degradation of Acacia xanthophloea along the shores of Lake Nakuru.

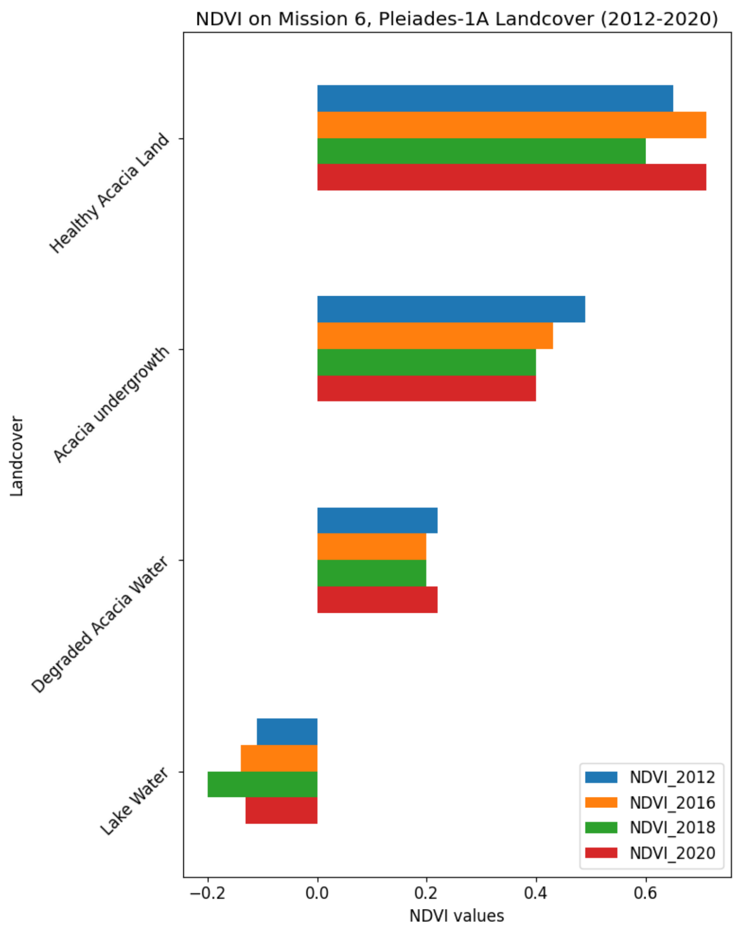

Figure 8.19: NDVI time series on Mission 6 Pleiades imagery

8.6 **CONCLUSION**

The study was centred on time series analysis using Very High Resolution (VHR) multispectral Pleiades imageries to examine changes in the vegetation surrounding the Lake Nakuru riparian reserve in Kenya, with a focus on the Acacia xanthophloea tree species and associated vegetation species. For segmentation, sample selection, and classification, the study used the OBIA-RF (Object-Based Image Analysis with Random Forest) paradigm and the eCognition Developer environment. During UAV (Unmanned Aerial Vehicle) flight missions, the researchers gathered Ground Control Points (GCP) as reference points for evaluating categorization accuracy. On the time series of Pleiades imageries extending from 2012 to 2020, various traditional algorithms available in WEKA Machine Learning software were used (Hempattarasuwan et al., 2019).

The overall accuracy (OA) and Cohen's Kappa (Kappa) values of the ensemble Random Forest technique, when applied to the Pleiades-1A spectral bands along with various shape variables (rectangular fit, Border index, Shape index, and Roundness), were on average 88% and kappa 0.83, respectively. Cross-validation (10-fold) was determined to be the most effective classification method, with an average OA of 92% and a Cohen's Kappa of 0.87 across all datasets. This work used VHR multispectral imaging and machine learning approaches to examine the temporal changes in vegetation, specifically the Acacia xanthophloea tree species and allied vegetation, with a focus on the Lake Nakuru riparian reserve in Kenya.

The investigation of vegetation changes around the Lake Nakuru riparian reserve in Kenya, particularly those connected to the Acacia xanthophloea tree species and accompanying vegetation was emphasized in this study. This workflow used Object-Based Image Analysis with Random Forest (OBIA-RF) paradigm for classification using Very High Resolution (VHR) multispectral

Pleiades imageries. The main purpose of the study was to evaluate how well different machine learning algorithms and classification approaches perform at identifying and analysing changes in vegetation. The algorithms and techniques are compared for significant differences using one-way analysis of variance (ANOVA). Other issues involved in the study entails correctly mapping short vegetation in water bodies and noted the confusion between target vegetation and related classes (Cian et al.,2018). when it comes to vegetation classification. This was possible achieved by utilizing binary change detection and post-classification comparison approaches.

The work used image differencing (Yaseen et al., 2012) and post-classification analysis to shed light on the changes seen in the target vegetation and related classes over time. It covered the cumulative rise and fall in vegetation cover over the course of the research period (2012-2020) and draws attention to certain spatio-temporal trends. Moreso, the study used machine learning and remote sensing methods to map and monitor vegetation in the Lake Nakuru riparian reserve area while also analysing vegetation changes and classifying problems. The analysis of changes and spatial patterns in the Acacia xanthophloea tree species and associated vegetation in flood-affected areas near the Lake Nakuru riparian reserve in Kenya is the main goal of this study, as stated herein. The study made used Pleiades images and combined post-classification comparison techniques with image differencing techniques.

The study also emphasized relationships between various vegetation types, such as a negative association between the area covered by healthy Acacia xanthophloea trees (HA_Land) and the area covered by Acacia in water that had been degraded (D.A_Water). This relationship suggests that the amount of degraded Acacia in water increased as the number of healthy tree species dropped. Similar results were reported in earlier research and verified by UAV flight surveys conducted in Lake Nakuru National Park (Osio et al., 2022)

The study also covers the temporal variations in vegetation coverage seen between 2012 and 2020 on Mission 3 of Pleiades imagery. In particular, the class "Healthy Acacia xanthophloea on Land" (HA_Land) pattern is highlighted since it reflects increases and declines in several classes. According to the study, there are correlations between the classes of "Lake waters" and "Degraded Acacia xanthophloea_water," showing that the Acacia xanthophloea trees became buried in water as the lake's water level rose. According to the study's main objective is to compare it's findings to those of other studies that have also used Sentinel-1 backscatter indices. The study emphasizes the post-classification comparison approach's potential for analysing vegetation's spatial patterns. It does, however, imply that the study's image differencing methodology was subjective and lacked a quantitative connection to specific land use and land cover groups.

The study's main goal is to give ecologists and Kenya Wildlife Service management decision-making tools. The results are meant to assist in addressing the dangers of extinction and degradation that the Acacia xanthophloea tree species near Lake Nakuru's edges confront.

In conclusion, the study seeks to advance knowledge of geographic patterns and changes in vegetation, notably Acacia xanthophloea, and to offer useful resources for conservation activities around Lake Nakuru. This research may be able to further characterize and distinguish Acacia xanthophloea in comparable flood-prone areas by using OBIA-RF modelling and a mix of Pleiades-1A and UAV-based imagery, according to the study. In addition, the study directions are recommended to improve Acacia xanthophloea analysis and monitoring using cutting-edge methods and data sources.

CHAPTER NINE:

GENERAL DISCUSSION, CONCLUSION AND RECOMMENDATION

9.1 GENERAL DISCUSSION

In this section, the summary of the results is presented as per the outlined specific objectives of the study (see Table 9.1). The general discussions captured from the summary of the results give a brief outlook of the results presented herein. In the conclusion part, the author gives an overall conclusion about the various approaches used in the study. Final recommendation is also given at the end of this section.

9.2 SUMMARY OF THE RESULTS

Acacia xanthophloea tree species was detected in this study using OBIA Times Series imageries captured from different airborne and space borne sensors. In this section, the results realized per each experiment using different types of images are discussed and compared herein. Each type of image was unique according to their spatial, spectral and temporal aspects, hence the presentation of unique results. At the end of this chapter conclusion are made with suggested recommendations and future works.

9.2.1 Capability of OBIA in Acacia xanthophloea detection

The capability of Object Based Image Analysis (OBIA) to detect Acacia xanthophloea is presented in this subsection. The selection of segmentation scale and modelling strategy, as well as the inclusion of particular bands and layer weights, had varying effects on the classification accuracy for vegetation detection using the mentioned models and datasets at the various sites when

Sentinel-1 (Single Look Complex) datasets were used. The OBIA-KNN model performed effectively in 2017, obtaining excellent overall accuracy and Cohen's kappa values on both the northern and southern sites. The Southern site's addition of the PCA-1 band led to an even greater boost in categorization precision. The ANOVA analysis also provided insights into the performance of the algorithms by highlighting significant differences between them. The findings imply that the segmentation techniques, PCA band inclusion, and modelling approach selection had an effect on the accuracy of the classification. Although spectral separability was increased by the PCA band, there were still some occasions when the class “other” and Acacia undergrowth were confused. The way each image was specifically treated also had an impact on the model's performance. Overally, our findings shed light on the efficacy of various strategies and point out prospective directions for the future development of vegetation categorization tasks.

Random Forest and J48 performed remarkably well with complete agreement utilizing the entire training approach to the analysis results obtained on Landsat 5TM and Landsat 8OLI and consistently attained high agreement using both cross-validation and the 2/3-1/3 train-test approach. The statistically significant difference among all the utilized classifiers shows that the classification accuracy was significantly impacted by the classifier choice. Additionally, the classification accuracy was impacted by the use of various multi-resolution segmentation scales.

The inclusion of textural variables, multi-temporal data, haralick features, and particular data transformations (such as attribute profile bands) can significantly increase the classification accuracy of remote sensing data, according to analysis results obtained on Sentinel-1 (GRD). While support vector and MLP showed various degrees of accuracy, random forest typically performed well in a variety of settings. The three tested methodologies did not perform significantly differently from one another. Additionally, the random forest-based on attribute profile classification attained a high overall accuracy of 94.25%.

Results from the Pleiades-1 imagery, Random Forest (RF) consistently demonstrated high classification performance across datasets, according to a dataset employing a post-classification technique, whereas other traditional algorithms had marginally worse accuracy. The cross-validation strategy validated Random Forest's impressive performance even more. Additionally, the algorithms differed significantly according to ANOVA and post-hoc analysis, with Random Forest standing out as the best method. The same categorized images were subjected to image differencing, which revealed information about how Acacia undergrowth and healthy Acacia xanthophloea changed throughout the course of various missions. The data indicate the key periods of change and stability in the studied area and suggest variances in vegetation dynamics.

Retina-Net and Faster R-CNN both showed almost equal performance in Acacia xanthophloea recognition and classification when compared to the results of the research utilizing UAV datasets, with RetinaNet slightly outperforming Faster R-CNN in terms of overall precision and recall. However, when an IoU threshold of 0.75 was used, the models had trouble achieving high accuracy. The statistical study verified that the two models performed significantly differently based on the selected evaluation metrics and IoU thresholds. Detailed Results are summarized in Table 9.1 as shown below.

Table 9.1*:* Summary of the Results

Specific objectives	**Data used**	**Results**
Capability of OBIA in *Acacia xanthophloea* detection and characterization.	Sentinel-1(SAR), Single Look Complex (SLC) Time series images (2014-2020) **(Chapter 3)**	Sentinel-1 (SAR) SLC bands C11, C22 and RVI were able to detect the target vegetation (Acacia xanthophloea). • Increase in segmentation scale affects the OBIA-KNN model on the Southern part (2015) image hence reducing the OA by 5% against the North Western (2015) site which had an OBIA-KNN model results of OA (87%) and Cohen Kappa (0.86). The layer weights (2) added onto band C11 and RVI couldn't improve on the model results. • Random Forest using the cross-validation (10-fold) approach performed better in the North Western site (2015) by realizing an OA (96.7%) and Cohen Kappa (0.94), against the Southern site (2015) which realized an OA (96.3%) and Cohen kappa (0.93). Increase in segmentation scale on the Southern site (2015) reduced its classification accuracy by 0.05%. • However, Random Forest using the 2/3 train and 1/3 test approach performed better on the Southern site (2015) imagery, realizing an OA (96.8%) and Cohen kappa (0.95). The same OBIA-RF model implemented on the North Western (2015) site realized an OA (96.1%) and Cohen kappa (0.93). This means that increase in layer weights on bands C11 and RVI improved its classification accuracy by 0.5%. • On the North Western (2017) site, OBIA-KNN model achieved an OA (97%) and Cohen kappa (0.95), while on the Southern (2017) site the same model achieved OA (98.7%) and a Copen kappa (0.97). Both imageries were given same treatment with the same segmentation parameter settings i.e. scale (10), shape (0.6) and compactness (0.8) and spectral segmentation scale (10). More treatment was given to the Southern site (an addition of the PCA texture band). The additional PCA-1 band increased the classification accuracy on the OBIA-KNN model by 1.7%, and OBIA-RF model using cross-validation (k-fold) by 3% while OBIA-RF using 2/3-1/3 train-test split approach, an increase by 6.6% respectively. • PCA band improved boundary spectral separability between the target vegetation (*Acacia xanthophloea*) and the grassland species i.e. *sporobolus spicatus* and *chloris gayana*. • Despite the achievement of high classification accuracy, some of the instances were confused as Acacia undergrowth and class, 'other'. • An additional treatment was implemented on the North Western (2019) image. SLICO segmentation algorithm was used instead of the previously used Spectral Difference segmentation on the Southern (2017) image. From the C11, C22, PCA-2 band combination,

		with additional geometric features e.g. roundness, ecliptic fit, rectangular fit etc., OBIA-KNN model had a perfect agreement at 100% overall accuracy and Cohen kappa (1.0) likewise on the Southern (2019) imagery. OBIA-RF model on the North Western (2019) image using cross-validation (10-fold) yielded an OA (97.9%) and kappa (0.96), while 2/3-1/3 train-test split, an OA (98.3%) and Cohen kappa (0.97). On the Southern (2019) image the OBIA-RF using cross validation (10-fold) yielded an OA (86.1%) and kappa (0.78). OBIA-RF model on the same image using 2/3-1/3 train-test split approach yielded an OA (86.7%) and Cohen kappa (0.79). • ANOVA (One Way) was used to find out the significant difference between and amongst the algorithms used. e.g. Naïve Bayes (NB), Random Forest (RF) and Decision Tree (DT) at p-value (0.02) achieved by 3 groups, while p-value (0.01) significant for two groups i.e. Random Forest and Decision Tree.
Capability of OBIA in *Acacia xanthophloea* detection and characterization.	Landsat 5 TM & Landsat 8 OLI. **(Chapter 4)**	• Algorithms used were J48, Random Forest, Naïve Bayes and Binary Support Vector (SMO). Random Forest and J48 had perfect agreement (1.0) using the full training approach. • J48 and Random Forest had the same agreements (0.99) using both cross-validation (10-fold) and 2/3-1/3 train-test approach. • Multi-resolution segmentation scales used across the different datasets, influenced the outcome of the classification accuracy. • There was a significance difference amongst all the classifiers used using Fstats (5.33) > Fcrit (2.90) significant at $p<0.05$ (p-value 0.004)
Capability of OBIA in *Acacia xanthophloea* detection and characterization	Sentinel-1 (GRD) Sentinel-2A and VHR aerial image. **(Chapter 5)**	• VHR aerial image mixed with textural variables i.e. GLCM Mean, Contrast, Homogeneity, Correlation yield RF (99.7%), Support Vector (75%), MLP (91.6%). • An 8-date stack multi-temporal image dated May 2018-August 2019 consisting of 32 master and slave imageries with stack averaging, using SLICO with minimum region size of 25 and Spectral Difference segmentation (scale-10) yielded RF (82.3%), MLP (80.3%) and Support Vector (76.6%). • Sentinel-1 GRD with VV & VH intensity bands. Their Haralick features i.e. GLCM_Mean, GLCM_Contrast, GLCM_Variance total of 8-bands. Pixel-based supervised classification with Random Forest (N-Tree 500) used to classify an image with 5000 samples used for training and 500 for validation. RF on July 2018 image (96%), RF on November 2018(94%) and RF on May 2019 image (95%).

		• Supervised OBIA classification on S-1 GRD intensity bands, no Haralick features involved yielded an RF (89.2%) on February 2019 image; RF (87.9%) on the May 2019 image; RF (94%) on the August 2019 imagery. • S-1 GRD Polarimetric bands are suitable for detecting riparian vegetation classes along Lake Nakuru riparian • Random Forest results of different dates yielded Overall Accuracies i.e. 87.7%, 84.93% and 92.35% respectively. Incorporating Haralick features into the classification improved the pure polarimetric intensity-based imagery by 1% to 3%, the improvement resulted in an average Overall Accuracy of 93.95%. • The conversion of the VV and VH backscatter bands and their related Haralick bands (total = 8 bands) into Attribute Profile bands improved the classification by 1%-6% respectively. • To test the difference significance between the three approaches, one-way ANOVA was implemented. There was no significant difference existing amongst the three approaches used since Fstats (0.955) < Fcritical (5.143) at ϕ >0.05 and p-value (0.43). • Attribute Profile based classification by Random Forest working on 62,067 instances and 200 trees yielded 94.25% overall accuracy.
Capability of OBIA in *Acacia xanthophloea* detection and characterization	High Resolution Multispectral Imagery (Pleiades-1A) **(Chapter 8)**	• Random Forest classification achieved best across the three-time series datasets with an OA score of 80% and a Kappa of 0.78. Other classical algorithms that follow include J48 with average OA of 73.7% and Kappa 0.69, Naïve Bayes OA 66.2% and Kappa of 0.64, Binary SVM OA 63.3% and Kappa 0.60 respectively. • Cross-validation (10-fold) approach achieved average Random Forest OA of 92% and Kappa (0.87) across all the algorithms. • The full training approach achieved RF OA (91.9%) and Kappa (0.9). The 2/3 train and 1/3 test approach yielded an OA of 84% and Kappa (0.81). • The Average Random Forest classification achieved in Mission 3 stood at OA of 87.5% and Kappa (0.86), Mission 1 yielded an OA of 79.5% and Kappa (0.77) and Mission 6 an average RF with an OA of 72.1% and Kappa (0.71) respectively.

		• One Way ANOVA implemented on the classified time series (36) Pleiades Imageries revealed that there was a significant difference between and amongst the algorithms used i.e. Random Forest (RF), J48, Binary SVM and Naïve Bayes. • The F-Critical value derived from interpolating DF1 against DF2 was 2.901. Since the F-Statistic value is 3.03, then F-stat > F-Critical is achieved from the values they represent, i.e. 3.03 >2.90 meaning that there was a significant difference between and amongst groups at (P = 0.04). • Post-Hoc Tukey's HSD analysis revealed a significance difference between Random Forest (RF) and the Binary SVM at $\phi < 0.05$ and p-value 0.04.
Capability of OBIA in *Acacia xanthophloea* detection and characterization	Very High Resolution (VHR) UAV Imageries. (Single-date) **(Chapter 7)**	• Two CNN models i.e. Faster R-CNN and RetinaNet were used in Acacia xanthophloea detection and classification at individual scale. • The networks were trained and assessed using a dataset made of 9,056 image patches and 7,590 annotations on bounding boxes. • RetinaNet achieved overall Precision of 38.9% and Recall of 57.9% with the setting IoU ≥ 0.5. • Faster R-CNN achieved the overall Precision of 37.2% and Recall of 53.2% with the setting IoU ≥ 0.5. • Retina-Net achieved a slightly higher Result than Faster R-CNN i.e. 1.64% higher. • Nevertheless, the difference remains within a small margin. In terms of Average Precision per class, RetinaNet performs best for both classes "Land" and "Water" (with improvement of 2-4%) but worse for class "Mudflat" (degradation of 2%). • The results achieved from both RetinaNet and Faster R-CNN using the IoU ≥ 0.75 were very low. • RetinaNet achieved overall Precision of 14.1% and Recall of 29.0 % setting IoU ≥ 0.75. • Faster R-CNN achieved the overall Precision of 14.0% and Recall of 27.7 % setting IoU ≥ 0.75

		• One Way ANOVA revealed that there was a significant difference between RetinaNet and Faster R-CNN models using IoU $\geq$ 0.5 and IoU $\geq$ 0.75 significant at ϕ < 0.05 and p-value 0.008. • This was also fulfilled by the expression: Fstats(15.01) > FCritical(5.99)
The effect of integrating Object Based Approach into Remote Sensing & GIS?	Landsat 5 TM &Landsat 8 OLI. **(Chapter 4)**	• Thematic re-classification is possible when OBIA is integrated into a GIS environment. • Re-classification led to detection of additional sub-classes on the Landsat 8 OLI 2014 image. • Transition of OBIA datasets into WEKA Machine Learning reduced the performance of J48 algorithm, hence realizing substantial agreement (72%). • Landsat 5 TM 2011 was not exposed to re-classification and hence a perfect agreement (100%) with J48 algorithm. • The vector shapefiles transited from eCognition Developer, were attached to the link tables which could be visualized in ArcGIS attribute table. • The attribute table had datasets which needed to be cleansed (removal of redundant data) in the ArcGIS environment before transiting the cleaned data into WEKA Machine Learning software for further processing. • The OBIA-based classification in WEKA depended on the number of variables and instances imported into WEKA. The higher the number of instances, the lower the agreement achieved. • Re-classification required that vectors (image objects) captured from segmentation images be merged to form new subclasses. However, this depends on the segmentation scales used.
Spatio-temporal changes on Acacia xanthophloea spp	Sentinel-1 (SAR), Single Look Complex (SLC) time series images (2014-2020) **(Chapter 3)**	• Reduction in the area covered by healthy Acacia on both training and testing sites. However, training site 2 (Southern) part of Lake Nakuru suffered the greatest impact in terms of *Acacia xanthophloea* degradation. • Spatio-temporal change on Lake surface water (2014-2020) was as follows: 52.2 km^2 in 2014, 54.11 km^2 in 2016, 57.24 km^2 in 2018, and 59.8 km^2 in 2020. • Spatio-temporal changes (2014-2020) on the Acacia xanthophloea strands on the Training site 1 (North Western part) was as follows: (n=16,528 pixels) in 2014, (n=13,320 pixels) in 2016, (n=10,650 pixels) in 2018, and (n=10,302 pixels) in 2020.

		• A strong negative correlation of R = -0.94 between the area of the lake against the area covered by healthy Acacia x. per each year. Meaning that as the lake surface water increased, the area covered by Healthy Acacia reduced drastically over the years. • Between 2014 and 2020 the area covered by the degraded Acacia X. Spp trees on the North Western side of the lake was (n=6,236 pixels), on the Southern part where the largest strands of acacia forest were existing (n=22,522 pixels), and on the South Western side (n=8,129 pixels) were degraded. • Hence confirming previous reports by (Mutangah, 1994), that the main cause of stress and eventual death of the Acacia Xanthophloea was due to the rising water table in a closed drainage system (i.e. Lake Nakuru Basin). • The equation to the regression line in relation to this correlation being y = 57870-808.9x
Spatio-temporal changes on Acacia xanthophloea spp	Landsat 5 TM & Landsat 8 OLI. (2011-2016) **(Chapter 4)**	• The Lake Nakuru area was observed to have increased from (n= 860) in 2011 to (n=1024) in 2016, thus confirming reports by (Onywere et al., 2013) that the lake has been flooding its banks. • The area covered by Acacia xanthophloea was (n= 891 pixels) in 2011 but reduced to (n=465 pixels) in 2016. • Thus, the difference in spatial coverage (n=426 pixels) of Acacia Xanthophloea was covered by the flooded lake. • The sedges and marshes whose area was (n=87 pixels) and Cynodon Chloris Themada grasslands with area of 264 pixels on Landsat 5 TM 2011, were not detected on the 2016 classified image. • Cynodon Niemfluensis grasslands seem to have thrived in the flooded plain and thus an increase in their spatial coverage from (n=597 pixels) in 2011 to (n=2317 pixels) in 2016. • Other vegetation species whose area reduced by year 2016 are as follows: Chloris Gayana (n=44 pixels), Bushed Themanda Triandra (n=78 pixels), Tachonandus Bush land (n=18 pixels), Sporobolus Spicatus grasslands (n=81 pixels), highland vegetation (n=73 pixels) and Olive & Teclea forest (n=266 pixels)

Spatio-temporal changes on Acacia xanthophloea spp	High Resolution Multispectral Imagery (Pleiades-1A) (2012-2020) **(Chapter 8)** (Mission 1)	• Post-classification comparison approach on Mission 1 revealed that the target vegetation (Acacia xanthophloea) have been on the decline since 2012-2018, as follows: 2012-2016 (decrease n=27.7ha), 2016-2018 (decrease n=5.3ha) but with an increase (n=8.4ha) noted in the period 2018-2020. • Class Acacia undergrowth (Understory vegetation) on Mission 1 revealed a decline of (n=3.5ha) during the 2012-2016 period. A further decrease (n=2.7ha) was noted between year 2016-2020, while it remained constant (n=2.7ha) during the 2018-2020 epoch. • The area covered by the class bareground also continued to decrease between the year 2012 and 2018, but remained constant (n=9.1ha) during 2018-2020 epoch. • Other class associated with the target vegetation (Acacia crown gap), also experienced a decrease (n=28.3ha) during the 2012-2016 epoch, a further decrease (n=6.2ha) in the 2016-2018 epoch. However, an increase(n=15.6) was noted between 2018 and 2020.
	High Resolution Multispectral Imagery (Pleiades-1A) (2012-2020) **(Chapter 8)** (Mission 3)	• Post-classification realized the following classes: Healthy Acacia Land, Degraded Acacia Land, Degraded Acacia water, Lake water, National Park roads, Open bushland, Acacia undergrowth and sewage plant. • Class Healthy Acacia_Land was noted to have been degrading between 2012 and 2020. In the period 2012-2016, the area covered by this class was (n=24.7ha), 2016-2018 an increase by (n=19.0ha) and a decrease by (n=5.4ha) on the 2018-2020 epoch. • Class Acacia undergrowth (Acacia understorey species) increased by (n=5.1ha), a decrease of (n=19.0ha) and an increase (n=1.8ha). • Class Degraded Acacia_water increased by (n=0.2ha) during 2012-2016 epoch. A further increase (n=0.6ha) during the 2016-2018 epoch, and a decrease (n=0.95ha) during 2018-2020 period. • During the 2012-2016 epoch, class Lake water (Lake Nakuru), increased by (n=0.2ha), another increase (n=0.38ha) was noted during the 2016-2018 epoch. A further increase (n=0.5ha) was noted during the 2018-2020 epoch.

	High Resolution Multispectral Imagery (Pleiades-1A) (2012-2020) **(Chapter 8)** (Mission 6)	• Post-classification realized the following classes: Healthy Acacia Land, Degraded Acacia water, Lake water, Acacia undergrowth and bareland. • Class Healthy Acacia_Land was noted to have been degrading between 2012 and 2020. In the period 2012-2016, the area covered by this class was (n=10.3ha), 2016-2018 a decrease by (n=7.3ha) and a decrease by (n=7.1ha) on the 2018-2020 epoch. • Class Degraded Acacia water decreased by (n=0.3ha) during 2012-2016 epoch. A further increase (n=1.2ha) during the 2016-2018 epoch, and an increase (n=3.4ha) during 2018-2020 period. • Class Acacia undergrowth (Acacia understorey species) increased by (n=3.0ha) during the 2012-2016 epoch, a decrease of (n=6.3ha) during the 2016-2018 epoch and a further decrease (n=1.8ha) during the 2018-2020 epoch. • During the 2012-2016 epoch, class Lake water (Lake Nakuru), increased by (n=5.7ha), another increase (n=5.4ha) was noted during the 2016-2018 epoch. A decrease (n=3.9ha) was noted during the 2018-2020 epoch.
Spectral changes on *Acacia xanthophloea spp*	Sentinel-1 (SAR), Single Look Complex (SLC) time series images (2014-2020) **(Chapter 3)**	• The Sentinel-1 SLC covariance bands were used to detect the riparian vegetation degradation along Lake Nakuru Riparian reserve. • The average covariance matrix generated bands with the greatest response captured from 2014-2020 imageries were as follows: C11 (First), C22 (Second), while the band with the least spectral response was C12. • Radar vegetation indices were generated from the Sentinel-1 Single Look Complex polarimetric bands collected between 2014-2020. • The Radar Vegetation Indices response across the time series images were as follows; The band with the greatest spectral response was Radar Vegetation Index (RVI), second Dual Polarimetric Vegetation Index (DpRVI), third Degree of Polarization (DOP) while the band with the least response was Polarimetric Radar Vegetation Index (PRVI). • The bands with the greatest response (C11, C22 & RVI) were imported into eCognition Developer for Acacia xanthophloea (and related vegetation) classification along Lake Nakuru Riparian reserve.

Spectral changes on *Acacia xanthophloea spp*	Landsat 5 TM & Landsat 8 OLI. (2011-2016) **(Chapter 4)**	• The spectral response of vegetation types along Lake Nakuru from the greatest to the least were as follows; Sand & Mudflats, Chloris gayana grasslands, Sporobolus spicatus grasslands, Cynodon chloris Themada grasslands, Cynodon niemfluensis grasslands, Cynodon niemfluensis_wooded acacia grasslands, Olive & Teclea Forest, Sedges & Marshes, Acacia Forest and Lake Nakuru respectively. • Generally, the NDVI around Lake Nakuru National Park was at its best with the Maximum NDVI at (+1), classified as “Very Healthy vegetation” as retrieved from the Landsat 7 ETM image captured in year 2000. • One year down the line (2011) after the onset of Lake Nakuru floods (Onywere et al., 2013) the maximum NDVI was at +0.68 classified as “Healthy Vegetation” retrieved from the 2011 Landsat 5 TM image. • In the year 2014 the maximum NDVI value in Lake Nakuru was (+0.87) re-emergence of the class, “Very Healthy Vegetation” but this time not at (+1) but reduction by (+0.13) observed. • In the year 2016 and 2020 the same maximum NDVI (+0.87) was retained. However, it is important that within-class variation was noted e.g. the class “Moderate vegetation” (mostly grassland species) on the 2020 map depicted a lower maximum NDVI value (0.54) than the same class on image 2016 which had an NDVI value (0.57). • The same pattern was observed with class “Low vegetation”, whereby on the 2016 image the NDVI value (0.4) while the same class on image 2020 achieved an NDVI value (0.3). • These results depict an overall state of Vegetation Health as “Very Healthy”, but the existence in alternative patterns of “increase” and “decrease” between and within classes along the NDVI time series confirms the existence of vegetation species disturbance (degradation) and re-vegetation (re-generation). • These NDVI results indicate the general state of health of all vegetation in the park including the Forest, Bush/Thicket and grassland species in the park. It was noting that the class “Low vegetation” (NDVI, +0.2) derived from the Year 2000 (Figure 4.4) could possibly be due to the presence of the blue-green algae (Spirulina) on the water surface. • From the statistical information derived from OBIA-based NDVI values derived for different vegetation species across the Lake Nakuru National Park, it was noted that the following species exhibited negative NDVI values, i.e., Cynodon chloris themada grassland, Sand and Mudflat, sedges & mudflats and sewage plants as shown in Figure 4.9 and Figure 4.10. This

		means that they were immersed in water as shown by the spatial land cover statistics reported on the same vegetation species as shown in Figure 4.7. • Other species within the park which were noted to have exhibited negative NDVI values were Tachonandus bushland, Escarpment vegetation & Euphorbia Candelabra, possibly due to stress and not necessarily flooding as the other riparian vegetation.
Spectral changes on *Acacia xanthophloea spp*	Sentinel-1 (GRD) Sentinel-2A **(Chapter 5)**	• In this study the backscatter indices σ_{db} (VV) and σ_{db} (VH) had the capability of detecting four classes: degraded submerged forest, degraded forest, non-degraded forest and urban. • The degraded forest and urban classes were captured in VV polarization mode, non-degraded forest was best captured in VH polarization mode since healthy tree strands experience volume scattering on the crown and double bounce from their bark. • Time series imagery of Sentinel-1 (GRD) captured between July 2018 and May 2019 had their statistical backscatter response depicted on Figure 5.4 and Figure 5.5. • Class "Lake water" had the lowest backscatter response in the VH channel, followed by Degraded Submerged Acacia Forest (VH), Degraded Forest (VV), Non-Degraded Forest (VV and VH) in equal measure and Urban area with the highest response in the (VV) channel. • The backscatter response patterns as observed in (Santos et al., 2021) were evident in this study where the increase in backscatter response signals was observed at growing levels from the open water (OW), dry land (DL) and flooded vegetation (FV). • Pearson correlation analysis between Normalized Vegetation Burnt indices (NBR) values derived from Sentinel-2MSI and the backscatter indices from the Sentinel-1 (GRD) channels revealed a strong negative correlation (-0.96), meaning that as the health of the Acacia xanthophloea continued to degrade, the backscatter response continued to increase. • This was confirmed by the high backscatter response noted on the degraded submerged acacia (degraded tree biomass) along Lake Nakuru riparian (Richards et al., 1987).
Spectral changes on *Acacia xanthophloea spp*	Landsat 5 TM & Landsat 7ETM (2008-2017) and Sentinel-2. (2014-2017)	• The newly developed OBIATS.py code was able to extract clusters on the North-western part of lake Nakuru riparian. The three clusters of interest to this study detected three classes i.e., non-degraded forest, degraded forest and degraded submerged forest respectively.

	(Chapter 6)	• Temporal profiles for each class category were generated using TIMESAT software. In addition, phenology metrics (NDVI Values) were also detected. • The phenology metrics representing NDVI values were the peak values (PV) and the Base Values(BV) per each category. • The non-degraded forest realized the highest NDVI values across the 8 seasons. Pearsons correlation realized a strong positive correlation (R=0.87) between the base values (BV)and the Peak Values(PV). • Degraded submerged Forest category realized the second highest NDVI values recorded in 5 seasons (3 seasons less than the non-degraded). Pearsons correlation realized a weak positive correlation (R=0.33) between the base values (BV) and the Peak Values(PV). • Degraded forest category realized the lowest NDVI values recorded in 5 seasons (same number of seasons as degraded submerged forest). Pearsons correlation realized a weak positive correlation (R=0.29) between the base values (BV) and the Peak Values(PV). • Despite the lowest number of seasonal occurrence, degraded forest had the highest peak value (PV) which represents the highest NDVI value at 60.76. This unique occurrence could have been caused by low vegetated species re-generation during the eighth season. • The high number of small integral (SI) values recorded under the degraded forest category represents the presence of low vegetation such as bush and thicket. This was also confirmed by the Plateau observed on the Sentinel-2 related temporal profile. • There was poor correlation noted between the Length of the season(LS) and their corresponding peak values (NDVI values) on the Landsat 5TM and Landsat 7 ETM temporal profiles, meaning that NDVI values were not controlled by Length of the season in the specific datasets. • However, a different outcome was noted with Sentinel-2, whereby a high correlation (R=0.87) existed between the Length of the season(LS) and the Peak values(PV) on this dataset. • The high correlation (R=0.95) existing between the Base values in Sentinel-2 in relation to the Base Values in Landsat 7ETM & Landsat 5TM led to the conclusion that all the datasets have the capability of realizing phenological metrics which are suitable for forest health cover. However Sentinel-2 proved to be more competent against Landsat 5 TM and Landsat 7 ETM.

Spectral changes on *Acacia xanthophloea spp*	High Resolution Multispectral Imagery (Pleiades-1A) (2012-2020) **(Chapter 8)** (Mission 1)	• Acacia xanthophloea was noted to be on the decline from 2012-2018. • However, re-generation was noted in year 2020 where the maximum NDVI (0.74) calculated from the 2020 Pleiades Mission 1. • Pearson's correlation coefficient was used to calculate the correlation between the land cover types and their corresponding NDVI values as demonstrated by (Hammer et al., 2001). • There was a strong positive correlation (R=0.87) existing between the land cover variables i.e. Acacia xanthophloea, Acacia undergrowth and bareland against their NDVI values. • This means that NDVI is a suitable index for measuring the health of vegetation in Lake Nakuru National Park.
	High Resolution Multispectral Imagery (Pleiades-1A) (2012-2020) **(Chapter 8)** (Mission 3)	• The same pattern on Mission 1 was observed in the case of Mission 3, where NDVI values were noted to be on the decline between 2012 and 2018. • However, Acacia xanthophloea re-generation was noted in the year 2020, with an NDVI of 0.70. • Pearson's correlation coefficient was used to calculate the correlation between the land cover types and their corresponding NDVI values as demonstrated by (Hammer et al., 2001). • A strong positive correlation (R = 0.97) was noted between the areas covered by the class Healthy Acacia Land, Acacia undergrowth, Bareland and Lake waters against their NDVI values in the year 2012. • Likewise, a strong positive correlation (R = 0.97) was observed on the 2016 image. • However, in the year 2018, a slight decrease in their relationships between these variables (R = 0.89) was noted. • In the year 2020 a strong positive correlation (R=0.96) was also noted between the land cover and their respective NDVI values. Meaning that NDVI is suitable index in measuring vegetation health in Lake Nakuru National Park.

	High Resolution Multispectral Imagery (Pleiades-1A) (2012-2020) **(Chapter 8)** (Mission 6)	• In the case of Mission 6, NDVI values were noted to be on the decline between 2012 and 2016. • However, Acacia xanthophloea re-generation (NDVI=0.71) was noted on both 2018 and 2020 imageries. • Pearson's correlation coefficient was used to calculate the correlation between the land cover types and their corresponding NDVI values as demonstrated by (Hammer et al., 2001). • A strong positive correlation *(R* = 0.89) between the areas covered by the class Healthy Acacia Land, Acacia undergrowth, Degraded Acacia water and Lake waters against their NDVI values in the year 2012. • Likewise, in the year 2016, there was a strong positive correlation (*R*=0.89) achieved. • During the subsequent years 2018 (*R*=0.68) score was realized, while in 2020 (*R*=0.88).

9.2.2 Integrating Object Based Approach into GIS and Remote Sensing

Thematic reclassification is made possible by integrating Object-Based Image Analysis (OBIA) into a GIS system. This implies that using OBIA techniques within the GIS system, the classification of objects or features in an image may be changed or improved. Landsat 8 OLI 2014 image underwent reclassification, which led to the discovery of new subclasses. This means that through the process of reclassification, new classes or categories were discovered or distinguished within the image. OBIA datasets' conversion to WEKA Machine Learning software had an effect on how well the J48 algorithm performed. The J48 algorithm and the reclassification findings' agreement declined, yielding a significant agreement of 72%. This implies that the inclusion of OBIA generated datasets in WEKA may have had an impact on the J48 algorithm's classification precision. Without any reclassification, the Landsat 5 TM 2011 image displayed full agreement (100%) with the J48 algorithm. This shows that the original classification of this image was extremely accurate and in line with the outcomes of the J48 algorithm.

The vector shape files produced by the eCognition Developer software could be seen in the ArcGIS attribute table since they were linked to the attribute tables. This implies that the vector shapefile attribute data might be retrieved and examined within the ArcGIS environment. The attribute table comprised datasets that needed to be cleaned up or redundant data removed before being transmitted to WEKA Machine Learning software for additional processing in the ArcGIS environment. This shows that in order to assure the quality and integrity of the attribute data before using it in the machine learning study, data cleaning procedures were required. The quantity of characteristics and samples that were imported into WEKA had an impact on how well OBIA-based categorization performed. As the number increased, it was noticed that the agreement between the categorization findings dropped as the number of occurrences rose. As a result, there may be less agreement in the classification process as more examples introduce complexity and unpredictability. In order to create new subclasses, the segmentation vectors or image objects have to be combined. The segmentation scales employed, however, are what determine whether this merging procedure is successful. In terms of the creation of new subclasses, different segmentation scales may have varying results.

These findings demonstrate the possibility of thematic re-classification using OBIA and GIS integration, the impact of data transition on algorithm performance, the value of data cleaning, and the role of variables and cases on classification agreement. In the course of the reclassification process, they additionally underline the function of segmentation scales in the creation of subclasses.

9.2.3 Spatio-Temporal Change on Acacia xanthophloea tree species

The results presented herein, describe a number of tests carried out utilizing various remote sensing data sources, such as Sentinel-1 (SAR), Landsat 5 TM, Landsat 8 OLI, and Very High-Resolution Pleiades-1A imagery. The experiments had two main objectives: to evaluate the spatiotemporal changes in vegetation and water surface areas in Lake Nakuru National Park and to investigate the link between these variables as outlined below:

SAR Sentinel-1 Experiment:

Between the regions where the water surface was present and the strands of the Acacia xanthophloea tree, there was a significant negative association (R = -0.94). This shows that the area occupied by healthy Acacia xanthophloea shrank as the water surface rose. These findings confirm earlier studies by Mutangah, 1994 that linked stress and the demise of Acacia xanthophloea in Lake Nakuru National Park to rising water levels in a closed drainage system. Southern Acacia strands in Lake Nakuru Park, specifically, were discovered to be the most adversely affected areas in terms of Acacia degradation at Test and Training Site number 2.

Experiment using Landsat 5 TM and Landsat 8 OLI:

From 2011 to 2016, the lake's surface area grew by 83.9%, supporting earlier conclusions that the lake had overflowed its banks. Conversely between the year 2011 and 2016, the area occupied by healthy Acacia xanthophloea strands shrank by 53.1%. The difference (9.6ha) represents the submerged Acacia xanthophloea tree species in Lake Nakuru. Other vegetation classes also underwent changes, with some grasslands and forests losing ground.

Time Series Experiment using Pleiades-1A:

For the purpose of evaluating the spatiotemporal patterns in vegetation, three plots designated Mission 1, Mission 3, and Mission 6 were chosen. Between 2012 and 2018, the area occupied by Acacia xanthophloea steadily decreased, according to Mission 1. between 2018 and 2020, increasing, pointing to a re-vegetation timeframe. Other vegetation classifications connected to Acacia xanthophloea and the undergrowth showed similar patterns, with some experiencing decreases and rises at various times. Throughout the missions, the class "Degraded Acacia_water" shows a variety of patterns of decline and growth. The ‘lake water’ class showed variations in area, with rises and falls seen in various missions.

These findings demonstrate Lake Nakuru National Park's changing vegetation and water surface areas. They show how Acacia xanthophloea and other vegetation species are being negatively impacted by rising water levels. The results validate earlier studies on the topic and help us better comprehend the spatiotemporal changes taking place in the studied area.

9.2.4 Spectral Change on Acacia xanthophloea tree species.

Results from three distinct studies were examined using remote sensing data in the riparian reserve of Lake Nakuru to determine changes in the health of Acacia xanthophloea trees and allied vegetation species. Sentinel-1 (SLC) SAR time series that were taken between 2014 and 2020 were used in the first trial. The imageries were used to create covariance matrix indices and radar-based vegetation indices. The bands C11 and C22 from the covariance matrix showed the strongest spectral response. The spectral response with the greatest value was the Radar-based Vegetation Index (RVI). These bands and indices played a crucial role in later classification procedures.

Images from Landsat 5 TM and Landsat 8 OLI taken between 2011 and 2016 were used in the second experiment. Sand and Mudflats, Chloris gayana grasslands, and Sporobolus spicatus grasslands showed the greatest to lowest spectral responses, respectively, when the spectral response of various land cover categories was evaluated. The health of the vegetation was assessed using the Normalized Difference Vegetation Index (NDVI). Acacia xanthophloea trees in the Lake Nakuru area were at their healthiest in 2000, according to the highest NDVI readings. However, the overall state of the vegetation began to deteriorate in 2011, and as a result of species regeneration in 2014, a new category of "Very Healthy Vegetation" developed. In 2016 and 2020, the same high NDVI value was seen, but differences in NDVI patterns within and between classes were identified, indicating alternate patterns of re-vegetation and deterioration. For some classifications of land cover, negative NDVI values were discovered, indicating the existence of water or flooded vegetation.

In the third experiment, riparian vegetation status was evaluated using Sentinel-1 SAR Ground Range Detected (GRD) imageries. The deteriorated Acacia xanthophloea trees along the riparian reserve were identified using polarimetric bands and backscatter responses. Based on backscatter indices, four categories degraded submerged forest, degraded forest, non-degraded forest, and urban were determined. The "Lake Nakuru" class had the lowest backscatter response, whereas the urban class showed the highest backscatter response. Both VV and VH polarizations of the backscatter response from the degraded submerged forest were equal. The largest backscatter response in VH polarization was seen on the healthy Acacia forest category, primarily because of volume scattering on tree crown surfaces. The amount of moisture in the leaves of healthy Acacia trees has an impact on the backscatter response in VH polarization.

These findings offer insightful information on the dynamics of land cover and vegetation health in the Lake Nakuru riparian reserve during the analysed time periods.

9.3 CONCLUSION

The document's findings demonstrate the value of various methods for identifying and categorizing vegetation using remote sensing data. The capacity of Object-Based Image Analysis (OBIA) to identify Acacia xanthophloea was proven, with classification accuracy depending on the segmentation scale, modelling approach, and band inclusion. On Landsat datasets, Random Forest and J48 classifiers performed very well, displaying excellent agreement and accuracy. The accuracy of the categorization was increased when textural factors were embraced using multitemporal data, and using particular data transformations. In classification challenges, Random Forest routinely defeated other conventional methods. Additionally, Acacia xanthophloea identification performance for RetinaNet and Faster R-CNN models was comparable, with Retina-Net showing somewhat improved precision and recall. But both models struggled to achieve high accuracy with some evaluations thresholds for metrics and IoU. Overally, these findings help to direct future research in this area by offering insightful information about the efficacy of various methods and algorithms for the detection and classification of vegetation.

The improvement and adjustment of object or feature classification in images is made possible by thematic reclassification utilizing Object-Based Image Analysis (OBIA) connected with a GIS system. Reclassification of the Landsat 8 OLI 2014 image led to the identification of new subclasses, demonstrating how reclassification can disclose classes or categories that were previously hidden in an image. The performance of the J48 algorithm was affected by the translation of OBIA datasets to WEKA Machine Learning software. The decline in agreement between the J48 algorithm and the reclassification results suggests that the WEKA algorithm's classification accuracy may have been impacted by the inclusion of OBIA data. Without any further classification, the Landsat 5 TM 2011 image displayed total agreement (100%) with the J48 algorithm, demonstrating that the initial classification of this image was quite accurate. Generated vector shape files using eCognition The ArcGIS attribute table could be linked to developer tools, allowing for the retrieval and analysis of attribute data inside the ArcGIS environment.

Before employing attribute data into machine learning analysis, data cleaning processes were required to assure the quality and integrity of the data. The effectiveness of OBIA-based categorization was impacted by the quantity of characteristics and samples input into WEKA. The agreement between categorization results decreased as the number of occurrences increased, indicating that complexity and predictability increase as the number of cases increases. Vectors or image objects from segmentation images must be combined in order to create new subclasses. The outcome of this merging process and how it affects the development of new subclasses depend on the segmentation scales chosen. The implications of these findings highlight the possibility for thematic reclassification through the integration of OBIA and GIS, the impact of data transition on algorithm performance, the importance of data cleaning, and the contribution of variables and instances to classification agreement.

The results also highlight how crucial it is to choose the right segmentation scales to create useful subclasses during the reclassification process.

SAR Sentinel-1 Experiment depicted the water surface area and the presence of healthy Acacia xanthophloea threads were significantly negatively correlated. Acacia xanthophloea territory is reduced when the water's surface rises. This supports earlier research that connected the dwindling Acacia xanthophloea population to the accumulating water in Lake Nakuru National Park.

Landsat 5TM and Landsat 8 OLI Experiment: The lake's surface area has increased over time, showing that its banks have been overtaken. At the same time, the area covered by healthy Acacia xanthophloea strands has shrunk, and many of the trees are now buried in water. There have been changes in other vegetation classes as well, including losses of acreage in grasslands and forests.

Pleiades-1A Time Series Experiment: Examining spatiotemporal trends in Acacia xanthophloea acreage was steadily reduced by vegetation between 2012 and 2018, then increased from 2018 to 2020, indicating a phase of re-vegetation. Associated with Acacia xanthophloea and undergrowth, other vegetation groupings show comparable patterns of change through time. Additionally, the lake's water quality varies in area depending on the mission.

Overally, these findings show that Lake Nakuru National Park's vegetation and water surface areas are changing. It is clear that Acacia xanthophloea and other plant species suffer from rising water levels. The findings support past research and advance our knowledge of the spatiotemporal dynamics taking place in the studied area.

In conclusion, the results of the three studies performed in the Lake Nakuru riparian reserve shed important light on how remote sensing data can be used to track changes in the health of Acacia xanthophloea trees and associated vegetation species. The primary conclusions are as follows:

Sentinel-1 SAR (SLC) Experiment: The categorization processes relied heavily on covariance matrix indices and radar-based vegetation indices acquired from Sentinel-1 SAR images. The largest spectral responses were seen in bands C11 and C22, and the Radar-based Vegetation Index

(RVI) had the highest value. These metrics were critical in determining the condition of the vegetation. Analysis of the spectral responses of several land cover categories from the scene imageries.

Landsat 5 TM and Landsat 8 OLI experiment revealed distinct patterns. Acacia xanthophloea tree health as assessed by the Normalized Difference Vegetation Index (NDVI) peaked in 2000 but then started to decline. In 2014, a brand-new classification dubbed "Very Healthy Vegetation" emerged, indicating species regeneration. Alternate patterns of re-vegetation and degradation were indicated by the NDVI trends in 2016 and 2020. In several land cover classes, negative NDVI readings indicated the presence of water or flooding.

SAR Sentinel-1(GRD) Experiment: Using Sentinel-1 SAR GRD images to assess the condition of the riparian vegetation, it was possible to spot damaged Acacia xanthophloea trees thanks to polarimetric bands and backscatter signals. Based on backscatter indices, four categories degraded submerged forest, degraded forest, non-degraded forest, and urban were established. The "Lake Nakuru" class had the lowest response, and the "Urban" class had the highest response, when it came to backscatter responses. the amount of moisture in the leaves impacted the backscatter response in VH polarization of healthy Acacia plants.

Our understanding of the dynamics of land cover and vegetation health in the Lake Nakuru riparian reserve during the examined time periods is improved by these findings. Monitoring changes and determining the health of the vegetation in the study area were made easier with the incorporation of remote sensing data and indices.

A number of hypothesis tested on the different airborne and Space borne sensors showed significant difference between and amongst the algorithms used. Engagement of OBIA+Machine Learning models improved on classification accuracies and hence are suitable for monitoring tree species on riparian Landscape at Local Scale. Implementation of off the shelve deep learning framework was instrumental in capturing Acacia xanthophloea at Individual scale. This workflow can be applied in other areas whose Landscape are similar. The newly developed OBIATS.py algorithm was instrumental in dividing the landscape into clusters hence enabling classification of trees and in addition production of temporal profiles. The use of Morphological Attribute Profiles (textural variables) caused an improvement on the classified Radar based S1-GRD resultant maps.

In relation to study limitations, there was lack of Lidar, hyperspectral data and multi-temporal Radar data based on L-Band. Unavailability of funds to capture UAV based RGB imageries on annual basis was also experienced. There was no enough time to engage deep learning paradigm for the detection of Acacia xanthophloea based on UAV point clouds. A deep learning framework specifically tailored and fine-tuned to handle UAV data sets containing degraded fallen trees on flood inundated areas was lacking, hence the inferior results achieved. Due to time limitations other indices such as Radar Vegetation Index(RVI), Green Normalized Difference Vegetation Index(GNDVI) and Perpendicular Vegetation Index (PVI) into the OBIATS.py for generation of temporal profiles.

Future Research should engage the use of Radar data with longer wavelengths (L-Band) which are more sensitive to tree biomass on floodplains. The Use of Lidar based Time series datasets will open up new insights into the number of trees that are degraded but still standing inside the lake waters. Off the shelve deep learning frameworks were used to detect fallen trees on water, mudflat and Land. To compliment Lidar Data, photogrammetric point clouds from the UAV/RGB imageries could be used to investigate (visualization) the condition of the fallen trees on flood inundated riparian reserve. Time series of other vegetation indices such as Radar Vegetation Index(RVI), Green Normalized Difference Vegetation Index (GNDVI), Perpendicular Vegetation Index (PVI) could also be tested in OBIATS.py code for the production of Temporal profiles. Future studies to engage the use of hyperspectral bands in conjunction with OBIA + ML in mapping trees on flood inundated areas.

9.4 RECOMMENDATIONS

The study revealed that Acacia xanthophloea trees have been degrading due to the persistent floods around Lake Nakuru, Kenya. Remote sensing technology was instrumental in drawing these conclusions. In order to cope with the current problem at hand, the recommendations are outlined herein as follows:

1. Continuous monitoring and evaluation of the general state of health of Acacia xanthophloea trees using Unmanned Aerial Vehicles (UAV) on an annual basis.
2. Object Based Image Analysis (OBIA) in conjunction with Machine Learning approaches are recommended for classification at local and regional scales using high to medium resolution remote sensing.
3. Deep Learning architectures in conjunction with Very High Resolution (VHR) RGB imageries are recommended for detection of the geometric structures of tree species (Acacia xanthophloea) individual scale.
4. Fine-tuning of the Deep Learning parameters would help in enhancing the detection rates of fallen trees and in similar environments where tree species have been affected by the floods.
5. The workflows provided herein proposed to be used to update Land Cover and Land Use Mapping of Lake Nakuru as required by the Kenya Vision 2030 initiative that requires lead mapping agency to comprehensively map all land use patterns in Kenya.
6. Kenya Wildlife services (KWS) in conjunction with Kenya Forest services (KFS), ecologists, hydrologists, Conservationists, Community living around Lake Nakuru and the

relevant policy makers need to come up with a strategy of clearing off the fallen trees from the wildlife corridors as inscribed in Kenya Vision 2030 flagship number 4.

REFERENCES

Abbasov, R., Karimov, R., & Jafarova, N. (2022). Mountain Ecosystem Values. In *Ecosystem Services in Azerbaijan: Value and Losses* (pp. 29–69). Springer.

Abdul Aziz, A., Phinn, S., Dargusch, P., Omar, H., & Arjasakusuma, S. (2015). Assessing the potential applications of Landsat image archive in the ecological monitoring and management of a production mangrove forest in Malaysia. *Wetlands Ecology and Management*, *23*, 1049–1066.

Achieng Osio, A., Lê, H.-Â., Ayugi, S., Onyango, F., Odwe, P., & Lefèvre, S. (2022). Detection of Degraded Acacia tree species using deep neural networks on uav drone imagery. *ArXiv E-Prints*, arXiv-2204.

Aguilar, M. A., Aguilar, F. J., García Lorca, A., Guirado, E., Betlej, M., Cichon, P., Nemmaoui, A., Vallario, A., & Parente, C. (2016). Assessment of multiresolution segmentation for extracting greenhouses from WorldView-2 imagery. *International Archives of the Photogrammetry, Remote Sensing and Spatial Information Sciences - ISPRS Archives*, *41*(July), 145–152. https://doi.org/10.5194/isprsarchives-XLI-B7-145-2016

Airoldi, L., Abbiati, M., Beck, M. W., Hawkins, S. J., Jonsson, P. R., Martin, D., Moschella, P. S., Sundelöf, A., Thompson, R. C., & Åberg, P. (2005). An ecological perspective on the deployment and design of low-crested and other hard coastal defence structures. *Coastal Engineering*,*52*(10),1073https://doi.org/https://doi.org/10.1016/j.coastaleng.2005.09.007

Al-Mulla, S., Ari, I., & Koç, M. (2022). Social media for sustainability education: Gaining knowledge and skills into actions for sustainable living. *International Journal of Sustainable Development & World Ecology*, *29*(5), 455–471.

Alon, A. S., Festijo, E. D., & Juanico, D. E. O. (2019). Tree detection using genus-specific RetinaNet from orthophoto for segmentation access of airborne LiDAR data. *2019 IEEE 6th International Conference on Engineering Technologies and Applied Sciences (ICETAS)*, 1–6.

Alqurashi, A. F., & Kumar, L. (2016). Spatiotemporal patterns of urban change and associated environmental impacts in five Saudi Arabian cities: A case study using remote sensing data.

Habitat International,*58*,75–8https://doi.org/https://doi.org/10.1016/j.habitatint.2016.10.001

Amani, M., Mahdavi, S., Afshar, M., Brisco, B., Huang, W., Mirzadeh, S. M. J., White, L., Banks, S., Montgomery, J., & Hopkinson, C. (2019). Canadian wetland inventory using Google Earth Engine: The first map and preliminary results. *Remote Sensing*, *11*(7), 1–20. https://doi.org/10.3390/RS11070842

Amani, M., & Mobasheri, M. R. (2015). A parametric method for estimation of leaf area index using landsat ETM+ data. *GIScience and Remote Sensing*, *52*(4), 478–497. https://doi.org/10.1080/15481603.2015.1055540

Anderson, T. M., Dempewolf, J., Metzger, K. L., Reed, D. N., & Serneels, S. (2008). Generation and maintenance of heterogeneity in the Serengeti ecosystem. *Serengeti III: Human Impacts on Ecosystem Dynamics*, 135–182.

Ansari, A., & Golabi, M. H. (2019). Prediction of spatial land use changes based on LCM in a GIS environment for Desert Wetlands–A case study: Meighan Wetland, Iran. *International Soil and Water Conservation Research*, *7*(1), 64–70.

Anusha, N., & Bharathi, B. (2020). Flood detection and flood mapping using multi-temporal synthetic aperture radar and optical data. *The Egyptian Journal of Remote Sensing and Space Science*, *23*(2), 207–219.

Arthington, A. H., Dulvy, N. K., Gladstone, W., & Winfield, I. J. (2016). Fish conservation in freshwater and marine realms: status, threats and management. *Aquatic Conservation: Marine and Freshwater Ecosystems*, *26*(5), 838–857. https://doi.org/10.1002/aqc.2712

Asgher, M. S., Sharma, S., Singh, R., & Singh, D. (2021). Assessing human interactions and sustainability of Wetlands in Jammu, India using Geospatial technique. *Modeling Earth Systems and Environment*, *7*, 2793–2807.

Atay Kaya, İ., & Kut Görgün, E. (2020). Land use and land cover change monitoring in Bandırma (Turkey) using remote sensing and geographic information systems. *Environmental Monitoring and Assessment*, *192*(7), 1–18.

Atta-ur-Rahman, Farzana, Rahman, G., & Shaw, R. (2017). *Flood Disasters and Land Use Planning in Swat Valley, Eastern Hindu Kush*. 179–195. https://doi.org/10.1007/978-4-431-56442-3_10

Austin, G. (2014). *Green infrastructure for landscape planning: integrating human and natural* *systems*. Routledge.

Avni, R. D. (2020). *Status and Causes of Deterioration of Wetlands in the Eastern Riftvalley, Case Studyof Lake Nakuru-Kenya*. *November*. http://erepository.uonbi.ac.ke/handle/11295/153696

Baatz, M., Benz, U., Dehghani, S., Heynen, M., Höltje, A., Hofmann, P., Lingenfelder, I., Mimler, M., Sohlbach, M., & Weber, M. (2004). eCognition professional user guide 4. *Munich: Definiens-Imaging*, 72.

Bai, Y., Ochuodho, T. O., & Yang, J. (2019). Impact of land use and climate change on water-related ecosystem services in Kentucky, USA. *Ecological Indicators*, *102*, 51–64. https://doi.org/https://doi.org/10.1016/j.ecolind.2019.01.079

Baker, B., Kennedy, J., Stower, K., & Rodiles, N. (n.d.). *Public Engagement : Urban Tree Canopy Update*.

Barančeková, M., Krojerová-Prokešová, J., & Homolka, M. (2007). Impact of deer browsing on natural and artificial regeneration in floodplain forest. *Folia Zool*, *56*(4), 354–364.

Berhane, T., Lane, C., Wu, Q., Anenkhonov, O., Chepinoga, V., Autrey, B., & Liu, H. (2017). Comparing Pixel- and Object-Based Approaches in Effectively Classifying Wetland-Dominated Landscapes. *Remote Sensing*, *10*(2), 46. https://doi.org/10.3390/rs10010046

Berhane, T. M., Costa, H., Lane, C. R., Anenkhonov, O. A., Chepinoga, V. V., & Autrey, B. C. (2019). The influence of region of interest heterogeneity on classification accuracy in wetland systems. *Remote Sensing*, *11*(5), 1–16. https://doi.org/10.3390/rs11050551

Berkeley, U. C., Girshick, R., & Berkeley, U. C. (2017). Contextual Action Recognition with R * CNN. *Iccv*, 1080–1088.

Bezerra, U. A., Cunha, J., Valente, F., Magna, S., Moura, B., Verhoef, A., Perez-marin, A. M., Grande, C., Park, S., Road, B., Science, E., & Kingdom, U. (n.d.). *Ulisses A. Bezerra*.

Blaschke, T. (2010). Object based image analysis for remote sensing. *ISPRS Journal of PhotogrammetryandRemoteSensing*,*65*(1),2,16https://doi.org/10.1016/j.isprsjprs.2009.06.004

Blaschke, Thomas. (2010). Object based image analysis for remote sensing. *ISPRS Journal of Photogrammetry and Remote Sensing*, *65*(1), 2–16.

Boon, M. A., Greenfield, R., & Tesfamichael, S. (2016). Wetland assessment using unmanned aerial vehicle (UAV) photogrammetry. *International Archives of the Photogrammetry*, *Remote Sensing and Spatial Information Sciences - ISPRS Archives*, *41*(July), 781–788. https://doi.org/10.5194/isprsarchives-XLI-B1-781-2016

Borah, S. B., Sivasankar, T., Ramya, M. N. S., & Raju, P. L. N. (2018). Flood inundation mapping and monitoring in Kaziranga National Park, Assam using Sentinel-1 SAR data. *Environmental Monitoring and Assessment*, *190*(9), 1–11. https://doi.org/10.1007/s10661-018-6893-y

Bronge, L. B., & Näslund-Landenmark, B. (2002). Wetland classification for swedish corine land cover adopting a semi-automatic interactive approach. *Canadian Journal of Remote Sensing*, *28*(2), 139–155. https://doi.org/10.5589/m02-011

Brönmark, C., & Hansson, L.-A. (2002). Environmental issues in lakes and ponds: current state and perspectives. *Environmental Conservation*, *29*(3), 290–307.

Busetto, L., Zwart, S. J., & Boschetti, M. (2019). Analysing spatial–temporal changes in rice cultivation practices in the Senegal River Valley using MODIS time-series and the PhenoRice algorithm. *International Journal of Applied Earth Observation and Geoinformation*, *75*, 15–28. https://doi.org/https://doi.org/10.1016/j.jag.2018.09.016

Byun, Y., & Han, D. (2018). Relative radiometric normalization of bitemporal very high-resolution satellite images for flood change detection. *Journal of Applied Remote Sensing*, *12*(02), 1. https://doi.org/10.1117/1.jrs.12.026021

Cai, Y., Lin, H., & Zhang, M. (2019). Mapping paddy rice by the object-based random forest method using time series Sentinel-1/Sentinel-2 data. *Advances in Space Research*, *64*(11), 2233–2244.

Cai, Z., Jönsson, P., Jin, H., & Eklundh, L. (2017). Performance of smoothing methods for reconstructing NDVI time-series and estimating vegetation phenology from MODIS data. *Remote Sensing*, *9*(12), 1271.

Camargo, F. F., Sano, E. E., Almeida, C. M., Mura, J. C., & Almeida, T. (2019). A comparative assessment of machine-learning techniques for land use and land cover classification of the Brazilian tropical savanna using ALOS-2/PALSAR-2 polarimetric images. *Remote Sensing*, *11*(13). https://doi.org/10.3390/rs11131600

Carrion Gordon, L. C. (2018). *Digital data heritage preservation (DHP) modelling and design*.

Chatziantoniou, A., Petropoulos, G. P., & Psomiadis, E. (2017). Co-Orbital Sentinel 1 and 2 for

LULC mapping with emphasis on wetlands in a mediterranean setting based on machine learning. *Remote Sensing*, *9*(12). https://doi.org/10.3390/rs9121259

Chen, C., He, X., Guo, B., Zhao, X., & Chu, Y. (2020). A pixel-level fusion method for multi-source optical remote sensing image combining the principal component analysis and curvelet transform. *Earth Science Informatics*, *13*(4), 1005–1013. https://doi.org/10.1007/s12145-020-00472-7

Chen, Yuanyuan, He, X., Xu, J., Zhang, R., & Lu, Y. (2020). Scattering feature set optimization and polarimetric SAR classification using object-oriented RF-SFS algorithm in coastal wetlands. *Remote Sensing*, *12*(3). https://doi.org/10.3390/rs12030407

Chen, Yujia, & Tian, S. (2020). Comparison of pixel-and object-based image analysis for tea plantation mapping using hyperspectral Gaofen-5 and synthetic aperture radar data. *Journal of Applied Remote Sensing*, *14*(4), 44516.

Chettri, N., Uddin, K., Chaudhary, S., & Sharma, E. (2013). Linking Spatio-temporal land cover change to biodiversity conservation in the koshi tappu wildlife reserve, Nepal. *Diversity*, *5*(2), 335–351. https://doi.org/10.3390/d5020335

Chouari, W. (2021). Wetland land cover change detection using multitemporal Landsat data: a case study of the Al-Asfar wetland, Kingdom of Saudi Arabia. *Arabian Journal of Geosciences*, *14*(6), 523. https://doi.org/10.1007/s12517-021-06815-y

Chrisphine, O. M., Mary, O. A., & Mark, B. K. (2016). Assessment of hydrological impacts of Mau Forest, Kenya. *Hydrology: Current Research*, *7*(1).

Cian, F., Marconcini, M., & Ceccato, P. (2018). Normalized Difference Flood Index for rapid flood mapping: Taking advantage of EO big data. *Remote Sensing of Environment*, *209*, 712–730. https://doi.org/https://doi.org/10.1016/j.rse.2018.03.006

Colditz, R. R., Conrad, C., Wehrmann, T., Schmidt, M., & Dech, S. (2008). TiSeG: A flexible software tool for time-series generation of MODIS data utilizing the quality assessment science data set. *IEEE Transactions on Geoscience and Remote Sensing*, *46*(10), 3296–3308. https://doi.org/10.1109/TGRS.2008.921412

Colloff, M. J., & Baldwin, D. S. (2010). Resilience of floodplain ecosystems in a semi-arid environment. *The Rangeland Journal*, *32*(3), 305–314.

Congalton, R. G., & Green, K. (2019). *Assessing the accuracy of remotely sensed data: principles* *and practices*. CRC press.

Cordeiro, C. L. de O., & Rossetti, D. de F. (2015). Mapping vegetation in a late Quaternary landform of the Amazonian wetlands using object-based image analysis and decision tree classification. *International Journal of Remote Sensing*, *36*(13), 3397–3422. https://doi.org/10.1080/01431161.2015.1060644

Csillik, O., Belgiu, M., Asner, G. P., Kelly, M., Csillik, O., Belgiu, M., Asner, G. P., & Kelly, M. (2019). Object-Based Time-Constrained Dynamic Time Warping Classification of Crops Using Sentinel-2. *Remote Sensing*, *11*(10), 1257. https://doi.org/10.3390/rs11101257

Csillik, O., Cherbini, J., Johnson, R., Lyons, A., & Kelly, M. (2018). Identification of Citrus Trees from Unmanned Aerial Vehicle Imagery Using Convolutional Neural Networks. *Drones*, *2*(4), 39. https://doi.org/10.3390/drones2040039

Cuba,N.,Lawrence,D.,Rogan,J.,&Williams,C.A. (2018). Local variability in the timing and intensity of tropical dry forest deciduousness is explained by differences in forest stand age. *GIScienceandRemoteSensing*,*55*(3),437~456https://doi.org/10.1080/15481603.2017.1403136

Cui,Y.,Zhong,Z.,Wang,D.,Wang,W.U.,&Lieber,C.M. (2003). High Performance Silicon Nano wire Field Effect Transistors.*NanoLetters*,*3*(2),149~152https://doi.org/10.1021/nl025875l

Dabiri, Z., & Lang, S. (2018). *Spectral-spatial dimensionality reduction of APEX hyperspectral imagery for tree species classification ; a case study of Salzach riparian mixed forest*. *June*, 1–12. https://doi.org/10.20944/preprints201806.0188.v1

Dalla Mura, M., Benediktsson, J. A., Waske, B., & Bruzzone, L. (2010). Morphological attribute profiles for the analysis of very high resolution images. *IEEE Transactions on Geoscience and Remote Sensing*, *48*(10), 3747–3762.

Dalponte, M., Ene, L. T., Gobakken, T., Næsset, E., & Gianelle, D. (2018). Predicting selected forest stand characteristics with multispectral ALS data. *Remote Sensing*, *10*(4), 1–15. https://doi.org/10.3390/rs10040586

Davidson, N. C., Dinesen, L., Fennessy, S., Finlayson, C. M., Grillas, P., Grobicki, A., McInnes, R. J., & Stroud, D. A. (2019). A review of the adequacy of reporting to the Ramsar Convention on change in the ecological character of wetlands. *Marine and Freshwater Research*, *71*(1), 117–126. https://doi.org/10.1071/MF18328 de Castro, A. I., Six, J., Plant, R. E., & Peña, J. M. (2018). Mapping crop calendar events and phenology-related metrics at the parcel level by object-based image analysis (OBIA) of MODIS-NDVI time-series: A case study in central California. *Remote Sensing*, *10*(11). https://doi.org/10.3390/rs10111745

De Medici, S. (2021). Italian architectural heritage and photovoltaic systems. Matching style with sustainability. *Sustainability*, *13*(4), 2108.

Deus, D. (2016). Integration of ALOS PALSAR and Landsat data for land cover and forest mapping in northern Tanzania. *Land*, *5*(4). https://doi.org/10.3390/land5040043

Dewan, A. M., & Yamaguchi, Y. (2009). Land use and land cover change in Greater Dhaka, Bangladesh: Using remote sensing to promote sustainable urbanization. *Applied Geography*, *29*(3), 390–401.

Dharani, N., Kinyamario, J. I., & Onyari, J. M. (2006). Structure and composition of Acacia xanthophloea woodland in Lake Nakuru National Park, Kenya. *African Journal of Ecology*, *44*(4), 523–530.

Dong, J., Xiao, X., Kou, W., Qin, Y., Zhang, G., Li, L., Jin, C., Zhou, Y., Wang, J., Biradar, C., Liu, J., & Moore, B. (2015). Tracking the dynamics of paddy rice planting area in 1986-2010 through time series Landsat images and phenology-based algorithms. *Remote Sensing of Environment*, *160*, 99–113. https://doi.org/10.1016/j.rse.2015.01.004

Dong, Q., Chen, X., Chen, J., Zhang, C., Liu, L., Cao, X., Zang, Y., Zhu, X., & Cui, X. (2020). Mapping winter wheat in North China using Sentinel 2A/B data: A method based on phenology-time weighted dynamic time warping. *Remote Sensing*, *12*(8), 1274.

dos Santos, A. A., Marcato Junior, J., Araújo, M. S., Di Martini, D. R., Tetila, E. C., Siqueira, H. L., Aoki, C., Eltner, A., Matsubara, E. T., Pistori, H., Feitosa, R. Q., Liesenberg, V., & Gonçalves, W. N. (2019). Assessment of CNN-based methods for individual tree detection on images captured by RGB cameras attached to UAVS. *Sensors (Switzerland)*, *19*(16), 1–11. https://doi.org/10.3390/s19163595

dos Santos, E. P., Da Silva, D. D., & do Amaral, C. H. (2021). Vegetation cover monitoring in tropical regions using SAR-C dual-polarization index: seasonal and spatial influences. *International Journal of Remote Sensing*, *42*(19), 7581–7609.

Dronova, I. (2015). Object-based image analysis in wetland research: A review. *Remote Sensing*, *7*(5), 6380–6413. https://doi.org/10.3390/rs70506380

Du, B., Mao, D., Wang, Z., Qiu, Z., Yan, H., Feng, K., & Zhang, Z. (2021). Mapping wetland plant communities using unmanned aerial vehicle hyperspectral imagery by comparing object/pixel-based classifications combining multiple machine-learning algorithms. *IEEE Journal of Selected Topics in Applied Earth Observations and Remote Sensing*, *14*, 8249–8258.

Dubois, C., Mueller, M. M., Pathe, C., Jagdhuber, T., Cremer, F., Thiel, C., & Schmullius, C. (2020). Characterization of land cover seasonality in sentinel-1 time series data. *ISPRS Annals of the Photogrammetry, Remote Sensing and Spatial Information Sciences*, *5*(3), 97–104. https://doi.org/10.5194/isprs-Annals-V-3-2020-97-2020

Dupuy, S., Barbe, E., & Balestrat, M. (2012). *An Object-Based Image Analysis Method for Monitoring Land*. *1997*, 404–423. https://doi.org/10.3390/rs4020404

Durieux, L., Lagabrielle, E., & Nelson, A. (2008). *A method for monitoring building construction in urban sprawl areas using object-based analysis of Spot 5 images and existing GIS data A method for monitoring building construction in urban sprawl areas using object-based analysis of Spot 5 images and exi*. *May 2016*. https://doi.org/10.1016/j.isprsjprs.2008.01.005

Effiom, A. E., van Leeuwen, L. M., Nyktas, P., Okojie, J. A., & Erdbrügger, J. (2019). Combining unmanned aerial vehicle and multispectral Pleiades data for tree species identification, a prerequisite for accurate carbon estimation. *Journal of Applied Remote Sensing*, *13*(03), 1. https://doi.org/10.1117/1.jrs.13.034530

Eid, A. N. M., Olatubara, C. O., Ewemoje, T. A., El-Hennawy, M. T., & Farouk, H. (2020). Inland wetland time-series digital change detection based on SAVI and NDWI indecies: Wadi El-Rayan lakes, Egypt. *Remote Sensing Applications: Society and Environment*, *19*, 100347. https://doi.org/https://doi.org/10.1016/j.rsase.2020.100347

Eklundh, L., & Jönsson, P. (2015). *TIMESAT 3.2 with parallel processing Software Manual*. 1–88.

Eliud, L. (2013). *Spatio-temporal variations in Physico-Chemical Parameters, Nutrirnts and concentration of heavy metals along a gradient of of anthropogenic activities within kapsabet river,Kenya,july*.

ENVI. (2009). ENVI Atmospheric Correction Module: QUAC and FLAASH user's guide. *Module*

Version,44.http://scholar.google.com/scholar?hl=en&btnG=Search&q=intitle:ENVI+Atmospheric+Correction+Module:+QUAC+and+FLAASH+user's+guide#0

Eric odada;Jackson Raini;Robert Ndetei. (1981). *Experiences and Lessons learned Brief for lake nakuru*. 1–50.

Evans, H. L., Soule, E. H., & Winkelmann, R. K. (1979). Atypical lipoma, atypical intramuscular lipoma, and well differentiated retroperitoneal liposarcoma. A reappraisal of 30 cases formerly classified as well differentiated liposarcoma. *Cancer*, *43*(2), 574–584.

Fallatah, A., Jones, S., & Mitchell, D. (2018). *Mapping Informal Settlements in the Middle East Environment using an Object-Based Machine- Learning Approach*. *September*. https://doi.org/10.20944/preprints201809.0219.v1

Farooq, S., & Govil, H. (2014). Mapping Regolith and Gossan for Mineral Exploration in the Eastern Kumaon Himalaya, India using hyperion data and object oriented image classification. *AdvancesinSpaceResearch*,*53*(12),1676~1685.https://doi.org/https://doi.org/10.1016/j.asr.2013.04.002

Fawagreh, K., Gaber, M. M., & Elyan, E. (2014). Random forests: From early developments to recent advancements. *Systems Science and Control Engineering*, *2*(1), 602–609. https://doi.org/10.1080/21642583.2014.956265

Feizizadeh, B., Mohammadzade Alajujeh, K., Lakes, T., Blaschke, T., & Omarzadeh, D. (2021). A comparison of the integrated fuzzy object-based deep learning approach and three machine learning techniques for land use/cover change monitoring and environmental impacts assessment.*GIScienceandRemoteSensing*,*58*(8),1543~1570.https://doi.org/10.1080/15481603.2021.2000350

Felde, G. W., Anderson, G. P., Gardner, J. A., Adler-Golden, S. M., Matthew, M. W., & Berk, A. (2004). Water vapor retrieval using the FLAASH atmospheric correction algorithm. *Algorithms and Technologies for Multispectral, Hyperspectral, and Ultraspectral Imagery X*, *5425*, 357–367.

Feng, S., & Fan, F. (2019). A Hierarchical Extraction Method of Impervious Surface Based on NDVI Thresholding Integrated With Multispectral and High-Resolution Remote Sensing Imageries. *IEEE Journal of Selected Topics in Applied Earth Observations and Remote Sensing*, *12*(5), 1461–1470. https://doi.org/10.1109/JSTARS.2019.2909129

Feranec, J., Soukup, T., Hazeu, G., & Jaffrain, G. (2016). *European landscape dynamics: CORINE land cover data*. CRC Press.

Fernerkundung, D. (2017). *Technology Institute Scientific Record 2013 – 2017*.

Foody, G. M. (2002). Status of land cover classification accuracy assessment. In *Remote Sensing of Environment* (Vol. 80, Issue 1, pp. 185–201). Elsevier Inc. https://doi.org/10.1016/S0034-4257(01)00295-4

Franklin, S. E., & Ahmed, O. S. (2017). Object-based wetland characterization using radarsat-2 quad-polarimetric SAR data, landsat-8 OLI imagery, and airborne lidar-derived geomorphometric variables. *Photogrammetric Engineering and Remote Sensing*, *83*(1), 27–36. https://doi.org/10.14358/PERS.83.1.27

Füzy, A., Kovács, R., Cseresnyés, I., Parádi, I., Szili-Kovács, T., Kelemen, B., Rajkai, K., & Takács, T. (2019). Selection of plant physiological parameters to detect stress effects in pot experiments using principal component analysis. *Acta Physiologiae Plantarum*, *41*(5), 1–10. https://doi.org/10.1007/s11738-019-2842-9

Galidaki, G. N., Zianis, D., Gitas, I. Z., Radoglou, K., Karathanassi, V., Tsakiri-Strati, M., Woodhouse, I. H., & Mallinis, G. (2017). Vegetation biomass estimation with remote sensing: focus on forest and other wooded land over the Mediterranean ecosystem. *International Journal of Remote Sensing*, *38*, 1940–1966.

Galvin, K. A., Thornton, P. K., Boone, R. B., & Sunderland, J. (2004). Climate variability and impacts on East African livestock herders: the Maasai of Ngorongoro Conservation Area, Tanzania. *African Journal of Range and Forage Science*, *21*(3), 183–189.

Gao, Y., & Mas, J. F. (2008). *A Comparison of the Performance of Pixel Based and Object Based Classifications over Images with Various Spatial Resolutions*.

Gašparović, M., & Dobrinić, D. (2020). Comparative assessment of machine learning methods for urban vegetation mapping using multitemporal Sentinel-1 imagery. *Remote Sensing*, *12*(12). https://doi.org/10.3390/rs12121952

Gašparović, M., & Jogun, T. (2018). Theeffect of fusing Sentinel-2 bands on land-cover classification.*InternationalJournalofRemoteSensing*,*39*(3),822~841.https://doi.org/10.1080/01431161.2017.1392640

Gašparović, M., & Klobučar, D. (2021). Mapping floods in lowland forest using sentinel-1 and sentinel-2 data and an object-based approach. *Forests*, *12*(5), 553.

Geng, L., Ma, M., & Wang, H. (2016). An Effective Compound Algorithm for Reconstructing MODIS NDVI Time Series Data and Its Validation Based on Ground Measurements. *IEEE Journal of Selected Topics in Applied Earth Observations and Remote Sensing*, *9*(8), 3588–3597. https://doi.org/10.1109/JSTARS.2015.2495112

Girshick, R., Donahue, J., Darrell, T., Malik, J., Berkeley, U. C., & Malik, J. (2014). 1043.0690. *Proceedings of the IEEE Computer Society Conference on Computer Vision and Pattern Recognition*, *1*, 5000. https://doi.org/10.1109/CVPR.2014.81

Githumbi, E. N., Courtney Mustaphi, C. J., Yun, K. J., Muiruri, V., Rucina, S. M., & Marchant, R. (2018). Late Holocene wetland transgression and 500 years of vegetation and fire variability in the semi-arid Amboseli landscape, southern Kenya. *Ambio*, *47*, 682–696.

Gomes, M. F., Maillard, P., & Deng, H. (2018). Individual tree crown detection in sub-meter satellite imagery using Marked Point Processes and a geometrical-optical model. *Remote Sensing of Environment*, *211*, 184–195.

Gorelick, N., Hancher, M., Dixon, M., Ilyushchenko, S., Thau, D., & Moore, R. (2017). Google Earth Engine: Planetary-scale geospatial analysis for everyone. *Remote Sensing of Environment*, *202*, 18–27.

Gössling, S., Peeters, P., Hall, C. M., Ceron, J.-P., Dubois, G., & Scott, D. (2012). Tourism and water use: Supply, demand, and security. An international review. *Tourism Management*, *33*(1), 1–15.

Goulder,L.H.,&Kennedy,D.(2011).Interpreting and estimating the value of ecosystem services. *Natural Capital: Theory and Practice of Mapping Ecosystem Services*, *15*.

Gowreesunkar, V. G. B., Maingi, S. W., & Ming'ate, F. L. M. (2022). *Management of Tourism Ecosystem Services in a Post Pandemic Context: Global Perspectives*. Taylor & Francis.

Granata, F., Gargano, R., & de Marinis, G. (2020). Artificial intelligence based approaches to evaluate actual evapotranspiration in wetlands. *Science of The Total Environment*, *703*, 135653. https://doi.org/https://doi.org/10.1016/j.scitotenv.2019.135653

Griffith, J. A., Martinko, E. A., Whistler, J. L., & Price, K. P. (2002a). Index (NDVI) Relationships to Central Plains Stream Conditions. *Landscape*, *859*, 846–859.

Griffith, J. A., Martinko, E. A., Whistler, J. L., & Price, K. P. (2002b). Interrelationships among landscapes, NDVI, and stream water quality in the US Central Plains. *Ecological Applications*, *12*(6), 1702–1718.

Grishkin, V. M., & Karimov, S. I. (2022). Use of satellite imagery and index control to monitor and analyze the agricultural lands of Bukhara region, which is a world historical heritage. *2021 Asia-Pacific Conference on Applied Mathematics and Statistics*, *2471*, 060004. https://doi.org/10.1063/5.0089537

Gu, F., & Liu, W. (2010). Applications of Remote Sensing and GIS to the Assessment of Riparian Zones for Environmental Restoration in Agricultural Watersheds. *Geo-Spatial Information Science*, *13*(4), 263–268. https://doi.org/10.1007/s11806-010-0368-9

Guan, H., Li, J., Chapman, M., Deng, F., Ji, Z., & Yang, X. (2013). Integration of orthoimagery and lidar data for object-based urban thematic mapping using random forests. *International Journal of Remote Sensing*, *34*(14), 5166–5186.

Gudmann, A., Csikós, N., Szilassi, P., & Mucsi, L. (2020). Improvement in satellite image-based land cover classification with landscape metrics. *Remote Sensing*, *12*(21), 3580.

Gumma, M. K., Kadiyala, M. D. M., Panjala, P., Ray, S. S., Akuraju, V. R., Dubey, S., Smith, A. P., Das, R., & Whitbread, A. M. (2022). Assimilation of Remote Sensing Data into Crop Growth Model for Yield Estimation: A Case Study from India. *Journal of the Indian Society of Remote Sensing*, *50*(2), 257–270. https://doi.org/10.1007/s12524-021-01341-6

Günen, M. A. (2022). Performance comparison of deep learning and machine learning methods in determining wetland water areas using EuroSAT dataset. *Environmental Science and Pollution Research*, *29*(14), 21092–21106. https://doi.org/10.1007/s11356-021-17177-z

Guo, M., Li, J., Sheng, C., Xu, J., & Wu, L. (2017). A review of wetland remote sensing. *Sensors (Switzerland)*, *17*(4), 1–36. https://doi.org/10.3390/s17040777

Guo, Q., Liu, J., & Kaliuzhnyi, M. (2022). YOLOX-SAR: High-Precision Object Detection System Based on Visible and Infrared Sensors for SAR Remote Sensing. *IEEE Sensors Journal*, *22*(17), 17243–17253. https://doi.org/10.1109/JSEN.2022.3186889

Gutman, G., Oceanic, N., & Reissell, A. (2008). *Land-Cover and Land-Use Change Under Changing Climate in the Eurasian Metadata of the book that will be visualized online* (Vol. 1, Issue September 2018).

Hägele, M., Seegerer, P., Lapuschkin, S., Bockmayr, M., Samek, W., Klauschen, F., Müller, K.-

R., & Binder, A. (2020). Resolving challenges in deep learning-based analyses of histopathological images using explanation methods. *Scientific Reports*, *10*(1), 1–12.

Hajjaji, Y., Boulila, W., Farah, I. R., Romdhani, I., & Hussain, A. (2021). Big data and IoT-based applications in smart environments: A systematic review. *Computer Science Review*, *39*, 100318. https://doi.org/https://doi.org/10.1016/j.cosrev.2020.100318

Hake, B. J. (2022). The French connection at the Council of Europe: éducation permanente as a pan-European policy repertoire. *International Journal of Lifelong Education*, *41*(4–5), 476–492.

Halabisky, M., Babcock, C., & Moskal, L. M. (2018). *Harnessing the Temporal Dimension to Improve,ObjectBasedImageAnalysisClassificationofWetlands*.https://doi.org/10.3390/rs10091467

Hammer, Ø., Harper, D. A. T., & Ryan, P. D. (2001). PAST: Paleontological statistics software package for education and data analysis. *Palaeontologia Electronica*, *4*(1), 9.

Han, H., Han, C., Lan, T., Huang, L., Hu, C., & Xue, X. (2020). Automatic shadow detection for multispectral satellite remote sensing images in invariant color spaces. *Applied Sciences (Switzerland)*, *10*(18), 1–25. https://doi.org/10.3390/APP10186467

Harvey, K. R., & Hill, G. J. E. (2001). Vegetation mapping of a tropical freshwater swamp in the northern territory, australia: A comparison of aerial photography, landsat tm and spot satellite imagery.*InternationalJournalofRemoteSensing*,*22*(15),2911~2925https://doi.org/10.1080/01431160119174

Hausmann, A., Toivonen, T., Fink, C., Heikinheimo, V., Tenkanen, H., Butchart, S. H. M., Brooks, T. M., & Di Minin, E. (2019). Assessing global popularity and threats to Important Bird and Biodiversity Areas using social media data. *Science of the Total Environment*, *683*, 617–623.

Hay, G. J., Castilla, G., Wulder, M. A., & Ruiz, J. R. (2005). An automated object-based approach for the multiscale image segmentation of forest scenes. *International Journal of Applied Earth Observation and Geoinformation*, *7*(4), 339–359.

He, J., Liu, Y., Qiao, Y., & Dong, C. (2020). Conditional sequential modulation for efficient global image retouching. *Computer Vision–ECCV 2020: 16th European Conference, Glasgow, UK, August 23–28, 2020, Proceedings, Part XIII 16*, 679–695.

Hempattarasuwan, N., Christakos, G., & Wu, J. (2019). Changes of Wiang Nong Lom and Nong

Luang Wetlands in Chiang Saen Valley (Chiang Rai Province, Thailand) during the Period 1988-2017. *IEEE Journal of Selected Topics in Applied Earth Observations and Remote Sensing*, *12*(11), 4224–4238. https://doi.org/10.1109/JSTARS.2019.2937949

Hess, J., & Kelman, I. (2017). Tourism industry financing of climate change adaptation: exploring the potential in small island developing states. *Climate, Disaster and Development Journal*, *2*(2), 33–45.

Heumann, B. W. (2011a). Remote Sensing of Mangrove Composition and Structure in the Galapagos Islands. *Department of Geography*, *PhD*, 168.

Heumann, B. W. (2011b). Satellite remote sensing of mangrove forests: Recent advances and futureopportunities.*ProgressinPhysicalGeography*.https://doi.org/10.1177/03091333103853 71

Hird, J. N., & McDermid, G. J. (2009). Noise reduction of NDVI time series: An empirical comparison of selected techniques. *Remote Sensing of Environment*, *113*(1), 248–258. https://doi.org/10.1016/j.rse.2008.09.003

Hnatushenko, V. V, & Vasyliev, V. V. (2016). REMOTE SENSING IMAGE FUSION USING ICA AND OPTIMIZED WAVELET TRANSFORM. *The International Archives of the Photogrammetry, Remote Sensing and Spatial Information Sciences*, *XLI-B7*, 653–659. https://doi.org/10.5194/isprs-archives-XLI-B7-653-2016

Houphlet, S. D. K., Dusseux, P., Adiko, A. E. G., Konan-Waidhet, A. B., Munoz, F., Bigot, S., & Adou Yao, C. Y. (2023). Object-based characterization of vegetation heterogeneity with sentinel images proves efficient in a highly human-influenced National Park of Côte d’Ivoire. *Environmental Monitoring and Assessment*, *195*(1), 200.

Huang, H., & Zhang, L. (2007). A study of the population dynamics of Spartina alterniflora at Jiuduansha shoals, Shanghai, China. *Ecological Engineering*, *29*(2), 164–172. https://doi.org/https://doi.org/10.1016/j.ecoleng.2006.06.005

Huang, Q., Parker, D. C., Filatova, T., & Sun, S. (2014). A review of urban residential choice models using agent-based modeling. *Environment and Planning B: Planning and Design*, *41*(4), 661–689.

Huo, L. Z., Boschetti, L., & Sparks, A. M. (2019). Object-based classification of forest disturbance typesintheconterminousUnitedStates.*RemoteSensing*,*11*(5).1https://doi.org/10.3390/rs11050

477

Huqa, T. J. (2015). *The impact of climate variability on the ecology of a lion (Panthera leo Linnaeus 1758) population and lion livestock conflicts in the Amboseli ecosystem–Kenya*. Leiden University.

Ienco, D., Interdonato, R., Gaetano, R., & Minh, D. H. T. (2019). Combining Sentinel-1 and Sentinel-2 Satellite Image Time Series for land cover mapping via a multi-source deep learning architecture. *ISPRS Journal of Photogrammetry and Remote Sensing*, *158*, 11–22.

Immitzer, M., Vuolo, F., & Atzberger, C. (2016). First Experience with Sentinel-2 Data for Crop and Tree Species Classifications in Central Europe. *Remote Sensing*, *8*(3), 166. https://doi.org/10.3390/rs8030166

Iradukunda, P., Sang, J. K., Nyadawa, M. O., & Maina, C. W. (2020). Sedimentation Effect on the Storage Capacity in Lake Nakuru, Kenya. *Open Access Journal Journal of Sustainable Research in Engineering*, *5*(3), 149–158.

Jahjah, M., & Ulivieri, C. (2010). Automatic archaeological feature extraction from satellite VHR images.*ActaAstronautica*,*66*(9),1302~1310.https://doi.org/https://doi.org/10.1016/j.actaastro.2009.10.028

Jardine, M. A., Miller, J. A., & Becker, M. (2018). Coupled X-ray computed tomography and grey level co-occurrence matrices as a method for quantification of mineralogy and texture in 3D. *Computers & Geosciences*, *111*, 105–117.

Jensen, J. R. (1996). *Introductory digital image processing: a remote sensing perspective.* (Issue Ed. 2). Prentice-Hall Inc.

Ji, W., Xu, X., & Murambadoro, D. (2015). Understanding urban wetland dynamics: cross-scale detection and analysis of remote sensing. *International Journal of Remote Sensing*, *36*(7), 1763–1788. https://doi.org/10.1080/01431161.2015.1024895

Jiang, S., Yao, W., & Heurich, M. (2019). Dead wood detection based on semantic segmentation of VHR aerial CIR imagery using optimized FCN-Densenet. *International Archives of the Photogrammetry, Remote Sensing and Spatial Information Sciences - ISPRS Archives*, *42*(2/W16), 127–133. https://doi.org/10.5194/isprs-archives-XLII-2-W16-127-2019

Jönsson, P., & Eklundh, L. (2004). TIMESAT—a program for analyzing time-series of satellite sensordata.*Computers&Geosciences*,*30*(8),833~845.https://doi.org/https://doi.org/10.1016/j.

cageo.2004.05.006

Kaiser, M. F. (2009). Environmental changes, remote sensing, and infrastructure development: The case of Egypt's East Port Said harbour. *Applied Geography*, *29*(2), 280–288.

Kaplan, G., & Avdan, U. (2017). Water extraction technique in mountainous areas from satellite images.*Journalof Applied Remote Sensing*, *11*(04), 1. https://doi.org/10.1117/1.jrs.11.046002

Kaplan, G., & Avdan, U. (2018a). Sentinel-1 and Sentinel-2 Data Fusion for Mapping and MonitoringWetlands.*Preprints*,*July*,1–12. https://doi.org/10.20944/preprints201807.0244.v1

Kaplan, G., & Avdan, U. (2018b). Sentinel-1 and Sentinel-2 Data Fusion For Wetlands Mapping: Balikdami, Turkey. *International Archives of the Photogrammetry, Remote Sensing & Spatial Information Sciences*, *42*(3).

Kaplan, G., & Avdan, U. (2018c). Sentinel-1 and Sentinel-2 data fusion for wetlands mapping: Balikdami, Turkey. *International Archives of the Photogrammetry, Remote Sensing and SpatialInformation Sciences - ISPRS Archives*, *42*(3), 729–734. https://doi.org/10.5194/isprs-archives-XLII-3-729-2018

Kaplan, G., & Avdan, U. (2019). Evaluating the utilization of the red edge and radar bands from sentinel sensors for wetland classification. *Catena*, *178*, 109–119.

Karasiak, N, Fauvel, M., Monteil, C., & Sheeren, D. (2020). Sentinel-2 Time Series in South West France. *ISPRS Annals of the Photogrammy, 5(3),* 469–476.

Karasiak, Nicolas, Fauvel, M., Dejoux, J.-F., Monteil, C., & Sheeren, D. (2020). Optimal dates for deciduous tree species mapping using full years sentinel-2 time series in south west France. *ISPRS Annals of the Photogrammetry, Remote Sensing and Spatial Information Sciences*, *3*, 469–476.

Karlson, M., Reese, H., & Ostwald, M. (2014). Tree crown mapping in managed woodlands (Parklands) of semi-arid West Africa using WorldView-2 imagery and geographic object basedimageanalysis.*Sensors(Switzerland)*,*14*(12),22643~22669.https://doi.org/10.3390/s141222643

Kaushik, S., Ravanel, L., Magnin, F., Trouve, E., Yan, Y., & Cusicanqui, D. (n.d.). Ice Aprons in the Mont-Blanc Massif (Western European Alps): Topographic Characteristics and Relations with Other Types of Glaciers. *Available at SSRN 4051434*.

Kavzoglu, T. (2017). Object-Oriented Random Forest for High Resolution Land Cover Mapping

UsingQuickbird-2Imagery.In*HandbookofNeuralComputation*.https://doi.org/10.1016/B978-0-12-811318-9.00033-8

Kavzoglu, T., & Tonbul, H. (2017). A comparative study of segmentation quality for multi-resolution segmentation and watershed transform. *2017 8th International Conference on Recent Advances in Space Technologies (RAST)*, 113–117.

Kennedy, R. E., Andréfouët, S., Cohen, W. B., Gómez, C., Griffiths, P., Hais, M., Healey, S. P., Helmer, E. H., Hostert, P., Lyons, M. B., Meigs, G. W., Pflugmacher, D., Phinn, S. R., Powell, S. L., Scarth, P., Sen, S., Schroeder, T. A., Schneider, A., Sonnenschein, R., Zhu, Z. (2014). *BringinganecologicalviewofchangetoLandsatbasedremotesensing*.https://doi.org/10.1890/130066

Kennedy, R. E., Yang, Z., & Cohen, W. B. (2010). Detecting trends in forest disturbance and recovery using yearly Landsat time series: 1. LandTrendr - Temporal segmentation algorithms.*RemoteSensingofEnvironment*,*114*(12),2897~2910https://doi.org/10.1016/j.rse.2010.07.008

Kenya, R. of. (2007). *Kenya Vision 2030 REPUBLIC OF KENYA July - August, 2007*. 1–28.

Keram, A., Halik, Ü., Keyimu, M., Aishan, T., Mamat, Z., & Rouzi, A. (2019). Gap dynamics of natural Populus euphratica floodplain forests affected by hydrological alteration along the Tarim River: Implications for restoration of the riparian forests. *Forest Ecology and Management*, *438*, 103–113.

Keshtkar, H., Voigt, W., & Alizadeh, E. (2017). Land-cover classification and analysis of change using machine-learning classifiers and multi-temporal remote sensing imagery. *Arabian Journal of Geosciences*, *10*(6). https://doi.org/10.1007/s12517-017-2899-y

Kiffner, C., Rheault, H., Miller, E., Scheetz, T., Enriquez, V., Swafford, R., Kioko, J., & Prins, H. H. T. (2017). Long-term population dynamics in a multi-species assemblage of large herbivores in East Africa. *Ecosphere*, *8*(12), e02027.

Kim, M., & Song, M. H. (2023). High Performing Facial Skin Problem Diagnosis with Enhanced Mask R-CNN and Super Resolution GAN. *Applied Sciences (Switzerland)*, *13*(2). https://doi.org/10.3390/app13020989

Koppe, W., Gnyp, M. L., Hütt, C., Yao, Y., Miao, Y., Chen, X., & Bareth, G. (2013). Rice monitoring with multi-temporal and dual-polarimetric TerraSAR-X data. *International*

Journal of Applied Earth Observation and Geoinformation, *21*, 568–576.

Kotaridis, I., & Lazaridou, M. (2022). Integrating object-based image analysis and geographic information systems for waterbodies delineation on synthetic aperture radar data. *Geocarto International*, *37*(16), 4655–4670.

Krankina, O. N., Pflugmacher, D., Hayes, D. J., McGuire, A. D., Hansen, M. C., Häme, T., Elsakov, V., & Nelson, P. (2010). Vegetation cover in the eurasian arctic: Distribution, monitoring, and role in carbon cycling. In *Eurasian arctic land cover and land use in a changing climate* (pp. 79–108). Springer.

Kumsa, A., Legas, A., Nemomissa, S., & Gurmessa, D. (2019). *Remote Sensing and GIS Application for Land use/ Land cover Change Analysis: case study of Jarmet Wet-land and itssurroundingenvironmentsinwesternEthiopia*.*July*.https://doi.org/10.20944/preprints201907.0275.v1

Kuntsevich, V. M., Gubarev, V. F., Kondratenko, Y. P., Lebedev, D. V., & Lysenko, V. P. (2018). Control systems: Theory and applications. In *Control Systems: Theory and Applications*.

Lambin, E. F., Geist, H. J., & Lepers, E. (2003). Dynamics of land-use and land-cover change in tropical regions. *Annual Review of Environment and Resources*, *28*(1), 205–241.

Landis, R. ., & Koch, G. (1977). An Application of Hierarchical Kappa-type Statistics in the Assessment of Majority Agreement among Multiple Observers Author (s): J . Richard Landis and Gary G . Koch Published by : International Biometric Society Stable URL : https://www.jstor.org/stab. *Biometrics*, *33*(2), 363–374.

Lang, S. (2014). *Different Approaches for IDP Camp Analyses in West Darfur (Sudan) – a status report*. *July*. https://doi.org/10.13140/2.1.1656.6409

Lark, T. J., Mueller, R. M., Johnson, D. M., & Gibbs, H. K. (2017). Measuring land-use and land-cover change using the US department of agriculture's cropland data layer: Cautions and recommendations. *International Journal of Applied Earth Observation and Geoinformation*, *62*, 224–235.

Lebourgeois, V., Vintrou, É., Ameline, M., & Butler, S. (2017). *A Combined Random Forest and OBIA Classification Scheme for Mapping Smallholder Agriculture at Different Nomenclature Levels Using Multisource Data (Simulated Sentinel-2 Time Series , VHRS and DEM)*. 1–20. https://doi.org/10.3390/rs9030259

Lee, C. T., & Marsh, S. E. (1995). The use of archival Landsat MSS and ancillary data in a GIS environment to map historical change in an urban riparian habitat. *Photogrammetric Engineering and Remote Sensing*, *61*(8), 999–1008.

Lee, J.-S., & Pottier, E. (2017). *Polarimetric radar imaging: from basics to applications*. CRC press.

Lemenkova, P., & Debeir, O. (2022). R Libraries for Remote Sensing Data Classification by K-Means Clustering and NDVI Computation in Congo River Basin, DRC. *Applied Sciences (Switzerland)*, *12*(24), 1–26. https://doi.org/10.3390/app122412554

Li, N., Zhou, D., Duan, F., Wang, S., & Cui, Y. (2010). Application of unmanned airship image system and processing techniques for identifying of fresh water wetlands at a community scale. *2010 18th International Conference on Geoinformatics, Geoinformatics 2010*, *40871241*. https://doi.org/10.1109/GEOINFORMATICS.2010.5567533

Li, Q., Wang, C., Zhang, B., & Lu, L. (2015). *Object-Based Crop Classification with Landsat-MODISEnhancedTime-SeriesData*.*October*,16091~16107https://doi.org/10.3390/rs71215820

Liao, A., Chen, L., Chen, J., He, C., Cao, X., Chen, J., Peng, S., Sun, F., & Gong, P. (2014). High-resolution remote sensing mapping of global land water. *Science China Earth Sciences*, *57*(10), 2305–2316. https://doi.org/10.1007/s11430-014-4918-0

Lin, C., Zhong, L., Song, X. P., Dong, J., Lobell, D. B., & Jin, Z. (2022). Early- and in-season crop type mapping without current-year ground truth: Generating labels from historical information via a topology-based approach. *Remote Sensing of Environment*, *274*(March). https://doi.org/10.1016/j.rse.2022.112994

Lin, T.-Y., Dollár, P., Girshick, R., He, K., Hariharan, B., & Belongie, S. (2017). Feature pyramid networks for object detection. *Proceedings of the IEEE Conference on Computer Vision and Pattern Recognition*, 2117–2125.

Lin, T.-Y., Goyal, P., Girshick, R., He, K., & Dollár, P. (2017). Focal loss for dense object detection. *Proceedings of the IEEE International Conference on Computer Vision*, 2980–2988.

Liu, H., Li, X.-M., & Guo, H. (2015). The dynamic processes of sea ice on the east coast of Antarctica—A case study based on spaceborne synthetic aperture radar data from TerraSAR-

X. *IEEE Journal of Selected Topics in Applied Earth Observations and Remote Sensing*, *9*(3), 1187–1198.

Liu, J., Liu, M., Zhuang, D., Zhang, Z., & Deng, X. (2003). Study on spatial pattern of land-use change in China during 1995–2000. *Science in China Series D: Earth Sciences*, *46*(4), 373–384.

Liu, M. W., Ozdogan, M., & Zhu, X. (2013). Crop type classification by simultaneous use of satellite images of different resolutions. *IEEE Transactions on Geoscience and Remote Sensing*, *52*(6), 3637–3649.

Liu, S., Qi, Z., Li, X., & Yeh, A. G.-O. (2019). Integration of convolutional neural networks and object-based post-classification refinement for land use and land cover mapping with optical and SAR data. *Remote Sensing*, *11*(6), 690.

Liu, X., Liu, C., Kang, Q., & Yin, B. (2018). Vegetation response to climate change in the southern part of Qinghai-Tibet plateau at basinal Scale. *International Archives of the Photogrammetry, Remote Sensing and Spatial Information Sciences - ISPRS Archives*, *42*(3), 1145–1152. https://doi.org/10.5194/isprs-archives-XLII-3-1145-2018

Long, X., Li, X., Lin, H., & Zhang, M. (2021). Mapping the vegetation distribution and dynamics of a wetland using adaptive-stacking and Google Earth Engine based on multi-source remote sensing data. *International Journal of Applied Earth Observation and Geoinformation*, *102*, 102453. https://doi.org/https://doi.org/10.1016/j.jag.2021.102453

Lu, D., Mausel, P., Brondízio, E., & Moran, E. (2004). Change detection techniques. *International Journal of Remote Sensing*, *25*(12), 2365–2401. https://doi.org/10.1080/0143116031000139863

Lunetta, R. S., Knight, J. F., Ediriwickrema, J., Lyon, J. G., & Worthy, L. D. (2006). Land-cover change detection using multi-temporal MODIS NDVI data. *Remote Sensing of Environment*, *105*(2), 142–154.

Luo, K., & Mornya, P. M. P. (2019). Fine Monitoring of Wetlands at Provincial Large-Scale Using Object-Based Technique and Medium-Resolution Image. *IEEE Journal of Selected Topics in AppliedEarthObservationsandRemoteSensing*,*12*(8),2878~2888.https://doi.org/10.1109/JSTARS.2019.2918321

Ma, H.-R., Cheng, X., Chen, L., Zhang, H., & Xiong, H. (2016). Automatic identification of shallow landslides based on Worldview2 remote sensing images. *Journal of Applied Remote Sensing*, *10*(1), 16008.

Ma, X. (2017). A review of supervised object-based land-cover image classification. *ISPRS JournalofPhotogrammetryandRemoteSensing*,*130*(August),277~293.https://doi.org/10.1016/j.isprsjprs.2017.06.001

MacFaden, S. W., Raney, P. A., & O'Neil-Dunne, J. (2021). LiDAR-aided hydrogeologic modeling and object-based wetland mapping approach for Pennsylvania. *Journal of Applied Remote Sensing*, *15*(2), 26503.

MacGregor, S. D. (2000). *Influence of drought or elephant on the dynamics of key woodland species in a semiarid African savanna.*

Macleod, R. D., & Congalton, R. G. (1998). A quantitative comparison of change-detection algorithms for monitoring eelgrass from remotely sensed data. *Photogrammetric Engineering and Remote Sensing*, *64*(3), 207–216.

Mahdianpari, M., Granger, J. E., Mohammadimanesh, F., Salehi, B., Brisco, B., Homayouni, S., Gill, E., Huberty, B., & Lang, M. (2020). Meta-analysis of wetland classification using remote sensing: A systematic review of a 40-year trend in North America. *Remote Sensing*, *12*(11), 1882.

Main-Knorn, M., Pflug, B., Louis, J., Debaecker, V., Müller-Wilm, U., & Gascon, F. (2017). *Sen2Cor for Sentinel-2*. *October 2018*, 3. https://doi.org/10.1117/12.2278218

Maithya, J. K. (2021). *Wetland utilization and community perception on payment of ecosystem services in conservation of Nyando Wetland of the Lake Victoria basin, Kenya. Kenyatta university.*

Maleki, S., Soffianian, A. R., Soltani Koupaei, S., Saatchi, S., Pourmanafi, S., & Sheikholeslam, F. (2016). Habitat mapping as a tool for water birds conservation planning in an arid zone wetland: The case study Hamun wetland. *Ecological Engineering*, *95*, 594–603. https://doi.org/https://doi.org/10.1016/j.ecoleng.2016.06.115

Malik, K., & Robertson, C. (2021). Landscape similarity analysis using texture encoded deep-learning features on unclassified remote sensing imagery. *Remote Sensing*, *13*(3), 1–26. https://doi.org/10.3390/rs13030492

Manaf, S. A., Mustapha, N., Sulaiman, M. N., Husin, N. A., Shafri, H. Z. M., & Razali, M. N.

(2018). Hybridization of SLIC and Extra Tree for Object Based Image Analysis in Extracting Shoreline from Medium Resolution Satellite Images. *International Journal of Intelligent Engineering & Systems, 11*(1).

Mandal, D., Kumar, V., Ratha, D., Dey, S., Bhattacharya, A., Lopez-Sanchez, J. M., McNairn, H.& Rao, Y. S. (2020). Dual polarimetric radar vegetation index for crop growth monitoring usingsentinel1SARdata.*RemoteSensingofEnvironment*,*247*.https://doi.org/10.1016/j.rse.2020.111954

Mandal, D., Ratha, D., Bhattacharya, A., Kumar, V., McNairn, H., Rao, Y. S., & Frery, A. C. (2020). A radar vegetation index for crop monitoring using compact polarimetric SAR data. *IEEE Transactions on Geoscience and Remote Sensing*, *58*(9), 6321–6335.

Mangi, H. O., Onywere, S. M., Kitur, E. C., Lalika, M. C. S., & Chilagane, N. A. (2022). Hydrological response to land use and land cover change on the slopes of Kilimanjaro and Meru Mountains. *Ecohydrology & Hydrobiology*.

Manzanera, J. A., García-Abril, A., Pascual, C., Tejera, R., Martín-Fernández, S., Tokola, T., & Valbuena, R. (2016). Fusion of airborne LiDAR and multispectral sensors reveals synergic capabilities in forest structure characterization. *GIScience and Remote Sensing*, *53*(6), 723–738. https://doi.org/10.1080/15481603.2016.1231605

Masek, J. G., Goward, S. N., Kennedy, R. E., Cohen, W. B., Moisen, G. G., Schleeweis, K., & Huang, C. (2013). United States forest disturbance trends observed using Landsat time series. *Ecosystems*, *16*(6), 1087–1104.

Mbithi, P. (2016). *University of Nairobi: About the University of Nairobi*. *December*.

McCallum, I., Obersteiner, M., Nilsson, S., & Shvidenko, A. (2006). A spatial comparison of four satellite derived 1 km global land cover datasets. *International Journal of Applied Earth Observation and Geoinformation*, *8*(4), 246–255.

McFeeters, S. K. (1996). The use of the Normalized Difference Water Index (NDWI) in the delineation of open water features. *International Journal of Remote Sensing*, *17*(7), 1425–1432.

McNairn, H., & Brisco, B. (2004). The application of C-band polarimetric SAR for agriculture: A review. *Canadian Journal of Remote Sensing*, *30*(3), 525–542.

Mehmood, M., Shahzad, A., Zafar, B., Shabbir, A., & Ali, N. (2022). Remote Sensing Image

Classification: A Comprehensive Review and Applications. *Mathematical Problems in Engineering*, *2022*. https://doi.org/10.1155/2022/5880959

Meng, Y., Wei, C., Guo, Y., & Tang, Z. (2022). A Planted Forest Mapping Method Based on Long-Term Change Trend Features Derived from Dense Landsat Time Series in an Ecological Restoration Region. *Remote Sensing*, *14*(4). https://doi.org/10.3390/rs14040961

Merchant, M. A., Warren, R. K., Edwards, R., & Kenyon, J. K. (2019). An Object-Based Assessment of Multi-Wavelength SAR, Optical Imagery and Topographical Datasets for Operational Wetland Mapping in Boreal Yukon, Canada. *Canadian Journal of Remote Sensing*, *45*(3–4), 308–332. https://doi.org/10.1080/07038992.2019.1605500

Mi, L., & Chen, Z. (2020). Superpixel-enhanced deep neural forest for remote sensing image semantic segmentation. *ISPRS Journal of Photogrammetry and Remote Sensing*, *159*, 140–152.

Mishra, N. B., & Crews, K. A. (2014). Mapping vegetation morphology types in a dry savanna ecosystem: integrating hierarchical object-based image analysis with Random Forest. *InternationalJournalofRemoteSensing*,*35*(3),1175~1198.https://doi.org/10.1080/01431161.2013.876120

Moayedi, H., Jamali, A., Gibril, M. B. A., Kok Foong, L., & Bahiraei, M. (2020). Evaluation of tree-base data mining algorithms in land used/land cover mapping in a semi-arid environment through Landsat 8 OLI image; Shiraz, Iran. *Geomatics, Natural Hazards and Risk*, *11*(1), 724–741.

Mohan Vamsee, A., Kamala, P., Martha, T. R., Vinod Kumar, K., Jai sankar, G., & Amminedu, E. (2018). A Tool Assessing Optimal Multi-Scale Image Segmentation. *Journal of the Indian Society of Remote Sensing*, *46*(1), 31–41. https://doi.org/10.1007/s12524-017-0685-7

Moskal, L. M., Styers, D. M., & Halabisky, M. (2011a). Monitoring urban tree cover using object-based image analysis and public domain remotely sensed data. *Remote Sensing*, *3*(10), 2243–2262.

Moskal, L. M., Styers, D. M., & Halabisky, M. (2011b). Monitoring urban tree cover using object-based image analysis and public domain remotely sensed data. *Remote Sensing*, *3*(10), 2243–2262. https://doi.org/10.3390/rs3102243

Moss, C. J., Croze, H., & Lee, P. C. (2011). *The Amboseli elephants: a long-term perspective on* *a long-lived mammal*. University of Chicago Press.

Mubea, K., & Menz, G. (2012). Monitoring Land-Use Change in Nakuru (Kenya) Using Multi-SensorSatelliteData.*AdvancesinRemoteSensing*,*01*(03),74~84.https://doi.org/10.4236/ars.2012.13008

Mukherjee, K., & Pal, S. (2021). Hydrological and landscape dynamics of floodplain wetlands of the Diara region, Eastern India. *Ecological Indicators*, *121*, 106961. https://doi.org/https://doi.org/10.1016/j.ecolind.2020.106961

Muñoz, D. F., Cissell, J. R., & Moftakhari, H. (2019a). Adjusting emergent herbaceous wetland elevation with object-based image analysis, random forest and the 2016 NLCD. *Remote Sensing*, *11*(20), 2346.

Muñoz, D. F., Cissell, J. R., & Moftakhari, H. (2019b). Adjusting emergent herbaceous wetland elevation with object-based image analysis, random forest and the 2016 NLCD. *Remote Sensing*, *11*(20). https://doi.org/10.3390/rs11202346

Mustafa, Yaseen T, Ali, R., Najimaldeen, R., Mustafa, Y. T., Ali, R. T., & Saleh, R. M. (2012). Monitoring and evaluating land cover change in the Duhok city, Kurdistan region-Iraq, by using remote sensing and GIS Climate change in Iraq View project Spatial estimation View project Monitoring and Evaluating Land Cover Change in The Duhok City, Kurdis.InternationalJournalofEngineering,Inventions,*I*(11),2833.www.ijeijournal.comPage%7C28.

Mustafa, Yaseen Taha, Ali, R. T., & Saleh, R. M. (2012). Monitoring and evaluating land cover change in the Duhok city, Kurdistan region-Iraq, by using remote sensing and GIS. *International Journal of Engineering Inventions*, *1*(11), 28–33.

Muster, S., Heim, B., Abnizova, A., & Boike, J. (2013). Water body distributions across scales: A remote sensing based comparison of three arctic tundra wetlands. *Remote Sensing*, *5*(4), 1498–1523.

Mutangah, J. G. (1994). The vegetation of Lake Nakuru National Park, Kenya: A synopsis of the vegetation types with annotated species list. *Journal of East African Natural History*, *83*(1), 71–96.

Myneni, R. B., Hall, F. G., Sellers, P. J., & Marshak, A. L. (1995). The interpretation of spectral vegetation indexes. *IEEE Transactions on Geoscience and Remote Sensing*, *33*(2), 481–486.

Naik, P., Dalponte, M., & Bruzzone, L. (2021). Prediction of forest aboveground biomass using multitemporal multispectral remote sensing data. *Remote Sensing*, *13*(7). https://doi.org/10.3390/rs13071282

Neupane, B., Horanont, T., & Aryal, J. (2021). Deep learning-based semantic segmentation of urban features in satellite images: A review and meta-analysis. *Remote Sensing*, *13*(4), 808.

Ng'weno, C. C., Mwasi, S. M., & Kairu, J. K. (2010a). Distribution, density and impact of invasive plants in Lake Nakuru National Park, Kenya. *African Journal of Ecology*, *48*(4), 905–913. https://doi.org/10.1111/j.1365-2028.2009.01191.x

Ng'weno, C. C., Mwasi, S. M., & Kairu, J. K. (2010b). Distribution, density and impact of invasive plants in Lake Nakuru National Park, Kenya. *African Journal of Ecology*, *48*(4), 905–913. https://doi.org/10.1111/j.1365-2028.2009.01191.x

Nico, G., Pappalepore, M., Pasquariello, G., Refice, A., & Samarelli, S. (2000). Comparison of SAR amplitude vs. coherence flood detection methods - a GIS application. *International Journal of Remote Sensing*, *21*(8), 1619–1631. https://doi.org/10.1080/014311600209931

Nieuwenhuis, B. O., Marchese, F., Casartelli, M., Sabino, A., Van der Meij, S. E. T., & Benzoni, F. (2022). Integrating a UAV-derived DEM in object-based image analysis increases habitat classification accuracy on coral reefs. *Remote Sensing*, *14*(19), 5017.

Noori, L., Pour, A. B., Askari, G., Taghipour, N., Pradhan, B., Lee, C.-W., & Honarmand, M. (2019). Comparison of different algorithms to map hydrothermal alteration zones using ASTER remote sensing data for polymetallic vein-type ore exploration: Toroud–Chahshirin Magmatic Belt (TCMB), North Iran. *Remote Sensing*, *11*(5), 495.

Nordin, N. H., Rahman, A. H. A., Wahab, N. A., bin Tengku Sembok, T. M., bin Mohd Shukran, M. A., Yunus, M. S. F. M., Isnan, S., & Abdul, M. R. Bin. (2022). Monitoring of mangroves changes in Pulau Kukup using geographical information system (GIS). *IOP Conference Series: Earth and Environmental Science*, *1064*(1), 12009.

Nzimande, N., Mutanga, O., Kiala, Z., & Sibanda, M. (2021). Mapping the spatial distribution of the yellowwood tree (Podocarpus henkelii) in the Weza-Ngele forest using the newly launched Sentinel-2 multispectral imager data. *South African Geographical Journal*, *103*(2), 204–222. https://doi.org/10.1080/03736245.2020.1722211

O, O. A., O, O. E., a, F. O., S, F. A., & Olabiyisi, S. O. (2012). *Effect of Modified Wiener Algorithm* *on Noise Models*. *2*(8), 1439–1448.

Odada, E., Raini, J., & Ndetei, R. (2004). Experiences and lessons learned brief, Lake Nakuru. *Lake Basin Management Initiative: Main Report*.

Oddi, L., Cremonese, E., Ascari, L., Filippa, G., Galvagno, M., Serafino, D., & Cella, U. M. di. (2021). Using UAV imagery to detect and map woody species encroachment in a subalpine grassland: advantages and limits. *Remote Sensing*, *13*(7), 1239.

Okello, B. D. (2007). *Effects of herbivores, fire and harvesting on the population dynamics of Acacia drepanolobium sjoestedt in Laikipia, Kenya.*

Oliver, T. S. N., Rogers, K., Chafer, C. J., & Woodroffe, C. D. (2012). Measuring, mapping and modelling: an integrated approach to the management of mangrove and saltmarsh in the Minnamurra River estuary, southeast Australia. *Wetlands Ecology and Management*, *20*(4), 353–371. https://doi.org/10.1007/s11273-012-9258-2

Omara, T., Nagawa, C. B., Kyarimpa, C., Böhmdorfer, S., Rosenau, T., Lugasi, S. O., Matovu, H., Odongo, S., & Ssebugere, P. (2023). Lacustrine Cyanobacteria, Algal Blooms and Cyanotoxins in East Africa: Implications for Human and Ecological Health Protection. *Phycology*, *3*(1), 147–167.

Onywere, S., Shisanya, C., Obando, J., Ndubi, A., Masiga, D., Irura, Z., Mariita, N., & Maragia, H. (2013). Geospatial extent of 2011–2013 flooding from the Eastern African Rift Valley Lakes in Kenya and its implication on the ecosystems. *Papers, Kenya Soda Lakes Workshop. Kenya Wildlife Service Training Institute, Naivasha*.

Osio, A. A., Lê, H.-Â., Ayugi, S., Onyango, F., Odwe, P., & Lefèvre, S. (2022). Detection of Degraded Acacia Tree Species Using Deep Neural Networks on Uav Drone Imagery. *ISPRS Annals of the Photogrammetry, Remote Sensing and Spatial Information Sciences*, *V-3–2022*(April), 455–462. https://doi.org/10.5194/isprs-annals-v-3-2022-455-2022

Osio, A., & Lefèvre, S. (2021). Object-based change detection on acacia xanthophloea species degradation along lake nakuru riparian reserve. *International Archives of the Photogrammetry, Remote Sensing and Spatial Information Sciences - ISPRS Archives*, *43*(B3-2021), 347–352. https://doi.org/10.5194/isprs-archives-XLIII-B3-2021-347-2021

Osio, A., Pham, M. T., & Lefèvre, S. (2020). Spatial processing of sentinel imagery for monitoring of acacia forest degradation in lake nakuru riparian reserve. *ISPRS Annals of the*

Photogrammetry, Remote Sensing and Spatial Information Sciences, *5*(3), 525–532. https://doi.org/10.5194/isprs-Annals-V-3-2020-525-2020

Osio, Anne, Lefèvre, S., Ogao, P., & Ayugi, S. (2018a). OBIA-based Monitoring of Riparian Vegetation Applied to the Identification of Degraded Acacia Xanthophloea along Lake Nakuru, Kenya. *GEOBIA 2018-From Pixels to Ecosystems and Global Sustainability*, 18–22.

Osio, Anne, Lefèvre, S., Ogao, P., & Ayugi, S. (2018b). OBIA-based Monitoring of Riparian Vegetation Applied to the Identification of Degraded Acacia Xanthophloea along Lake Nakuru, Kenya. *GEOBIA 2018-From Pixels to Ecosystems and Global Sustainability*, 18–22.

Otianga-Owiti, G. E., Okori, J. J. L., Nyamasyo, S., & Amwata, D. A. (2021). Governance and Challenges of Wildlife Conservation and Management in Kenya. *Wildlife Biodiversity Conservation: Multidisciplinary and Forensic Approaches*, 67–99.

Özcan, O., Bookhagen, B., & Musaoğlu, N. (2018). Impact of the Atatürk dam lake on agro-meteorological aspects of the southeastern Anatolia region, turkey. *Journal of the Indian Society of Remote Sensing*, *46*(3), 471–481.

Ozesmi, S. L., & Bauer, M. E. (2002). Satellite remote sensing of wetlands. *Wetlands Ecology and Management*, *10*(5), 381–402. https://doi.org/10.1023/A:1020908432489

Ozigis, M. S., Kaduk, J., & Jarvis, C. (2018). *Synergistic application of Sentinel 1 and Sentinel 2 derivativesforterrestrialoilspillimpactmapping*.*November*,27.https://doi.org/10.1117/12.232 5107

Paliwal, A., Laborte, A., Nelson, A., Singh, R. K., Paliwal, A., Laborte, A., Nelson, A., & Salinity, R. K. S. (2019). Salinity stress detection in rice crops using time series MODIS VI data. *InternationalJournalofRemoteSensing*,*40*(21),8186~8202.https://doi.org/10.1080/01431161. 2018.1513667

Pan, Z., Huang, J., Zhou, Q., Wang, L., Cheng, Y., Zhang, H., & Alan, G. (2015). Mapping crop seasonality parameters using NDVI time-series derived from HJ-1 A / B data. *Accepted Manuscript*, 1–19.

Panigrahi, S., Verma, K., & Tripathi, P. (2019). Land cover change detection using focused time delay neural network. *Soft Computing*, *23*(17), 7699–7713.

Panuju, D. R., Paull, D. J., & Griffin, A. L. (2020). Change detection techniques based on multispectral images for investigating land cover dynamics. *Remote Sensing*, *12*(11), 1–36.

https://doi.org/10.3390/rs12111781

Payn, T., Carnus, J.-M., Freer-Smith, P., Kimberley, M., Kollert, W., Liu, S., Orazio, C., Rodriguez, L., Silva, L. N., & Wingfield, M. J. (2015). Changes in planted forests and future global implications. *Forest Ecology and Management*, *352*, 57–67.

Pellew, R. A. (1983). The giraffe and its food resource in the Serengeti. I. Composition, biomass and production of available browse. *African Journal of Ecology*, *21*(4), 241–267.

Pellew, R. A. P. (1983). The impacts of elephant, giraffe and fire upon the Acacia tortilis woodlands of the Serengeti. *African Journal of Ecology*, *21*(1), 41–74.

Pham, M.-T., Lefevre, S., & Aptoula, E. (2017). Local feature-based attribute profiles for optical remote sensing image classification. *IEEE Transactions on Geoscience and Remote Sensing*, *56*(2), 1199–1212.

Pham, M.-T., Lefèvre, S., & Aptoula, E. (2018). Local Feature-Based Attribute Profiles for Optical Remote Sensing Image Classification. *IEEE Transactions on Geoscience and Remote Sensing*, *56*(2), 1199–1212. https://doi.org/10.1109/TGRS.2017.2761402

Pham, M.-T., Lefèvre, S., Aptoula, E., & Bruzzone, L. (2018). Recent developments from attribute profiles for remote sensing image classification. *ArXiv Preprint ArXiv:1803.10036*.

Pham, M.-T., Lefèvre, S., & Merciol, F. (2018). Attribute Profiles on Derived Textural Features for Highly Textured Optical Image Classification. *IEEE Geoscience and Remote Sensing Letters*, *15*(7), 1125–1129. https://doi.org/10.1109/LGRS.2018.2820817

Phiri, D., Simwanda, M., Salekin, S., Ryirenda, V. R., Murayama, Y., Ranagalage, M., Oktaviani, N., Kusuma, H. A., Zhang, T., Su, J., Liu, C., Chen, W. H., Liu, H., Liu, G., Cavur, M., Duzgun, H. S., Kemec, S., Demirkan, D. C., Chairet, R., … Peerbhay, K. (2019). remote sensing Sentinel-2 Data for Land Cover / Use Mapping : A Review. *Remote Sensing*, *42*(3), 14.

Platt, R. V, & Rapoza, L. (2008). An evaluation of an object-oriented paradigm for land use/land cover classification. *The Professional Geographer*, *60*(1), 87–100.

Prasad, V. K., Anuradha, E., & Badarinath, K. V. S. (2005). Climatic controls of vegetation vigor in four contrasting forest types of India—evaluation from National Oceanic and Atmospheric Administration’s Advanced Very High Resolution Radiometer datasets (1990–2000). *International Journal of Biometeorology*, *50*(1), 6–16.

Pulvirenti, L., Chini, M., Pierdicca, N., Guerriero, L., & Ferrazzoli, P. (2011). Flood monitoring using multi-temporal COSMO-SkyMed data: Image segmentation and signature interpretation. *Remote Sensing of Environment*, *115*(4), 990–1002. https://doi.org/https://doi.org/10.1016/j.rse.2010.12.002

Qi, X., Li, K., Liu, P., Zhou, X., & Sun, M. (2020). Deep attention and multi-scale networks for accurate remote sensing image segmentation. *IEEE Access, 8*, 146627–146639.

Raczko, E., & Zagajewski, B. (2017). Comparison of support vector machine , random forest and neural network classifiers for tree species classification on airborne hyperspectral APEX images.*EuropeanJournalofRemoteSensing*,*50*(1).https://doi.org/10.1080/22797254.2017.1299557

Reddy, G. P. O., Kumar, N., Sahu, N., Srivastava, R., Singh, S. K., Naidu, L. G. K., Chary, G. R., Biradar, C. M., Gumma, M. K., & Reddy, B. S. (2020). Assessment of spatio-temporal vegetation dynamics in tropical arid ecosystem of India using MODIS time-series vegetation indices. *Arabian Journal of Geosciences*, *13*(15), 1–13.

Ren, Y., Zhu, C., & Xiao, S. (2018). Small object detection in optical remote sensing images via modifiedFasterRCNN.*AppliedSciences(Switzerland)*,*8*(5).https://doi.org/10.3390/app8050813

Richards, J. A., Woodgate, P. W., & Skidmore, A. K. (1987). An explanation of enhanced radar backscattering from flooded forests. *International Journal of Remote Sensing*, *8*(7), 1093–1100.

Rida, A., Hicham, A., & Abderrahim, N. (2022). Optimization of object-based image analysis with genetic programming to generate explicit knowledge from WorldView-2 data for urban mapping. *Geospatial Intelligence: Applications and Future Trends*, 157–169.

Rodriguez-Galiano, V. F., Dash, J., & Atkinson, P. M. (2015). Intercomparison of satellite sensor land surface phenology and ground phenology in Europe. *Geophysical Research Letters*, *42*(7), 2253–2260. https://doi.org/10.1002/2015GL063586

Rodriguez-Galiano, V. F., Ghimire, B., Rogan, J., Chica-Olmo, M., & Rigol-Sanchez, J. P. (2012). An assessment of the effectiveness of a random forest classifier for land-cover classification. *ISPRSJournalofPhotogrammetryandRemoteSensing*,*67*(1),93~104.https://doi.org/10.1016/j.isprsjprs.2011.11.002

Roerink, G. J., Menenti, M., & Verhoef, W. (2000). Reconstructing cloudfree NDVI composites using Fourier analysis of time series. *International Journal of Remote Sensing*, *21*(9), 1911–1917. https://doi.org/10.1080/014311600209814

Rokni, K., Ahmad, A., Selamat, A., & Hazini, S. (2014). Water feature extraction and change detection using multitemporal landsat imagery. *Remote Sensing*, *6*(5), 4173–4189. https://doi.org/10.3390/rs6054173

Román, A., Navarro, G., Caballero, I., & Tovar-Sánchez, A. (2022). High-spatial resolution UAV multispectral data complementing satellite imagery to characterize a chinstrap penguin colony ecosystem on deception island (Antarctica). *GIScience & Remote Sensing*, *59*(1), 1159–1176. https://doi.org/10.1080/15481603.2022.2101702

Rusmadi, R., & Hasan, R. C. (2020). Performance of Different Classifiers for Marine Habitat Mapping using Side Scan Sonar and Object-Based Image Analysis. *IOP Conference Series: Earth and Environmental Science*, *540*(1). https://doi.org/10.1088/1755-1315/540/1/012087

Sakamoto, T., Van Nguyen, N., Kotera, A., Ohno, H., Ishitsuka, N., & Yokozawa, M. (2007). Detecting temporal changes in the extent of annual flooding within the Cambodia and the Vietnamese Mekong Delta from MODIS time-series imagery. *Remote Sensing of Environment*, *109*(3), 295–313.

Schagerl, M., Angel, R., Donabaum, U., Gschwandner, A. M., & Woebken, D. (2022). Limnospira fusiformis harbors dinitrogenase reductase (nifH)-like genes, but does not show N2 fixation activity. *Algal Research*, *66*, 102771.

Scheme, C. (2019). Detailed Urban Land Use Land Cover Classification at. *Sensors*, *19*, 3120;

Schoening, B. S., & Kasper, E. T. (2011). *Don't stop thinking about the music: The politics of songs and musicians in presidential campaigns*. Lexington Books.

Schumann, G., Di Baldassarre, G., Alsdorf, D., & Bates, P. D. (2010). Near real-time flood wave approximation on large rivers from space: Application to the River Po, Italy. *Water Resources Research*, *46*(5).

Serra, P., & Pons, X. (2008). Monitoring farmers' decisions on Mediterranean irrigated crops using satellite image time series. *International Journal of Remote Sensing*, *29*(8), 2293–2316. https://doi.org/10.1080/01431160701408444

Sharma, S., & Singh, P. (2021). *Wetlands Conservation: Current Challenges and Future*

Strategies. John Wiley & Sons.

She, X., Zhang, L., Cen, Y., Wu, T., Huang, C., & Baig, M. H. A. (2015). Comparison of the continuity of vegetation indices derived from Landsat 8 OLI and Landsat 7 ETM+ data among differentvegetationtypes.*RemoteSensing*,*7*(10),13485~13506.https://doi.org/10.3390/rs71013485

Shi, S., Wang, Y., Chen, X., & Zhang, Q. (2020). Conceptualization of omnichannel customer experience and its impact on shopping intention: A mixed-method approach. *International Journal of Information Management*, *50*, 325–336.

Simanjuntak, R. M., Kuffer, M., & Reckien, D. (2019). Object-based image analysis to map local climate zones: The case of Bandung, Indonesia. *Applied Geography*, *106*, 108–121.

Simonneaux, V., Duchemin, B., Helson, D., Er-Raki, S., Olioso, A., & Chehbouni, A. G. (2008). The use of high-resolution image time series for crop classification and evapotranspiration estimate over an irrigated area in central Morocco. *International Journal of Remote Sensing*, *29*(1), 95–116. https://doi.org/10.1080/01431160701250390

Singh, A. (1989). Review article digital change detection techniques using remotely-sensed data. *International Journal of Remote Sensing*, *10*(6), 989–1003.

Sola, I., García-Martín, A., Sandonís-Pozo, L., Álvarez-Mozos, J., Pérez-Cabello, F., González-Audícana, M., & Montorio Llovería, R. (2018). Assessment of atmospheric correction methods for Sentinel-2 images in Mediterranean landscapes. *International Journal of Applied Earth Observation and Geoinformation*, *73*, 63–76. https://doi.org/10.1016/j.jag.2018.05.020

Song, D., Tan, X., Wang, B., Zhang, L., Shan, X., & Cui, J. (2020). Integration of super-pixel segmentation and deep-learning methods for evaluating earthquake-damaged buildings using single-phase remote sensing imagery. *International Journal of Remote Sensing*, *41*(3), 1040–1066. https://doi.org/10.1080/01431161.2019.1655175

Southworth, J., Munroe, D., & Nagendra, H. (2004). Land cover change and landscape fragmentation—comparing the utility of continuous and discrete analyses for a western Honduras region. *Agriculture, Ecosystems & Environment*, *101*(2), 185–205. https://doi.org/https://doi.org/10.1016/j.agee.2003.09.011

Souza, T. do V. S. B., Chidakel, A., Child, B., Chang, W.-H., & Gorsevski, V. (2021). Economic effects assessment approaches: Tourism Economic Model for Protected Areas (TEMPA) for developing countries. In *Handbook for Sustainable Tourism Practitioners* (pp. 393–409). Edward Elgar Publishing.

Strasser, T., & Lang, S. (2015). Object-based class modelling for multi-scale riparian forest habitat mapping. *International Journal of Applied Earth Observation and Geoinformation*, *37*, 29–37.

Sun, L., Yu, H., Mingxing, S., & Wang, Y. (n.d.). *Pr ep rin t n ot pe er r Pr ep rin t n ot pe er ed*.

Tan, H. T., Yusoff, F. M., Khaw, Y. S., Noor Mazli, N. A. I., Nazarudin, M. F., Shaharuddin, N. A., Katayama, T., & Ahmad, S. A. (2022). A Review on a Hidden Gem: Phycoerythrin from Blue-Green Algae. *Marine Drugs*, *21*(1), 28.

Tan, K., Zhang, Y., Wang, X., & Chen, Y. (2019). Object-based change detection using multiple classifiers and multi-scale uncertainty analysis. *Remote Sensing*, *11*(3), 359.

Tassi, A., Gigante, D., Modica, G., Di Martino, L., & Vizzari, M. (2021). Pixel-vs. Object-based landsat 8 data classification in google earth engine using random forest: The case study of maiella national park. *Remote Sensing*, *13*(12), 2299.

Thampy, R. J. (2023). *Wetland Conservation and Development : the Lake Nakuru Case Study*.

Thiel, C., Mueller, M. M., Epple, L., Thau, C., Hese, S., Voltersen, M., & Henkel, A. (2020). Uas imagery-based mapping of coarse wood debris in a natural deciduous forest in central germany (hainich national park). *Remote Sensing*, *12*(20), 3293.

Tian, S., Zhang, X., Tian, J., & Sun, Q. (2016). Random forest classification of wetland landcovers from multi-sensor data in the arid region of Xinjiang, China. *Remote Sensing*, *8*(11), 1–14. https://doi.org/10.3390/rs8110954

Titus, J. H. (1990). Microtopography and woody plant regeneration in a hardwood floodplain swamp in Florida. *Bulletin of the Torrey Botanical Club*, 429–437.

Tonbul, H., & Kavzaoğlu, T. (2019). Application of Taguchi Optimization and ANOVA Statistics in Optimal Parameter Setting of Multi-Resolution Segmentation. *2019 9th International Conference on Recent Advances in Space Technologies (RAST)*, 387–391.

Tormos, T., Kosuth, P., Durrieu, S., Dupuy, S., Villeneuve, B., Wasson, J. G., Kosuth, P., Durrieu, S., Dupuy, S., Villeneuve, B., & Wasson, J. G. (2012). *Object-based image analysis for operational fine- scale regional mapping of land cover within river corridors from multispectralimageryandthematicdata.1161*. https://doi.org/10.1080/01431161.2011.637093

Torres-Bejarano, F., Torregroza-Espinosa, A. C., Martínez-Mera, E., & González-Márquez, L. C. (2022). Impact of land cover changes on water quality: an application to the Guájaro reservoir, Colombia. *International Journal of Environmental Science and Technology*, 1–14.

Torres, P., Rodes-blanco, M., Viana-soto, A., Nieto, H., & García, M. (2021). The role of remote sensing for the assessment and monitoring of forest health: A systematic evidence synthesis. *Forests*, *12*(8), 1–35. https://doi.org/10.3390/f12081134

Touhami, I., Moutahir, H., Assoul, D., Bergaoui, K., Aouinti, H., Bellot, J., & Andreu, J. M. (2022). Multi-year monitoring land surface phenology in relation to climatic variables using MODIS-NDVI time-series in Mediterranean forest, Northeast Tunisia. *Acta Oecologica*, *114*, 103804.

Tsoeleng, L. T., Odindi, J., Mhangara, P., & Malahlela, O. (2020). Assessing the performance of the multi-morphological profiles in urban land cover mapping using pixel based classifiers and very high resolution satellite imagery. *Scientific African*, *10*, e00629.

Tsyganskaya, V., Martinis, S., Marzahn, P., & Ludwig, R. (2018). Detection of temporary flooded vegetation using Sentinel-1 time series data. *Remote Sensing*, *10*(8), 1286.

Tucker, C. J., Elgin, J. H., McMurtrey, J. E., & Fan, C. J. (1979). Monitoring corn and soybean crop development with hand-held radiometer spectral data. *Remote Sensing of Environment*, *8*(3), 237–248. https://doi.org/https://doi.org/10.1016/0034-4257(79)90004-X

Tulbure, M. G., & Broich, M. (2013). Spatiotemporal dynamic of surface water bodies using Landsat time-series data from 1999 to 2011. *ISPRS Journal of Photogrammetry and Remote Sensing*, *79*, 44–52.

Tuominen, S., & Pekkarinen, A. (2005). Performance of different spectral and textural aerial photograph features in multi-source forest inventory. *Remote Sensing of Environment*, *94*(2), 256–268.

Turner, K., & Jones, T. (2013). *Wetlands: Market and intervention failures: Four case studies*. Routledge.

Turner, M. G., & Gardner, R. H. (1991). *Quantitative methods in landscape ecology : the analysis and interpretation of landscape heterogeneity*.

Udelhoven, T. (2011). TimeStats: A Software Tool for the Retrieval of Temporal Patterns From Global Satellite Archives. *IEEE Journal of Selected Topics in Applied Earth Observations and Remote Sensing*, *4*(2), 310–317. https://doi.org/10.1109/JSTARS.2010.2051942

Uijlings, J. R. R., Van De Sande, K. E. A., Gevers, T., & Smeulders, A. W. M. (2013). Selective search for object recognition. *International Journal of Computer Vision*, *104*(2), 154–171. https://doi.org/10.1007/s11263-013-0620-5

Umar, A. B., & Magawata, Z. U. (2019). Remote sensing as a tool for reconnaissance in groundwater exploration. *Advance and Innovative Research*, *6*(2), 190.

Val, C., Gascon, F., Cadau, E., Colin, O., Hoersch, B., Isola, C., Gascon, F., Cadau, E., Colin, O., Hoersch, B., Isola, C., & Fernández, B. L. (2022). *Copernicus Sentinel-2 Mission : September 2014*. https://doi.org/10.1117/12.2062260

Verburg, P. H., Neumann, K., & Nol, L. (2011). Challenges in using land use and land cover data forglobalchangestudies.*GlobalChangeBiology*,*17*(2),974~989.https://doi.org/10.1111/j.1365-2486.2010.02307.x

Wang, B., Choi, J., Choi, S., Lee, S., Wu, P., & Gao, Y. (2017). Image fusion-based land cover change detection using multi-temporal high-resolution satellite images. *Remote Sensing*, *9*(8), 1–19. https://doi.org/10.3390/rs9080804

Wang, C., Pavlowsky, R. T., Huang, Q., & Chang, C. (2016). Channel bar feature extraction for a mining-contaminated river using high-spatial multispectral remote-sensing imagery. *GIScienceandRemoteSensing*,*53*(3),283~302.https://doi.org/10.1080/15481603.2016.1148229

Wang, Q., & Atkinson, P. M. (2018). Spatio-temporal fusion for daily Sentinel-2 images. *Remote Sensing of Environment*, *204*, 31–42.

Wanjala, J. A., Sichangi, A. W., Mundia, C. N., & Makokha, G. O. (2020). Modelling the dry season inundation pattern of Yala Swamp in Kenya. *Modeling Earth Systems and Environment*, *6*(4), 2091–2101. https://doi.org/10.1007/s40808-020-00816-8

Weih, R. C., & Riggan, N. D. (2010). Object-based classification vs. pixel-based classification: Comparative importance of multi-resolution imagery. *The International Archives of the Photogrammetry, Remote Sensing and Spatial Information Sciences*, *38*(4), C7.

Western, D., Nightingale, D. L. M., Mose, V. N., Sipitiek, J. O., & Kimiti, K. S. (2019). Variability and change in Maasai views of wildlife and the implications for conservation. *Human Ecology*, *47*(2), 205–216.

Whistler, J. L., Egbert, S. L., Jakubauskas, M. E., Martinko, E. A., Baumgartner, D. W., & Lee, R.-Y. (1995). The Kansas land cover mapping project: regional scale land use/land cover mapping using Landsat Thematic Mapper data. *ACSM/ASPRS Annual Convention and Exposition Technical Papers, 3*, 773–785.

White, L., Brisco, B., Dabboor, M., Schmitt, A., & Pratt, A. (2015). *A Collection of SAR Methodologies for Monitoring Wetlands*. https://doi.org/10.3390/rs70607615

White, R. C., Bowles, J. M., Enanga, E. M., Creed, I. F., & Trick, C. G. (2019). Fever tree woodlands at risk from intensification of land management activities associated with human and wildlife utilization. *Forest Ecology and Management*, *435*, 187–195.

Wijesingha, J., Astor, T., Schulze-Brueninghoff, D., & Wachendorf, M. (2020). Mapping invasive Lupinus polyphyllus Lindl. in semi-natural grasslands using object-based image analysis of UAV-borne images. *PFG–Journal of Photogrammetry, Remote Sensing and Geoinformation Science*, *88*(5), 391–406.

Wilson, R., Hancock, E., Bors, A., & Smith, W. (2013). *Computer Analysis of Images and Patterns: 15th International Conference, CAIP 2013, York, UK, August 27-29, 2013, Proceedings, Part I* (Vol. 8047). Springer.

Woodhouse, I. H. (2017). *Introduction to microwave remote sensing*. CRC press.

Wulder, M. A., Dechka, J. A., Gillis, M. A., Luther, J. E., Hall, R. J., Beaudoin, A., & Franklin, S. E. (2003). Operational mapping of the land cover of the forested area of Canada with Landsat data: EOSD land cover program. *The Forestry Chronicle*, *79*(6), 1075–1083.

Xie, Y., Zhao, X., Li, L., & Wang, H. (2010). Calculating NDVI for Landsat7-ETM data after atmospheric correction using 6S model: A case study in Zhangye city, China. *2010 18th International Conference on Geoinformatics*, 1–4.

Xu, H. (2006). Modification of normalised difference water index (NDWI) to enhance open water features in remotely sensed imagery. *International Journal of Remote Sensing*, *27*(14), 3025–3033. https://doi.org/10.1080/01431160600589179

Yan, L., & Roy, D. P. (2014). Automated crop field extraction from multi-temporal Web Enabled Landsat Data. *Remote Sensing of Environment*, *144*, 42–64.

Yan, X., Niu, Z., Li, Y., Han, Q., & Zhang, H. (2020). Reliability Evaluation of Wetland Samples Based on Historical Thematic Maps. *IGARSS 2020-2020 IEEE International Geoscience and Remote Sensing Symposium*, 4754–4757.

Yang, J., He, Y., & Caspersen, J. (2017). Region merging using local spectral angle thresholds: A more accurate method for hybrid segmentation of remote sensing images. *Remote Sensing of Environment*, *190*, 137–148.

Yang, J., He, Y., & Weng, Q. (2015). An Automated Method to Parameterize Segmentation Scale by Enhancing Intrasegment Homogeneity and Intersegment Heterogeneity. *IEEE Geoscience and Remote Sensing Letters*, *12*(6), 1282–1286. https://doi.org/10.1109/LGRS.2015.2393255

Yang, X., Li, F., Fan, W., Liu, G., & Yu, Y. (2021). Evaluating the efficiency of wind protection by windbreaks based on remote sensing and geographic information systems. *Agroforestry Systems*, *95*(2), 353–365. https://doi.org/10.1007/s10457-021-00594-x

Zakhvatkina, N., Korosov, A., Muckenhuber, S., Sandven, S., & Babiker, M. (2017). Operational algorithm for ice–water classification on dual-polarized RADARSAT-2 images. *The Cryosphere*, *11*(1), 33–46.

Zarkami, R., Hesami, H., & Sadeghi Pasvisheh, R. (2020). Assessment, monitoring and modelling of the abundance of Dunaliella salina Teod in the Meighan wetland, Iran using decision tree model.*EnvironmentalMonitoringandAssessment*,*192*(3),172.https://doi.org/10.1007/s10661-020-8148-y

Zhang, W., Liljedahl, A. K., Kanevskiy, M., Epstein, H. E., Jones, B. M., Jorgenson, M. T., & Kent, K. (2020). Transferability of the deep learning mask R-CNN model for automated mapping of ice-wedge polygons in high-resolution satellite and UAV images. *Remote Sensing*, *12*(7). https://doi.org/10.3390/rs12071085

Zhang, X., Han, L., Han, L., & Zhu, L. (2020). How well do deep learning-based methods for land cover classification and object detection perform on high resolution remote sensing imagery? *Remote Sensing*, *12*(3), 417.

Zhao, W., Du, S., Wang, Q., & Emery, W. J. (2017). Contextually guided very-high-resolution imagery classification with semantic segments. *ISPRS Journal of Photogrammetry and Remote Sensing*, *132*, 48–60. https://doi.org/https://doi.org/10.1016/j.isprsjprs.2017.08.011

Zhao, Yi, & Jiang, M. (2022). Integration of Optical and SAR Imagery for Dual PolSAR Features Optimization and Land Cover Mapping. *IEEE Journal on Miniaturization for Air and Space Systems*, *3*(2), 67–76. https://doi.org/10.1109/JMASS.2022.3195955

Zhao, Yongqiang, Han, R., & Rao, Y. (2019). A new feature pyramid network for object detection.

Proceedings - 2019 International Conference on Virtual Reality and Intelligent Systems, ICVRIS 2019, 428–431. https://doi.org/10.1109/ICVRIS.2019.00110

Zheng, J.-Y., Hao, Y.-Y., Wang, Y.-C., Zhou, S.-Q., Wu, W.-B., Yuan, Q., Gao, Y., Guo, H.-Q., Cai, X.-X., & Zhao, B. (2022). Coastal Wetland Vegetation Classification Using Pixel-Based, Object-Based and Deep Learning Methods Based on RGB-UAV. *Land*, *11*(11), 2039.

Zhou, R., Yang, C., Li, E., Cai, X., Yang, J., & Xia, Y. (2021a). Object-based wetland vegetation classification using multi-feature selection of unoccupied aerial vehicle rgb imagery. *Remote Sensing*, *13*(23). https://doi.org/10.3390/rs13234910

Zhou, R., Yang, C., Li, E., Cai, X., Yang, J., & Xia, Y. (2021b). Object-based wetland vegetation classification using multi-feature selection of unoccupied aerial vehicle RGB imagery. *Remote Sensing*, *13*(23), 4910.

Zhu, X., Hou, Y., Weng, Q., & Chen, L. (2019). Integrating UAV optical imagery and LiDAR data for assessing the spatial relationship between mangrove and inundation across a subtropical estuarine wetland. *ISPRS Journal of Photogrammetry and Remote Sensing*, *149*, 146–156. https://doi.org/https://doi.org/10.1016/j.isprsjprs.2019.01.021

Zhu, Z., Zhang, J., Yang, Z., Aljaddani, A. H., Cohen, W. B., Qiu, S., & Zhou, C. (2020). Continuous monitoring of land disturbance based on Landsat time series. *Remote Sensing of Environment*, *238*, 111116.

APPENDICES:

APPENDIX I: ONE WAY ANOVA CONVERSION TABLE

CRITICAL VALUES for the "F" Distribution, ALPHA = .05.

Denominator DF	Numerator DF 1	2	3	4	5	6	7	8	9	10
1	161.448	199.500	215.707	224.583	230.162	233.986	236.768	238.883	240.543	241.882
2	18.513	19.000	19.164	19.247	19.296	19.330	19.353	19.371	19.385	19.396
3	10.128	9.552	9.277	9.117	9.013	8.941	8.887	8.845	8.812	8.786
4	7.709	6.944	6.591	6.388	6.256	6.163	6.094	6.041	5.999	5.964
5	6.608	5.786	5.409	5.192	5.050	4.950	4.876	4.818	4.772	4.735
6	5.987	5.143	4.757	4.534	4.387	4.284	4.207	4.147	4.099	4.060
7	5.591	4.737	4.347	4.120	3.972	3.866	3.787	3.726	3.677	3.637
8	5.318	4.459	4.066	3.838	3.687	3.581	3.500	3.438	3.388	3.347
9	5.117	4.256	3.863	3.633	3.482	3.374	3.293	3.230	3.179	3.137
10	4.965	4.103	3.708	3.478	3.326	3.217	3.135	3.072	3.020	2.978
11	4.844	3.982	3.587	3.357	3.204	3.095	3.012	2.948	2.896	2.854
12	4.747	3.885	3.490	3.259	3.106	2.996	2.913	2.849	2.796	2.753
13	4.667	3.806	3.411	3.179	3.025	2.915	2.832	2.767	2.714	2.671
14	4.600	3.739	3.344	3.112	2.958	2.848	2.764	2.699	2.646	2.602
15	4.543	3.682	3.287	3.056	2.901	2.790	2.707	2.641	2.588	2.544
16	4.494	3.634	3.239	3.007	2.852	2.741	2.657	2.591	2.538	2.494
17	4.451	3.592	3.197	2.965	2.810	2.699	2.614	2.548	2.494	2.450
18	4.414	3.555	3.160	2.928	2.773	2.661	2.577	2.510	2.456	2.412
19	4.381	3.522	3.127	2.895	2.740	2.628	2.544	2.477	2.423	2.378
20	4.351	3.493	3.098	2.866	2.711	2.599	2.514	2.447	2.393	2.348
21	4.325	3.467	3.072	2.840	2.685	2.573	2.488	2.420	2.366	2.321
22	4.301	3.443	3.049	2.817	2.661	2.549	2.464	2.397	2.342	2.297
23	4.279	3.422	3.028	2.796	2.640	2.528	2.442	2.375	2.320	2.275
24	4.260	3.403	3.009	2.776	2.621	2.508	2.423	2.355	2.300	2.255
25	4.242	3.385	2.991	2.759	2.603	2.490	2.405	2.337	2.282	2.236
26	4.225	3.369	2.975	2.743	2.587	2.474	2.388	2.321	2.265	2.220
27	4.210	3.354	2.960	2.728	2.572	2.459	2.373	2.305	2.250	2.204
28	4.196	3.340	2.947	2.714	2.558	2.445	2.359	2.291	2.236	2.190
29	4.183	3.328	2.934	2.701	2.545	2.432	2.346	2.278	2.223	2.177
30	4.171	3.316	2.922	2.690	2.534	2.421	2.334	2.266	2.211	2.165
31	4.160	3.305	2.911	2.679	2.523	2.409	2.323	2.255	2.199	2.153
32	4.149	3.295	2.901	2.668	2.512	2.399	2.313	2.244	2.189	2.142
33	4.139	3.285	2.892	2.659	2.503	2.389	2.303	2.235	2.179	2.133
34	4.130	3.276	2.883	2.650	2.494	2.380	2.294	2.225	2.170	2.123
35	4.121	3.267	2.874	2.641	2.485	2.372	2.285	2.217	2.161	2.114
36	4.113	3.259	2.866	2.634	2.477	2.364	2.277	2.209	2.153	2.106
37	4.105	3.252	2.859	2.626	2.470	2.356	2.270	2.201	2.145	2.098
38	4.098	3.245	2.852	2.619	2.463	2.349	2.262	2.194	2.138	2.091
39	4.091	3.238	2.845	2.612	2.456	2.342	2.255	2.187	2.131	2.084
40	4.085	3.232	2.839	2.606	2.449	2.336	2.249	2.180	2.124	2.077
41	4.079	3.226	2.833	2.600	2.443	2.330	2.243	2.174	2.118	2.071
42	4.073	3.220	2.827	2.594	2.438	2.324	2.237	2.168	2.112	2.065
43	4.067	3.214	2.822	2.589	2.432	2.318	2.232	2.163	2.106	2.059
44	4.062	3.209	2.816	2.584	2.427	2.313	2.226	2.157	2.101	2.054
45	4.057	3.204	2.812	2.579	2.422	2.308	2.221	2.152	2.096	2.049
46	4.052	3.200	2.807	2.574	2.417	2.304	2.216	2.147	2.091	2.044
47	4.047	3.195	2.802	2.570	2.413	2.299	2.212	2.143	2.086	2.039
48	4.043	3.191	2.798	2.565	2.409	2.295	2.207	2.138	2.082	2.035
49	4.038	3.187	2.794	2.561	2.404	2.290	2.203	2.134	2.077	2.030
50	4.034	3.183	2.790	2.557	2.400	2.286	2.199	2.130	2.073	2.026

APPENDIX II : RESEARCH APPROVAL

REPUBLIC OF KENYA

NATIONAL COMMISSION FOR SCIENCE,TECHNOLOGY & INNOVATION

Ref No: **814985**

Date of Issue: **08/December/2020**

RESEARCH LICENSE

This is to Certify that Miss.. Anne Achieng Osio of Technical University of Kenya, has been licensed to conduct research in Nakuru on the topic: Monitoring of Tree Species using OBJECT BASED Time Series for the period ending : 08/December/2021.

License No: **NACOSTI/P/20/8070**

814985

Applicant Identification Number

Director General

NATIONAL COMMISSION FOR SCIENCE,TECHNOLOGY & INNOVATION

Verification QR Code

NOTE: This is a computer generated License. To verify the authenticity of this document, Scan the QR Code using QR scanner application.

APPENDIX III: RESEARCH PERMIT PROVIDED BY KENYA WILDLIFE SERVICE (KWS)

KENYA WILDLIFE SERVICE

KWS/BRP/5001

23 November 2020

Ann Achieng **OSIO**
Technical University of Kenya (TUK)
Department of Geoinformatics and Earth Sciences
P. O. Box 52428 - 00200
Nairobi
Email: ansiyo22@gmail.com

Dear Ann,

PERMISSION TO CONDUCT RESEARCH ON THE PROJECT "MONITORING OF ACACIA XANTHOPHLOEA SPP OF TREE SPECIES USING OBJECT BASED TIME SERIES: A CASE STUDY OF LAKE NAKURU NATIONAL PARK"

We acknowledge receipt of your application requesting permission to conduct your PhD Project on ***"Monitoring of Acacia Xanthophloea Spp of Tree Species Using Object Based Time Series: A Case Study of Lake Nakuru National Park".*** It is considered that the study will generate important information for the country on monitoring the distribution of tree species crown using Object Based Time series.

You have been granted permission as agreed upon under the Prior Informed Consent (PIC), to conduct your research for the period **December 2020 – November 2021.** However, this approval is subject to meeting the following terms and conditions:

1. That you will pay to KWS Research fees of **KSh. 12,000** (PhD. study);
2. That you will discuss your research project with the KWS Senior Scientist in-charge of Central Rift Conservation Area before embarking on your field work;
3. That you will get all necessary government permits to use UAV drones in your study;
4. That you will abide by the set KWS regulations and guidelines regarding the carrying out of research in and outside wildlife Protected Areas;
5. That you will submit to the Director, Biodiversity Research and Planning, annual reports on your findings and at the end of your research, a copy of your thesis.

Yours

DR. PATRICK OMONDI, *OGW*
DIRECTOR
BIODIVERSITY, RESEARCH & PLANNING

P.O Box 40241-00100, Nairobi, Kenya.
Tel: +254-020-2379407/8/9 - 15. Mobile: +254-735 663 421, +254-726 610 508/9.
Email: kws@kws.go.ke Website: www.kws.go.ke

APPENDIX IV: KENYA CIVIL AVIATION AUTHORITY (KCAA) DRONE APPROVAL

4.0 LICENSES, PERMITS, AND REGISTRATION

4.1 **Drone Space Limited** shall comply with all state, and local laws, rules, and regulations in Kenya with regard to necessary licenses and registrations in the performance of the services of this Agreement. Any regulated services performed under this contract shall be done by those authorized and licensed in that locality, state or nation to perform such services.

4.2 **Drone Space Limited** shall ensure that they are in compliance with the most current CAA regulations for the commercial operation of drones at the time of completing the Task Orders. If the drone weighs more than 25kgs, **Drone Space Limited** shall ensure that they are in a possession of KCAA grant of exemption, an approval or Authorization, Certificate of registratio n (COR) of the aircraft with the KCAA, a pilot with a Remote Pilot License (RPL) and, any other requirements of KCAA. If the drone weighs less than 25kgs **Drone Space Limited** shall ensure that they are in compliance with **The Civil Aviation (Unmanned Aircraft Systems) regulations 2020** and with other KCAA requirements.

4.3 **Technical University of Kenya** will operate under **Drone Space Remote Operator's Certificate** Reference no: **KCCAA/OPS/2117/ROC/02** having been authorized by KCAA to conduct commercial UAS Operations.

This contract is only valid when signed and sealed by Drone Space Ltd

DRONE SPACE

Ensuring a Safety Culture

4.4 **Technical University of Kenya** will have their Pilot in command (PIC) **Adams Nyaribo** holding a Remote Pilot License **Ref no: YK-RPL-00118A**

4.5 **Technical University of Kenya** will operate UAS **DJI - P H A N T O M 4 Serial Number** OAXDECD00S1563 with Certificate of Registration – **5Y-0031A** - APPROVED BY KCAA.

APPENDIX V: PHD ACCEPTANCE LETTER (TUK)

Technical University of Kenya, Haile Selassie Avenue, P. O. Box 52428- 00200 NAIROBI
Tel +254 (020) 343672, 2249974, 2251300, 251300, 251822, 2250522

SCHOOL OF GRADUATE AND ADVANCED STUDIES

May 4, 2017

REF: PHD/EEGX/06446P/2017

Mrs. Osio Achieng Anne
Department of Geo-information and Earth Observation
School of Surveying and Geospatial Sciences
Technical University of Kenya.

Dear Mrs Osio Achieng Anne

RE: ADMISSION INTO A PHD PROGRAMME

I am pleased to inform you that your application for admission into a PhD degree programme in GIS and Remote Sensing in the Department of Geo-information and Earth Observation, School of Surveying and Geospatial Sciences, Technical University of Kenya, has been successful.

Your Admission Number is EEGX/06446P/2017.

You will be supervised by Prof. Patrick Ogao, Prof. Sebastain Levfvere and Dr. Samson Ayugi, Department of Geo-information and Earth Observation, School of Surveying and Geospatial Sciences. Your PhD programme is a three-year course by research and thesis only, starting from the date stated on this letter. Other conditions and rules guiding your study can be found in the 'Regulations for Postgraduate Studies' of the Technical University of Kenya, a copy of which is available in the university website. Please complete and forward your medical report and letter of acceptance of this offer, both forms available on our website, to the School of Graduate and Advanced studies as soon as possible.

Yours sincerely

SCHOOL OF GRADUATE & ADVANCED STUDIES
DIRECTOR
04 MAY 2017

Prof. J.O. Lalah

cc. Chairperson- Geo-information and Earth Observation.
Director- School of Surveying and Geospatial Sciences.
Prof. P. Ogao, Prof. S. Levfvere and Dr. S. Ayugi.

APPENDIX VI: OBIATS.PY CODE

```
import numpy as np
import os as os
import sys

def help(badParmMessage=False):
    if not badParmMessage:
        print("================================================")
        print("OBIATS - Object Based Image Analysis on Time Series")
        print("================================================")
        print("Performs computation of polygons temporal profiles on a raster time series, uses unsupervised K-Means clustering on the temporal profiles
        print("-------------")
        print("[PARAMETERS]\n")
        print("### MANDATORY ###\n")
        print("-ts [path to input folder containing time series of georeferenced images in format YYYYMMDD.tif]")
        print(" OR")
        print("-tp [Path to file containing temporal profiles]")
        print("# NOTE: If the file does not exist, temporal profiles will be computed and stored into the specifyied file name.")
        print("# Otherwise, temporal profiles contained in the file will be imported, then passed directly to K-Means.\n")
        print("-shp [path to georeferenced polygons shapefile]\n")
        print("-nb [number of clusters to compute]")
        print(" OR")
        print("-cmin [Minimum number of clusters used to find automatically the optimal number of clusters]")
        print("-cmax [Maximum number of clusters used to find automatically the optimal number of clusters]\n")
        print("### OPTIONAL ###\n")
        print("-out [path to folder where output shapefiles will be created, default: ./output]\n")
        print("-min [Minimum pixels mean value to be taken into account (value will be ignored if mean < min)]\n")
        print("-max [Maximum pixels mean value to be taken into account (value will be ignored if mean > max)]\n")
        print("-nodata [No data pixels value, default: -1]\n")


class Obiats():
    TIME_SERIES_FOLDER = None
    SHAPE_FILE = None
    TEMPORAL_PROFILES = None
    OUTPUT = None
    NB_CLUSTERS = None
    NB_CLUSTERS_MIN = None
    NB_CLUSTERS_MAX = None
    MIN_VALUE = None
    MAX_VALUE = None
    NO_DATA = -1

    def __init__(self):
```

```
    def __init__(self):
        args = sys.argv
        if args == None:
            help()
        elif len(args) <= 1:
            help()
        else:
            start = True
            for i in range(len(args) - 1):
                if args[i] == '-ts':
                    self.TIME_SERIES_FOLDER = os.path.abspath(args[i+1])

                elif args[i] == '-tp':
                    self.TEMPORAL_PROFILES = os.path.abspath(args[i+1])

                elif args[i] == '-shp':
                    self.SHAPE_FILE = os.path.abspath(args[i+1])

                elif args[i] == '-cmin':
                    self.NB_CLUSTERS_MIN = args[i+1]

                elif args[i] == '-cmax':
                    self.NB_CLUSTERS_MAX = args[i+1]

                elif args[i] == '-out':
                    self.OUTPUT = os.path.abspath(args[i+1])

                elif args[i] == '-nb':
                    try:
                        self.NB_CLUSTERS = int(args[i+1])
                        if self.NB_CLUSTERS <= 0:
                            print("Error: Please enter a valid number of clusters to be computed (-nb param)")
                            start = False
                    except:
                        print("Error: Please enter a valid number of clusters to be computed (-nb param)")
                        start = False
                elif args[i] == '-min':
                    self.MIN_VALUE = args[i+1]

                elif args[i] == '-max':
                    self.MAX_VALUE = args[i+1]

                elif args[i] == '-nodata':
```

```
            elif args[i] == '-nodata':
                self.NO_DATA = args[i+1]

        # Checking input validity
        if start:
            if self.TIME_SERIES_FOLDER == None:
                if self.TEMPORAL_PROFILES == None:
                    print("Error: Please specify either an input time series folder (-ts param) or an existing temporal profiles file (-tp param)")
                    start = False
                #elif not os.path.isfile(self.TEMPORAL_PROFILES):
                #    print("Error: {} input temporal profiles file not found !".format(self.TEMPORAL_PROFILES))
                #    start = False
            elif not os.path.isdir(self.TIME_SERIES_FOLDER):
                print("Error: {} input folder not found !".format(self.TIME_SERIES_FOLDER))
                start = False
            if self.SHAPE_FILE == None:
                print("Error: Please enter an input polygons shapefile (-shp param)")
                start = False
            elif not os.path.isfile(self.SHAPE_FILE):
                print("Error: {} shapefile not found !".format(self.SHAPE_FILE))
                start = False
            if self.NB_CLUSTERS == None:
                if self.NB_CLUSTERS_MIN == None or self.NB_CLUSTERS_MAX == None:
                    print("Error: Please enter a number of clusters to be computed (-nb param)")
                    start = False
                else:
                    try:
                        self.NB_CLUSTERS_MIN = int(self.NB_CLUSTERS_MIN)
                        self.NB_CLUSTERS_MAX = int(self.NB_CLUSTERS_MAX)
                        if self.NB_CLUSTERS_MIN <= 0 or self.NB_CLUSTERS_MIN >= self.NB_CLUSTERS_MAX:
                            print("Error: Please enter a valid min and max number of clusters to be computed (-cmin and -cmax params)")
                            start = False
                    except:
                        print("Error: Please enter a valid min and max number of clusters to be computed (-cmin and -cmax params)")
                        start = False
            if self.OUTPUT != None:
                if not os.path.isdir(self.OUTPUT):
                    print("Error: {} output folder not found !".format(self.OUTPUT))
                    start = False
            if start and (self.MIN_VALUE != None or self.MAX_VALUE != None):
                try:
                    self.MIN_VALUE = float(self.MIN_VALUE)
                    self.MAX_VALUE = float(self.MAX_VALUE)
```

```
                    self.MIN_VALUE = float(self.MIN_VALUE)
                    self.MAX_VALUE = float(self.MAX_VALUE)
                    if self.MIN_VALUE >= self.MAX_VALUE:
                        print("Error: Ensure that min < max")
                        start = False
                except:
                    print("Error: Please enter a valid min and/or max values (-min and/or -max params)")
                    start = False
        if start:
            self.start()
        else:
            help(True)

    def start(self):
        import fiona
        if self.OUTPUT == None:
            self.OUTPUT = os.path.join(os.path.dirname(os.path.abspath(__file__)),"output")
            try:
                os.mkdir(self.OUTPUT,0o744)
            except:
                os.rmdir(self.OUTPUT)
                os.mkdir(self.OUTPUT,0o744)

        timeSeries = None
        is_temporal_profiles_existing = False
        is_temporal_profiles_defined = False
        if (not self.TEMPORAL_PROFILES == None):
            is_temporal_profiles_defined = True
            print("Temp Prof Defined")
            if os.path.isfile(self.TEMPORAL_PROFILES):
                is_temporal_profiles_existing = True
                print("Temp Prof Existing")

        if not self.TIME_SERIES_FOLDER == None and not is_temporal_profiles_existing:
            img_temp = np.array([], dtype=int)
            images = []
            for f in os.listdir(self.TIME_SERIES_FOLDER):
                file = os.path.join(self.TIME_SERIES_FOLDER, f)
                if os.path.isfile(file):
                    img_temp = np.append(img_temp, int(f[:8]))
                else:
                    print("Error: Your time series images names must be in the format \"YYYYMMDD\"")
                    sys.exit(-1)
```

```
        sys.exit(-1)

    img_temp = np.sort(img_temp)
    for date in img_temp:
        images.append(os.path.join(self.TIME_SERIES_FOLDER, "{}.{}".format(str(date), "tif")))

    print("### Computing temporal profile of each polygon... |1/5| ###")
    from rasterstats import zonal_stats as zs
    nbPolygons = len(fiona.open(self.SHAPE_FILE))
    nbImages = len(images)
    timeSeries = np.zeros((nbPolygons, nbImages))
    for imageNb in range(0, nbImages):
        print("Computing statistics for {} ({} over {})...".format(os.path.basename(images[imageNb]), imageNb + 1, nbImages),flush=True)
        stats = zs(self.SHAPE_FILE, images[imageNb], stats=['mean'], nodata=self.NO_DATA)

        # For each polygon...
        for lineNb in range(0, len(stats)):
            line = stats[lineNb]
            # Replace mean values that do not respect user's configuration by numpy nodata value.
            if (not self.MAX_VALUE == None) and (not self.MIN_VALUE == None):
                if line['mean'] == None or line['mean'] > self.MAX_VALUE or line['mean'] < self.MIN_VALUE:
                    timeSeries[lineNb][imageNb] = np.nan
                else:
                    timeSeries[lineNb][imageNb] = line['mean']
            elif (not self.MAX_VALUE == None):
                if line['mean'] == None or line['mean'] > self.MAX_VALUE:
                    timeSeries[lineNb][imageNb] = np.nan
                else:
                    timeSeries[lineNb][imageNb] = line['mean']
            elif (not self.MIN_VALUE == None):
                if line['mean'] == None or line['mean'] < self.MIN_VALUE:
                    timeSeries[lineNb][imageNb] = np.nan
                else:
                    timeSeries[lineNb][imageNb] = line['mean']
            else:
                if line['mean'] == None:
                    timeSeries[lineNb][imageNb] = np.nan
                else:
                    timeSeries[lineNb][imageNb] = line['mean']

    print("---TEMPORAL PROFILES COMPUTED---\n")
    #In case the user asked to save the temporal profiles
    if is_temporal_profiles_defined:
```

```
    if is_temporal_profiles_defined:
        print("Exporting temporal profiles to {}...\n".format(self.TEMPORAL_PROFILES))
        outfile = open(self.TEMPORAL_PROFILES,'w')
        for polygon in range(0,nbPolygons):
            for image in range(0, nbImages):
                outfile.write(str(timeSeries[polygon][image]))
                outfile.write("\n")
            outfile.write("*\n")
        outfile.write("end")
        outfile.close()
        print("Temporal profiles saved !\n")
elif is_temporal_profiles_existing:
    readFile = open(self.TEMPORAL_PROFILES, 'r')
    line = readFile.readline().rstrip()
    if not line == "":
        readFile.seek(0)
        timeSeries = []
        column = []
        end = False
        while not end:
            line = readFile.readline().rstrip()
            if line == "*":
                column = np.array(column)
                timeSeries.append(column)
                column = []
            elif line == "nan":
                column.append(np.nan)
            elif line == "end":
                end = True
            else:
                column.append(float(line))
        timeSeries = np.array(timeSeries)
        print("---TEMPORAL PROFILES IMPORTED---\n")
    else:
        print("ERROR: EMPTY TEMPORAL PROFILES FILE !")
        sys.exit(-1)
    if not readFile.closed:
        readFile.close()


print("### Fill empty temporal profiles... |2/5| ###")
# Check for empty polygon temporal profile
print(timeSeries.shape)
```

```
        print("### Fill empty temporal profiles... |2/5| ###")
        # Check for empty polygon temporal profile
        print(timeSeries.shape)
        print(timeSeries[0].shape)
        print(timeSeries[1].shape)
        print(timeSeries[2].shape)
        emptyPolygonsIds = []
        i = 0
        while (i < len(timeSeries)):
            j = 0
            canContinue = True
            while (j < len(timeSeries[i])) and (canContinue == True):
                if not np.isnan(timeSeries[i][j]):
                    canContinue = False
                j += 1
            if canContinue == True:
                emptyPolygonsIds.append(i)
            i += 1

        # Fill empty temporal profiles with NO_DATA value
        for i in emptyPolygonsIds:
            for j in range(0, len(timeSeries[i])):
                timeSeries[i][j] = self.NO_DATA
        print("---FILLED {} EMPTY TEMPORAL PROFILES---\n".format(len(emptyPolygonsIds)))

        print("### Performing linear interpolation on missing temporal profile values... |3/5| ###")
        import pandas as pd
        interpTS = timeSeries.copy()
        for i in range(0, interpTS.shape[0]):
            serieInterp = pd.Series(interpTS[i]).interpolate(method='linear')
            interpTS[i] = np.array(serieInterp)

        #Replaces NaN values of first temporal index by the following values (havn't been removed by linear interpolation)
        for i in range(0, interpTS.shape[0]):
            if np.isnan(interpTS[i][0]):
                interpTS[i][0] = interpTS[i][1]
        print("---LINEAR INTERPOLATION DONE---\n")

        print("### Temporal profiles lustering |4/5| ###\n")
        from sklearn.cluster import KMeans
        if self.NB_CLUSTERS == None:
            print("Computing best number of clusters (may take some time)...")
```


```
        print("### Temporal profiles lustering |4/5| ###\n")
        from sklearn.cluster import KMeans
        if self.NB_CLUSTERS == None:
            print("Computing best number of clusters (may take some time)...")
```


```
            from sklearn.metrics import silhouette_score
            best = (-1,-1)
            for i in range(self.NB_CLUSTERS_MIN, self.NB_CLUSTERS_MAX + 1):
                kmeans = KMeans(n_clusters=i).fit(interpTS)
                score = silhouette_score(interpTS,kmeans.labels_)
                if score > best[1]:
                    best = (i,score)
            self.NB_CLUSTERS = best[0]
        print("---BEST NUMBER OF CLUSTERS: {}---".format(self.NB_CLUSTERS))


        print("Performing K-Means clustering...")
        kmeans = KMeans(n_clusters=self.NB_CLUSTERS,n_init=10).fit(interpTS)
        labels = kmeans.labels_
        print("---CLUSTERING FINISHED---")

        print("### Exporting shapefiles (one file per label) |5/5|")
        with fiona.open(self.SHAPE_FILE, 'r') as shapes:
            source_driver = shapes.driver       source_crs = shapes.crs
            source_schema = shapes.schema
            for label in range(np.max(labels) + 1):  # nb of labels
                shapeFile = fiona.open("{}/{}.shp".format(self.OUTPUT,label), 'w',
                                       driver=source_driver, crs=source_crs, schema=source_schema)
                for polygonId in range(0, len(shapes)):
                    if labels[polygonId] == label:
                        shapeFile.write(shapes[polygonId])
                print("Label {} shapefile exported !".format(label))
                shapeFile.close()
        if not shapes.closed:
            print("Warning: Polygons shapeFile not closed correctly !")

        print("---SHAPEFILES EXPORTED---")


if __name__ == "__main__":
    Obiats()
    sys.exit()
```

Turnitin Originality Report

Processed on: 14-Nov-2022 23:52 EAT
ID: 1953964811
Word Count: 80445
Submitted: 1

ao By A O

Similarity Index	Similarity by Source	
14%	Internet Sources:	14%
	Publications:	8%
	Student Papers:	1%

7% match (Internet from 20-Oct-2022)
https://www.int-arch-photogramm-remote-sens-spatial-inf-sci.net/XLIII-B3-2021/347/2021/isprs-archives-XLIII-B3-2021-347-2021.pdf

7% match (Internet from 30-Dec-2021)
https://hal.archives-ouvertes.fr/hal-03213874/file/isprs-annals-V-3-2020-525-2020.pdf

1% match (A. Osio, M. T. Pham, S. Lefèvre. "SPATIAL PROCESSING OF SENTINEL IMAGERY FOR MONITORING OF ACACIA FOREST DEGRADATION IN LAKE NAKURU RIPARIAN RESERVE", ISPRS Annals of Photogrammetry, Remote Sensing and Spatial Information Sciences, 2020)
A. Osio, M. T. Pham, S. Lefèvre. "SPATIAL PROCESSING OF SENTINEL IMAGERY FOR MONITORING OF ACACIA FOREST DEGRADATION IN LAKE NAKURU RIPARIAN RESERVE", ISPRS Annals of Photogrammetry, Remote Sensing and Spatial Information Sciences, 2020

MONITORING OF TREE SPECIES USING OBJECT BASED TIME SERIES ANALYSIS: -A CASE STUDY OF ACACIA XANTHOPHLOEA SPP IN LAKE NAKURU NATIONAL PARK, KENYA. ANNE ACHIENG OSIO B.Sc. (TUK); M.Sc. (Egerton) EEGX/06446P/2017 A Thesis Submitted in Partial Fulfilment of the Requirements for the Award of the Degree of Doctor of Philosophy in Geoinformatics in The School of Surveying and Spatial Sciences of The Technical University of Kenya (November, 2022) 1 DECLARATION This Thesis is my original work and has not been presented in any other Institution for a degree award or other qualification. ANNE ACHIENG OSIO REG. No EEGX/06446P/2017 Signature...Date.. This Thesis has been submitted with our Approval as Supervisors Signature........ ....Date..........10/11/2022.................. PROF. SEBASTIEN LEFEVRE UNIVERSITY OF SOUTH BRITTANY, VANNES, FRANCE Signature.................................Date... DR. SAMSON AYUGI THE TECHNICAL UNIVERSITY OF KENYA. i DEDICATION This work is dedicated to my entire family, friends and colleagues, who made this journey possible. Thank you all for your support and encouragement. May God bless you. ii ACKNOWLEDGMENT I would wish to thank the institutions and persons whose assistance and guidance were instrumental in the completion of this project: I want to express my thankfulness to God, without whom I could not have finished my course. My earnest gratitude to my supervisors, Dr. Samson Ayugi and Prof. Sebastien Lefèvre, for their advice throughout this study. The Kenya National Research Fund (K-NRF), the Kenya National Council for Science, Technology, and Innovation (NACOSTI), The University of South Brittany (UBS), The Hubert Curien Partnership (PHC), and Campus France were the organizations that provided funding for the collaboration between The Technical University and the University of South Brittany (UBS), France. Sincere thanks to Dr. Kirui and Dr. Simon Langat (NACOSTI), who in the initial stages made arrangements for my internship at the UBS Laboratory in France. To Dr. Onsare, who took up the responsibility of grants management from NACOSTI. To Kenya wildlife services (KWS) who gave us the chance to conduct Drone surveys at Lake Nakuru National Park. To The Technical University Vice-Chancellor Prof. Francis Aduol, who has consistently provided me study leave whenever